In situ and *ex situ* characterization studies of transition metal containing nanoporous catalysts

Martin Martis

University College London

A thesis presented in partial fulfilment of the
requirements for the degree of Doctor of Philosophy

2011

Declaration

I, Martin Martis, confirm that the work presented in this thesis is my own. Where information has been derived from other sources, I confirm that this has been indicated in the thesis.

Abstract

The research within this thesis has concentrated around characterization of nanoporous catalysts with metals incorporated or substituted inside the framework, and inside the cavities as small clusters, and in very low concentrations. The main objective has been to advance the understanding of the structure and active sites, and relate them to their catalytic properties through the use of combination *in situ* and *ex situ* methods and in some cases combination with optical spectroscopic techniques. Characterisation methods include synchrotron radiation based techniques, high-resolution powder diffraction (HRPD) and X-ray absorption spectroscopy (XAS), and laboratory based X-Ray Diffraction (XRD), Infrared Spectroscopy (IR), Raman Spectroscopy (RS), Scanning Electron Microscopy (SEM) and Transmission Electron Microscopy TEM

A combination of techniques is used to investigate cobalt substituted AlPO-18 prepared by different compositions. The determination of the nature of cobalt ions, in particular their location in the samples was carried by XAS. Additionally, a new *in situ* IR cell was developed which allowed to determine the nature of the redox chemistry of cobalt ions in the samples.

Structural changes during calcinations and methanol to olefins reaction (MTO) were studied on transition metals substituted (Co, Zn, Si) small pore AlPO-18. Using diffraction methods it was possible to accurately determine the changes in the lattice parameters and correlate this with metal ion incorporation into the lattice, and also determine the negative thermal properties of these materials prior to catalytic reactions; the study also allowed us to follow their stability during calcination. High energy X-ray diffraction (HEXRD PDF method) measurements gave an insight into the direction of possible lattice contraction during calcination which may be related to shape-selective catalytic properties of these solids.

Characterization of a series of vanadium containing ZSM-5 was carried by *in situ* XAS and Raman spectroscopy. The catalytic activity was very different, and detailed understanding of the vanadium environment using XAS and Raman spectroscopy provided an insight into the nature of vanadium ions in the zeolites.

In the last part of the thesis, a series of platinum impregnated zeolite beta and ferrierite were characterized to understand how the nano clustered platinum metal particles (active centres) were created during activation, and the study also allowed us to estimate the size and sitting of the platinum cluster inside the zeolite lattice.

Table of Contents

Chapter 2 Experimental Methods 51

List of Figures

List of Tables

List of Equations

List of Abbreviations

JM	Johnson Matthey Plc.
XAS	X-ray absorption Spectroscopy
EXAFS	Extended X-ray Absorption Fine Structure
XANES	X-ray absorption Near Edge Structure
LCF	Linear Combination Fit
WLI	White Line Intensity
XRD	X-ray Diffraction
HRPD	High Resolution Powder Diffraction
HEXRD	High Energy X-ray Diffraction
XES	X-ray Emission Spectroscopy
PDF	Pair Distribution Function
IR	Infrared Spectroscopy
FTIR	Fourier Transform Infrared Spectroscopy
RAMAN	Raman Spectroscopy
SEM	Scanning Electron Microscopy
TEM	Transmission Electron Microscopy
HREM	High Resolution Electron Microscopy (TEM)
HAADF	High Angle Annular Dark Field (TEM)
UV-Vis	Ultraviolet-Visible Spectroscopy
DRS	Diffuse Reflectance (IR and UV Vis spectroscopies)
NTE	Negative Thermal Expansion
CCD	Charged-Coupled Device

Acknowledgements

I would like to thank my supervisor first of all Professor Gopinathan Sankar for his help, guidance, encouragement, and knowledge throughout the last few years. I would also like to thank my industrial supervisors Dr. Xavier Baucherel, Dr. Mike Watson, Dr. Tim Hyde from Johnson Matthey for their help and advice. Also I have to thank Mrs Michelle Coles from Johnson Matthey for sample preparation. Big thanks to Mike Sheehy for building the *in situ* FTIR cell. It has been a pleasure working with all of them and I appreciate them taking me on for this project.

Over the period of this research, I have obtained assistance and guidance from many people in UCL, Johnson Matthey, and all the staff at the BM26, BM29, and ID 26 beamlines of the ESRF synchrotron and to the staff at the I11 and B18 beamlines of Diamond Light Source, and would like to express my gratitude.

I would also like to say a big thank you to my friends and colleagues, Andy, Jon, Nazarudin, Rozie, Tom, Mohamed, Tiffany, Alistair, Jeff, Nuru for useful discussions, and brightening up the day during the time of my research project. In addition, I am extremely grateful to my brother Vladimir and Husn for very useful discussions and essentially for proof reading my thesis. Special thanks goes to all who I had a chance to work during beamtime for help, keeping awake, entertaining conversation, and all for many inspirational nights in the pub or student union.

I would like to thank my parents for their unconditional support and encouragement during all the stressful times that have passed during these years. Also big thanks to my brother, sister, Jamie, and to all my friends for support without whom none of this would have been possible.

Thank you all.

Chapter 1 Introduction

1.1 General introduction to nanoporous materials

Zeolites[1] form the largest group of nanoporous materials. They are characterized as crystalline aluminosilicates with a regular array of channels and pores with a diameter of up to 1 nm. A wider range of microporous zeolite-like materials are called zeotypes[2] where a T-atom is other than silicon (and aluminium), for example aluminophosphates (AlPO*s*). In general, nanoporous materials can be considered as ordered systems where the voids between the linked atoms have a free volume of between 0.25 nm and 100 nm in diameter[3]. The International Union of Pure and Applied Chemistry (IUPAC)[4] further classifies nanoporous materials into three categories based on their pore diameters:

- micropores are less than 2 nm in diameter
- mesopores are between 2 and 50 nm
- macropores have pores of greater than 50 nm.

Although nanoporous materials display a long-range periodic order which give rise to sharp diffraction peaks, many materials produce only short-range order with respect to atomic arrangement (amorphous) but contain pores of uniform size with long-range order. Diffraction maxima for such materials are seen at *d*-values reflecting the pore-to-pore distance. An example is MCM-41 which shows one large diffraction maxima at 3.98 nm[5].

The scientific and technological importance of nanoporous materials is vast, mainly due to their ability to adsorb and interact with atoms, ions and molecules on the large internal surfaces.

1.2 Structural chemistry of nanoporous materials

Typically, the structure of a nanoporous material constitutes corner-sharing TO_4 tetrahedra, where T is any tetrahedrally coordinated cation[6]. The TO_4 tetrahedra are called the primary building units (*PBU's*). Individual tetrahedra may then link together by sharing apical oxygen to form secondary building units (*SBU's*) as shown in **Figure 1.1**.

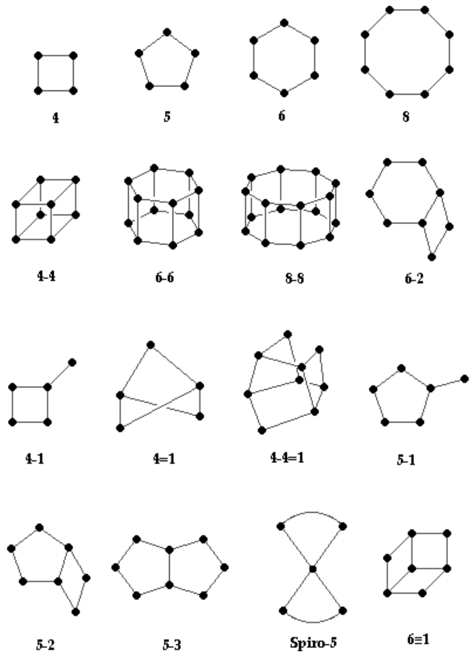

Figure 1.1. *Secondary Building Units (SBU's) in zeolites. The corner of the polyhedra represent tetrahedral atoms*[3].

Each dot in **Figure 1.1** represents the T atom of the TO_4 tetrahedron, and oxygen atoms are positioned at the mid-points of the lines between T-atoms, these are excluded from the image for clarity. SBU's contain up to 16 T atoms and are non-chiral, thus neither left nor right handed. A unit cell always contains the same number of *SBU's*, and although rare, some materials can have different combinations of *SBU's* within the zeolite framework[3].

Every porous structure can always be described in terms of size of the pore opening and the dimensionality of the channel system. The size of the ring that defines the pore at the pore opening is termed the *n*-ring, where *n* is the number of T-atoms on the ring. Other structural features common to several porous frameworks are cages, channels, chains, and sheets. Frameworks may be considered in terms of large polyhedral building blocks forming characteristic cages. For example, **Figure 1.2** displays the structures of four selected zeolites along with their respective void systems and pore dimensions[7]. The 24 tetrahedra linked together form a cubo-octahedron, or better known as sodalite unit or β-cage. Sodalite unit surface is defined by six 4-

membered rings and eight 6-membered rings, described as the $[4^6 8^8]$ cage. It is an important secondary building unit from which sodalite, zeolite A and zeolite X/Y (Faujasite) can all be generated.

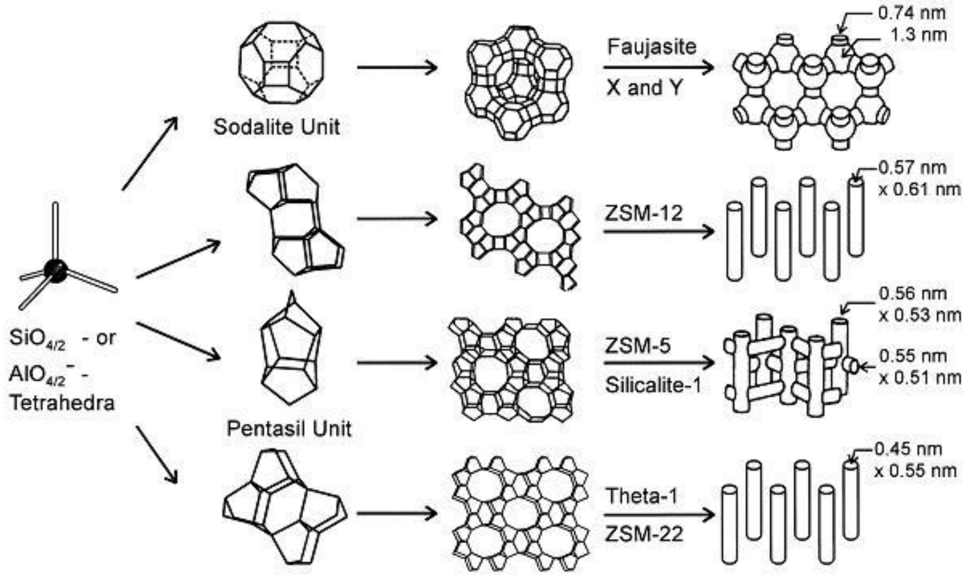

Figure 1.2. *Structures of four selected zeolites (from top to bottom: faujasite or zeolites X, Y; zeolite ZSM-12; zeolite ZSM-5 or silicalite-1; zeolite Theta-1 or ZSM-22) and their micropore systems and dimensions*[7].

Pentasil units are starting building blocks of zeolites ZSM-12 (12-membered-ring pores), ZSM-5 (10-membered-ring pores) and ZSM-22 (10-membered-ring pores which is isostructural to ZSM-12).

1.2.1 Zeolites

Zeolites form the largest group of nanoporous materials, and belong to a family of aluminosilicates which include 194 structures at present[8]. Many occur as natural minerals, but it is the synthetic varieties which are among the most widely used sorbents, catalysts and ion-exchange materials in the world[9]. Properties of zeolites are governed by their structures[6]. Ion-exchange capacity depends on the number, nature, and accessibility of the cation sites. Sorption capacity is closely related to the size of the pore openings and void volume. Similarly, shape selectivity and catalytic activity rely on pore openings and the dimensionality of the channel system. Particularly the ability of nanoporous materials to act as hosts in nanocomposite systems depends on the size and spacing of the cages.

The structure of a zeolite consists of 3-dimensional corner-sharing Si(IV)O_4 and Al(III)O_4 tetrahedra linked by oxygen atoms[6].

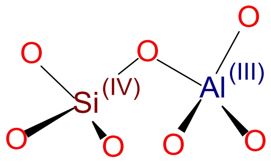

Figure 1.3. *Graphical representation of tetrahedral units of zeolites.*

The pure silicate zeolite framework is neutral. The negative charge deficiency in aluminosilicate framework is the result of Si(IV) replacement by Al(III). This negative charge has to be counter-balanced by mono- or di-valent cations, such as Na(I), K(I), Ca(II), Mg(II), or hydroxyl protons forming a weak Lewis acid site or a strong Brönsted acid site, respectively[10]. Hence, the chemical composition of an aluminosilicate zeolite can be represented by a formula of the type

Equation 1.1. *Chemical composition of an aluminosilicate zeolite.*

$$A^{m+}_{y/m}\left[(SiO_2)_x \cdot (AlO_2^-)_y\right] \cdot zH_2O,$$

where *A* is a cation with the charge *m*, *(x+y)* is the number of tetrahedra per crystallographic unit cell and *x/*y is the so-called framework silicon to aluminium (Si/Al)ratio n_{Si}/n_{Al}[11]. The hydroxyl protons acting as Brönsted acid sites are located on bridging oxygen atoms connecting silicon and aluminium cations on the framework positions. These are also known as structural or bridging OH groups (SiOHAl).

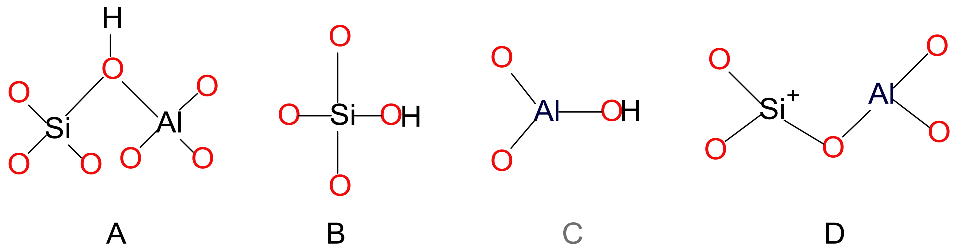

Figure 1.4. *Schematic representation of the different types of hydroxyl groups and acid sites in zeolites; (A) Bridging hydroxyl-Brönsted acid site; (B) silanol group; (C) extra-framework aluminium species; (D) Lewis acid sited at framework defects.*

Substitution of metal atoms (SiOHT, T = Al, Ga, Fe, etc.) on local positions of bridging OH groups can generate acid strengths of the hydroxyl protons which depend on the chemical behaviour of the substituting atoms. The acid strength and therefore the catalytic properties of the material are influenced by the metal atoms. In addition, the stability of a material is also directly affected by the charge imbalance caused by the substituted metal, hence silicates are more thermally stable than aluminosilicate[6].

The key feature affecting acid strength of SiOHAl groups and consequently the chemical behaviour of aluminosilicate zeolites is distribution of aluminium sites. The lower electronegativity of aluminium atoms in comparison to silicon forbids the direct linkage of two aluminium atoms by oxygen (Al-O-Al) (Lowensteins' rule), so the closest position of a second aluminium atom must be on the Next-Nearest-Neighbour position, or NNN-site[12]. Hence, the acid strength of SiOHAl groups in aluminosilicate zeolites depends on the number of framework aluminium atoms on NNN positions[12].

1.2.2 Introduction to Aluminophosphates

Similar to aluminosilicate zeolites, aluminophosphates (AlPO*s*) are highly crystalline microporous solids which can be prepared with different pore sizes ranging from large-, medium-, small-pores. They were first discovered at the Union Carbide Laboratories in 1982[13]. Their structures are constructed from strictly alternating, corner-sharing Al(III)O_4 and P(V)O_4 tetrahedral units[6] (where Al:P = 1)[14]. Due to the electro neutral-charge of the framework, substitution of metal ions into the aluminophosphate structure can introduce new and exciting properties. The isomorphic substitution of Al and P atoms in the framework is possible with many elements[15] and resulting materials are termed as: SAPO-*n* (S = Si), MeAlPO-*n*, (Me= Fe, Mg, Mn, Zn, Co, etc), MeSAPO-*n* and *n* is a structure type[16].

Redox and catalytic properties can be introduced by incorporation of metals into the framework[17]. Heteroatom incorporation can be achieved by incipient wetness impregnation, ion exchange or isoporphous substitution. Isomorphous substitution is of particular interest and is widely used for substitution in AlPO*s*. Flanigen et al.[18] are the first to propose rules for framework cation sitting of metal and silicon in AlPO frameworks:

I) Metal incorporation into a hypothetical Aluminium site

II) Silicon into a hypothetical Phosphorus site

III) Two Silicon for Aluminium + Phosphorus

In 1990 Martens and Jacobs[19] further elaborated the types of isomorphic substitution according to various substitution mechanism (SM). The classification is presented below and shown in the **Figure 1.5**:

i) SM I - substitution of Al(III) atoms. SM I*a*, SM I*b* and SM I*c* refer to monovalent, divalent and trivalent element substitutions of Al atoms, respectively, thus resulting in an M-O-P bond.

ii) SM II substitution of P atoms. SM II*a* and SM II*b* refer to tetravalent and pentavalent element substitutions, respectively, thus resulting in an M-O-Al bond.

iii) SM III substitution of pairs of adjacent Al and P atoms.

The origin of Bronsted acidity in SAPO*s* is the insertion of Si at the phosphorous site. This leads to the formation of negatively charged frameworks that are balanced by protons attached to Si-O-Al bridges (SM II mechanism)[16]. The substitution of silicon for aluminium (SM I mechanism) is another possible mechanism of Si insertion, which would lead to the formation of Si-O-P bridges but these are energetically unfavourable and have never been observed experimentally[16]. Often proposed mechanism for Si insertion is the SM III double substitution of neighbouring Al and P by two Si atoms, forming extended Si islands within the AlPO*s* frameworks[16].

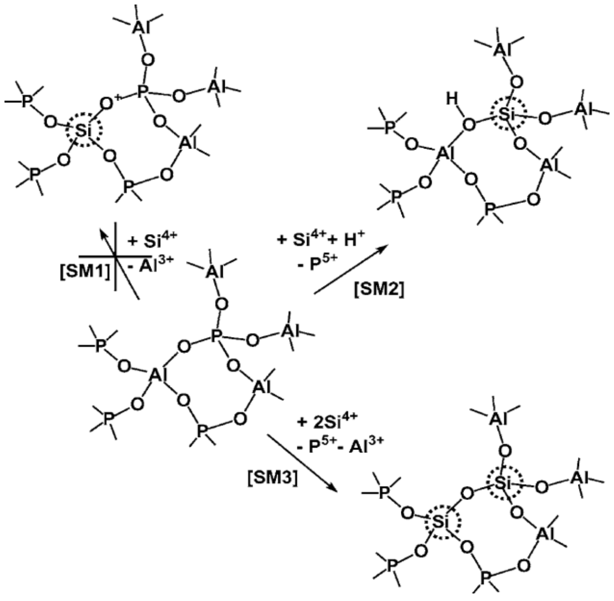

Figure 1.5. *Possible mechanism of the substitution of silicon for aluminium*[16].

Si is the only element that exhibits SM III substitution[15]. The net result when M(III) is substituted for Al(III) is a neutral framework structure and an anionic framework when M(II) substitutes for Al(III), thus the catalytic activity of each metal substituted $AlPO_4$ material depends upon the metal incorporated[9b]. For example, the incorporation of Co(II) cations for Al(III) cations generates one Brönsted acid site [Co(II)O(H)P] for each Co(II) cation incorporated in the structure. Oxidizing of Co(II) to Co(III) results in disappearance of the acid site and an electroneutral framework is generated in which [Co(III)O-P] sites are present (**Figure 1.6**).

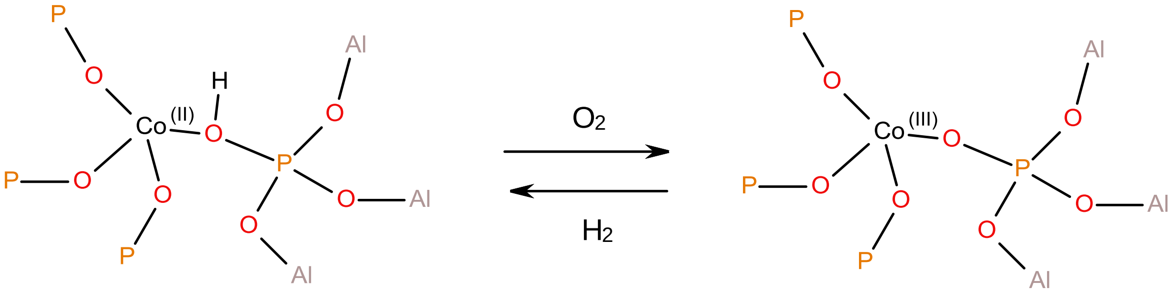

Figure 1.6. *The generation of Brönsted acid sites in cobalt substituted aluminophosphates.*

The evidence for this type of redox/acid behaviour on CoAPO-18 material was found by a combined EXAFS/XANES[20] and FTIR study[21], and subsequently confirmed by DR-UV-Vis and FTIR of probe molecules studies[22].

The introduction of silicon or divalent metal atoms in the AlPO framework leads to the appearance of Bronsted acidity relevant for acid-catalyzed reactions[16] such as methanol-to-olefins (MTO)[23], *n*-alkane cracking and hydrocracking[19, 24], oxidative dehydrogenation of alkanes[25], and more complex hydrocarbon transformations[26].

1.3 Classification of framework types

An ordered microporous or mesoporous material can be described in terms of a host structure, defined by a pore structure, that may contain guest species[27]. Therefore, the classification of nanoporous materials is based on the topology of the host structure that describes the connectivity without reference to chemical composition or observed symmetry. The nomenclature first used for classification of zeolites and zeolite-like materials has served as a basis for this terminology where the 3-dimensional framework is composed from corner sharing tetrahedra and shares the same host topology. Each confirmed porous framework type is assigned a three-letter code by the Structure Commission of the International Zeolite Association[8, 28] (IZA) and details of framework types are published in the Atlas of Zeolite Framework Types[28]. For example FAU is a code for a faujasite framework type, CHA for the zeolite chabazite and aluminophosphate AlPO-34. A three-letter code preceded by a hyphen has been assigned in a few cases to zeolite-like framework types that are not fully 4-connected (interrupted frameworks) such as that of the gallophosphate cloverite[28], whose topology has the code -CLO.

1.4 Preparation and modification of zeolites

The hydrothermal synthesis of a zeolite consists of two stages, the initial formation of the hydrated aluminosilicate gel and the crystallization process of the gel. In other words, the zeolite synthesis can be described as crystallization from an inhomogeneous gel created from silica and alumina sources, and a structure directing agent (SDA) in high pH (generated by high OH^- ion concentrations in water), and temperatures between 100-200 ^oC at different time frames[2, 9a]. Generally, the crystallization process consists of four stages:

- condensation of polysilicate and aluminate anions
- nucleation of zeolites
- growth of nuclei
- crystal growth of zeolites which sometimes results in secondary nucleation[15].

The formation process understanding is very difficult to achieve because it involves complicated chemical reactions, nucleation and growth of crystals under heterogeneous conditions, and the processes change over time. The synthesis are often affected by impurities present in the source material, and therefore, it is desirable to use pure chemicals as starting materials[29].

A typical synthesis process of zeolites containing sodium ions includes the mixing of sodium silicate ($Na_2O.xSiO_2$) and sodium aluminate ($NaAl(OH)_4$) in a basic medium with stirring until a homogeneous gel is formed, aging of the gel, and then crystallization in a sealed autoclave at elevated temperature and particular time. The resulting product is recovered and washed, dried and calcined to form the final molecular sieve[15]. Another important parameter for the control of the crystallization of zeolites is the alkalinity. It determines their composition and is to a great extent responsible for the type of the crystallization product[30]. In the systematic studies of the influence of the alkalinity on the product Si/Al–ratio, the alkalinity is generally used as a critical parameter. Silicate and aluminosilicate zeolites tend to crystallize at higher pH, where the OH- ion partially acts as a mineraliser and can be replaced by fluoride leading to a variety of new syntheses at lower pH values[30]. Generally, the kind of zeolites crystallized from the parent gel depends on many factors in the hydrothermal synthesis process and it is not yet clear how these factors work. The factors playing important role in the synthesis of zeolites are composition of the reactants, type and properties of the reactants, aging conditions, crystallization temperature and time, pH of the gel, inorganic or organic cations present in the synthetic system, the type of reaction container, and the Si/Al ratio present in the batch[15].

The Si/Al ratio in the synthesis gel plays an important role in determining the structure and composition of the final product, through there is no quantitative correlation between the Si/Al ratio in the product and in the batch composition[15]. Some aluminosilicate zeolites can be synthesized over a range of aluminium contents, for example ZSM-5 can be prepared with $Si/Al \approx 10$ to ∞. Additionally, a range of post-synthesis dealumination treatments of the framework have been developed which can be classified into thermal treatments, hydrothermal treatments, extraction of framework aluminium with acid and replacement of framework aluminium with silicon by reaction with silicon halides or hexafluorosilicates[31]. The removal of aluminium atoms from the framework of aluminosilicate zeolites is the most important origin for the occurrence of framework defects. Other properties affecting the framework aluminium content are the density of negative framework charges, the cation-exchange capacity, the density of Brönsted acid sites, their strength, the thermal stability, the hydrophilic or hydrophobic surface properties[27] and the unit cell dimensions. Depending on the dealumination conditions, healing of the framework defects by silicon migration, formation of silanol groups or formation of hydroxyl groups at extra-framework aluminium species may occur. Additionally, this might be the evidence for formation of Lewis acid sites at extra-framework aluminium species and framework defects[10]. Conversely, the aluminium insertion into the zeolite framework can also be achieved. The external surfaces of zeolite particles or framework defects are terminated by silanol groups whose acid strengths are low[10].

1.4.1 *Ion exchange*

The channels and cages of zeolites are usually filled with extra-framework species such as exchangeable cations (which balance the negative charge of the framework), removable water molecules, and or organic species. These can come from the synthesis mixture or they are the result of post-synthesis treatments. In the course of synthesis or post-synthesis treatment, small amount of transition metal ion can also be incorporated into the framework or extra-framework sites of the zeolite. In the post-synthesis treatment, these Brönsted acid sites can be generated by introducing ammonium ions followed by a heat treatment or by introducing multivalent metal cations, typically cations of the rare-earths, again followed by heat treatment[7].

Ion exchange is a very simple technique based on suspension of the zeolite in an aqueous solution of a soluble salt containing the desired cation. The conditions must be set to support the mass transfer, such as raised temperature (90 ^{o}C) and continuous stirring. This technique is limited by cations in the desired valence state or salts which are unstable or insoluble in water and cations which are too large to enter the to enter the zeolite pores. Alternatively, the specific cation can be incorporated by solid-state ion exchange. In this a H^+ form of zeolite and the specific cation containing compound are mixed and heated in inert gas[14, 32].

1.5 Preparation of aluminophosphates

Aluminophosphates (AlPO*s* and MeAlPO*s*) are typically prepared by hydrothermal synthesis with a structure directing agent (SDA) [33] which act both as a template (usually organic quaternary ammonium salts) and a space filling[17]. Aluminophosphates crystallization occur at 100-200 ^{o}C, in the absence of alkali elements, and typically in the pH range 3-10[6] the typical composition is[18]:

Equation 1.2. *Aluminophosphate starting gel composition.*

$$P_2O_5 : Al_2O_3 : xR : yH_2O$$

where x and y represent molar ratios, and R is the SDA. The amount of Al, P and R, the temperature, time, and pH are determining factors in the process of synthesis and in the successful crystallization of the desired product. The schematic route taken to produce aluminophosphates is shown in the **Figure 1.7**.

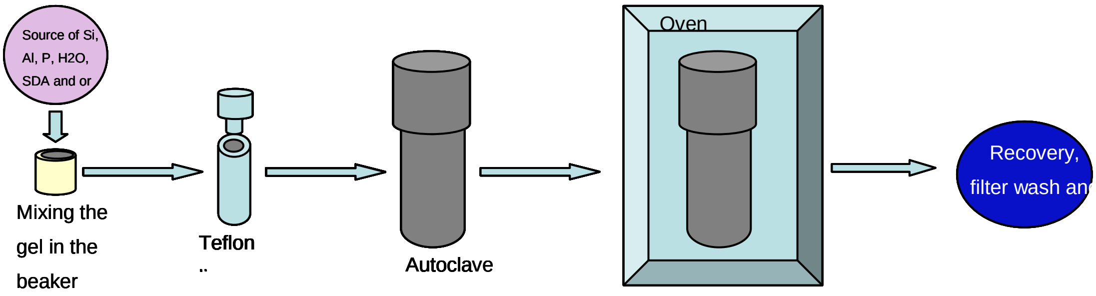

Figure 1.7. *Scheme of the synthesis procedure.*

Complications arise from the utilization of the SDA. For instance, one SDA is capable of producing more than one type of aluminophosphate framework. For example, one-dimensional AlPO-5 (AFI topology) [20, 34] structure can be formed by at least 25 different organic molecules, such as methyldicyclohexylamine (MCHA)[35], triethylamine (TEA) [36], tripropylamine (TPA) [37], ethyldicyclohexylamine (ECHA)[38] or tetraethylammonium hydroxide (TEAOH)[13, 39]. On the other hand, there are SDAs (templates) which can form a wide range of different structures under specific conditions. Perhaps the template with the least selectivity might be di- N-propylamine which is used to synthesise AlPO-11, -31, -39, -41, -43, -46, -50 and VPI-5[40]. It has to be noted, that the size and kind of the SDA cannot determine the type of the structure synthesized. In most cases, the preparation of microporous aluminophosphates is very sensitive to synthesis conditions and often yields multi-phase systems. Transition metal substitution complicates the matter further because the electronic balance in the gel is changed. The concentration and type of metal used, as well as the template concentration have a strong effect on the formation of the product. For those reasons, the overall synthetic conditions (starting gel ratio, raw materials, mixing, seeding, temperature, filling = pressure, drying, etc.) are very important. The gel chemistry and the interaction of the template with the developing structure play a very important role in forming the desired material inside the reactor[16]. SDAs are removed from the structure through calcination, i.e. heating the material in nitrogen and then oxygen at temperatures between 550 and 1000ºC[41], with most microporous AlPO*s* remaining intact after the removal of the organic molecule. SDA removal is essential to make AlPO*s* materials available for applications because the stability of the framework under industrial operating conditions is highly important. Most 3-dimensional microporous materials tend to stay intact after calcination; however with higher degrees of heteroatom inclusion the framework often becomes less stable. Further aspects that tend to play a role in synthesising a specific material are the synthesis duration and temperature, gel aging, agitation, the type of solvent used as well as the concentration of the solvent and the source of aluminium.

Typical aluminophosphate syntheses are performed in low to neutral pH conditions, although pH lower than 3 causes the appearance of dense phases such as $AlPO_4$-tridymite or quartz. pH's higher than 10 tend to either prevent the crystallization or solubilise the product, thus reducing yield[16]. Crystallization from a solution generally occurs by nucleation of a phase, or phases, dictated by the composition of the solution, followed by growth of the nuclei to larger sizes by incorporation of material from the solution[42]. Therefore, the composition of the solution is a major issue in the synthesis.

1.6 Preparation and synthesis

Principal reactants used in the zeolite synthesis include the silicon and aluminium source, metal ions, base, mineralizer, and water. In some cases, the inclusion of organic template or inorganic salts is crucial for the successful crystallization of the particular zeolite. Particularly, the source of silicon and aluminium are the two most important. The type of zeolite is determined by the reactant compositions[15].

1.6.1 Structure Directing Agents

The inclusion of a template (also termed as structure determining agent, or SDA) in the zeotype nanopores contributes to stability by forming new interactions such as hydrogen bonding, electrostatic and dispersion interactions. These control the formation of a particular topology through geometrical factors. The size and shape of an SDA dictates the structure formed, for example, tetramethylammonium (TMA^+) fits the sodalite cage and the ratio of Si/Al correlates to the occupation of cages of FAU materials [43].

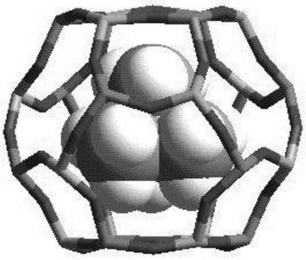

Figure 1.8. *Scheme of TMA+ locked in a sodalite cage.*

It is evident that changes in the cation density provoked by geometrical or physical properties of the template will be reflected in the chemical composition (Si/Al ratio) of a given topology. So far, the template theory has not been specific and able to give answers to the following observations:

i) one template can give rise to several different structures
ii) many templates can yield the same structure
iii) some structures require the presence of a particular template[44]

An example of the different structures obtained using the same template is shown in **Table 1.1.**

Table 1.1. *Structures obtained using TEA template[40b].*

Name	**Str. Code**	**Amine**
AlPO-18	AEI	TEAOH
AlPO5	AFI	TEAOH
SAPO-34	CHA	TEAOH

Many molecular sieves with large cages may also be templated by multiple small SDA*s* that are occluded in the cages[16].

The SDA*s* most effective in templating medium to high Si/Al zeolites and AlPO-based molecular sieves are quarternary ammonium cations. Increasing alkalinity favours the formation of aluminium rich zeolites. Zeolites with low Si/Al can be formed in a strong alkaline medium. Amines have previously been used to template AlPO-based molecular sieves and high-Si zeolites, and it is believed that the effective form of the amine is most certainly the protonated form in AlPO-based synthesis and probably the protonated form even at the higher pH range typical of the high Si zeolites[44].

Neutral molecules, cations or ion pairs, both organic and inorganic, are able to fulfil the structure- and composition-directing function. Some zeolites do not need an organic template to form, for example, formation of ZSM-5, or mordenite (MOR) which strongly depend on the Si/Al ratio[9a].

In aluminophosphates, water interaction with lattice aluminium through its oxygen atoms causes the formation of $AlO_4(OH_2)_2$ and these may bind to other water molecules through hydrogen bonding which results in formation of well structured water clusters within the aluminophosphate network[16]. The OH- bonded species in the lattice produces temporary negative charges which balance the occluded cationic template, whether quaternary ammonium or protonated amine[6].

The possibility of removing the cationic template and extra framework hydroxide with retention of the framework can be an important practical issue.

1.6.2 Temperature effect

The temperature and time also influences the type of zeolite which will crystallize. The temperature range for zeolitic synthesis is between 100-200 ^{o}C and the time varies from several hours up to days. Increasing temperature gives rise to denser phases, since under hydrothermal synthesis conditions the fraction of water in the liquid phase (which plays a role in stabilizing the porous products by filling the pores) becomes smaller. For instance, the initial product of the synthesis forms AlPO-5 but eventually forms tridimite. Therefore, there exist an upper temperature limit for the formation of each specific zeolite[9a].

1.6.3 Time effect

In the course of crystallization where the solid product is a mixture of zeolite and unreacted amorphous solids, the crystallinity of the product increases with time. However, zeolites are metastable phases and zeolite crystallization is governed, according to Ostwald's rule[45], by the occurrence of successive phase transformation. The least thermodynamically favourable phase crystallizes first, and is successively replaced, in time, by more stable (often denser) phases. A typical example is the crystallization sequence Na-Y – Na-P (gismondine type), or NaY – ZSM-4[9a, 43].

1.7 Properties of nanoporous materials

Applications of nanoporous materials application can be divided into the three traditional fields[15]:

1) separation, purification, drying and environment treatment processes;
2) petroleum refining, petrochemical, coal and fine chemical industries;
3) ion-exchange in detergents, radioactive waste storage removal and treatment of liquid waste.

Today, porous materials are also finding uses in new areas such as microelectronics, medical technologies, hydrogen storage and molecular device manufacturing[15].

The most important and prominent property of zeotypes is acidity which makes them ideal candidates for use in catalysis and shape-selective catalysis. The acidity needs to be understood in terms of[7]:

a) the nature of the acid sites (i.e. Brönsted vs. Lewis acidity),
b) the density or concentration of these sites,
c) their strength or strength distribution and, last but not least,
d) the precise location of the acid sites.

Shape selectivity depends on pore size which limits the entrance of the reacting molecule, the departure of the product molecule, or the formation of certain transition states[46]:

1. Reactant selectivity occurs when only part of the reactant molecules are small enough to diffuse through the catalyst pores (**Figure 1.9**).

2. Product selectivity occurs when some of the products formed within the pores are too bulky to diffuse out of the zeolite. They are either converted to less bulky molecules (e.g., by equilibration) or eventually deactivate the catalyst by blocking the pores (**Figure 1.9**).
3. Restricted transition-state selectivity occurs when certain reactions are prevented because the corresponding transition site would require more space than available in the cavities. Neither reactant nor potential product molecules are prevented from diffusing through the pores. Reactions requiring smaller transition states proceed unhindered.
4. Molecular traffic control may occur in zeolites with more than one type of pore system. Reactant molecules here may preferentially enter the catalyst through one of the pore systems while the products diffuse out by the other. Counter diffusion is thus minimized here.

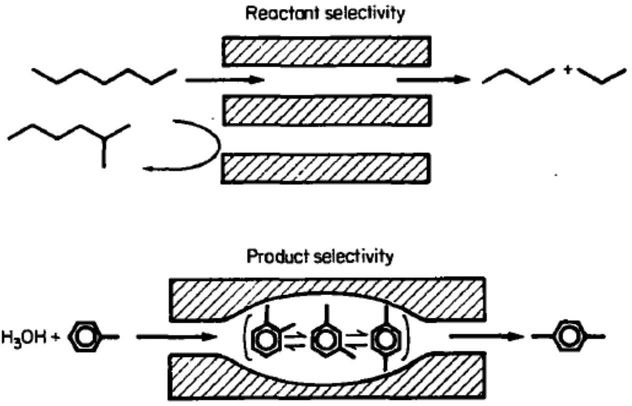

Figure 1.9. *Reaction selectivity and product selectivity*[46].

The shape-selective catalysis is controlled by diffusion. Hence, one type of molecule will react preferably and selectively at least one order of magnitude higher than that of competing molecular type. Large molecules will be unable to diffuse through small pores[46].

Acid zeolite catalysts are employed in various petroleum processes; for example, rare earth ultrastable zeolite Y is the main component in fluid catalytic cracking (FCC), and H-ZSM-5 is used as an additive for improving the octane number in gasoline production and enhancing the propane by-product[47]. Other petroleum refining processes that employ acid zeolites are benzene alkylation with ethane or propene, catalytic dewaxing, isomerisation of light gasoline, hydrocracking of heavy petroleum distillates, and isomerisation of xylenes[47].

1.7.1 Redox catalysis

A large number of organic reactions employing molecular sieves are selective oxidation. In organic chemistry, oxidations and reductions are different from ordinary redox reactions. In redox reactions, oxidation and reduction are defined as processes by which an element undergoes a net loss or gain of electrons, respectively. However, the oxidation of organic molecules is a process by which a carbon atom gains bonds to more electronegative elements, most commonly oxygen, and reduction is a process by which a carbon atom gains bonds to less electronegative elements, most commonly hydrogen. This definition is simplified and serves for quick identification of oxidation and reduction processes in organic reactions. In the **Figure 1.10** are displayed basic concepts applied to organic transformation of methane.

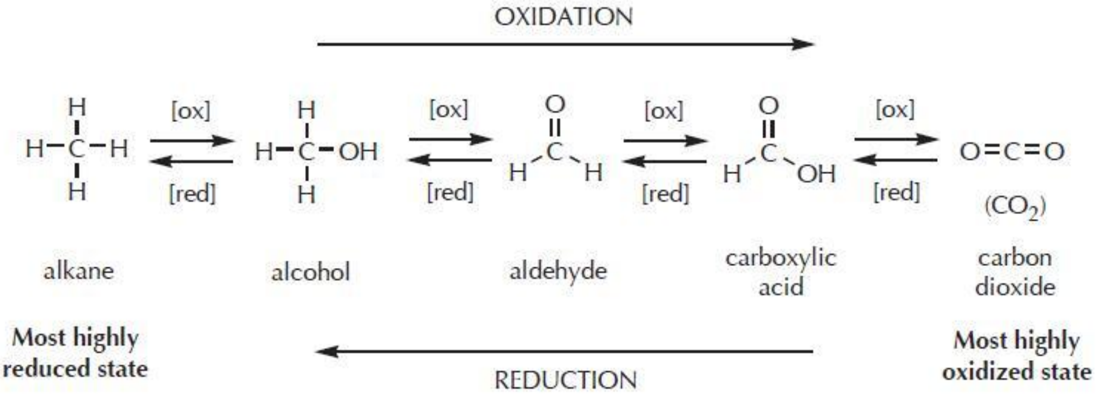

Figure 1.10. *Organic transformations of CH4, ox stands for oxidation, and red stands for reduction.*

In this case, a gain or loss of bonds means simply more or less bonds. Thus oxidation reactions are those in which the central carbon of a functional group is transformed into a more highly oxidized form, and reduction reactions are those in which the central carbon is transformed into a more highly reduced form. If several functional groups have the same oxidation state as the central carbon, the maximum oxidation state that a particular carbon can attain depends on how many other carbons it must remain attached to. Therefore, the maximum oxidation state possible for a carbon that is bonded to one other carbon is the carboxylic acid stage, and so on. This idea is illustrated in the **Figure 1.11**:

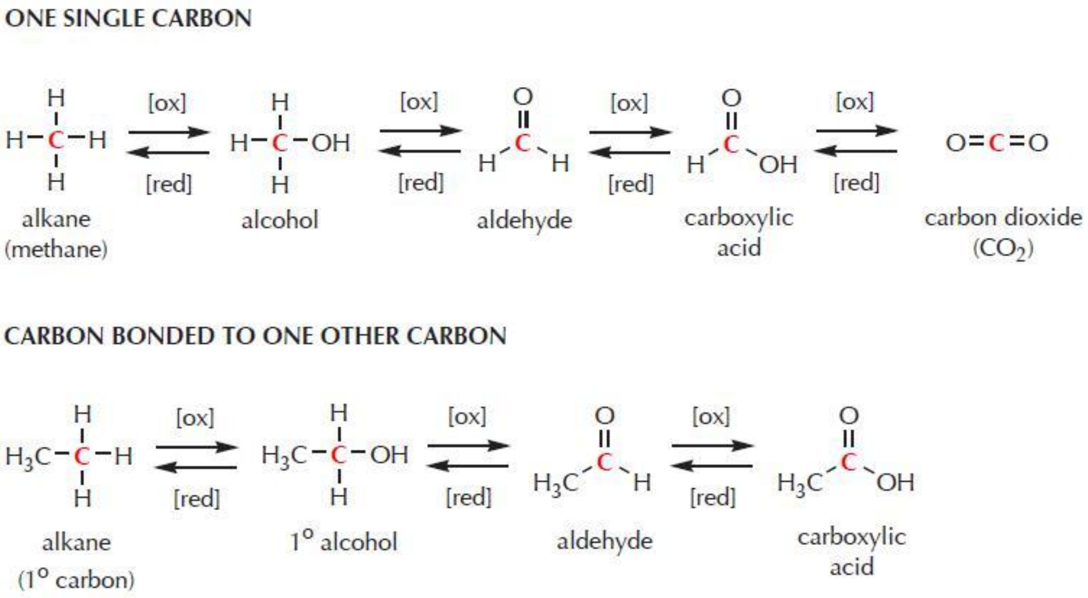

Figure 1.11. *Different stages during oxidation of methane and ethane.*

In addition, a substantial pressure is towards a development of environmentally friendly technologies, where the selective oxidation reactions make use of molecular oxygen or hydrogen peroxide and require minimal energy and produce minimal by-product waste. Alternative routes are sought to replace stoichiometric reactions that are environmentally unfriendly, expensive and largely inefficient[48].

Very promising materials able to achieve selective oxidation reactions using molecular oxygen are metal substituted aluminophosphate materials (MeAPO-*n*) which combine the useful catalytic reactivity of transition metal cations with a shape-selective environment provided by small channels. For example, SAPO-34 (structure related to chabazite), and MeAlPO-34 (where Me = Ni, Co) are very effective in converting methanol to both ethylene and propylene. Metal ion substituted AlPO-18 and AlPO-34 materials, in particular manganese or cobalt, can be employed to regio-selectively oxidise the terminal carbon atoms in *n*-hexane and other linear alkanes[23b, c, 24, 49]. In spite of these promising catalytic properties, hetero-atom substituted small-pore aluminophosphates have attracted considerable attention in the field of material science research.

1.7.2 Hydrogenation catalysis

The chemical reaction between an organic compound and hydrogen in the presence of a catalyst is called hydrogenation. There are several types of hydrogenation reactions, such as addition of hydrogen to unsaturated groups (for example in the reduction of ketones to alcohols), and addition of hydrogen across single bonds leading to cleavage of functional groups (hydrogenolysis). A second type of hydrogenation reactions involves breaking up a compound (hydrogenolysis, or destructive hydrogenation) and is of great importance in the petroleum industry. Hydrogenation is used extensively in industrial processes. Important examples are the synthesis of methanol from carbon monoxide, liquid fuels, hydrogenated vegetable oils, fatty alcohols from the corresponding carboxylic acids, cyclohexanol and cyclohexane from phenol and benzene, and hexamethylendiamine for the synthesis of nylon from adiponitrile[50,51,52].

Highly selective hydrogenation nanoporous catalysts can be prepared by impregnating noble metals inside a zeolite. The combination of shape-selectivity of the zeolite and hydrogenation function of the noble metal can improve the hydrogenation function. If selectivity to an intermediate product is required, zeolites with a hydrogenation function will not be preferred. Noble metals containing zeolites are beneficial to competitive hydrogenation reactions where only the molecules which are small enough to reach the catalytic site are expected to be converted[50,51].

This type of zeolite-based catalyst can achieve hydrogenation reactions, chemo-, regio- and stereoselectivity. Reactants having molecular dimensions close to those of the zeolite pores are expected to approach the metal cluster `end-on'. Thus, in the case of α,β-unsaturated aldehydes, this is expected to result in chemoselective hydrogenation to the unsaturated alcohol. Similarly, terminal olefins are expected to be converted more easily than internal double bonds (regioselectivity)[50,51].

1.8 Objectives of the study

The main objective of this thesis is the characterization of the active centres in metal containing aluminophosphate and zeolite materials. In order to perform detailed structural characterization of these catalysts and relate their structural properties to catalytic performance, it is important to use advanced synchrotron radiation techniques, in particular high-resolution powder diffraction (HRPD) and X-ray absorption spectroscopy (XAS). The aim is to use both *in situ* and *ex situ* methods and in some cases combine them with optical spectroscopic techniques.

In the first instance, the focus of the study was on small pore aluminophosphate systems containing cobalt, in particular CoAlPO-18 (AEI-type), and to determine the nature of the redox chemistry of cobalt ions in samples prepared by different chemical routes and compositions. CoAlPO-18 has been reported to be highly selective in oxidising terminal groups of a linear hydro-carbon but only if the cobalt is incorporated into the framework of the aluminophosphate. It has been shown by XAS that as prepared materials contain Co(II) ions which undergo a change in oxidation state to Co(III) in materials which contain cobalt in the framework[49c].

The aim of Chapter 3 was to prepare thermally stable CoAlPO-18 materials with a large concentration of Co ions incorporated into the framework. First, the ratio of aluminium to phosphorus (Al/P) in the starting synthesis gel, and the influence it has on the cobalt incorporation into the small pore aluminophosphate system was investigated by XAS and XRD. Secondly, the materials with constant Al/P = 1 ratio, but variable Co concentrations in the starting gel were investigated, together with the structural changes from the increased Co concentration. XRD and HRPD were the principal techniques in this investigation. Complementary to XAS, XRD, and HRPD, an *in situ* IR can be used as a screening technique for identifying the oxidation state of cobalt ions by creating a Brönsted acid centre during calcination process. For this purpose a novel *in situ* FTIR cell has been developed and built, which was used in determining the nature of redox chemistry of cobalt ions in samples prepared by different chemical routes and compositions.

In the Chapter 4, the best preparation methods identified in the previous chapter were used to prepare a transition metal substituted (Co, Zn, Si) small pore AlPO-18 materials. The structural changes taking place during calcination (activation) and MTO reaction were investigated by HRPD. These materials are known for negative thermal expansion during thermal treatment, which is an important property for catalytic reactions. Prior to HRPD studies, the cobalt substituted materials were studied by *in situ* XAS and FTIR to provide evidence for the presence of tetrahedrally coordinated metal ions. The metal incorporation in the other samples was confirmed by *in situ* FTIR.

HRPD study was carried out during calcinations and MTO reaction, which successfully showed that it is possible to accurately determine the changes in the lattice parameters and correlate this with metal ion incorporation. Not only was it possible to provide direct evidence for metal incorporation into the AEI-lattice by X-ray diffraction but also to determine the negative thermal coefficient of these materials and follow their stability during calcination. High energy X-ray diffraction (HEXRD) measurements gave an insight into the direction of possible lattice contraction during calcination which may be related to shape-selective catalytic properties of these solids.

The aim of Chapter 5 was to provide information about vanadium ions inside the zeolite ZSM-5, and correlate results back to the preparation methods of the materials. *In situ* XAS and *ex situ* Raman spectroscopy were used in this investigation.

Six materials were prepared by impregnation, and modified by post- and pre-synthesis methods after the initial impregnation. The catalytic activity was different, and therefore a detailed understanding of the vanadium environment can provide an insight into the nature of vanadium ions in the zeolites.

The aim of the Chapter 6 was to investigate the nature and location of platinum clusters impregnated into the zeolite ferrierite and beta. The size of Pt clusters inside the zeolites were studied by TEM. The changes of local environment of Pt during activation (reduction) were followed by XAS.

References

[1] a) D. W. Breck, W. G. Eversole and R. M. Milton, *Journal of the American Chemical Society* **1956**, *78*, 2338-2339; b) A. F. Cronstedt, *Ninth International Zeolite Conference* (Montreal) **1992**, pp. 3-9.

[2] A. Dyer, *An introduction to zeolite molecular sieves*, John Wiley & Sons, Chichester, **1988, 149**.

[3] L. B. McCusker, F. Liebau and G. Engelhardt, *Pure and Applied Chemistry* **2001**, *73*, 381-394.

[4] in *www.iupac.org*, International Union of Pure and Applied Chemistry.

[5] C. T. Kresge, M. E. Leonowicz, W. J. Roth, J. C. Vartuli and J. S. Beck, *Nature* **1992**, *359*, 710-712.

[6] H. van Bekkum, E. M. Flanigen, P. A. Jacobs and J. C. Jansen, *Introduction to zeolite science and practice*, 2nd edition, Elsevier, **2001, 1070**.

[7] J. Weitkamp, *Solid State Ionics* **2000**, *131*, 175-188.

[8] in *International Zeolite Association*, www.iza-online.org.

[9] a) R. M. Barrer, *Hydrothermal Chemistry of Zeolites*, Academic Press, **1982**; 348p. b) R. Szostack, *Molecular Sieves: principles of synthesis and identification*, 2nd ed., Blackie Academic & Professional, London, **1998,** 376p.

[10] J. Cejka, H. van Bekkum, A. Corma and F. Schuth, *Introduction to zeolite science and practice*, Elsevier, **2007**, 754p.

[11] J. Weitkamp, *Solid State Ionic* **1999**, *131*, 175-188.

[12] F. Tielens, W. Langenaeker and P. Geerlings, *Journal of Molecular Structure: THEOCHEM* **1999**, *496*, 153-162.

[13] S. T. Wilson, B. M. Lok, C. A. Messin, T. R. Cannan and E. M. Flanigen, *Journal of the American Chemical Society* **1982**, *104*, 1146-1147.

[14] M. E. Davis, *Industrial & Engineering Chemistry Research* **1991**, *30*, 1675-1683.

[15] R. Xu, W. Pang, J. Yu, Q. Huo and J. Chen, *Chemistry of Zeolites and Related Porous Materials: Synthesis and Structure*, Wiley, **2007**, 616 p.

[16] H. O. Pastore, S. Coluccia and L. Marchese, *Annual Reviews* **2005**, *35*, 351-395.

[17] S. T. Wilson and E. M. Flanigen, *Acs Symposium Series* **1989**, *398*, 329-345.

[18] E. M. Flanigen, B. M. Lok, R. L. Patton and S. T. Wilson, *Pure & Appl. Chem.* **1986** *58*, 1351-1358.

[19] J. A. Martens, P. J. Grobet and P. A. Jacobs, *Journal of Catalysis* **1990**, *126*, 299-305.

[20] P. A. Barrett, G. Sankar, C. R. A. Catlow, J. M. Thomas and Um, *Journal of Physical Chemistry* **1996**, *100,* 8977-8985.

[21] a) L. Marchese, J. S. Chen, J. M. Thomas, S. Collucia and A. Zecchina, *The Journal of physical chemistry* **1994**, *98*, 13350-13356; b) L. Marchese, E. Gianotti, N. Damilano and S. Coluccia, *Catalysis Letters* **1996**, *37*, 107-111.

[22] A. A. Verberckmoes, B. M. Weckhuysen and R. A. Schoonheydt, *Microporous and Mesoporous Materials* **1998**, *22*, 165-178.

[23] a) Z. Zhu, M. Hartmann and L. Kevan, *Chemistry of materials* **2000**, *12*, 2781-2787; b) M. Stocker, *Microporous and Mesoporous Materials* **1999**, *29*, 3-48; c) J. Chen, P. A. Wright, J. M. Thomas, S. Natarajan, P. L. Gai-Boyes, R. P. Townsed and C. M. Lok, *Journal of Physical Chemistry* **1994**, *98,* 10216-10224.

[24] a) L. Wang, C. Guo, S. Yan, X. Huang and Q. Li, *Microporous and Mesoporous Materials* **2003**, *64*, 63-68; b) B. L. Su, A. Lamy and S. Dzwigaj, *Applied Catalysis. A, General* **1991**, *75,* 311-320.

[25] L. Marchese, A. Frache, G. Gatti, S. Coluccia, L. Lisi, G. Ruoppolo, G. Russo and H. O. Pastore, *Journal of Catalysis* **2002**, *208,* 479-484.

[26] C. M. Lopez, K. Rodriguez, B. Mendez, A. Montes and F. J. Machado, *Applied Catalysis. A, General* **2000**, *197,* 131-139.

[27] J. C. Jansen, M. Stocker, H. G. Karge and J. Weitkamp, *Advanced Zeolite Science and Applications*, **1994**.

[28] C. Baerlocher, L. B. McCusker and D. H. Olson, *Atlas of Zeolite Framework Types, 6th edition*, Elsevier, Amsterdam, **2007**, 404 p.

[29] G. Kuhl in *Source material for zeolite synthesis, Vol. second* (Ed. H. Robson), Elsevier, London, **2001**, pp. 19-20.

[30] H. Lechert in *The pH-value and its importance for the crystallization of zeolites, Vol. 2* (Ed. H. Robson), Elsevier, London, **2001**, pp. 33-38.

[31] J. Weitkamp and L. Puppe, *Catalysis and Zeolites*, Springer-Verlag, Berlin Heidelber New York, **1999**, 564 p.

[32] H. G. Karge and J. Weitkamp, *Post-Synthesis Modification I,* Springer, **2002**.

[33] M. G. O'Brien, M. Sanchez-Sanchez, A. M. Beale, D. W. Lewis, G. Sankar and C. R. A. Catlow, *Journal of Physical Chemistry C* **2007**, *111,* 16951-16961.

[34] G. Sankar, R. Raja and J. M. Thomas, *Catalysis Letters* **1998**, *55,* 15-23.

[35] M. Sanchez-Sanchez, G. Sankar, A. Simperler, R. G. Bell, C. R. A. Catlow and J. M. Thomas, *Catalysis Letters* **2003**, *88*, 163-167.

[36] Y. Liu, R. L. Withers and L. Noren, *Solid State Sciences* **2003**, *5*, 427-434.

[37] O. Weiss, G. Ihlein and F. Schuth, *Microporous and Mesoporous Materials* **2000**, *35-6*, 617-620.

[38] J. M. Bennett, J. P. Cohen, E. M. Flanigen, J. J. Pluth and J. V. Smith, *Acs Symposium Series* **1983**, *218*, 109-118.

[39] D. J. Parrillo, C. Pereira, G. T. Kokotailo and R. J. Gorte, *Journal of Catalysis* **1992**, *138*, 377-385.

[40] a) B. M. Lok, C. A. Messina, R. L. Patton, R. T. Gajek, T. R. Cannan and E. M. Flanigen, *Journal of the American Chemical Society* **1984**, *106*, 6092-6093; b) H. E. Robson and K. P. Lillerud, *Verified syntheses of zeolitic materials, 2nd edition*, Elsevier, Amsterdam, **2001**, 267 p.

[41] J. Yu and R. Xu, *Chemical Society Review* **2006**, *35*, 593.

[42] R. W. Thompson in *Nucleation, growth, and seeding in zeolite synthesis*, *Vol. 2* (Ed. H. Robson), Elsevier, London, **2001**, pp. 21-23.

[43] in *UCL lectures in New Directions in Material Chemistry.*

[44] S. T. Wilson in *Templating in molecular sieve synthesis*, *Vol. 2* (Ed. H. Robson), Elsevier, London, **2001**, pp. 27-31.

[45] T. Threlfall, *Organic Process Research & Development* **2003**, *7*, 1017-1027.

[46] S. M. Csicsery, *Zeolites* **1984**, *4*, 202-213.

[47] a) K. D. Hammonds, V. Heine and M. T. Dove, *The Journal of physical chemistry B* **1998**, *102*, 1759-1767; b) A. W. Sleight, *Current Opinion in Solid State and Materials Science* **1998**, *3*, 128-131.

[48] N. R. Shiju and V. V. Guliants, *Applied Catalysis A: General* **2009**, *356*, 1-17.

[49] a) M. Dugal, G. Sankar, R. Raja and J. M. Thomas, *Angewandte Chemie* **2000**, *39*, 2310-2313; b) J. M. Thomas, R. Raja, G. Sankar and R. G. Bell, *American Chemical Society Journals* **2000**, *34*, 191-200; c) J. M. Thomas, R. Raja, G. Sankar and R. G. Bell, *Nature* **1998**, *398*, 227-230; d) R. Raja, G. Sankar and J. M. Thomas, *Chemical communications* **1999**, 829-830.

[50] E. J. Creyghton and R. S. Downing, *Journal of Molecular Catalysis A: Chemical* **1998**, *134*, 47-61.

[51] S. Nishimura, *Handbook of heterogeneous catalitic hydrogenation for organic synthesis,* John Wiley, New York, **2001**, 700 p**.**

[52] P. N. Rylander, *Hydrogenation methods*, Academic, London, **1985**, 193 p.

Chapter 2 Experimental Methods

2.1 Chapter Overview

The experimental techniques employed to examine the nanoporous materials within this thesis are described in this chapter. The chapter starts with an introduction to X-rays, and X-ray methods, X-ray diffraction (XRD) and X-ray absorption spectroscopy (XAS), followed by the data collection and data analysis. Other experimental methods mentioned are Infrared spectroscopy (IR), Raman Spectroscopy, total scattering, and high-energy-resolution fluorescence detection.

2.2 Introduction

The properties of nanoporous materials are controlled by their structure. Such properties include atomic arrangement and morphology, chemical composition, ability to sorb and retain molecules, and ability to chemically convert organic molecules. An extensive range of techniques are available to determine the structure and properties, in particular X-ray and neutron scattering, infrared spectroscopy (IR), Scanning Electron Microscopy (SEM), Transmission Electron Microscopy (TEM), X-ray absorption spectroscopy (XAS), and computational modelling. Utilizing only a single technique is limited to information about one particular structural characteristic of a material. Hence, a combination of characterization techniques is essential to provide comprehensive picture about structure of a complex nanoporous system[1].

X-ray scattering and spectroscopic techniques are the most widely used techniques for characterization of nanoporous materials, in that they are non-destructive, and can be used to study crystalline and amorphous materials at ambient as well as non-ambient conditions. X-rays are short-wavelength electromagnetic radiations, and are produced by either X-ray tubes or particle accelerators (synchrotron sources).

Laboratory X-rays, produced by X-ray tubes, are generated when a focused electron beam (electrons emitted by a heated tungsten filament or other material) accelerated across a high voltage field and bombards a stationary or rotating solid target. The cathode is electron emitter, and the electrons are attracted by the anode. As electrons collide with atoms in the target, a continuous spectrum of X-rays are emitted, which are termed Bremsstrahlung radiation[2]. The high energy incident electrons provide enough energy to allow ejection of inner *1s* (K-shell) electrons from atoms of the metal target through the ionization process. Consequently free outer orbital electrons (usually *2p* or *3p*) fill the empty *1s* shell, and X-rays specific to the orbital energy difference of the target material (anode) are emitted[3]. **Figure 2.1** shows characteristic *K*, *L,* and *M* X-ray line energies for elements with $3 \leq Z \leq 95$ (Z is the atomic number). Only the highest energy lines are included: $K\alpha_1$, $K\alpha_2$, $K\beta_1$, $L\alpha_1$, $L\alpha_2$, $L\beta_1$, $L\beta_2$, $L\gamma_1$, and $M\alpha_1$.

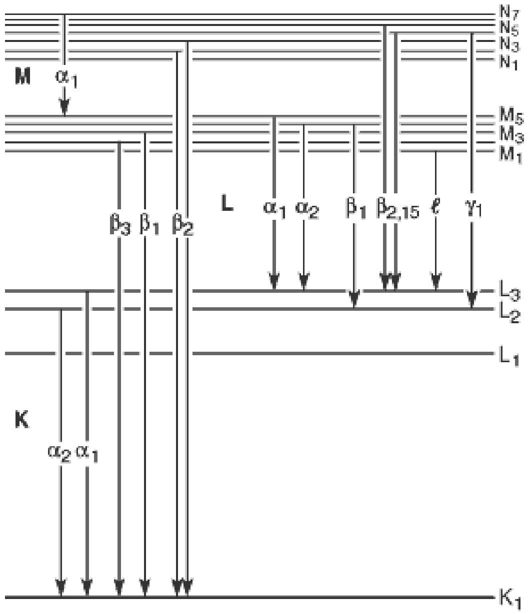

Figure 2.1. *Transitions that give rise to the various emission lines*[4].

Common targets used in X-ray tubes include Cu and Mo, which emit 8 keV and 17.5 keV X-rays with corresponding wavelengths of 1.54 Å and 0.71 Å, respectively.

2.2.1 Synchrotron radiation

Synchrotron radiation (SR) is the radiation which occurs when charged particles are accelerated to very high speed (close to speed of light) in a curved path or orbit. Wherever the trajectory bends, the particles accelerate, and emit electromagnetic radiation, called synchrotron radiation[5]. This can be better explained using a scheme of the European Synchrotron Radiation Facility (ESRF)[6] in Grenoble which operate with a 6-GeV storage ring , and the diagram is displayed **Figure 2.2**.

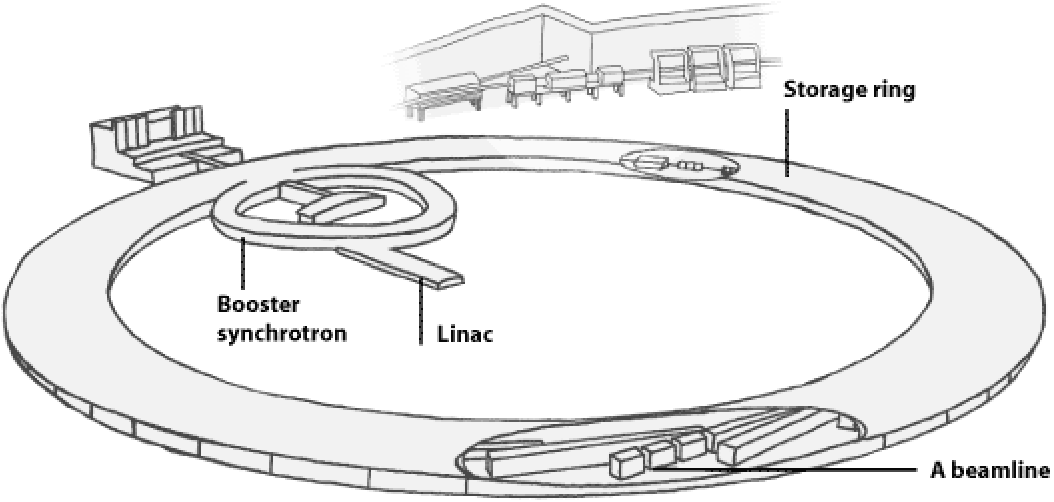

Figure 2.2. *A schematic illustration of the layout of the European Synchrotron Radiation Facility (ESRF) in Grenoble, France*[6].

The electrons are injected into the booster ring via a linear accelerator (Linac). The booster synchrotron accelerates the electrons up to 6 GeV, after which they are transferred to the storage ring. In the large storage ring (called synchrotron) which consists of evacuated pipes under ultrahigh (10^{-12} torr) vacuum, the electrons are constrained to orbit by passing through a powerful series of hexapole and quadrupole, and bending (dipole) magnets[5]. Quadrupole and sextupole magnets are used to keep the beam orbit stable in the directions transverse to the motion as well as the longitudinal direction along the beam path, and bending magnets are dipole magnets used to curve the electron beam around the storage ring[5].

The relativistic electrons travel in straight paths until they encounter a strong magnetic field in the vertical direction which is produced by bending magnets. While in the magnetic field, they experience a force that causes them to move in an arc with a radius of curvature on the order of tens of meters, after which they continue down another straight section. This continues until their path closes, so the path is more like a polygon with rounded corners than a circle. The same electrons recirculate for hours or days, while generating X-rays[5].

Wherever the path of the electrons bends, they accelerate, and therefore they radiate. The particle energy is replenished by passing the beam through RF cavities. Relativistic effects cause the radiation pattern to strongly tilt into the forward direction, i.e. in the same direction as the electron's instantaneous velocity. As the electrons sweep around their path the radiation is emitted in a fan that is of order $1/\gamma$ (radians) in angular width (perpendicular to the orbital plane), where $\gamma=E/mc^2$, where E is the electron energy, and mc^2 is the electron's rest energy (0.511 MeV)[5].

Bending magnets are used for conveying the synchrotron X-ray beam into the beamline and are capable to produce a very stable X-ray beam over a broad spectrum. The synchrotron X-rays can be inserted into the beamline by an insertion device, which produce more intense, tuneable X-ray beam. Insertion devices come in two main types: wigglers and undulators[5]. The differences in the radiation produced by different devices are compared in **Figure 2.3**.

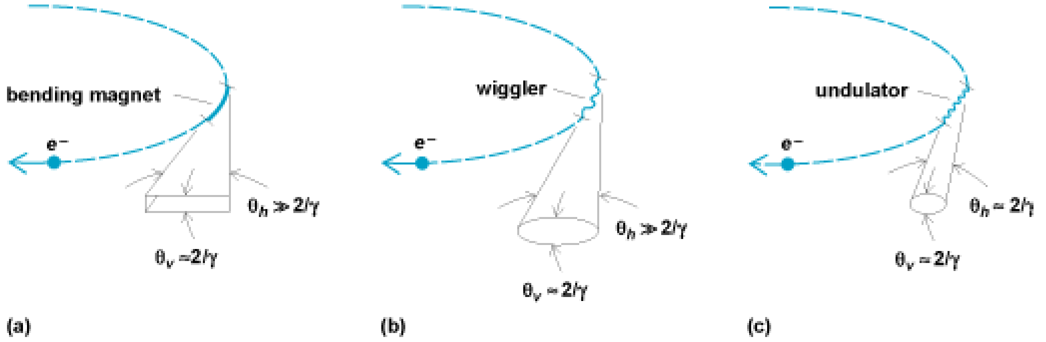

Figure 2.3. *Spatial characteristics of photon beams from (a) bending magnets, (b) wigglers, and (c) undulators*[7].

A wiggler produces a spectrum similar to that of a bending magnet radiation but with an angular excursion much larger than $1/\gamma$. Electrons are forced through a trajectory with a small radius of tight curvature, and results in a greater radial acceleration producing higher energy photons. This causes the light to be produced in a wide cone, spanning a broad spectrum of high energy X-rays of required wavelength[5].

Undulators are made up of a complex array of small magnets. They produce the electron beam and to execute transverse oscillations with an angular excursion of the order of $1/\gamma$. The beam of radiation emitted from an undulator is concentrated into a narrow, forward-directed cone with the smallest possible opening angle. The different bends of the undulator overlap and interfere with each other, which causes to generate a more intense beam of radiation than that generated by the bending magnets[5].

Focusing magnets are placed in the straight sections of the storage ring. They are used to focus the electron beam, and keep the beam in well defined and small in size. The small and well-defined electron beam will produce the very bright X-ray beam which is used for the experiments[6, 8].

There are several advantages to synchrotron radiation[9], and some of them are listed below:

- i) Intensity of synchrotron radiation is several orders of magnitude greater than laboratory X-ray sources. This allows fast data collection, investigations of very diluted samples, *in situ* reactions etc.
- ii) The wide spectrum of radiation ranges from the hard X-ray to the microwave.
- iii) Tunability of energy to an accuracy of better than 1 eV.
- iv) The beam is highly collimated in the plane of the synchrotron radiation (advantageous for powder diffraction experiments).
- v) The beam is strongly polarised in the plane of the synchrotron radiation (useful for probing magnetic systems).

2.3 X-ray diffraction

X-ray diffraction is an extremely powerful tool for the determination of the long range order in crystalline materials, which include nanoporous systems. The information obtained by XRD ranges from simple phase identification (or fingerprint) from known structures, to more advanced structure solution using refinement techniques from which good structural models are obtained[10]. This can include the positions of framework and extra-framework atoms, and sometimes properties such as average particle sizes and shapes[11].

2.3.1 Basic theory of XRD and Bragg's law

X-rays were first observed by W. C. Röntgen in 1895 during his studies of fluorescence induced by radiation from a cathode ray tube[12]. But it was more than ten years later that M. Laue thought to analyse the interaction of X-rays with crystals. Friedrich and Knipping, in collaboration with Laue and Ewald, built the first X-ray diffractometer and collected several patterns of well known crystals. The patterns revealed that the spot distribution varied with crystal orientation and followed simple symmetry rules for specific crystal orientations[13]. W.L. Bragg proposed that the interaction of X-rays could be explained in terms of reflection from crystal planes, which extend throughout the crystal, in so called Bragg's Law[10]:

Equation 2.1. *Bragg's law.*

$$n\lambda = 2d\sin\theta$$

there θ is the angle of the incident beam[14]. The variable d is the distance between atomic layers in a crystal, λ is the wavelength of the incident X-ray beam and n is an integer.

X-ray diffraction from crystals is an interference process that occurs when radiation of wavelength λ interact with a regular array of points whose interpoint spacing is of the same order of magnitude as λ. One way of looking at diffraction is to consider planes of lattice points such as those in **Figure 2.4**[2].

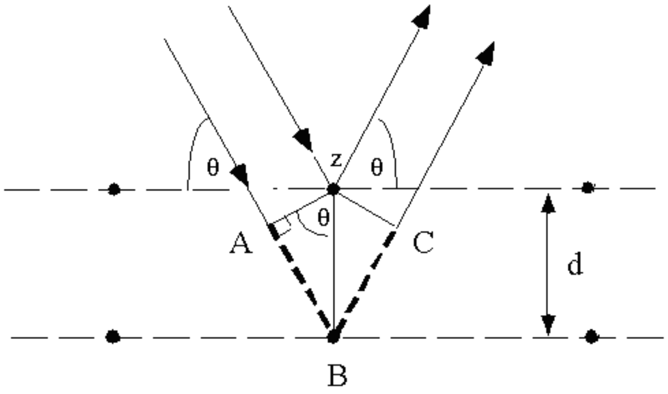

Figure 2.4. *Reflection of X-rays from two lattice planes belonging to the family H≡(h,k,l), d is the interplanar spacing*[14].

In other words, the Bragg's law states that the angles at which X-rays are reflected by a set of planes depend only on the *d*-spacing, if the wavelength is fixed. In the **Figure 2.4**, the A and B planes reflect at the same angle, and these two sets of reflection differ in phase to an extent that depends on *d*, λ, and they differ in amplitude if they arise from different atoms. Hence the resultant wave from the two sets of planes differs from its constituent waves in both phase and amplitude[3].

2.3.2 *Data collection*

Two experimental methods can be used to obtain diffraction pattern, independent of radiation:

1. The angular dispersive technique where the X-rays are monochromatic and the pattern is obtained by step-scanning the detector with small increments in 2θ. The 2θ stepsize is governed by instrumental, i.e. mechanical conditions of the diffractometer, and also by the time available to collect the diffraction pattern[11].
2. The energy dispersive technique where polychromatic X-rays are used and the energy of the diffracted X-rays is measured at a fixed diffraction angle 2θ using an energy dispersive detector. The energy dispersive technique is especially advantageous in experiments at extreme conditions or for kinetic studies, since the complete pattern is recorded at any given time[11].

In the laboratory condition, the angular dispersive technique of the powder diffraction data can be collected using either transmission or reflection geometry.

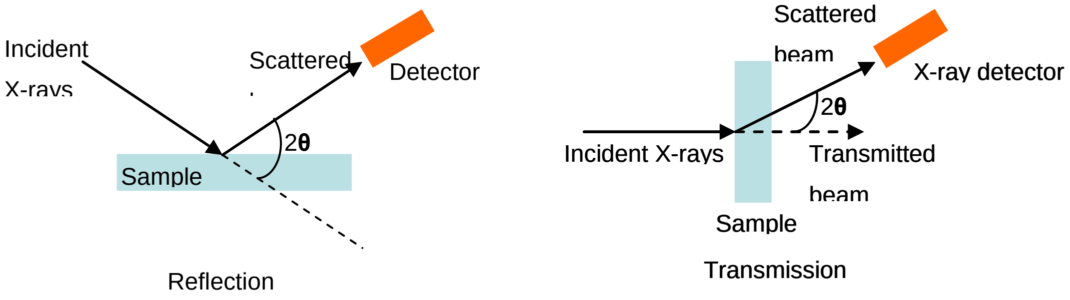

Figure 2.5. *A schematic illustration of XRD data collection. On the left side is reflection geometry and on the right is transmission geometry*[14].

Both these measurement geometries will yield the same information because of randomly oriented particles in powder samples[14]. The transmission geometry is a preferred choice if preferred orientation of the crystallites is suspected. Every crystallized solid material produces a unique diffraction pattern, exhibiting specific Bragg peaks which are used for its phase identification[15].

Powder diffraction

Powder XRD is the most widely used X-ray diffraction technique for characterizing materials when a single crystal is not available. The term 'powder' means that the crystalline domains are randomly oriented in the sample. Therefore when the 2-D diffraction pattern is recorded, it shows concentric rings of scattering peaks corresponding to the different *d* spacings in the crystal lattice. The positions and the intensities of the peaks are used for identifying the underlying structure (or phase) of the material[11].

The collapsing of the three-dimensional reciprocal space of the individual crystallites on the one-dimensional 2θ axis can result in the following consequences[3]:

- systematic overlap of diffraction peaks due to symmetry conditions
- accidental overlap caused by the limited experimental resolution
- difficult definition of the background
- non-random distribution of the crystallites in the specimen

The advantage of the powder diffraction to other methods is a relatively fast, non-destructive examination of multi- component materials, with relatively simple sample preparation[2]. These can be quickly analyzed, and identified by comparison to known standards or databases (such as International Centre for Diffraction Data, and Cambridge Structural Database). The powder diffraction also allows to determine the levels of crystallinity, phase transitions, lattice parameters, and size and strain broadening[11].

The analyses of powder diffraction pattern require the following steps[16]:

1) Collection of highly resolved powder diffraction patterns
2) Indexing the powder pattern
3) Determining the space group
4) Obtaining the integrated intensities
5) Refining of the structure by the Rietveld method.

The determination of the crystal structure from powder diffraction can be done, but it is extremely difficult due to overlap of the reflections in the experiment.

The atomic position within the cell is independent of the position of a diffraction peak, and is entirely determined by the size and shape of the unit cell. Each peak represents a certain lattice plane, and is characterized by a Miller index. The integrated intensities from a powder diffraction pattern can be obtained by two methods, the Pawley and Le Bail method[11]. The Pawley method is based on a non linear least squares refinement, and the integrated intensities are refinable variables in addition to the profile parameters (tens of parameters). The peak overlap can cause instability in the least squares, and sometimes provide negative integrated intensity values which must be discarded. For this reason the method needs positivity constraints. On the other hand, the Le Bail method is an iterative decomposition algorithm following the Rietveld formula, where the peak intensities are set to an arbitrary value (treated as calculated)[16].

In this thesis, the Pawley and Le Bail methods were used with the program Topas 4 Academic and FullProf. The profile shape functions commonly used in the profile fitting programs are:

$$Gaussian \qquad G = I_0 exp\left(-ln2\left(\frac{2\theta - 2\theta_0}{\omega}\right)^2\right)$$

$$Lorentzian \qquad L = I_0\left(1 + \left(\frac{2\theta - 2\theta_0}{\omega}\right)^2\right)^{-n} \qquad n = 1; 1.5; 2$$

$$Pseudo - Voigt \quad V = \eta L + (1 - \eta)G \quad (0 \leq \eta \leq 1)$$

$$Pearson\ VII \qquad P = I_0\left(1 + \left(\frac{2\theta - 2\theta_0}{ma^2}\right)^2\right)^{-m}$$

There the parameters are: $2\theta_0$ = peak position; I_0 = peak intensity; ω = *FWHM/2*; m = shape parameter; η = a variable proportion of pure Lorentzian to pure Gaussian[11].

The results of a refinement need to meet certain criteria, and have to be meaningful. The overall best criteria for the best fit are difference plots between observed and calculated data. In powder diffraction data, only R_p (profile factor) and R_{wp} (weighted profile factor) values (goodness of fit indicators) are of a real value, and are shown below[11].

Equation 2.2. *Profile Factor.*

$$R_p = \frac{\sum \left| y_i(obs) - \left(\frac{1}{c}\right) y_i(calc) \right|}{\sum w_i (y_i(obs))^2}$$

Equation 2.3. *Weighted profile Factor*

$$R_{wp} = \left[\frac{\sum w_i \left(y_i(obs) - \left(\frac{1}{c}\right) y_i(calc) \right)^2}{\sum w_i (y_i(obs))^2} \right]^{1/2}$$

There $y_i(obs)$ are the observed and $y_i(calc)$ the calculated intensity at each i, and w_i is the weighting factor.

2.4 X-ray absorption spectroscopy

X-ray absorption spectroscopy (XAS) is a very effective tool in studying the local structure around particular element at the atomistic and molecular level. The main advantage of XAS is that it can be applied not only to crystals, but also to materials that display minimal or no long-range order, such as glasses, amorphous materials, liquids, etc. *In situ* studies can be performed, not only during the formation of materials but also the activation process and of a particular reaction.

2.4.1 Basic principles of XAS

The absorption of an X-ray by an electronic core level can occur only if the binding energy of this core level is lower than the energy of the incident X-ray. During this process an electron may be removed from its core level (**Figure 2.6**). This results in absorption of the X-ray, and any released energy of the electronic binding energy is transferred to a photo-electron that is ejected from the atom. The full implications of this process when applied to molecules, liquids, and solids will give rise to XAS[17].

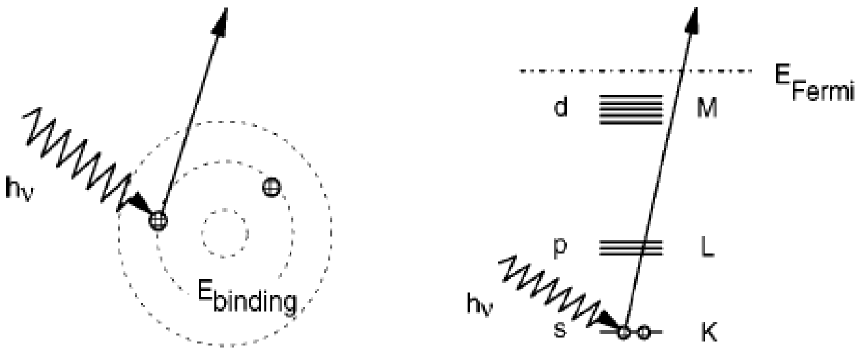

Figure 2.6. *A schematic illustration of the photoelectric effect in terms of excitation of the different orbital (left) or different energy levels (right)*[18].

The characteristic features of the X-ray absorption coefficient are the absorption edges: if the energy of the incoming photons is large enough to excite an electron from a deeper core level to a vacant excited state or to the continuum, a sharp rise in the absorption intensity appears. This sharp rise is denoted as the *threshold energy* or *absorption edge*[19]. At the absorption edge, E_{edge}, the kinetic energy of the electron (E_k) is defined to be equal to E_0, often referred to as the *zero-point energy* or "*inner potential*". The photoelectron kinetic energy is:

Equation 2.4. *Photoelectron kinetic energy.*

$$E_k = h\nu - E_{edge}$$

where, h is Planck's constant and v is frequency.

Quantum mechanically the outgoing photoelectron can be represented as a spherical wave with wavelength λ defined as:

Equation 2.5. *Wavelength and wave-vector equations.*

$$\lambda = \frac{2\pi}{k};$$

$$k = \sqrt{\left(\frac{8\pi^2 m}{h^2}\right)\left(h\nu + E_0 - E_{edge}\right)}$$

where k is the wave-vector, and m is the electron mass[20]. E_{edge} is the edge energy, and E_0 is applied as a correction when the data is analysed, as the zero energy is not well defined by the data.

The basic principles behind XAS can be understood by considering the transmission of X-rays through a thin sample (**Figure 2.7**):

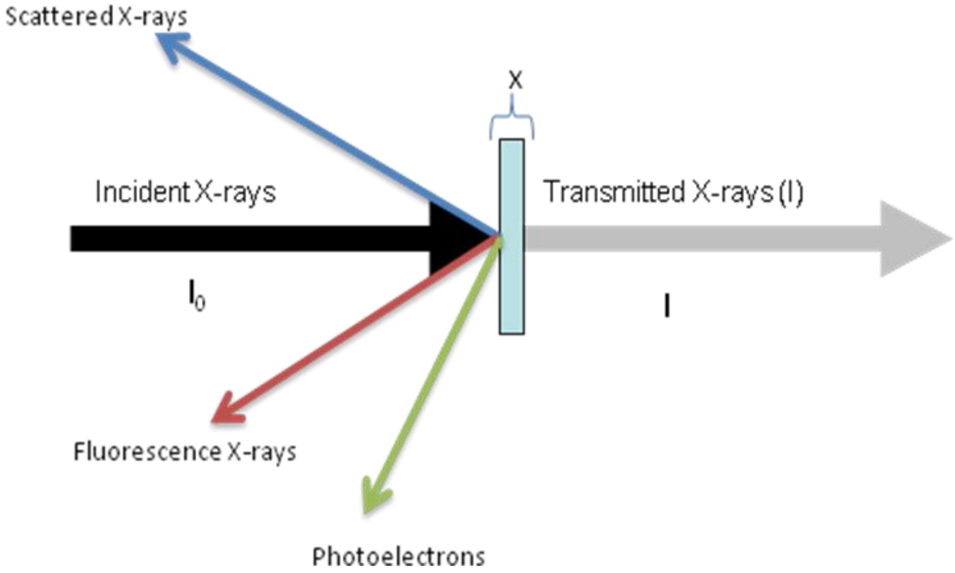

Figure 2.7. *A monochromatic beam of X-rays of intensity I_0 is transmitted through a thin sample. The various products which are produced as a result of X-ray scattering and adsorption processes are indicated by the differently coloured arrows.*

When a monochromatic beam of X-rays travel through a material, part of the X-rays are scattered (diffracted) and part absorbed. Atoms of the material will absorb part of the incoming photons which results in a decrease in the intensity of the transmitted X-ray beam. Hence, the incident intensity I_0 will be decreased by an amount that is determined by the absorption characteristics of the material. *Beer Lambert's law* is an empirical relationship that relates the absorption of X-rays to the properties of a material through which the X-rays are travelling[20].

Equation 2.6. *Beer Lambert's Law.*

$$I_t = I_0 e^{-\mu(E)x}$$

where $\mu(E)$ is the linear absorption coefficient (attenuation coefficient), I_0 and I_t are the incident and transmitted X-ray intensities respectively, and x is the thickness of a sample[5]. As the X-rays pass through the sample, interactions with the sample atoms cause the beam to be attenuated. The degree of attenuation is characterised by the absorption coefficient $\mu(E)$ which is related to the transmitted X-ray intensity. The X-ray absorption coefficient is determined by the decay in the X-ray beam intensity I with distance x[21].

When X-rays are absorbed by the photo-electric effect, the excited core-hole will relax back to the “ground state” of the atom. A higher level core electron drops into the core hole, and a *fluorescent x-ray* or *Auger electron* is emitted. X-ray fluorescence and Auger emission occur at discrete energies that are characteristic of the absorbing atom. *Fluorescence radiation* occurs as a result filling the core hole created by photoelectric effect. The hole is filled by an electron from an outer shell (for example the L shell) with simultaneous emission of a photon with an energy equivalent to the difference between the binding energies of the K and L electrons. The emitted radiation for the K shell is dominated by $K\alpha$ radiation. The energy of this radiation is characteristic of the absorbing element and is less than original exciting radiation[22].

The X-ray absorption spectrum is divided into the X-ray Absorption Near Edge Structure (XANES) and higher energy region known as Extended X-ray Absorption Fine Structure (EXAFS). XANES are used to determine the oxidation state and local coordination geometry, while EXAFS provide detailed information on the local structure, and the absorbing atom.

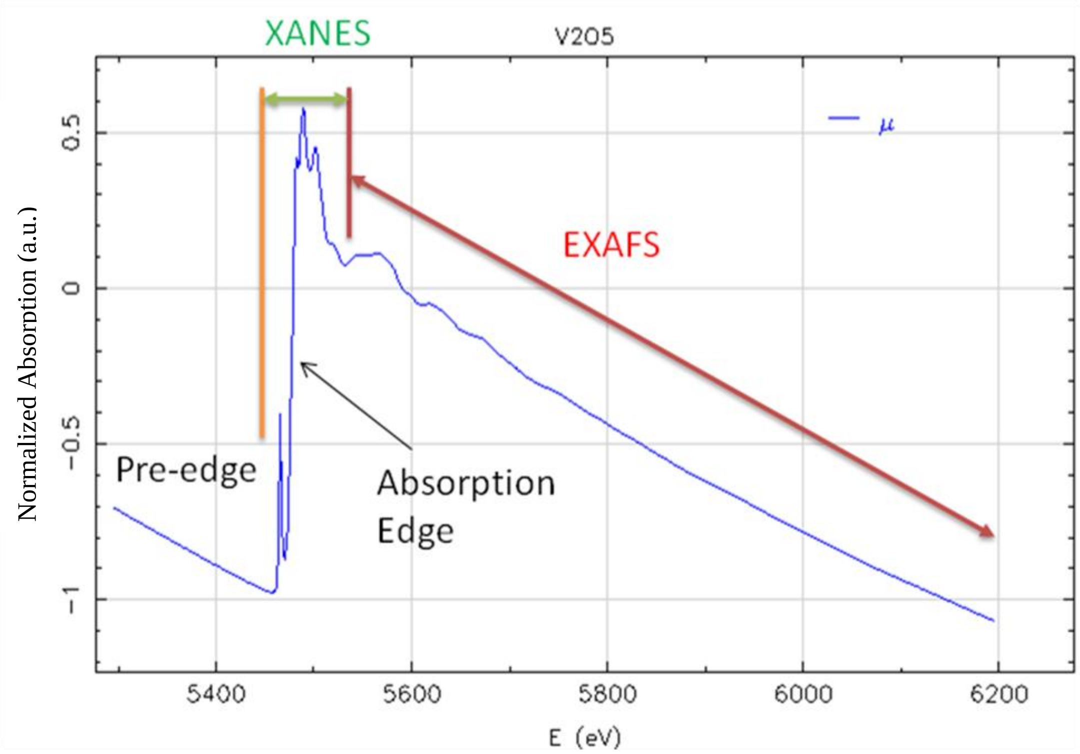

Figure 2.8. *An X-ray absorption spectrum of vanadium K-edge of* V_2O_5*.*

2.4.2 XANES

The XANES region starts about 50 eV below the absorption edge and extends to 100 eV after the edge. The spectrum is sensitive to the chemistry of the absorbing atom and hence can provide information about the oxidation state and geometry of the element of interest. The energy of emitted photoelectron in this region is relatively low because the energy of the incident X-ray photon is only just above the photoionisation threshold. Therefore, backscattering effects dominate the interactions between outgoing photoelectronic waves from the absorbing atomic species and neighbouring atoms[21]. The pre-edge region in XANES is caused by electronic transition to empty bound states and controlled by the dipolar selection rule $\Delta l = \pm 1$. Primary transition will be:

- $s \rightarrow p$ for K ($1s$ core electron) and L_1 ($2s$ core electron initial state) edges
- $p \rightarrow d$ for L2 ($2p_{1/2}$) and L_3 ($2p_{3/2}$) edges[23]

The $1s \rightarrow 3d$ transition is forbidden by the Laporte selection rule, but it is allowed when the metal is in tetrahedral coordination since there is *p-d* orbital mixing. Even so, a pre-edge feature is still observed for octahedral geometry according to Westre et al.[24] due to an electric quadrupole coupling mechanism. The coordination of the metal ion can be distinguished from the height and position of the pre-edge peaks, as shown in **Figure 2.9**.

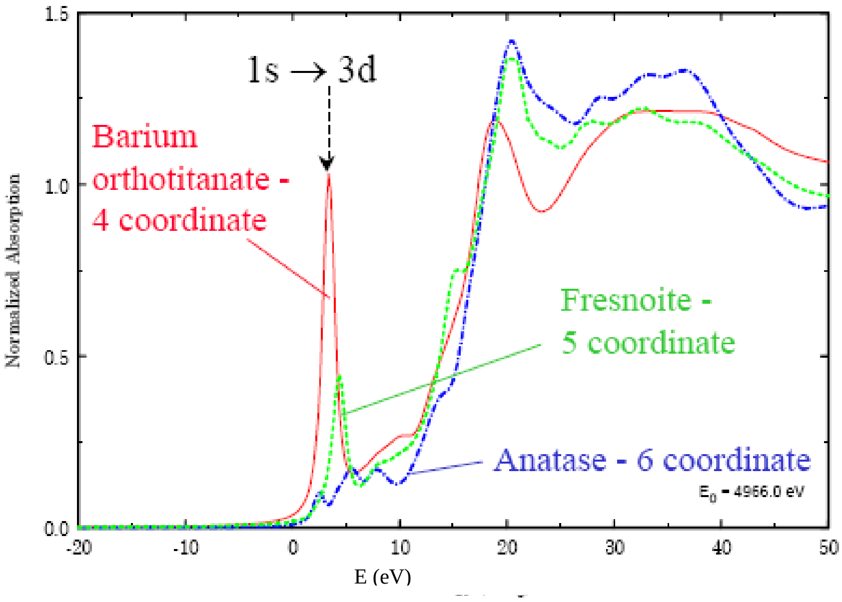

Figure 2.9. *Local Site Symmetry in Ti-containing compounds*[23].

More detailed information can be obtained by measuring high-energy-resolution fluorescence detection (HERFD) XAS. HERFD is a new tool for the identification of the bonding sites of reactants in supported metal catalysts. HERFD spectra have a much better energy resolved fine structure compared to the XANES spectra measured in transmission mode[25]. HERFD can be defined as detecting the fluorescence line with an energy bandwidth on the order or below the core hole lifetime broadening. This guarantees the best possible signal to background ratio, emission detection with lifetime resolution also yields line-sharpened absorption features. This effect considerably helps to analyze absorption features. For 3*d* transition metals it has been used to separate the K absorption pre-edges from the strong main edge[26].

2.4.3 EXAFS

The extended energy range of the X-ray absorption is the oscillatory fine structure, called EXAFS, and begins about 50 eV above the edge and extends up to 1000 eV past the absorption edge. The oscillatory structure is related to the influence of neighbouring atoms (**Figure 2.10**). Therefore, precise information of the local atomic structure around the absorbing atom can be achieved by the investigation of the scattering effect caused by the photoelectron.

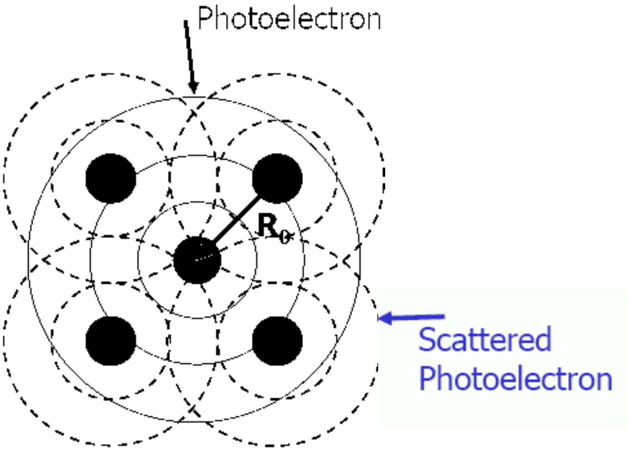

Figure 2.10. *A diagrammatic representation of the process involved in the generation of EXAFS oscillations*[23].

The use of EXAFS for structural determination started with the pioneering work of Sayers, Stern and Lytle[27]. They explained that a Fourier Transformation (FT) of the isolated EXAFS function with respect to the photoelectron wavenumber, would give a radial distribution function for the region surrounding the absorbing species. This function can be used for extracting information about the next nearest neighbour coordination shell of atoms, hence, information about the structure and the short-range environment of the X-ray absorbing atom could be obtained. So a common definition of EXAFS function $\chi(E)$ is extracted from the X-ray absorption coefficient $\mu(E)$ by subtracting the atomic background $\mu_0(E)$ and normalizing to the edge jump:

Equation 2.7. *Definition of the EXAFS function.*

$$\chi(E) = \frac{\mu(E) - \mu_0(E)}{\Delta\mu_0}$$

The EXAFS function can be derived by calculating the absorption coefficients for both the absorbing atom and the condensed phase.

2.4.3.1 EXAFS formula

EXAFS analysis is based on the backscattering of electron waves from atomic neighbours surrounding a central atom, which is excited by an X-ray photon of a high enough energy. The interaction between the outgoing photoelectron and the backscattered electron waves creates an interference pattern, which is subsequently analyzed to derive nature, number, and distance (plus disorder) of the neighbouring atoms. Within the multiple-scattering theory this oscillatory fine structure can be described by[19]:

Equation 2.8. *EXAFS formula.*

$$\chi(k) = \frac{\Delta\mu}{\mu_0} = \sum_j \left(\frac{N_j}{kR_j^2} \right) f_j(k) \exp(-2\sigma_j^2 k^2) \sin\left(2kR_j + \phi_j(k)\right)$$

where N_j is the coordination number of the j^{th} shell; R_j.is the mean distance between the absorbing atom and the j^{th} shell; σ_j is the Debey-Waller factor for the shell, k is the photoelectron wave vector, $f_j(k)$ is the magnitude of the backscattering amplitude of the j^{th} neighbouring atom and $\varphi(k)$ is the electronic phase shift due to the atomic potentials[5]. This equation has the same form as the formula given by Stern, Sayer and Lytle[27].

Analysis of the EXAFS data can give unique information on the local environment of the absorbing atom, in particular, the distances and coordination numbers of the shells of atoms immediately surrounding the absorbing species. Bond length may be obtained with good accuracy (<0.01Å). The thermal vibrational effects on the back scattering intensity is described by Debye-Waller factors and gives rise to small variations of the average absorber-backscatter distance within one shell[8].

2.4.4 Data collection

An X-ray absorption spectrum is generally collected by measuring the variation in absorption of monochromatic X-rays as the energy of incident photons is increased. The simplest experimental arrangement for such measurements is the transmission geometry. Ion chambers (a sealed chamber with X-ray entry and exit windows, filled with a gas which is ionized by the photons passing through), measuring the number of photons passing through them, are placed before, I_0 and after the sample I_t[5]:

Equation 2.9. *The X-ray absorption coefficient.*

$$\mu(E)x = \ln\left(\frac{I_0}{I_t}\right)$$

The gas fill of the ion chamber depends on the energy of edge to be studied. The first ion chamber (I_0) is filled with a mixture of gas to absorb approximately 20% of the incident flux. The second ion chamber (I_t, after the sample) is filled with gas to absorb 80% of the incident flux. $ln(I_0/I_t)$ is the absorption of the sample, which will change across the absorption edge[6].

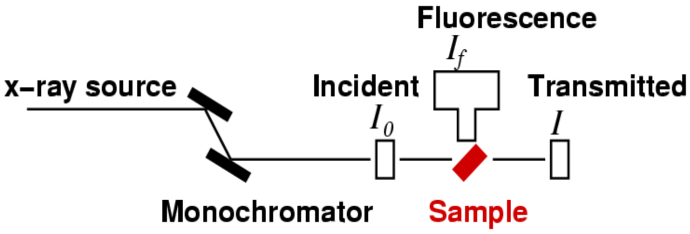

Figure 2.11. *A schematic illustration of a experimental set-up*[28].

For successful transmission measurement of EXAFS, there must be a significant change in absorption across the edge (edge step) but enough transmission of X-rays through the sample for that change to be observed. This requires a balance of concentration and total absorption. Sample homogeneity is also very important, as the most noise introduced to transmission spectra is related to non-uniform absorption of X-rays by the sample. Such problems are caused either by high-energy harmonics (which will be minimal if the experimental station is set up properly) or leakage of X-rays through pinholes in the sample[6, 28].

EXAFS spectra may also be obtained indirectly from the fluorescence photons and electrons produced in the absorption process:

Equation 2.10. *Calculation of the absorption coefficient in the fluorescence.*

$$\mu(E) \propto I_f / I_0 .$$

For fluorescence, photons produced by the element of interest during absorption are detected with a solid state detector. The detector is typically positioned orthogonal to the incident beam to minimise scatter, while still detecting the fluorescence. These signals are much smaller, (by several orders of magnitude) than ion chamber readings and so there is proportionally more electronic noise[29]. Fluorescence is superior method for measuring elements of interest in dilute samples. It may also be used where the sample is too absorbing for transmission measurements even with a concentration that would normally be high enough for transmission measurement[30]. The concentration of the element of interest in a sample controls the magnitude of the fluorescence signal, which can be measured with a solid state detector. The total absorption controls the proportion of X-rays which pass through the sample to reach I_f.

EXAFS data analysis

2.4.4.1 EXAFS data processing

The data processing in this thesis were completed the program Athena[31]. The first step of XAFS data analysis is to convert the recorded data to energy versus absorption coefficient. This step is followed by removal of the background and normalization of the data. After the pre-edge subtraction, the pre-edge energy E_{edge} (E_0) is defined. The atomic background (μ atomic) after the absorption edge is determined using a cubic spline.

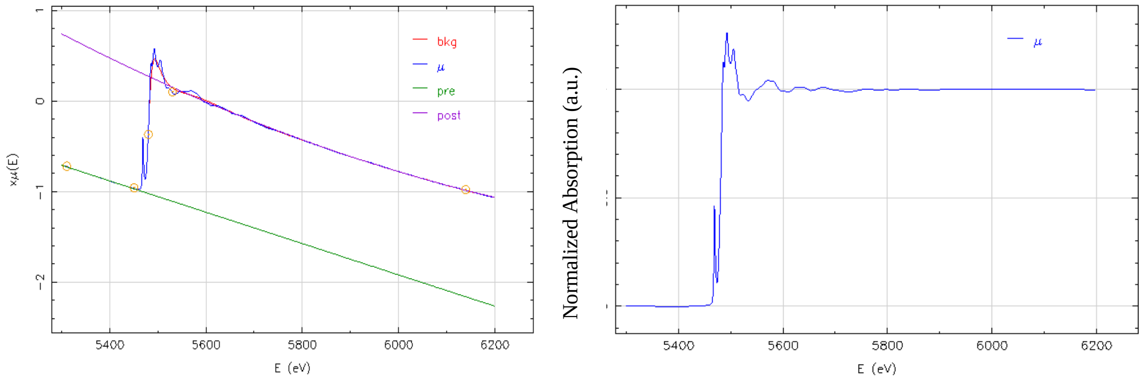

Figure 2.12. *Illustration of data analysis procedure on* V_2O_5*; (left) pre-edge and post-edge background, and (right) the normalised data (from Athena).*

EXAFS data $\chi(k)$ is the summation of all the interference patterns scattered off all neighbouring atoms and $\chi(E)$ is obtained (according to **Equation 2.7**). $\chi(E)$ is converted to $\chi(k)$ and it is multiplied by a power of k^n ($n = 3$ usually) to give $k^n(\chi(E))$ where k is the wave vector. This was done in order to compensate for the attenuation of the EXAFS at higher values and to prevent the larger oscillations at low k values from dominating spectrum[20]. Then the Fourier transformation is defined by:

Equation 2.11. *Fourier transformation equation.*

$$FT(R) = \frac{1}{\sqrt{2\pi}} \int_{k_{\min}}^{k_{\max}} k^n \chi(k) e^{i2kR} dk$$

The Fourier transform separates the neighbouring atoms according to their distances from the central atom. The magnitude not only depend on the type of backscattering atom but also on the number of the distances from the central atom[6].

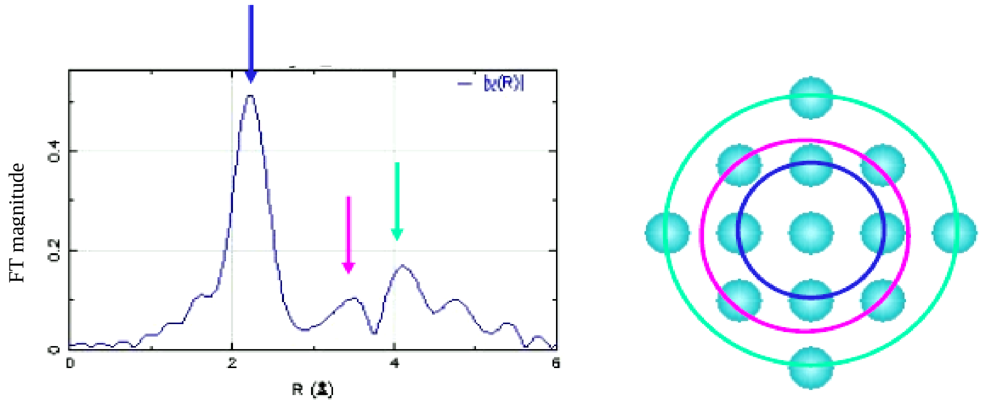

Figure 2.13. *A typical example of Fourier transform (left) and scattered photoelectrons (right)*[32]*. Blue colour displays the 1st shell, pink 2nd shell, and green 3rd shell.*

The radial distribution function is defined in *R*-space (distance from the absorber atom). FT can be taken with different k_weighting (multiplication by k^n)[20].

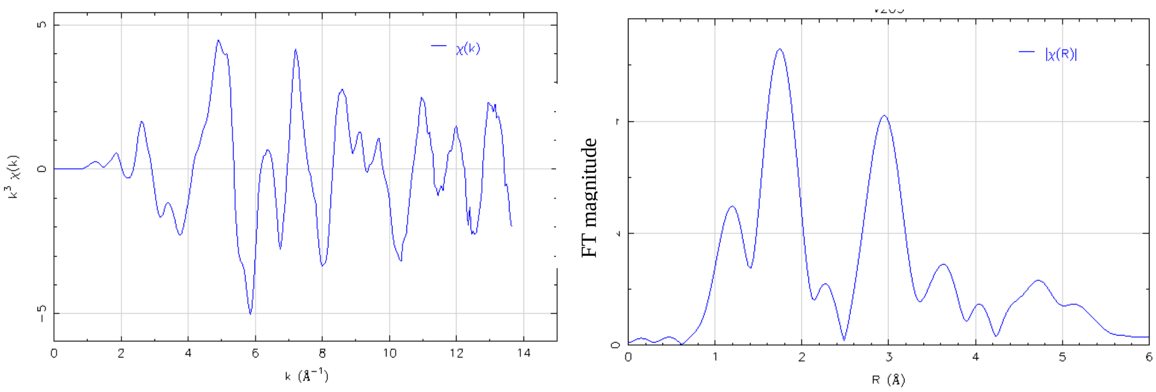

Figure 2.14. *EXAFS $k^3\chi(k)$ data (left) and FT magnitude illustrated on V K-edge of V_2O_5.*

2.4.4.2 Curve fitting deriving the structural parameters (EXCURV98)

The Excurve98 is a program designed to fit a structural model of a material which agrees with the available EXAFS spectra. First, a model must be defined in terms of one or more clusters of atoms, weighted according to the average composition of the material. Clusters can represent different atomic sites in a single phase, or multiple phases[33]. The parameters used to define the model may be refined until optimum agreement with the XAFS data is obtained. The refinement may use additional data to that given by EXAFS spectra, for example distance and angle restraints using bond distances obtained by other techniques. The structural parameters, R (interatomic distance) and $2\sigma^2$ (Debye-Waller factor) are refined till the best fit is obtained[33].

For crystalline solids, cryatallographic model can be used to define a cluster, and the point symmetry of each site is defined. For amorphous solids, pairs of atoms are defined by the partial radial distribution functions, and the calculation is generally limited to single scattering[33].

2.4.5 Other synchrotron techniques

Total scattering or Pair Distribution Function (PDF) is a method in which both Bragg and diffuse components of the scattering are analysed together, revealing the short and intermediate range order of the material independent of the degree of disorder. The characteristic of the PDF technique is that the measured diffraction intensities are Fourier transformed, and as a result the real-space arrangements of atom pairs are obtained from the Fourier transform[34].

In general, the PDF can be defined directly in real-space in terms of atomic coordinates, and can also be written as a Fourier transform of scattered X-ray or neutron intensities. The advantage of PDF in comparison to crystallographic techniques is that any crystallographically ordered or disordered materials can be studied, and the peaks in the PDF come directly from pairs of atoms in the solid[34].

The experiments are carried out in identical conditions to X-ray and neutron powder diffraction measurements, and at synchrotron X-ray sources and pulsed neutron sources. The advanced sources are used because it is important to measure data over a wide range of momentum transfer, Q, for high accuracy and adequate real-space resolution of the PDF peaks.

Equation 2.12. *Momentum transfer.*

$$Q = \frac{4\pi \sin\theta}{\lambda}$$

where θ is the angle, and λ is the wavelength. Very high values of Q, $Q > 30$ Å^{-1}, are desirable, and this means that short-wavelength, high energy X-rays or neutrons are required. X-rays of > 45 keV ($\lambda = 0.27$ Å) and up to 100 keV ($\lambda = 0.12$ Å) or more are typically used[34].

The data need to be corrected for experimental errors such as sample absorption, multiple scattering, etc., and normalized to get the structure function $S(Q)$. Special care needs to be taken at lower r-values, where errors can be caused by over interpreting of the data; through the data processing errors are rather small. A significant advantage of the PDF is that the useful structural data can be obtained to very high r distances. This allows the fits to be highly resistant to random and systematic errors in the data, and therefore provide very robust structural solutions[34, 37].

2.5 Infrared and Raman Spectroscopy

FTIR and Raman spectroscopy are both vibrational spectroscopies with electromagnetic radiation, and depending on symmetry, a certain phonon mode generates a peak in the IR and/or Raman spectrum. The peak position is determined from the phonon wavenumber, and the intensity of the peak is determined from the atomic vector displacement[38].

FTIR is based on absorption of infrared radiation from atomic vibrations. Raman spectroscopy consists of inelastic visible/near-visible light from atomic vibrations. Both techniques provide information on short- and intermediate-range ordering, and are very sensitive to atomic bonding, and thus can provide information about active sites and interactions between the framework atoms and embedded functional molecules[39]. Raman spectroscopy has better signal-to-noise ratio in the low-energy spectral range, and better spatial resolution and easy sample preparation. On the other hand, FTIR offers better surface-sensitivity[39]. Both, IR and Raman spectroscopy provide information about[38]:

- Structure and morphology
- Chemical composition
- Ability to sorb and retain molecules
- Ability to chemically convert these molecules.

The latter two are surface chemical properties of solids which might be difficult to probe. However, the surface of a zeolite is a three-dimensional periodic property which cannot be probed by straight forward surface-sensitive techniques.

2.5.1.1 IR spectroscopy

Information on bonds between atoms is provided by stimulating the vibration or rotation of two or more atoms in the probed matter. For a given concentration of bonds probed, the intensity of the response in an IR spectrum is proportional to the change in the dipole moment. Only vibrational aspect can be considered in the nanoporous science because the interactions are in solids or adsorbed molecules[38].

IR spectroscopy is purely absorption phenomenon, where the solid absorbs the incoming light photon with its particular wavelength, and a transition from the ground state to and excited state of phonon occurs[39].

The signal in an IR spectrum of a diatomic molecule is caused by the vibrational excitation, if the dipole moment changes in that action. Described in the form of a harmonic oscillator:

Equation 2.13. *Harmonic oscillator formula.*

$$\nu = \frac{1}{2\pi}\sqrt{\frac{k}{\mu}} \rightarrow \mu = \frac{m_1 m_2}{m_1 + m_2}$$

where υ is the frequency of vibration, k is the force constant and μ is the reduced mass. The frequency is directly proportional to the force constant and indirectly proportional to the mass of the atoms involved in the vibration. The force constant k is defined as the difference in the potential between the ground state and the state when both atoms in the bond are separated, and not as a measure of the bond strength[38].

Quantitative interpretation:

The vibrational spectrum can be separated into regions:

- (3800 – 3500 cm^{-1}) - stretching vibrations of the hydroxyl groups, lower frequencies are characteristic for hydroxyl groups with hydrogen bonding interactions.
- (1500 – 200 cm^{-1}) – stretching and bending modes of the T-O units.

- (2100 – 1800 cm^{-1}) – vibrational overtones of stretching and bending modes of the T-O units
- Presence of absorbed water – bands in the region 3600 cm^{-1} and 1600 cm^{-1}.

For the presence of adsorbed molecules such as alkanes, amines, nitrates, the assignment of the bands is based on the basis of typical group frequencies.

In this thesis, IR analysis has been applied as a qualitative tool to track hydroxyl groups, using in house build *in situ* cell, which is described in more detail in Chapter 3.

2.5.1.2 Raman spectroscopy

In Raman Spectroscopy, information are provided in the form of inelastic scattering of monochromatic light at an atom leading to an electronic excitation into a virtual state, with nearly coincident de-excitation and a change in vibrational energy leading to a lower or higher frequency compared to that of the stimulating light[38], depending on whether phonon absorption or phonon emission is involved. Raman cross-section depends on the deformability of electron shells. Therefore transition metal-oxygen bonds, which involve d- or f-electrons, are highly polarisable and generate much stronger Raman peaks than Si-O bonds. Raman spectroscopy is very efficient in studying transition metal-oxygen clusters or sub-nanoparticles embedded in a porous silicate system[39].

The Raman spectral vibrations of framework silicates (framework and amorphous) can be interpreted in terms of modes of rings of SiO_4 tetrahedra, and can be explained in following ranges[39]:

- 250 and 650cm^{-1} are caused by ring modes involving the vibrations of the bridging oxygen atoms.
- 650 – 600 cm^{-1} is related to three-membered rings
- 560 – 490 cm^{-1} four –membered rings
- 490 – 400 cm^{-1} to six-membered rings
- 400 – 300 cm^{-1} to five-membered rings.

Raman spectra of zeolites are difficult to obtain with acceptable signal-to-noise ratio, not only because they show strong fluorescence background which makes it difficult to measure and interpret[38].

Raman spectroscopy is used in this thesis qualitatively to characterize vanadium species in zeolite ZSM-5, and therefore is not discussed in full detail.

References

[1] J. Cejka, H. van Bekkum, A. Corma and F. Schuth, *Introduction to zeolite science and practice*, Elsevier, **2007**.

[2] W. I. F. David, K. Shankland, L. B. McCusker and C. Baerlocher, *Structure Determination from Powder Diffraction Data*, University Press, Oxford, **2006**.

[3] E. W. Nuffield, *X-ray diffraction methods*, John Willey & Sons, Inc., New York, London, Sydney, **1966**.

[4] J. B. Kortright and A. C. Thompson in *X-ray emission energies, Vol.* Eds.: A. C. Thompson and D. Vaughn), CA: Lawrence Berkeley Nat. Lab, Berkeley, **2001**.

[5] G. Bunker, *Introduction to XAFS; A Practical Guide to X-ray Absorption Fine Structure Spectroscopy*, University Press, Cambridge, **2010**.

[6] *www.esrf.eu.*

[7] A. S. Schlachter, A. L. Robinson, A. Bienenstock, D. Mills, G. Shenoy and H. Winick in *Synchrotron radiation*, *Vol.* McGraw-Hill Companies, **2008**.

[8] C. R. A. Catlow and G. Sankar in *Synchrotron radiation and solid state science*, *Vol. 453* Eds.: K. Wright and C. R. A. Catlow), Springer, **1999**.

[9] J. J. Rehr, C. H. Booth, F. Bridges and S. I. Zabinsky, *Physical Review B* **1993**, *49*.

[10] P. E. Ewald, *Fifty years of X-ray diffraction*, International Union of Crystallography, Utrecht, **1962**.

[11] G. Will, *Powder Diffraction: The Rietveld Method and the Two-Stage Method to Determine and Refine Crystal Structures from Powder Diffraction Data*, Springer-Verlag, Berlin Heidelberg, **2006**.

[12] T. M. Daniel, *The international journal of tuberculosis and lung disease* **2006**, *10*, 1212 -1214.

[13] J. L. Hodeau and R. Guinebretiere, *Applied physics A, Materials science & processing* **2007**, *89*, 813-823.

[14] C. Giacovazzo, H. L. Monaco, D. Viterbo, F. Scordari, G. Gilli, G. Zanotti and M. Catti, *Fundamentals of Crystallography*, University Press, Oxford, **1992**.

[15] a) A. K. Cheetham and P. Day, *Solid state chemistry techniques*, Clarendon press, Oxford, **1987**; b) H. L. M. C.Giacovazzo, D. Viterbo, F. Scordari, G. Gilli, G. Zanotti, M. Catti, *Fundamentals of Crystalography*, Oxford Science Publications, **1995**.

[16] A. Altomare, C. Giacovazzo, A. G. G. Moliterni and R. Rizzi, *Journal of Research of the National Institute of Standards and Technology* **2004**.

[17] M. Newville, *Consortium for Advanced Radiation Sources* **2004**.

[18] D. C. Koningsberger, B. L. Mojet, G. E. van Dorssen and D. E. Ramaker, *Topics in Catalysis* **2000**, *10*, 143-155.

[19] H. Wende, *Reports on Progress in Physycs* **2004**, *67*, 2105-2181.

[20] D. C. Koningsberger, B. L. Mojet, G. E. van Dorssena and D. E. Ramaker, *Topics in Catalysis* **2000**, *10*, 143-155.

[21] J. J. Rehr and R. C. Albers, *Reviews of Modern Physics* **2000**, *72*, 621654.

[22] E. A. Stern and S. M. Heald, *Handbook of synchrotron radiation* Elsevier Science Pub., New York, **1983**.

[23] in *http://cars9.uchicago.edu/xafs/NSLS_EDCA/July2003/Bare.pdf.*

[24] T. E. Westre, P. Kennepohl, J. G. DeWitt, B. Hedman, K. O. Hodgson and E. I. Solomon, *Journal of American Chemical Society* **1997**, *119*, 6297-6314.

[25] M. Tromp, J. A. Van Bokhoven, O. V. Safonova, F. M. F. De Groot, J. S. O. Evans and P. Glatzel, *http://www.slac.stanford.edu/econf/C060709/papers/194_TUPO45.PDF* **2008**.

[26] P. Glatzel, M. Sikora, S. G. Eeckhout, O. V. Safonova, G. Smolentsev, G. Pirngruber, J. A. van Bokhoven, J.-D. Grunewaldt and M. Tromp, *http://eprints.soton.ac.uk/46743/1/AIP_2007,_879,_1731.pdf* **2007**.

[27] D. E. Sayers, E. A. Stern and F. W. Lytle, *Physical Review Letters* **1971**, *27*, 1204-1207.

[28] R. Enjalbert and J. Galy, *Acta Cryst.* **1986**, *42*, 1467-1469.

[29] F. Hippert, E. Geissler, J. L. Hodeau, E. Lelievre-Berna and J. R. Regnard, *Neutron and X-ray Spectroscopy*, Springer, **2006**.

[30] in *Basics EXAFS sample guide, Sample properties and data collection*, http://srs.dl.ac.uk/.

[31] B. Ravel and M. Newville, *Journal of Synchrotron Radiation* **2004**.

[32] S. Kelly in *Basics of EXAFS data analysis.* http://www.mesg.anl.gov/Presentations/basics%20of%20exafs%20analysis%202003.pdf.

[33] N. Binsted in *EXCURV98: The manual, Vol.* CLRC Daresbury Laboratory **1998**.

[34] S. J. L. Billinge and M. G. Kanatzidis, *Chemical communications* **2004**, 749-760.

[35] B. E. Warren, *X-ray Diffraction*, Dover Publications, **1990**.

[36] T. Proffen, S. J. L. Billinge, T. Egami and D. Louca, *Z. Kristallogr* **2003**, *218*, 132-143.

[37] S. J. L. B. a. M. G. Kanatzidis, *Chemical communications* **2004**, 749-760.

[38] J. A. Lercher and A. Jentys in *Infrared and Raman Spectroscopy for Characterizing Zeolites, Vol.* Eds.: J. Cejka, H. van Bekkum, A. Corma and F. Schuth), Elsevier, Oxford, **2007**.

[39] B. Mihailova in *Modern Spectroscopic Methods Applied to Nanoscale Porous Materials, Vol.* Eds.: V. Valtchev, S. Mintova and M. Tsapatsis), Elsevier, Oxford, **2009**.

Chapter 3 Effect of chemical composition on cobalt incorporation into CoAlPO-18

3.1 Chapter overview

Results into the investigation of a series of CoAlPO-18 (AEI-type) samples prepared by different methods are discussed in this chapter. Four samples were prepared with variable Al/P ratios (Johnson Matthey) using identical conditions. The cobalt concentrations (0.1 wt%) was constant but the Al/P ratio was varied from 0.9 to 0.6. In addition, samples with a constant Al/P ratio but varied Co concentration were prepared and investigated. The local structure around cobalt ions during calcination of samples was investigated by *in situ* X-Ray Absorption Spectroscopy (XAS). This also allowed the determination of the nature of cobalt species and their location within the system. More detailed information on the degree of crystallinity and structural changes in the long range order were obtained by powder diffraction (XRD) and High Resolution Powder Diffraction (HRPD). These measurements revealed an expansion of the AEI lattice upon incorporation of the large divalent cobalt ions. A mixed phase of CoAlPO-18 and AlPO-18 was observed and confirmed by HRPD. To ascertain the mixed phase materials, Scanning Electron Microscopy (SEM) images were taken. The SEM could not however, fully confirm the mixed phase. The Brönsted acid centres were studied by *in situ* Fourier Transform Infrared Spectroscopy (FTIR) which was equipped with an *in situ* cell built in-house.

3.2 Introduction

Isomorphous substitution of transition metal ions (Me) into aluminophosphate systems (AlPO*s*), labelled as MeAlPO*s*[1], can give rise to interesting shape selective catalytic properties[2]. Among the various metal substitutions, cobalt substituted aluminophosphates, CoAlPO*s,* where small amounts of Co(II) ions) are substituted in place of Al(III), display very interesting catalytic properties for conversion of linear alkanes[3]. Linear hydrocarbons are among the most abundant of all naturally occurring organic molecules, and a complete oxidation can be achieved very easily. Yet to oxyfunctionalize them in a controlled manner at lower temperatures is extremely difficult. For example, *n*-hexane can resist attacks by aggressive and environmentally unfriendly reagents such as boiling nitric acid, concentrated sulphuric acid, chromic acid, or potassium permanganate. There is a need to develop suitable catalysts which can utilize more environmentally friendly oxidants, such as hydrogen peroxide or oxygen from air. Since terminally oxidized alkanes, such as linear alcohols or acids, are extremely desirable potential feedstocks for the chemical industry, there is significant interest in developing ways of selectively oxidizing the terminal methyl groups[2b]. In particular, a small pore CoAlPO-18 molecular sieve has been reported to regioselectively oxidize primary carbon atoms in linear alkanes, employing air as an oxidant[4] (**Figure 3.1**).

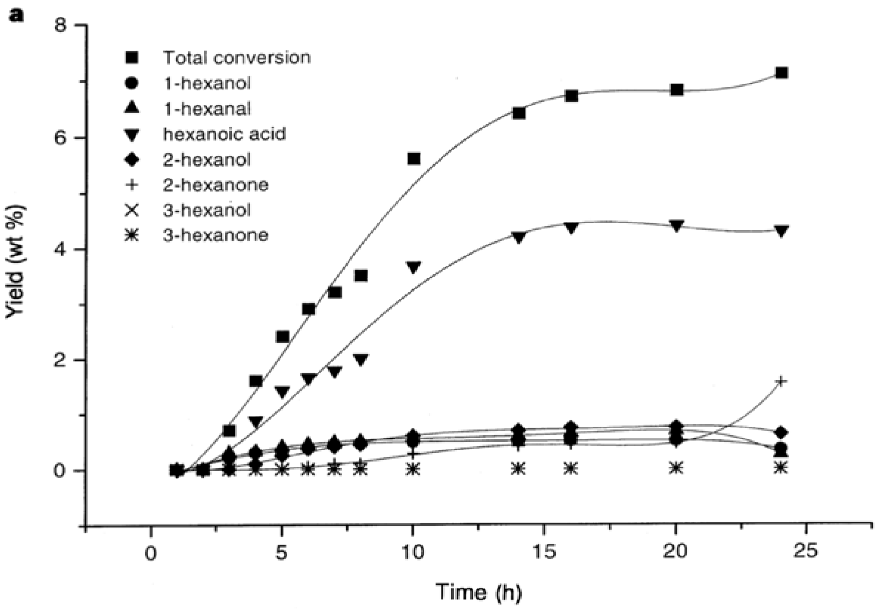

Figure 3.1. *Typical kinetic plots for the oxidation of n -hexane over CoAlPO-18 catalyst under the conditions given below. The kinetics of oxidation of n-hexane shows that the conversion increases linearly with time and levels off after ~15 h. At this stage, ~90% of the oxygen in the reactor is consumed, which could be the reason for the inhibition of the catalytic reaction. It is also possible that the alcohols and acids formed could also inhibit the reaction, owing to the hydrophilic nature of aluminophosphate molecular sieves*[4].

The oxidation reactions were preformed in a high-pressure stainless-steel catalytic reactor (Cambridge Reactor Design) lined with polyetheretherketone (PEEK) in dry air under pressure, in the reaction vessel (1.5 MPa). The sealed reactor was heated to the desired temperature of 373 K. CoAlPO-18 sample was activated by calcination in dry air at 550°C to remove the occluded organic template and to convert Co(II) ions to their (III) states. Small aliquots of the sample were removed at regular intervals to study the kinetics of the reaction in detail, and this was achieved using a liquid sampling valve without perturbing the pressure in the reactor[4].

Aluminophosphates are constructed from 3-dimensional corner-sharing TO_4 tetrahedra, where T is Al or P[6]. The divalent M(II) (M=Co, Zn, Mg etc.) substitution of Al(III) in AlPO*s* leads to formation of Brönsted acid sites (through charge compensation by a proton for the negatively charged framework), and similarly, the substitution of a tetravalent ion for a pentavalent one, such as Si(IV) for P(V), leads to the formation of strong acid sites. Most elements that substitute Al(III) to assume the tetrahedral coordination are much larger than the Al(III) vacancy. Thus the successful incorporation of these elements into the framework is attributed to the greater spatial accommodation of the microporous structures which allows larger cations to "bulge" into the open channels. Understanding the properties during detemplation and catalytic reaction is important for development efficient catalysts[7].

The CoAlPO-18 molecular sieve is classified as an AEI-type[6] structure in the International Zeolite Association database and can be synthesized using tetraethylammonium hydroxide (TEAOH)[8] or N,N-diisopropyl ethylamine (DIPE)[9] as a structure directing agent. DIPE is a more favourable SDA, since there are problems associated with the use of TEAOH which aids the formation of AlPO-34 (CHA-type) above a certain concentration of heteroatom (transition metal or silicon)[9-10]. AlPO-18 is a small pore monoclinic system defined by the C2/c space group. The 3-dimensional channel networks consist of six member rings, with an average pore size ≈ 3.8 Å[11] (**Figure 3.2**).

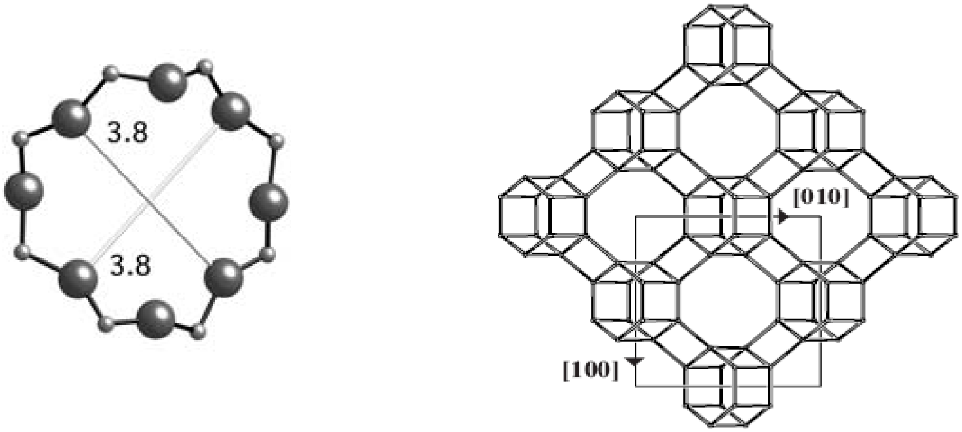

Figure 3.2. *8 member ring of AlPO-18 viewed along [100] plane. The three-dimensional channel system is obtained by connecting the cavities through common 8-rings and double 6-rings[12].*

Co(II) can be introduced into molecular sieves by ion exchange[13] and hydrothermal synthesis[14]. The hydrothermal synthesis can result in both framework and extra-framework Co(II) ions. The framework Co(II) are tetrahedrally coordinated, whilst the extra-framework Co(II) will simultaneously yield different geometries. Co(II) ions (d^7) are always present as the high-spin state in zeolites, therefore the oxygen atoms in zeolites can be considered as weak ligands[15]. Low-spin Co(II) complexes[13a] in zeolites are known as Schiff base complexes.

Cobalt[16], by itself, is an interesting transition metal with a very rich spectroscopy in its divalent state, and many characterization techniques have been employed to study cobalt substituted aluminophosphates. Indirect methods can be used to detect the incorporation. These methods include chemical analysis, tracking the expansion of the unit cell (by XRD)[17] and the formation of Brönsted acid sites, and measuring weight loss during calcination[18]. More direct methods used to determine the incorporation of cobalt in the framework are primarily spectroscopic techniques such as UV-Vis spectroscopy, electron spin resonance (ESR) and X-ray absorption spectroscopy (XAS). Useful spectroscopic techniques must be capable of discriminating between the different coordinations of high-spin Co(II). For example, X-ray diffraction gives average information on occupancy and coordination distances but cannot provide direct information about the incorporation, coordination and oxidation state; these are verified by XAS. Therefore, a number of techniques must be employed to verify successful incorporation, although some techniques are limited by their range (for example, EPR only works with very low concentrations of Co). Each technique offers many advantages and disadvantages suggesting that a combination of two or more complementary techniques can be an effective approach to elucidate whether a heteroatom has been incorporated into the framework of AlPO*s*.

3.2.1 Aims of the Work

Since others have not been able to reproduce[5] the catalytic results, the aim of this chapter is to study the synthesis method and resulting structure of the materials in more detail. The reported catalytic property of CoAlPO-18 is only possible from thermally stable (keeps the structure after calcination) and if the oxidation state of Co(II) can be raised to Co(III) through template removal through calcinations[19]. Because the incorporation always occurs in the synthesis, many studies were dedicated to understanding the synthesis factors influencing the cobalt incorporation most. Earlier ICP study of the active samples revealed that the (Co+Al)/P ratio was lower than 1. Therefore, samples with constant Co concentration (0.1w%) but lower Co+Al/P <1 ratio were prepared (prepared in Johnson Matthey Technology Centre), where the starting Al/P was 0.9, 0.8, 0.7 and 0.6, and the effect it had on cobalt incorporation, stability, and crystallinity investigated.

In addition, samples with constant Al/P=1 ratio but different cobalt concentration were prepared, in order to study the cobalt incorporation in more detail. Additionally, an *in situ* FTIR cell was developed for studies of Brönsted acid centres during activation (calcination), and these results were later correlated to the results obtained from XAS. The XAS was used to investigate the nature and incorporation of the active metal centres, and structural changes were studied by XRD, SEM, HRPD.

3.3Experimental

3.3.1 Hydrothermal synthesis

Samples of AlPO-18 and cobalt analogues were prepared using the method previously described in the literature using N,N-diisopropylethylamine as the structure directing agent[20]. The relative molar composition of gels used in this study was calculated employing the formula *(1-x)Al : xMe(II) : (1-y)P : yMe(IV) : 0.8 DIPE :*$25H_2O$*,* where Me(II) is a divalent metal ion, Me(IV) is a tetravalent metal ion and DIPE is N,N-diisopropylethylamine. The synthesis gels containing constant mole fractions of cobalt (0.1 w%) and a decreasing molar ratio of aluminium (with the total Co+Al/P content at < 1 molar equivalent) and a fixed amount of phosphorus and template were prepared first (please note these samples were prepared in Johnson Matthey by Michelle Coles). The molar ratios of the gels are given in **Table 3.1**. Firstly, aluminium hydroxide hydrate ($Al(OH)_3 \cdot xH_20$, Sigma-Aldrich) was dissolved in a solution of phosphoric acid (H_3PO_4, 85%, Sigma-Aldrich) with deionised water. An aqueous solution of cobalt(II) acetate tetrahydrate ($(CH_3COO)_2Co \cdot 4H_2O$, 98 %, Sigma-Aldrich) was then added to the mixture. After rigorous stirring of the gel for two hours, the *N.N-Diisopropylethylamine* ($[(CH_3)_2CH]_2NC_2H_5$, 99.5 %, Sigma-Aldrich) was added to form the final gel which was stirred for several hours. The Teflon liner was filled with the gel to 50% of the total volume and was placed in a stainless steel autoclave and heated at 170 ^oC for seven days.

Table 3.1. *Synthetic conditions using N.N-Diisopropylethylamine as a template, (Co+Al)/P<1.*

	Molar composition					Conditions
	Co	Al	P	DIPE	H_20	
AlPO-18	0	1	1	1.05	25	170°C, 3 days, pH 7.42
1A	0.1	0.9	1	1.05	40	170°C, 7 days, pH 7.48
2A	0.1	0.8	1	1.05	40	170°C, 7 days, pH 7.48
3A	0.1	0.7	1	1.05	40	170°C, 7 days, pH 7.47
4A	0.1	0.6	1	1.05	40	170°C, 7 days, pH 7.43

Prior to the preparation, the water concentration in $Al(OH)_3.xH_2O$ was determined as 45 w% water, and taken into consideration in the molar ratios calculations.

Furthermore, the synthesis of the same material but with constant (Co+Al)/P=1 ratio were prepared (in the laboratory). This time the cobalt concentration was changed, the starting gel ratios are displayed in **Table 3.3**.

Table 3.2. *Synthetic conditions using N.N-Diisopropylethylamine as a template, (Co+Al)/P=1.*

Molar composition					Conditions
Co	Al	P	DIPE	H_20	
0.005	0.995	1	1.05	40	160°C, 5 days
0.025	0.975	1	1.05	40	160°C, 5 days
0.040	0.960	1	1.05	40	160°C, 5 days
0.075	0.925	1	1.05	40	160°C, 5 days
0.100	0.900	1	1.05	40	160°C, 5 days

3.3.2 Ex situ *Characterisation*

3.3.2.1 Laboratory Characterization

X-ray diffraction measurements were performed on a Bruker D4 diffractometer Cu Kα radiation at room temperature. The spectra were collected using a position sensitive detector in 5 - 50° 2θ range in a 0.02 Å stepsize. The powders were closely packed onto a flat-plate sample holder. The SEM images were collected on a JEOL JSM-6301F (JEOL Ltd., Tokyo, Japan) with an INCA-sight detector (Oxford Instruments) at the

Institute of Archaeology UCL. In a typical experiment, SEM images were collected from finely grounded powder samples which were sprinkled on circular aluminium stubs with double-sided sticky tape and then coated with gold particles.

3.3.2.2 High Resolution Powder Diffraction (HRPD)

The high resolution powder diffraction data were collected at a synchrotron X-Ray powder diffraction beamline (I11) at the Diamond Light Source. The samples were loaded into 0.5 mm borosilicate capillaries, placed in the sample holder and aligned, and loaded onto the carrousel capable of holding 200 capillaries (see **Figure 3.3**)[21]. A robotic arm (ROB) mounted the capillaries automatically onto the diffractometer.

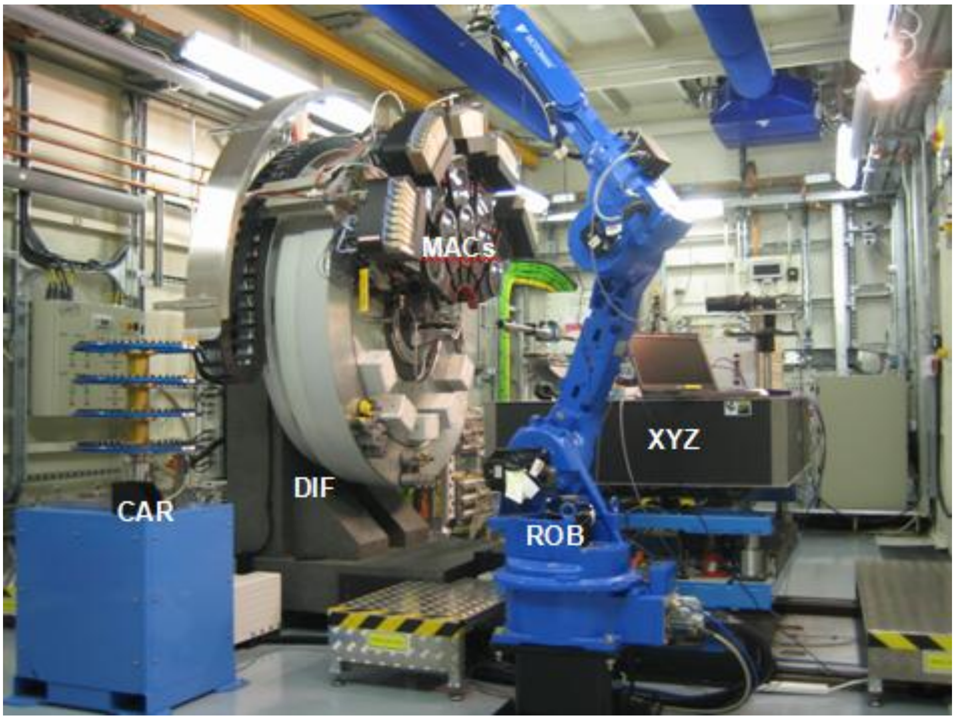

Figure 3.3. *I11 experimental hutch showing the heavy duty diffractometer (DIF), 5 arms for multi-analyzing crystal-detectors (MACs), robotic-arm (ROB), carousel with 200 specimen positions (CAR) and heavy duty table (XYZ)*[21].

The high resolution diffraction measurements were carried out using the multi-analysing crystals (MAC) detector with 45 channels, and capable of scanning in the 0-150° 2θ range. Overlap of gaps between detectors is eliminated by scanning forward and backward, and data from the 45 detectors are integrated to produce a final pattern. The wavelength was determined to be 0.826018 Å by measuring and refining a NIST Silicon standard. Sample data was collected with a step increment of 0.005° and a 10 sec time exposure. Acquisition time for each pattern was approximately 30 min. The LeBail fit was performed employing software FullProf[22].

3.3.3 In situ *characterisation*

3.3.3.1 X-ray absorption Spectroscopy

XAS measurements at Co K-edge for CoAPO-18 samples were performed at the Dutch-Belgian beamline (DUBBLE), BM26A, at the European Synchrotron Radiation Facility (ESRF). The storage ring was operated with electron current of 200 mA at 6.0 GeV energy. The energy resolution was 1 eV at the Co K edge (7709 eV). Ion chambers filled with appropriate gas mixtures were used to detect the intensities of the incident beam (I_0), and the transmitted beam (I_1). During temperature-programmed experiments, XAS spectra were acquired in step scans over a k range (k being the wave vector number of the X-ray excited cobalt photoelectron) of 3 $Å^{-1}$ to 12 $Å^{-1}$. Samples (50 mg of sample pelletized, 12.5 mm pellets) were suspended on a ceramic holder and placed inside *in situ* furnace, shown in **Figure 3.4**. Samples were calcined in air (Airgas). The calcination temperature was set to 530 ^{o}C which was reached at a rate of 5 ^{o}C/min. The samples were held at 530 ^{o}C for 30 min. After heat treatment in air, samples were cooled down to room temperature.

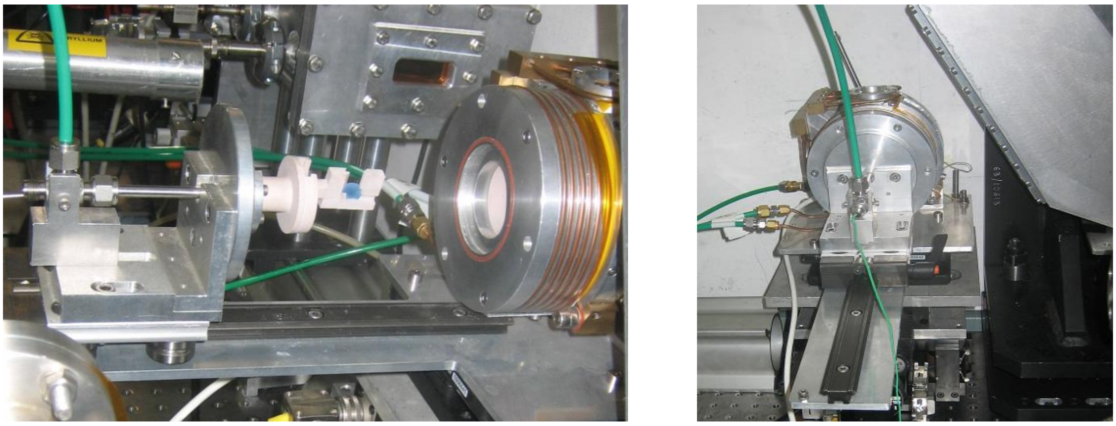

Figure 3.4. *In situ furnace with a ceramic sample holder used for XAS measurement.*

3.3.3.2 *In Situ* FTIR Spectroscopy.

FTIR spectra were measured, in transmission mode, using a Perkin Elmer Spectrum One spectrometer and an *in situ* flow cell (**Figure 3.5**) connected on the inlet stream to a controlling gas manifold. The in situ cell was specially designed and developed in our lab by Mr. Mike Sheehy. The main body is a quartz tube 180 mm long (inner Ø 30 mm, the thickness of the wall is 1 mm), on top of which the gas inlet and outlet connectors are attached (points 1 and 2 are gas inlet and outlet respectively), and are connected to the main gas supply through a gas manifold. The thermocouple (6) is inserted through KBr window and sealed in O-ring. The main body of the sample holder (4) is smaller quartz tube (inner Ø 20 mm, the thickness of the wall is 1 mm), inserted into an O-ring with second KBr window. Second O-ring is mounted onto the main quartz body (3), and both are securely sealed by a flange. The actual sample holder is a small stainless steel holder, in which the sample (Ø 13 mm) can be inserted. The main quartz body is securely held in place by the main body of the heater, which was built around it. The whole body of the *in situ* cell is mounted onto an aluminium plate from the spectrometer.

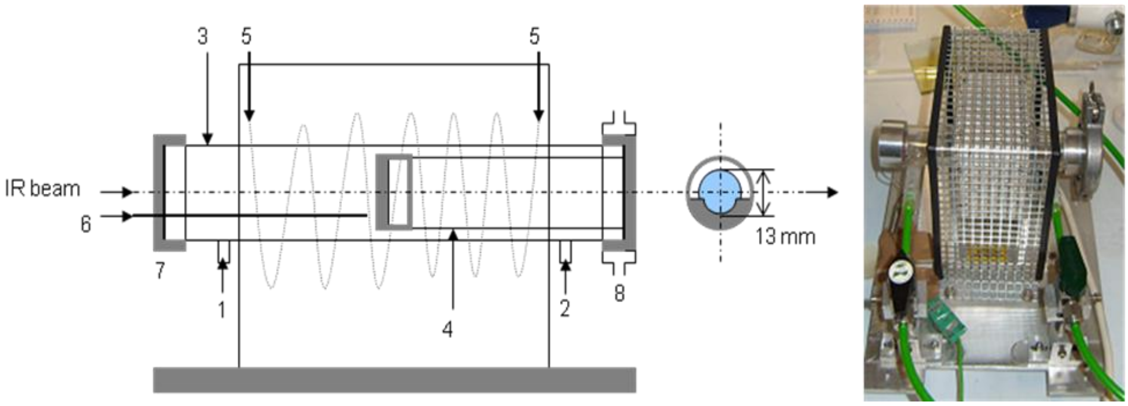

Figure 3.5. *Schematic representation of the high temperature in situ IR cell: 1 – gas inlet, 2 – gas outlet, 3 – quartz body, 4 - quartz sample tube with stainless steel sample holder, 5 – electrical connections, 6 – thermocouple, 7 – O-ring with KBr window, 8 – two O-ring with a flange and KBr window.*

In a typical experiment 15 mg of a sample was pelletized. The FTIR spectrum was recorded at an ambient temperature (25^{o}C) in a flow of dry air (Airgas, purified by 13X molecular sieve) between 500 and 4 000 cm^{-1}. The samples were then heated at a rate of 5^{o}C/min to 550^{o}C and held at the target temperature for 60 min to remove the template molecules trapped inside the microporous structure. FTIR spectra were collected every 10°C throughout this process to follow the formation and evolution of Brönsted acid bands; after experiments samples were cooled down to ambient temperature and purged with nitrogen (Airgas, UHP). If reduction reactions were carried out, the calcined sample was cooled to RT in nitrogen (Airgas), and the spectra were collected during heating in 2% H_2 in N_2 (Airgas) to 500^{o}C at 5 ^{o}C/min.

3.4Results and Discussion

3.4.1 Diffraction studies

Stacked plot of X-ray powder patterns, measured sequentially in the laboratory machine (Cu Kα) from four CoAlPO-18 samples (1A to 4A) and AlPO-18, is displayed in **Figure 3.6**. All four samples resemble the AlPO-18 pattern. There is a near linear decline of intensity for the cobalt substituted samples which can be linked to the quantity of crystalline fraction present since samples have reduced aluminium. The 2θ values of [002] reflection (first peak) from cobalt containing samples are lower than from the cobalt-free sample which can indicate increase in the lattice constants for this particular spacegroup. According to Löwenstein Rule[23], Co(II) ions should substitute for Al(III), and therefore the larger ionic radius of Co(II) (0.74 Å) in comparison to Al(III) (0.53 Å) should produce an expansion in the lattice. Furthermore, closer inspection of the largest peak exposes a shoulder-like feature, and there are some additional peaks in the pattern. Due to these variations in the patterns, all profiles were indexed to obtain information about the lattice parameters. AlPO-18 was indexed to C2/c, the monoclinic spacegroup reported in the literature[11]. Indexing of cobalt containing samples also revealed a monoclinic crystal system but not all peaks were possible to index. Lowering of symmetry from C2/c to $P2_1$ did not help. To resolve this issue, HRPD measurements were carried out on selected two samples, 1A and 4A.

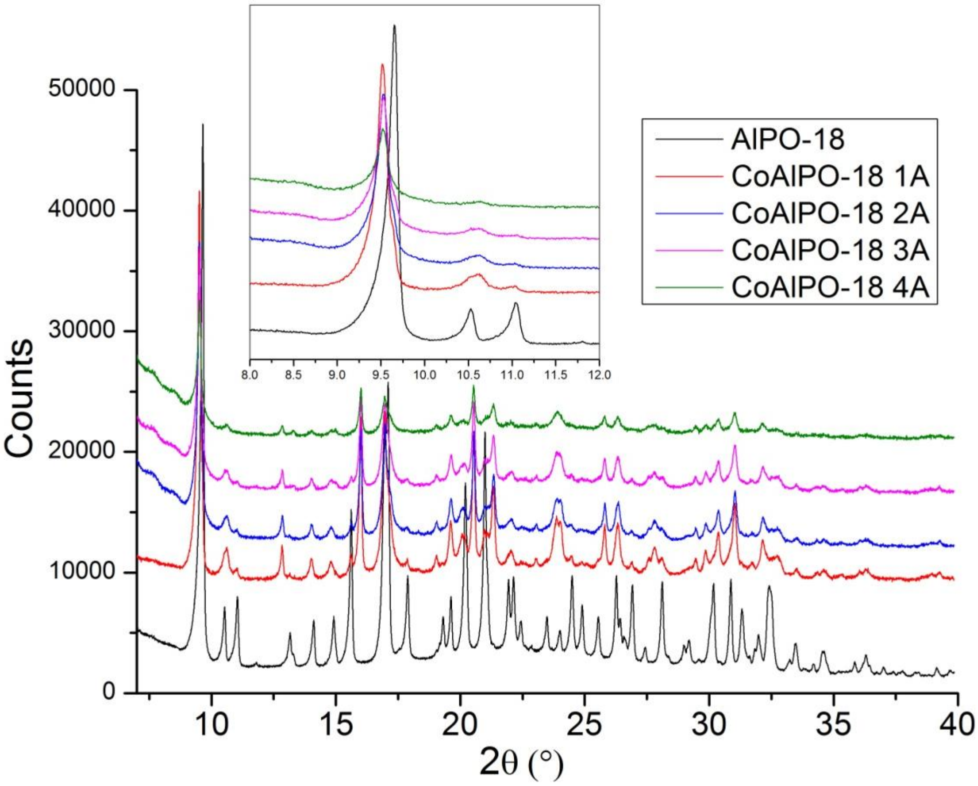

Figure 3.6. *XRD stacked plot of AlPO-18 and CoAlPO-18 samples synthesized with different Al/P ratio.*

HRPD data was collected from the most and least crystalline samples of CoAlPO-18, 1A and 4A respectively, and a cobalt-free AlPO-18 (**Figure 3.7**). The number of counts for sample 4A is much less than half of that for 1A, indicating decreased crystallinity. The shoulder mentioned above is now a well defined peak. Plotting the patterns of sample 1A and pure AlPO-18 (4A is not plotted for clarity) may explain the origin of the extra reflections (**Figure 3.8**). It was found that extra reflections are also produced by pure AlPO-18, and overlay perfectly with the unknown phase. Therefore, both phases can be indexed to the monoclinic C2/c spacgroup. LeBail fitting was performed to obtain unit cell parameters.

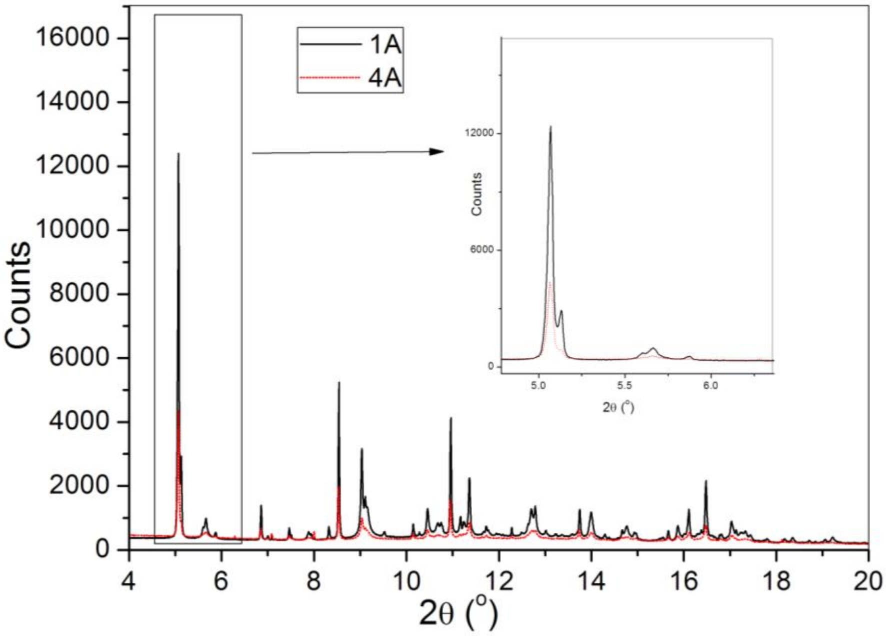

Figure 3.7. *Overlaid plot of HRPD powder pattern for samples 1A and 4A. Both samples display a shoulder-like feature in the first reflection, due to mixing of CoAlPO-18 and AlPO-18 phases.*

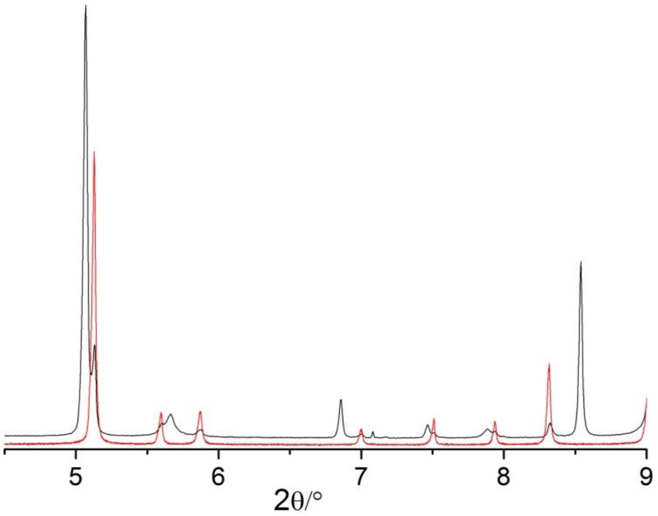

Figure 3.8. *A plot of HRPD diffraction pattern of CoAlPO-18 1A sample (black) and AlPO-18 sample (red). The first reflection of the pure AlPO-18 is at the same position as in the sample 1A, which is due to mixing of AlPO-18 and CoAlPO-18 phases.*

The LeBail structure profile fit was performed using Fullprof with Thompson-Cox-Hastings pseudo-Voigt profile shape. The results for both materials are shown in the **Table 3.3**, and the fit in **Figure 3.9**. Based on this evidence, the expanded unit cell can be assigned to CoAlPO-18 phase and the smaller one to AlPO-18.

Table 3.3. *The results of LeBail structure refinement of as-prepared samples.*

Temperature (^{o}C)	25			
Wavelength (Å)	0.826953			
step size (^{o})	0.005			
Profile range in refinement (2θ)	2-45			
Sample	4A		1A	
Phase type	Co-AEI	AEI	Co-AEI	AEI
Spacegroup	C2/c	C2/c	C2/c	C2/c
a (Å)	13.8274(1)	13.5666(8)	13.8131(1)	13.5839(7)
b (Å)	12.6931(3)	12.5990(6)	12.6943(1)	12.6205(7)
c (Å)	18.6473(2)	18.6937(7)	18.6536(1)	18.4835(5)
β (^{o})	89.96(1)	93.60(7)	89.97(1)	94.93(9)
V(Å^{3})	3272.8(3)	3188.9(9)	3270.9(1)	3157.0(11)
chi^{2}	6.95		20.4	
Rp	2.07		2.83	
Rwp	3.01		4.45	
Rexp	1.17		2.94	
Conv Rp	18.7		12.4	
Conv Rwp	15.4		12.9	
Conv Rexp	5.99		2.94	

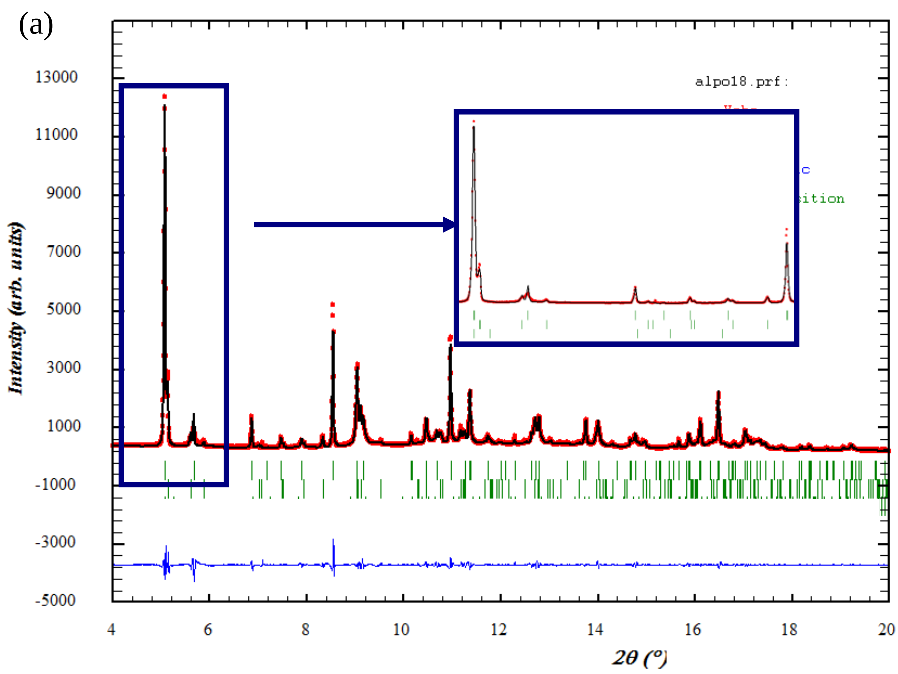

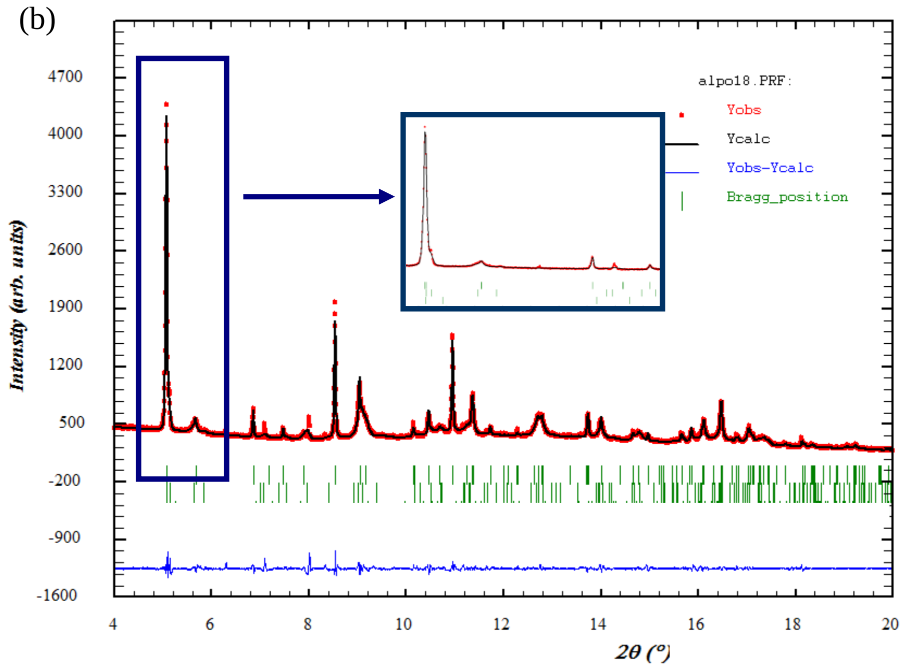

Figure 3.9. *The observed and calculated powder diffraction for: (a) CoAlPO-18 AG6714-1A and (b) CoAlPO-18 AG6714-4A.*

Further efforts were made to understand this fact, and synthesize pure CoAlPO-18 phase. The synthesis was modified that (Co+Al)/P equalled to 1, and the temperature lowered to 160^{o}C which lead to improved samples crystallinity. The metal incorporation investigation was also expanded. Different synthetic conditions, and gel preparations were tested but the final material still yielded mixed phases of AlPO-18 and CoAlPO-18 at low cobalt concentrations. The mixed phase of AlPO-18 and CoAlPO-18 were still detected in the samples with Co concentration 0.5, 2.5, 4 w% however pure phase is obtained with concentrations above 7.5 w% Co. **Figure 3.10** displays the stacked XRD plot of the samples, collected by the laboratory diffractometer. The first peak in the diffraction pattern is a good indicator of potential metal incorporation. The peak is very broad and the intensity very low for the sample with 0.5 % Co loading. The intensity increases and the width of the peak decreases with higher cobalt concentrations, from 2.5% to 7.5%. In addition, the fit Full Width Half Maxima (FWHM) revealed (**Figure 3.11**) of [002] reflection (first peak) that upon 0.5 w% incorporation, there is a big jump in the value. The FWHM value linearly decreases from 0.5 to 7.5 and then remains constant. The phase purity of the 10 w% CoAlPO-18 and SAPO-18 (20 w% Si) are confirmed by HRPD, displayed in **Figure 3.12**. Both materials displayed lattice expansion, and the cobalt substituted materials expand most in *c*-axis direction.

Therefore, the change in the FWHM of the [002] reflection is a good indicator of cobalt substitution (results in Chapter 4).

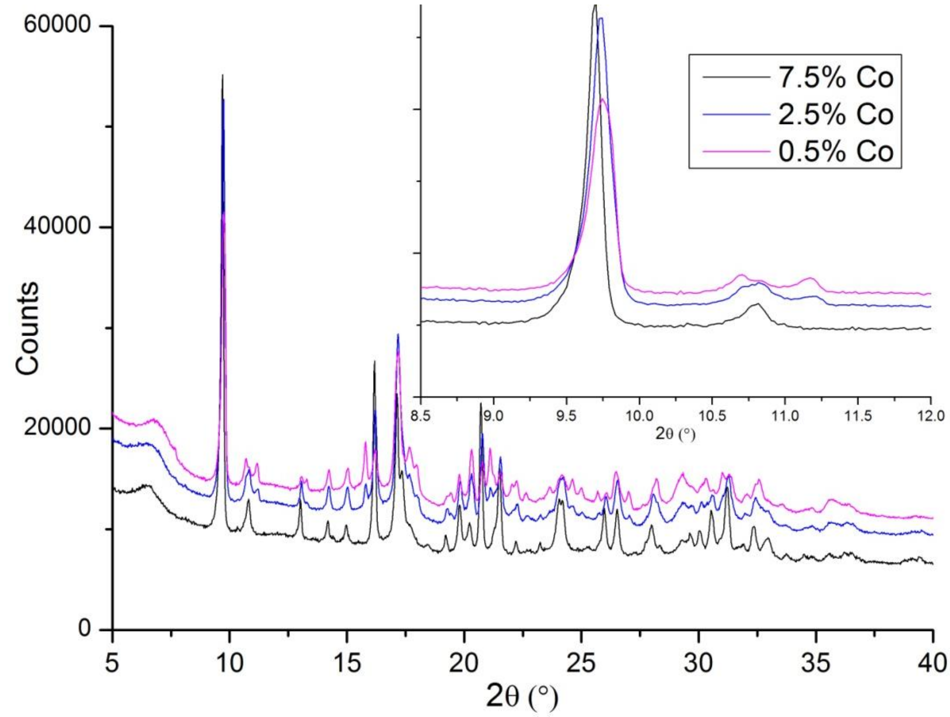

Figure 3.10. *XRD patterns of samples with different Co concentrations.*

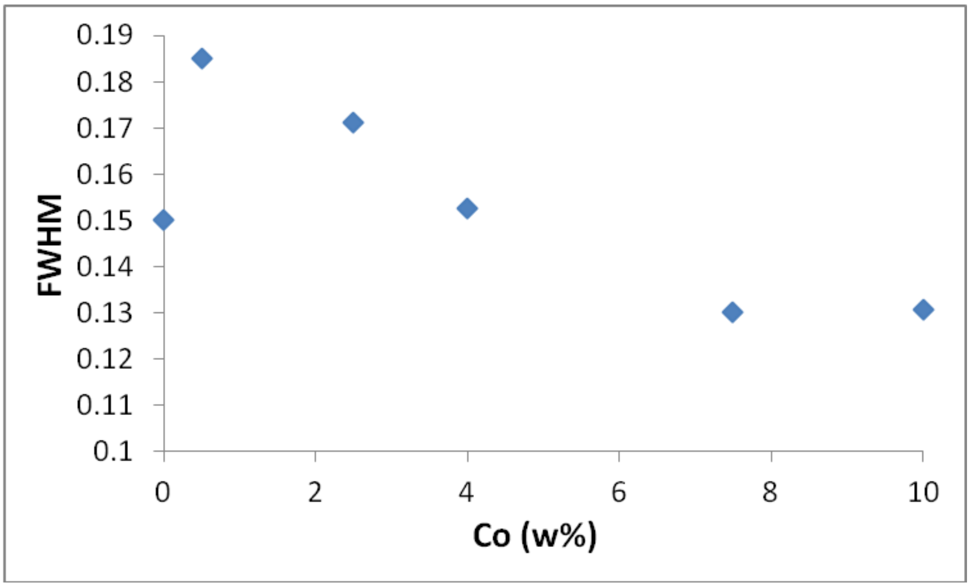

Figure 3.11. *A plot of cobalt concentration (w%) as a function of FWHM of the first peak ([002] reflection). Phase pure CoAlPO-18 materials is possible to prepare above the 7.5 w% concentration.*

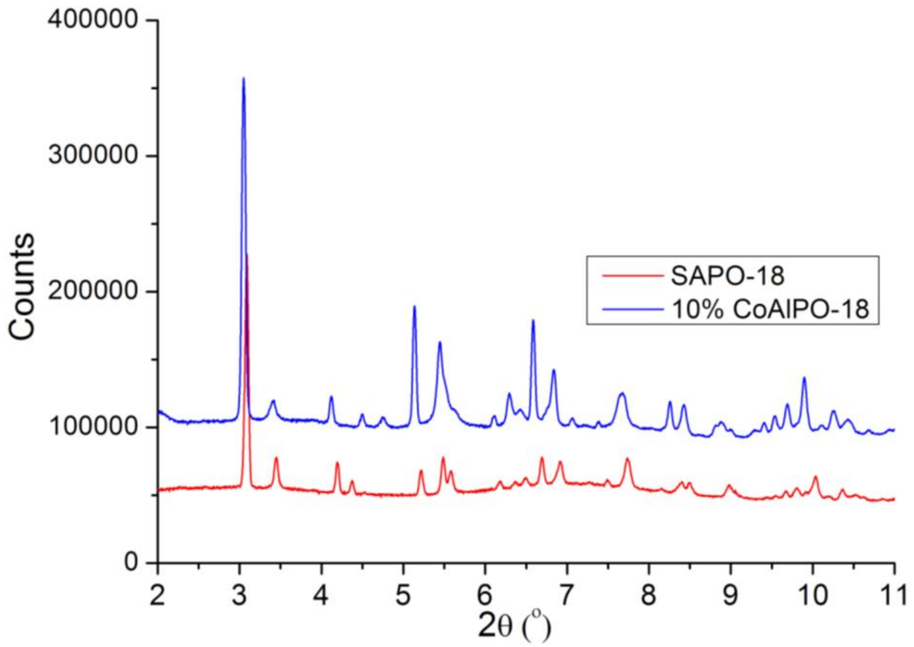

Figure 3.12. *Stacked plot of HRPD patterns of CoAlPO-18 (10 w%) and SAPO-18 (20 w% Si).*

One possible explanation of this phenomenon offered Van Breukelen et al.[24] in terms of cobalt clustering which was observed during a study of CoAPO-5 employing quantitative ^{31}P NMR spectroscopy. They found that the increasing cobalt content from 0.001 to 3.15 w% in CoAlPO-5 causes the cobalt ions of five or more to cluster. They observed this as a decrease in the cobalt NMR-visible from 97 to 42% surrounded by 10 NMR-invisible phosphorus atoms.

SEM images were taken to see changes in the morphology of the as prepared materials. AlPO-18, **Figure 3.13**, displays long crystal in the shape of chips with the average size of 1 µm. On the other hand, cobalt as-prepared materials show cubic crystal shapes with a large distribution of sizes, ranging from small 1 to 3 µm in sizes (**Figure 3.14** to **Figure 3.17**). SEM of sample 4A shows considerably lower amounts of cubic crystals, and more of uniform matter. The SEM images from 0.5, 2.5, 7.5 %, and 10 w% Co materials are displayed in **Figure 3.18**. These images were collected on the high resolution SEM machine at the Johnson Matthey Technology Centre in Reading. The cubic crystals are quite large but very uniform, and are surrounded by a faceted material. The faceted second phase seems more porous in appearance. The cube sizes are in the range of 1 to 3 µm.

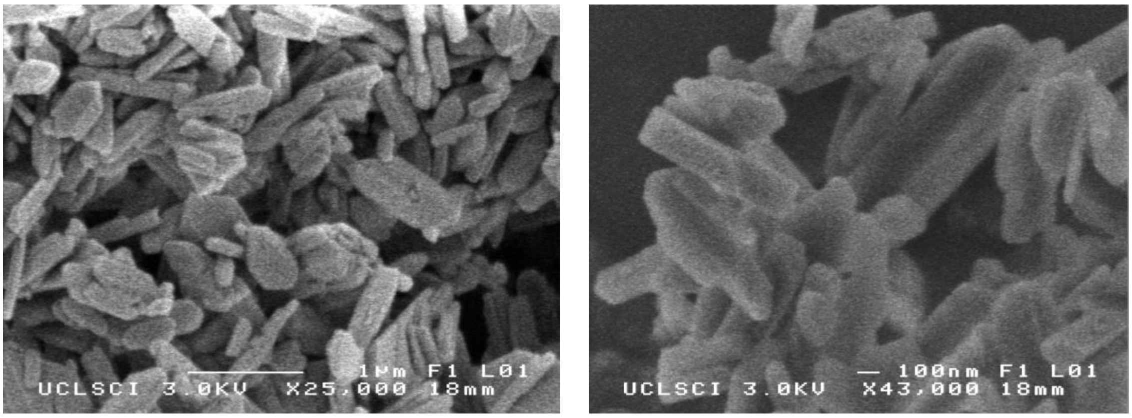

Figure 3.13. *SEM picture of as synthesized AlPO-18.*

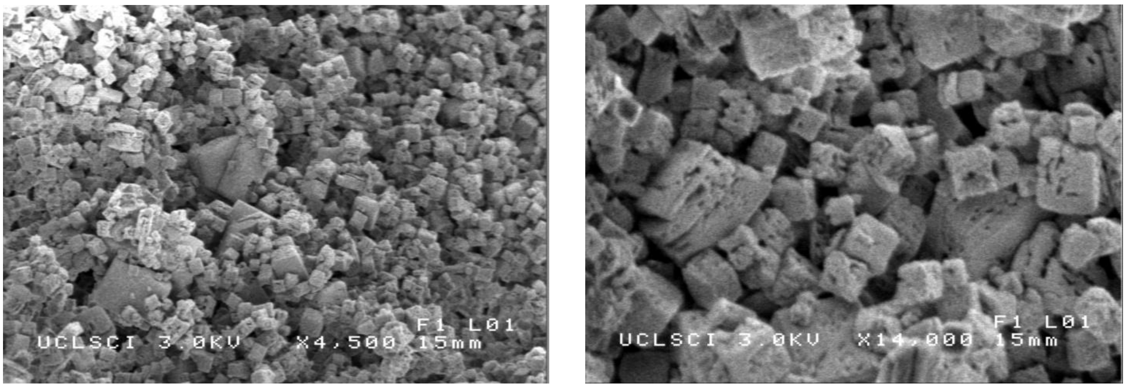

Figure 3.14. *SEM images of CoAlPO18 1A (Al/P = 0.9).*

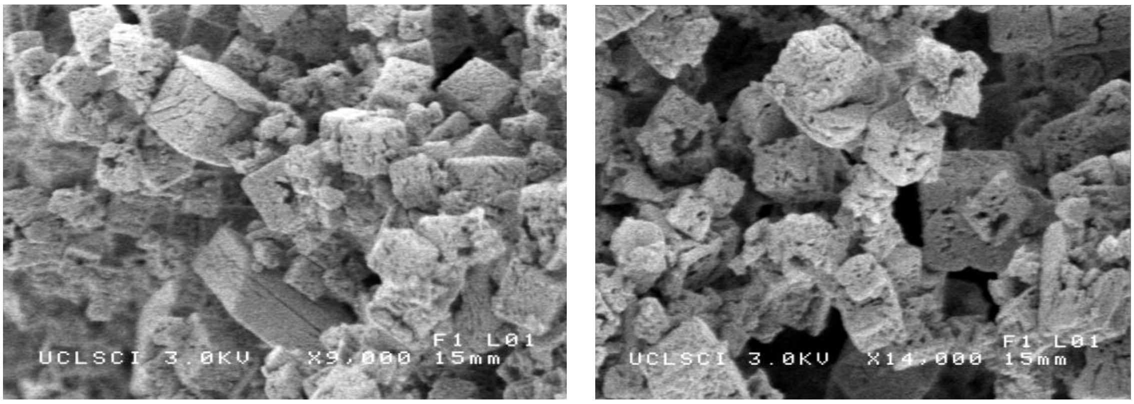

Figure 3.15. *SEM images of CoAlPO18 2A (Al/P = 0.8).*

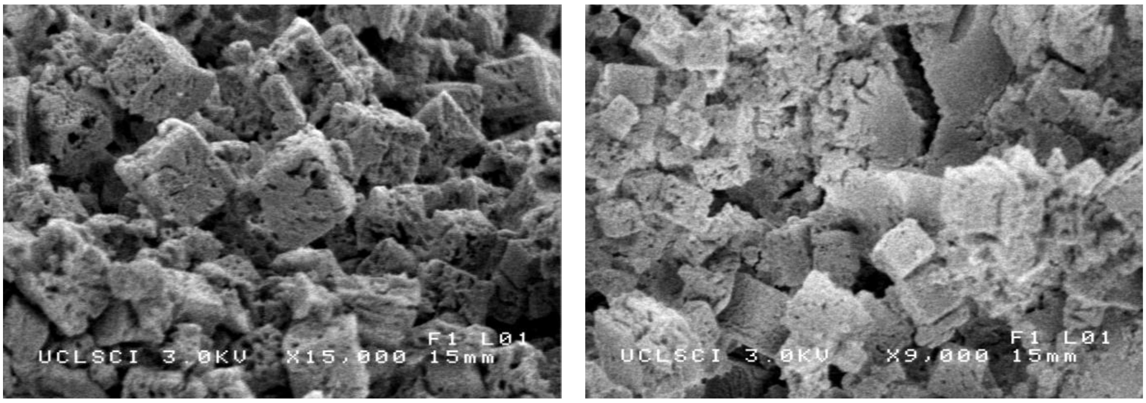

Figure 3.16. *SEM images of CoAlPO18 3A (Al/P = 0.7).*

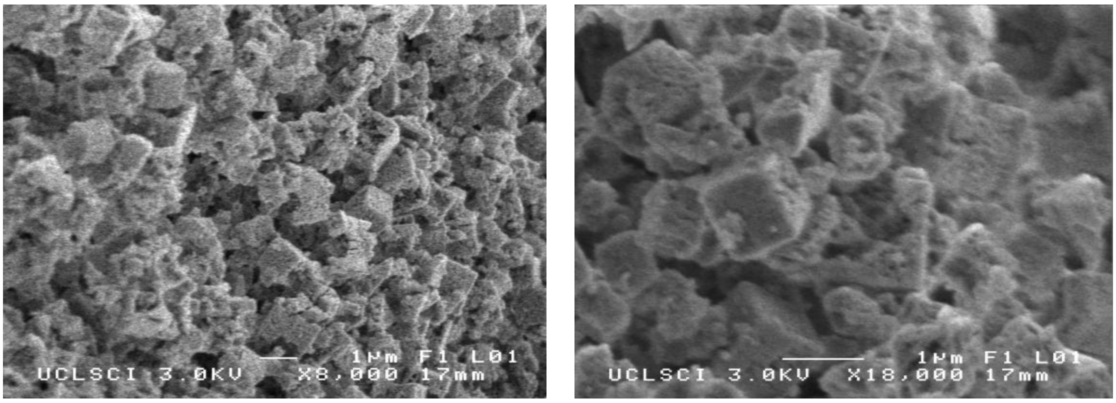

Figure 3.17. *SEM images of CoAlPO18 4A (Al/P = 0.6).*

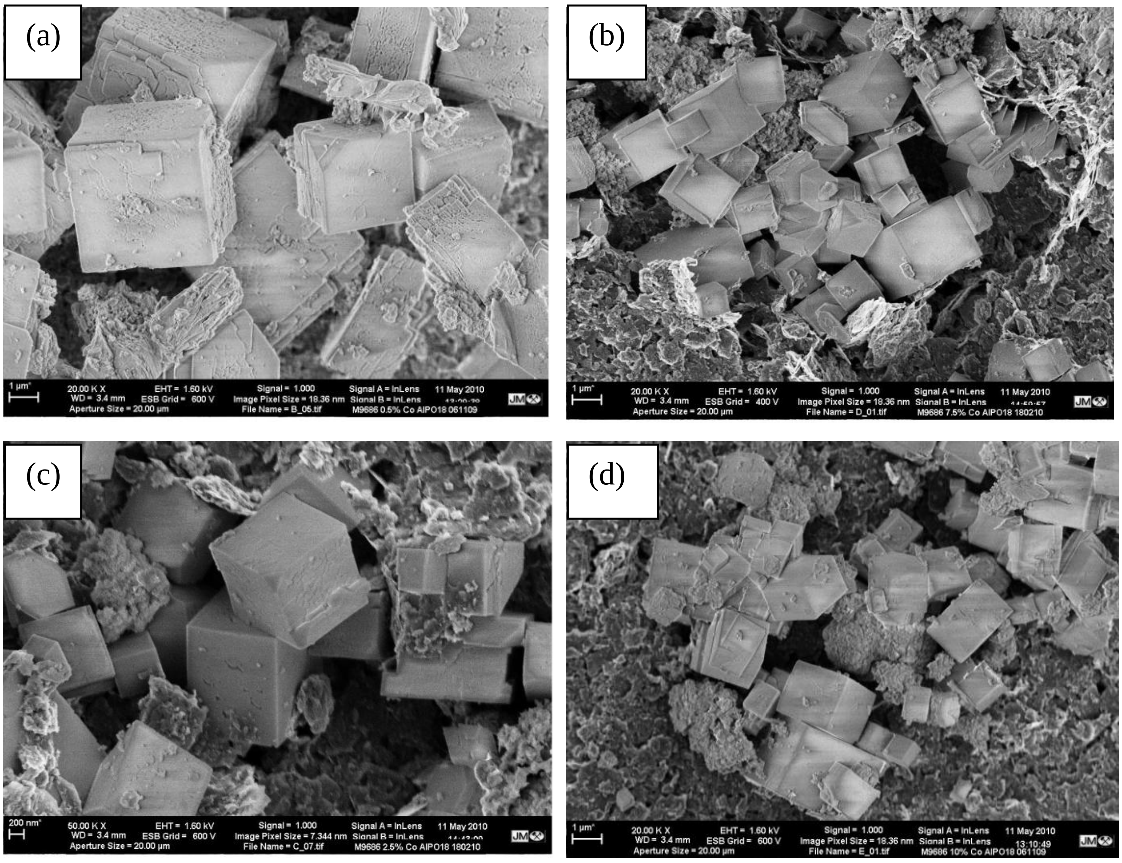

Figure 3.18. *SEM images from CoAlPO-18 samples, (a) 0.5 w%, (b) 2.5 w%, (c) 7.5 w%, (d) 10 w%.*

3.4.2 XAS of CoAPO-18

The effect to which the aluminium can influence the cobalt incorporation was examined by XAS. Co K-edge XANES spectra for cobalt aluminate ($CoAl_2O$) and cobalt acetate ($C_4H_6CoO_4$) were used to represent Co(II) in tetrahedral and octahedral environment and are displayed in **Figure 3.19**. Considerably larger absorption edge intensity, sometimes called white line intensity (WLI), is due to linear O-Co-O bonds which are evident in cobalt (II) in the octahedral coordination as evidenced by XANES from cobalt acetate. The absorption edge intensity arises from the $1s \rightarrow 4p$ transition, and is sensitive to changes in coordination that result in increased multiple scattering for octahedral coordination compared to the tetrahedral one[25]. On the other hand, $CoAl_2O_4$ is a spinel with Co(II) ions in tetrahedral sites[26]. The strong pre-edge feature in $CoAl_2O_4$ arises from the formally forbidden $1s \rightarrow 3d$ absorption transition, which appears most strongly for tetrahedral cobalt environment compared to octahedral environment[25]. The mechanism for this relaxation of the rule is through *d-p* mixing of Co-O molecular orbitals which can only occur in non-centrosymmetric situations, i.e. tetrahedral coordination. Cobalt acetate consists of octahedrally coordinated Co(II) ions to oxygen[27], and therefore the pre-edge feature is not strongly pronounced. For those reason, the XANES is equally sensitive to multiple scattering generated due to the presence of tetrahedral[28] or octahedral coordination[29] of transition metals in aluminophosphates, and can be used to distinguish between different coordination and oxidation states of transition metals.

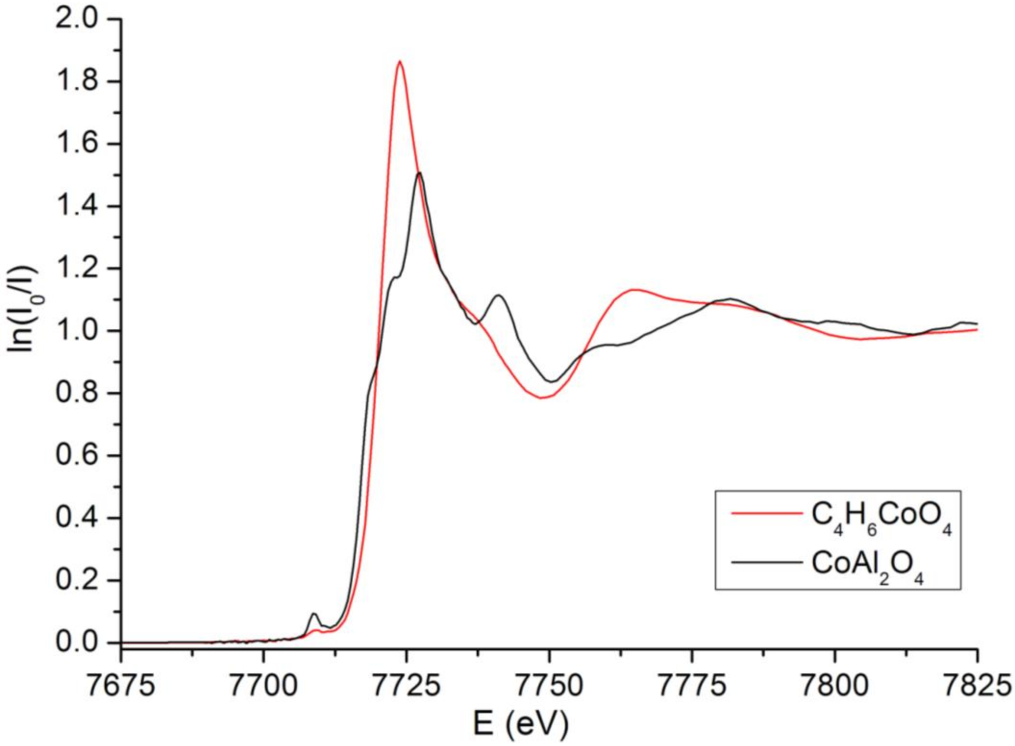

Figure 3.19. *Comparison of the Co K-edge normalized XANES of reference samples,* $C_4H_6CoO_4$ *(cobalt acetate) and* $CoAl_2O_4$*.*

The XANES from as-prepared samples, 1A to 4A, at room temperature (RT=22°C is the temperature in the air-conditioned experimental hall) are plotted in **Figure 3.20**. XANES collected during a dwell of 30 min at 530°C are shown in **Figure 3.21**. XANES spectra of individual samples are plotted in **Figure 3.22**. First, the room temperature data are discussed.

The white line intensity is gradually increasing from samples 2A, 3A, and 4A, in comparison to 1A. This intensity rise is caused by increased occurrence of octahedral Co(II) ions in extra framework positions, and the absorption edge intensity displays large sensitivity to coordination environment. Related pre-edge intensity also decreases for the sample 3A, although the largest intensity decrease is from the sample 4A by 11%. The decrease in main absorption edge intensity and the edge shift to higher energies is associated with oxidation of framework Co(II) to Co(III). The largest edge shift and drop of absorption edge intensity is observed for the 1A sample. The other three samples display comparable edge shifts but larger absorption edge intensities. The samples 2A and 3A display identical absorption edge intensities which are only marginally larger than in sample 4A.

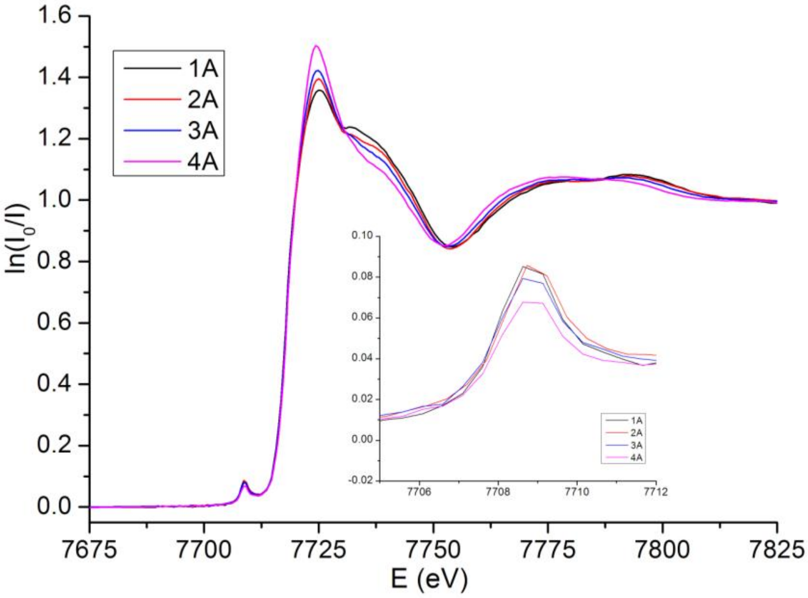

Figure 3.20. *Comparison of the Co K-edge normalized XANES of as-prepared 1A to 4A samples.*

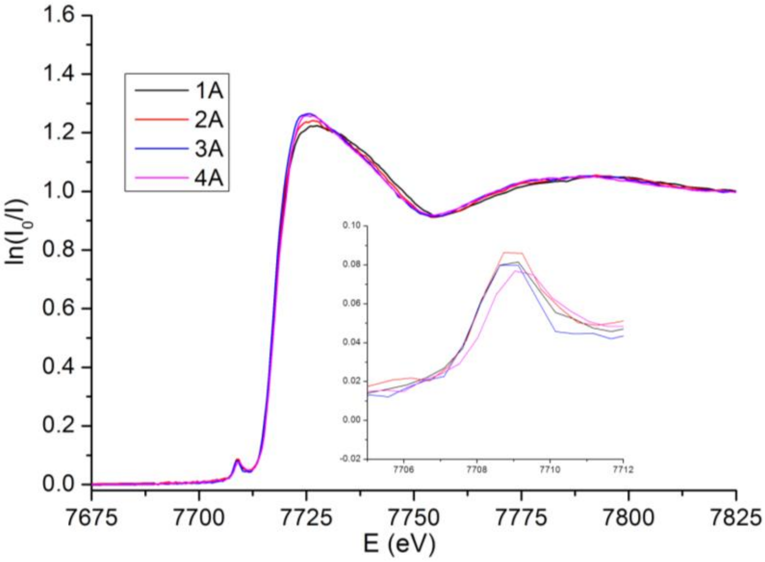

Figure 3.21. *Comparison of the Co K-edge normalized XANES of 1A to 4A samples after 30 min at 530^{o}C.*

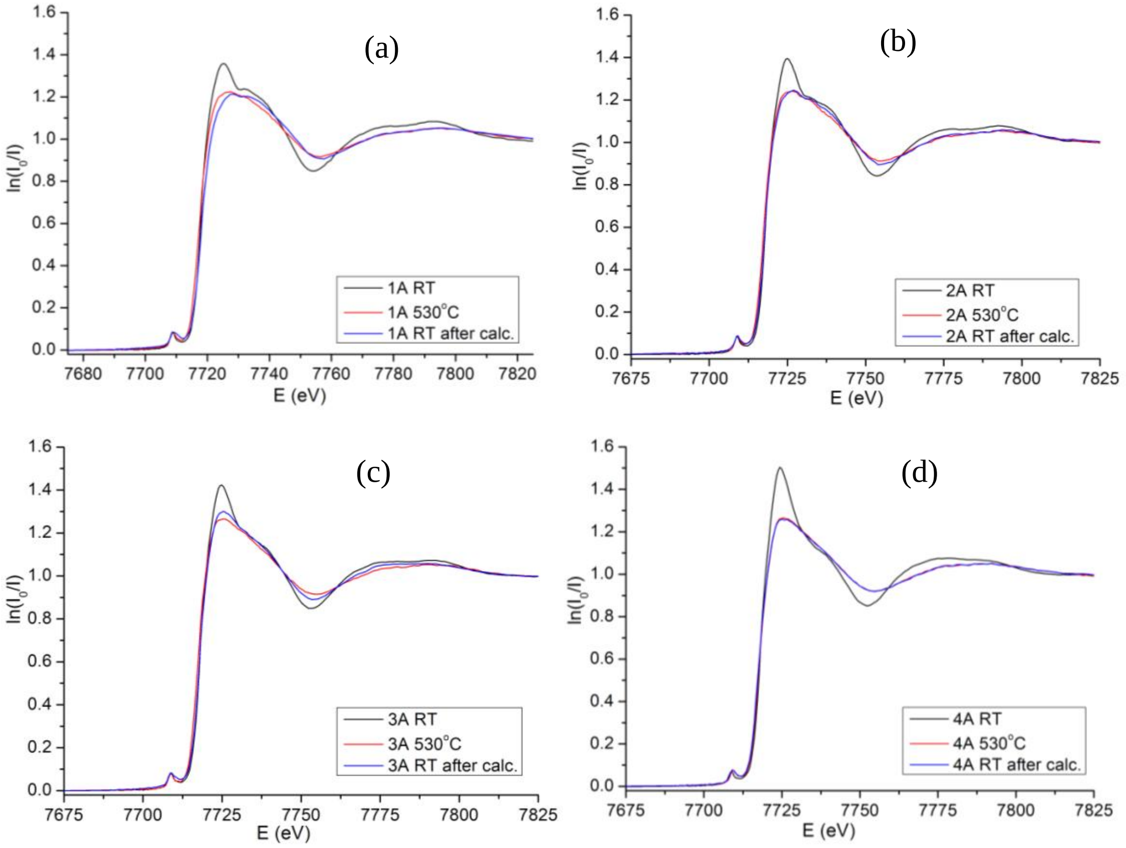

Figure 3.22. *Comparison of the Co K-edge XANES of as-prepared (blue), calcined (red), and calcined cooled to RT (dark blue) CoAlPO-18 materials: (a) 1A, (b) 2A, c(3A), (d) 4A.*

More detailed information and quantification of the cobalt active sites can be extracted from the analysis of the EXAFS data. **Table 3.4** shows the EXAFS fitting results which are graphically interpreted in **Figure 3.23** The figures from **Figure 3.24** to **Figure 3.28** show Co K-edge EXAFS spectra in *k*-space and calculated EXAFS with the corresponding Fourier transforms of studied samples. The analysis of the room temperature EXAFS data for the first coordination sphere revealed slightly larger static disorder (as indicated by the Debye−Waller factor) as the Al/P ratio is lower than 1. As the coordination number in the EXAFS formula strongly correlated with the Debye-Waller factor, it was kept at constant value of 4 during refinements. In $CoAl_2O_4$, Co surrounded by four tetrahedrally arranged oxygen atoms at 1.94 Å, whereas in $C_4H_6CoO_4$ it is surrounded by six octahedrally spaced oxygen atoms at 2.1 Å.

The bond distance in as-prepared sample is 1.94 Å in 1A, and 1.95 Å in 2A, with slightly larger static disorder for the latter. Much higher static disorder values and Co-O bond distances are from samples 3A and 4A which may indicate a mixture of 4-fold and 6-fold coordinations around cobalt ions, and thus the increase in the extra-framework Co(II) sites with the decrease in Al/P ratio. Upon the template removal, the decrease in Co-O bond distance is only to 1.90 Å in the sample 1A which is only smaller in comparison to 1.83 Å for the bond distance of tetrahedral Co(III) (derived from tetrahedrally coordinated Fe-O interatomic bond distance). Other three samples also show decrease in the Co-O bond distance. The fraction of oxidized Co(II) can be calculated using the average bond distances derived from EXAFS. Employing the formula $R_{EXAFS}=R_1x+R_2(1-x)$, derived by Barret et al.[30], R_1 is the Co(III)−O distance from the calcined sample, R_2 represents the Co(II)−O distance obtained from the as-prepared, R is the average distance obtained from the EXAFS analysis ($R_{Co(II)-O}$ = 1.93Å, $R_{Co(III)-O}$ = 1.83 Å) using a single oxygen shell, and x is the fraction of oxidized Co(III) in the material. The estimated fractions decrease, from 55% in 1A, to 19% in both 3A and 4A. The extra-framework cobalt ions can be in both octahedral (CoO) and tetrahedral sitting ($CoAl_2O_4$).

Table 3.4. *EXAFS fitting results and XAS characteristic. There N is coordination number; RT is room temperature; RTc is the room temperature after calcinations;* R_{EXAFS} *is the % of Co(II) oxidized to Co(III); WLI is white line intensity.*

Sample	Molar% Al	T (°C)	*N*	$R_{Co\text{-}O}$ (Å) (±0.01 Å)	$2\sigma^2$	R_{EXAFS} (%)	WLI
$CoAl_2O_4$	-	RT	4	1.94	0.007		1.50
Co(II) acetate	-	RT	6	2.10	0.014		1.82
AG6714-1A	0.9	RT	4	1.94	0.008		1.37
AG6714-1A	0.9	530	4	1.89	0.014	55	1.24
AG6714-1A	0.9	RTc	4	1.89	0.013		1.24
AG6714-2A	0.8	RT	4	1.95	0.010		1.41
AG6714-2A	0.8	530	4	1.91	0.015	36	1.28
AG6714-2A	0.8	RTc	4	1.92	0.013		1.28
AG6714-3A	0.7	RT	4	1.95	0.012		1.44
AG6714-3A	0.7	530	4	1.91	0.015	19	1.28
AG6714-3A	0.7	RTc	4	1.97	0.020		1.28
AG6714-4A	0.6	RT	4	1.97	0.016		1.52
AG6714-4A	0.6	530	4	1.92	0.020	19	1.27
AG6714-4A	0.6	RTc	4	1.92	0.019		1.27

Errors in the $R_{Co\text{-}O}$ *bond distances are ± 0.01 Å. Errors on* $2\sigma^2$ *are 10-20%.*

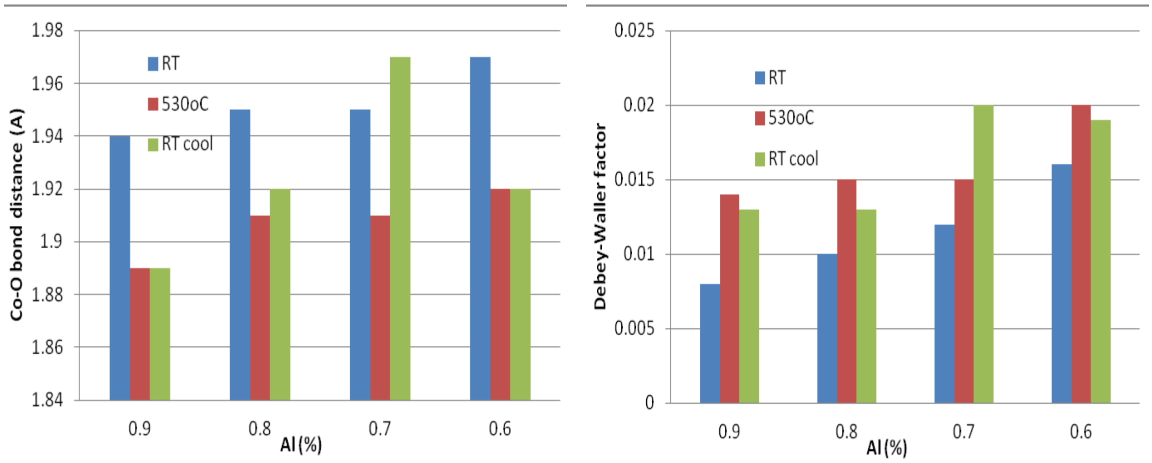

Figure 3.23. *Variation of Co-O interatomic distance with Al concentration.*

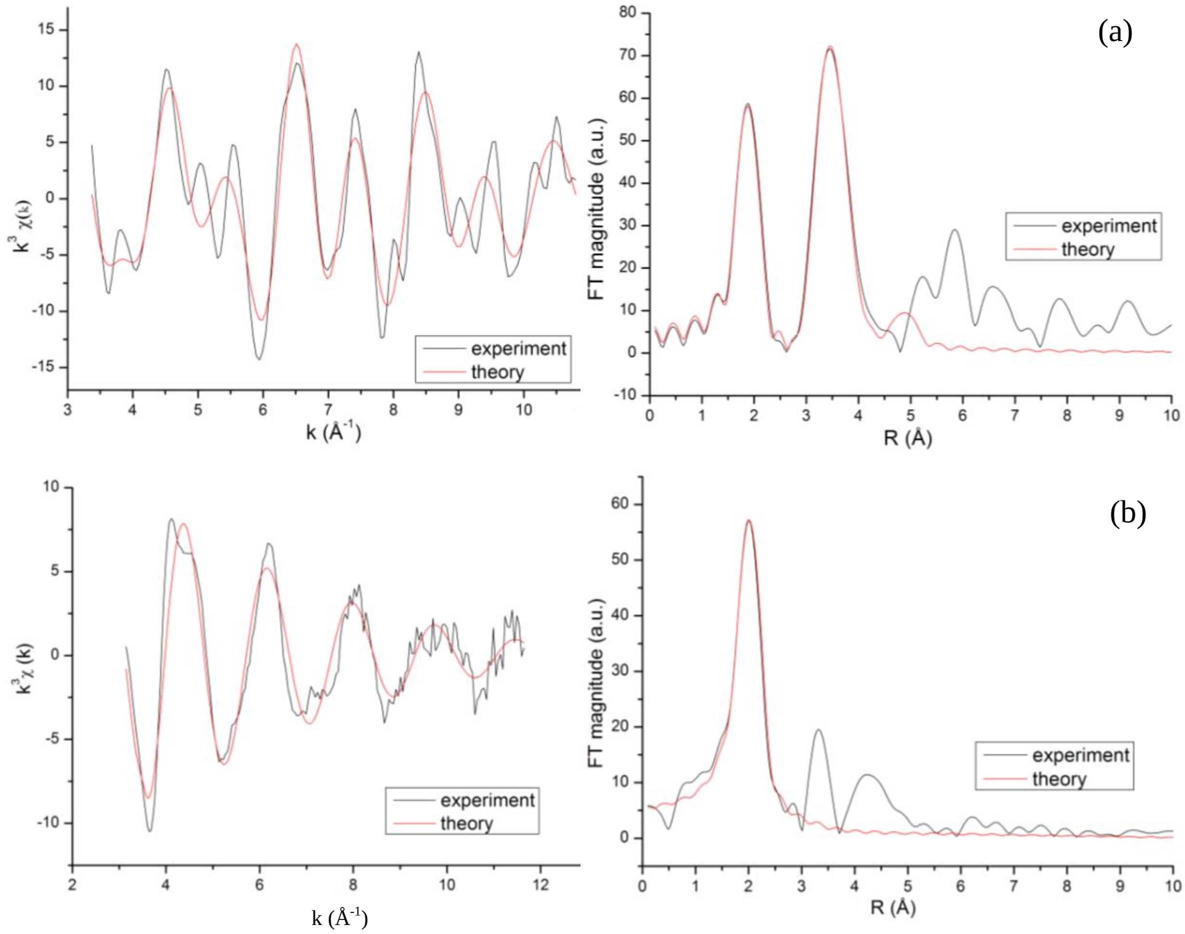

Figure 3.24. *Fits to Co K-edge EXAFS data analysed in k-space (k^3-weighted) with associated Fourier transforms for the: (a) $CoAl_2O_4$ at 25^{o}C; (b) Co(II) acetate at RT.*

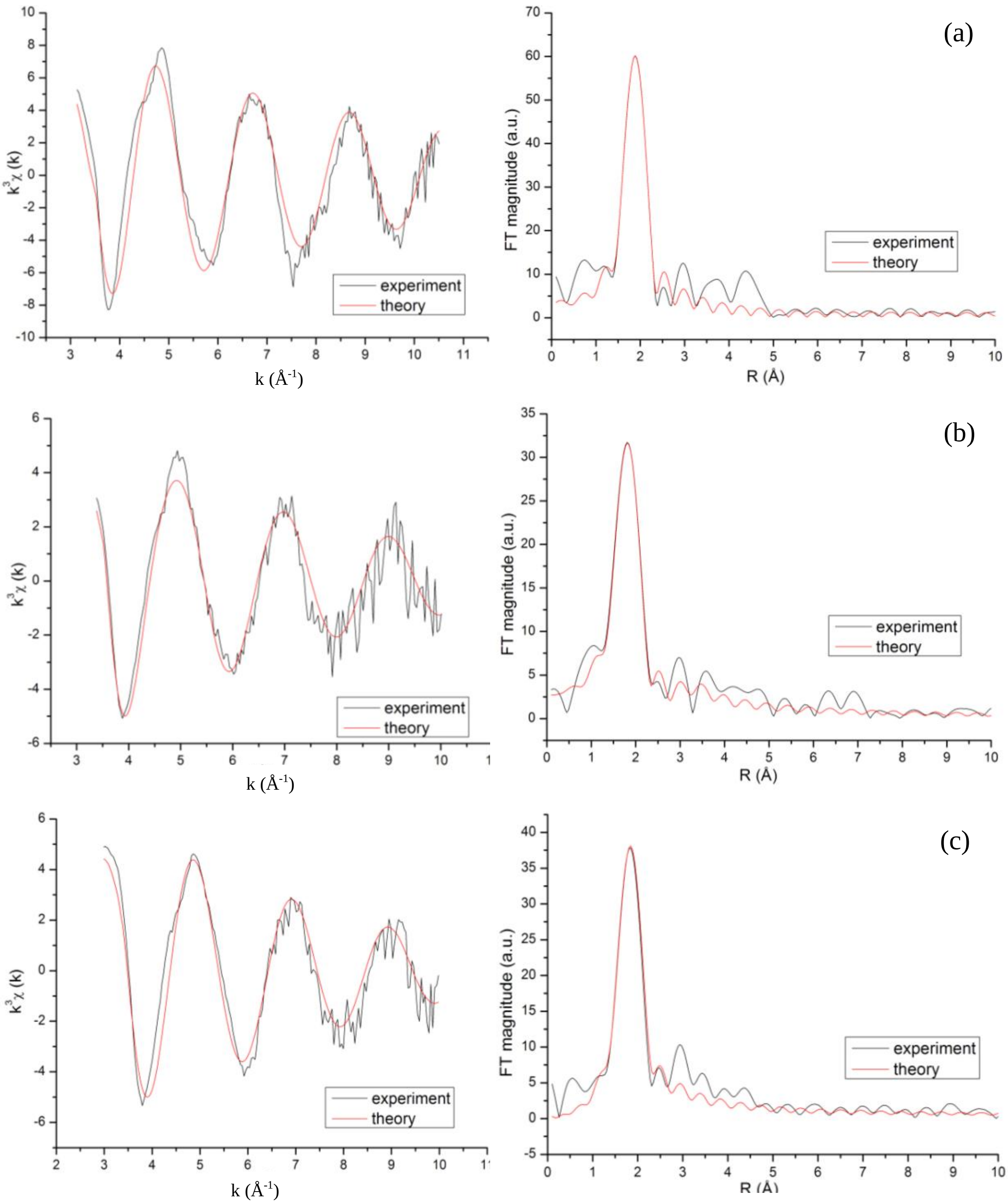

Figure 3.25. *Fits to Co K-edge EXAFS data analysed in k-space (k^3-weighted) with associated Fourier transforms for sample 1A whereis (a) freshly prepared material at RT; (b) calcined at 530^{o}C; (c) after calcination and cooling down to RT.*

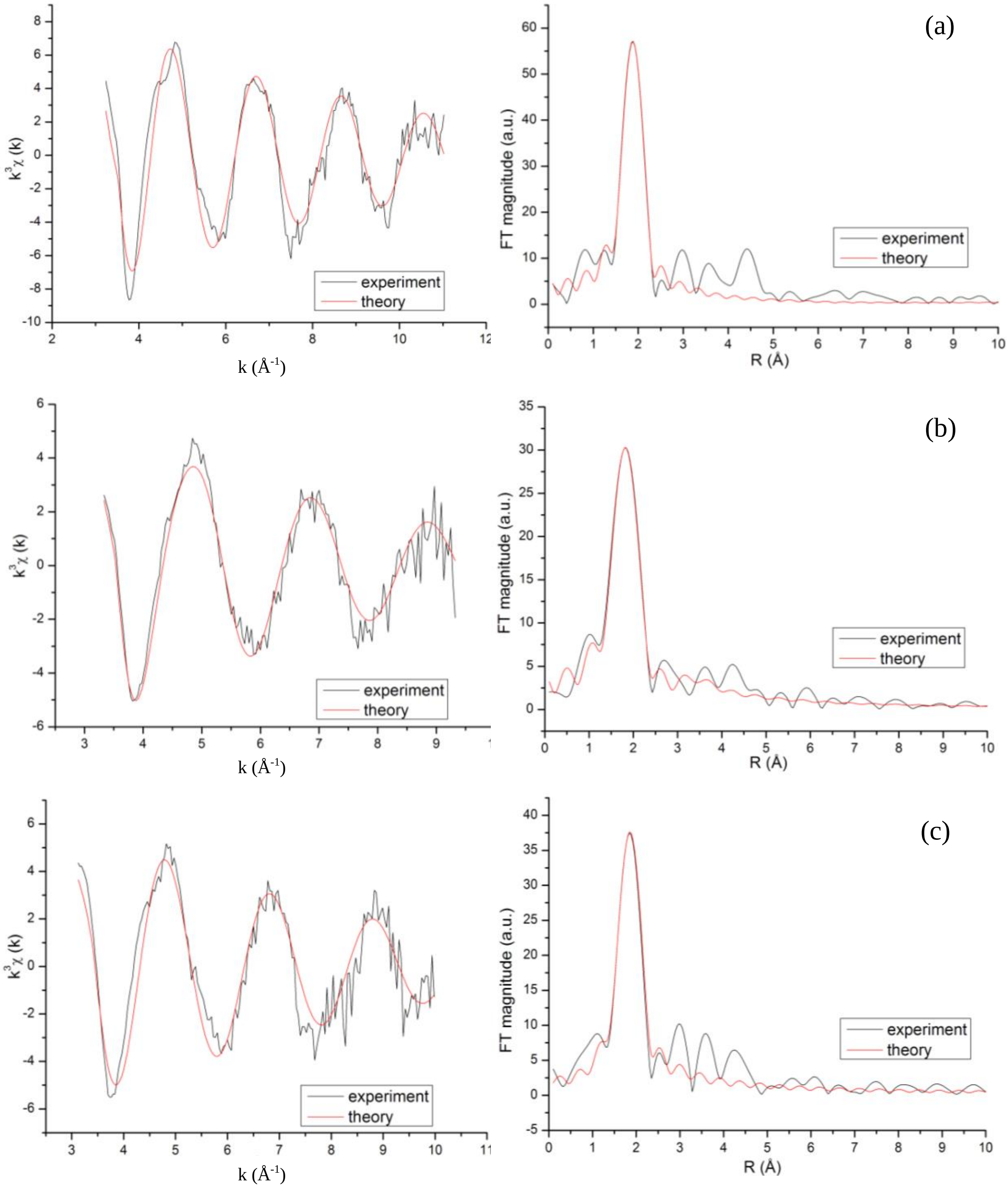

Figure 3.26. *Fits to Co K-edge EXAFS data analyzed in k-space (k^3-weighted) with associated Fourier transforms for sample 2A where (a) freshly prepared material at RT; (b) calcined at 530^{o}C; (c) after calcination and cooling down to RT.*

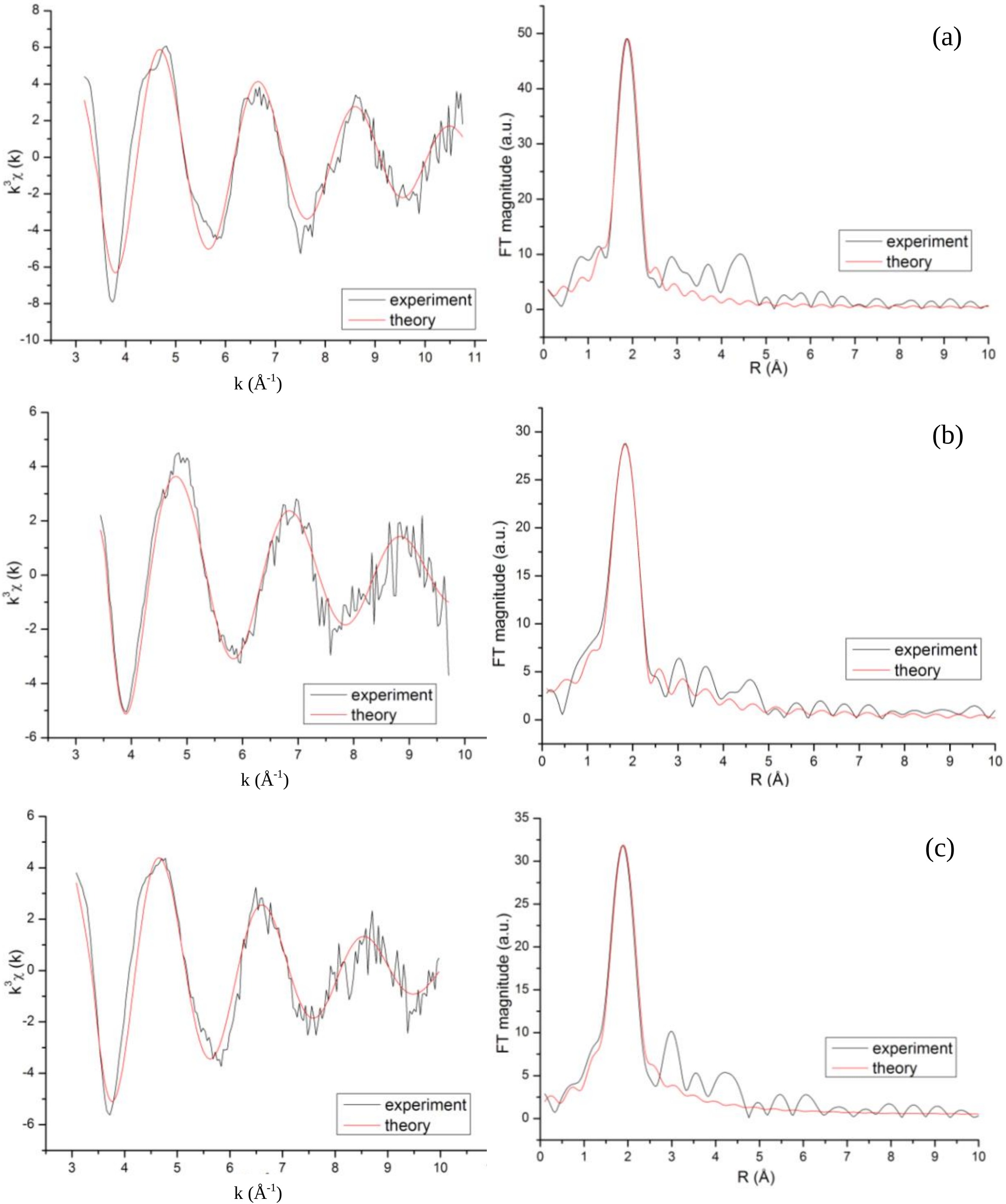

Figure 3.27. *Fits to Co K-edge EXAFS data analyzed in k-space(k^3-weighted) with associated Fourier transforms for sample 3A with (a) freshly prepared material at RT; (b) calcined at 530^{o}C; (c) after calcination and cooling down to RT.*

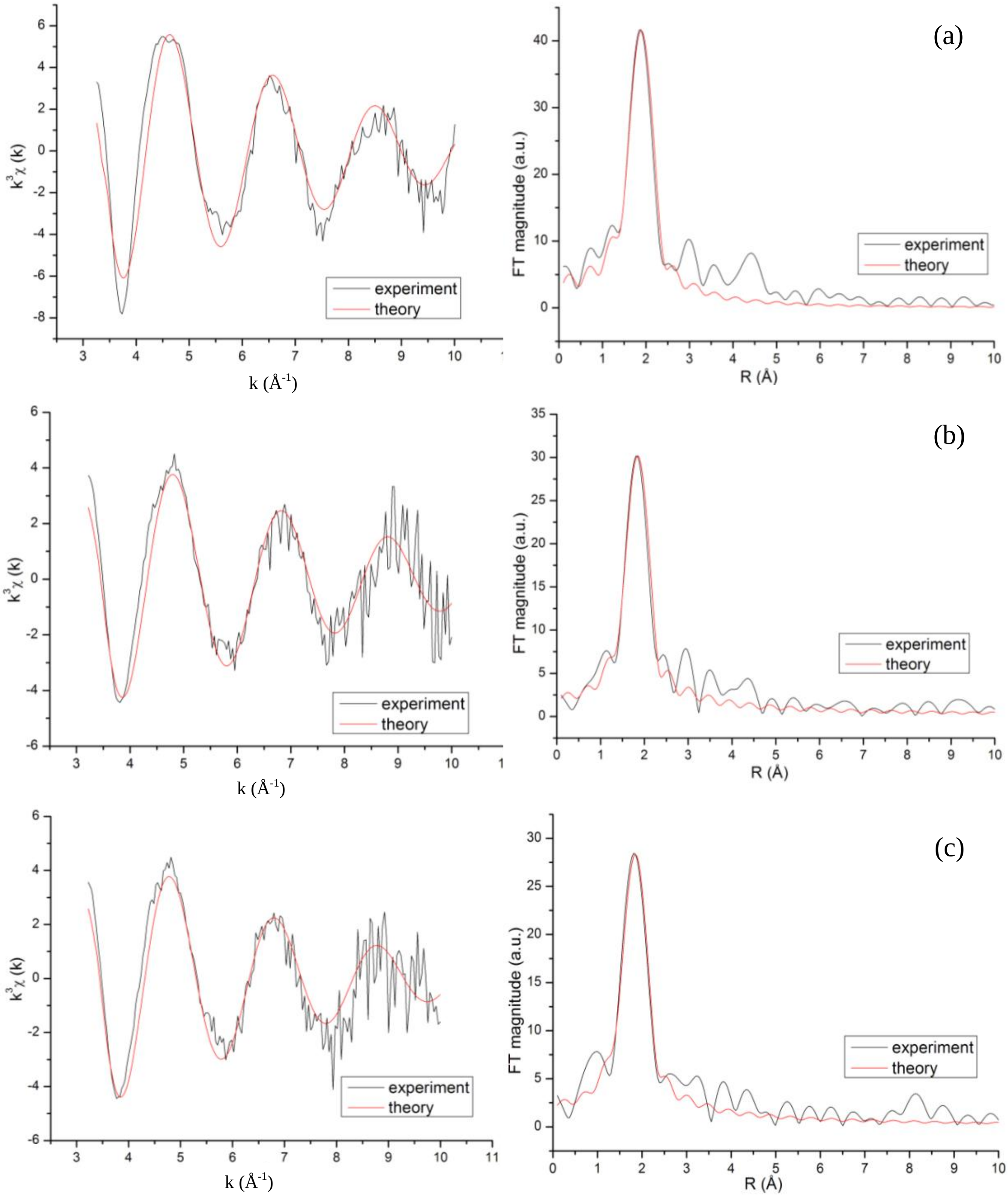

Figure 3.28. *Best fits obtained for Co K-edge EXAFS data (k^3-weighted) for sample 4A with associated Fourier transforms for: (a) freshly prepared material at RT; (b) calcined at 530°C; (c) after calcination and cooling down to RT.*

The multiple shells were investigated in $CoAl_2O_4$, and the results are displayed in **Table 3.5**.

Table 3.5. *EXAFS fitting results for $CoAl_2O_4$.*

Bonds	R (Å)	$2\sigma^2$
Co-O	1.94	0.007
Co-Al	3.24	0.013
Co-O	3.36	0.018
Co-Co	3.52	0.012

Errors in the bond distances are ± 0.01 Å. Errors on $2\sigma^2$ are 10-20%.

3.4.3 Probing the redox behaviour of CoAlPO-18 materials using in situ FTIR spectroscopy

FTIR is widely used in studies of zeolitic solids and catalyst strengths[31], and can provide further evidence for the changes in oxidation state upon oxidation and subsequent reduction. It is a relatively cheap but very effective way of obtaining information about acidity and metal substitution. In this *in situ* work we focused on studies of catalyst during detemplation: the period where the Brönsted acid centres can be observed. Individual IR scans were collected every 10^{o}C, but for the presentation purposes, only scans starting with 30^{o}C, 50^{o}C and then every 50^{o}C to 550^{o}C are plotted. The last displayed scan shows the system after 60 min of calcination at 550^{o}C and the one before last is at 550^{o}C at the beginning of calcination.

In **Figure 3.29**(a), a typical transmission spectrum of AlPO-18 in the stretching region of hydroxyl groups obtained during calcination in air is shown, while in **Figure 3.29**(b) a full spectrum obtained during the calcination is shown. AlPO-18, like all other aluminophosphate materials, is theoretically an electro-neutral structure and the peaks observed at 30^{o}C in the hydroxyl group stretching region, above 3676 cm^{-1} are attributable to isolated hydroxyl groups of P-OH; the peak at 3619 cm^{-1} is of hydroxyls hydrogen-bonded to framework or non-framework O atoms[32]. With increasing temperature, the sharp P-OH peak shifts to 3688 cm^{-1} and increases its intensity rapidly due to larger distortion as the template is slowly burning out. After complete template removal only a weak peak at 3666 cm^{-1} is observed.

C-H

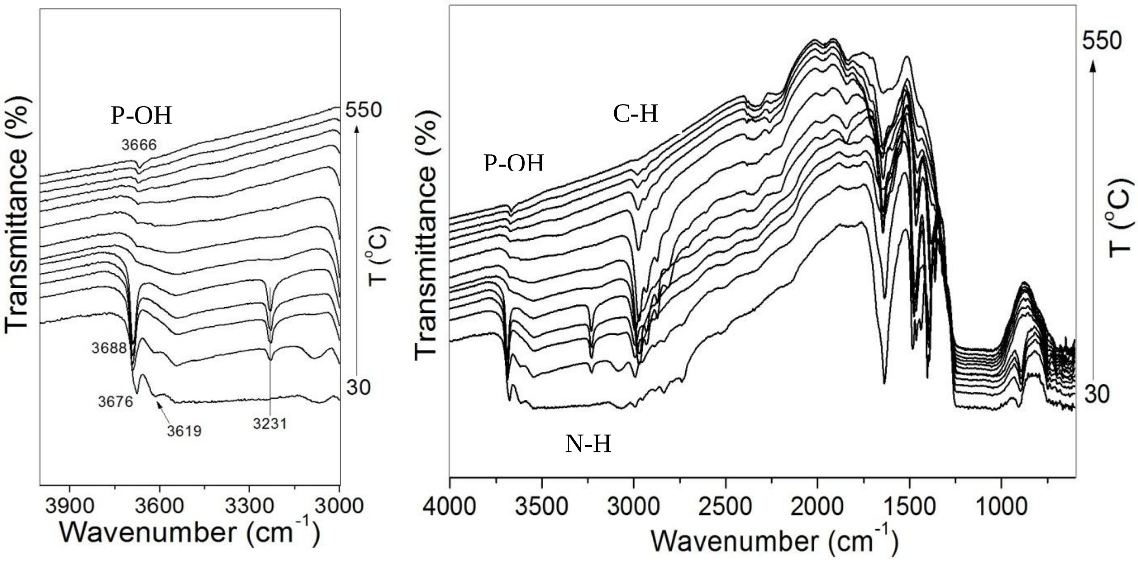

Figure 3.29. *IR spectra in the OH stretching region of (4000-2500 cm^{-1})(left) and full spectrum (right) of AlPO-18 (left) material.*

Figure 3.30 displays (in transmittance) the complete IR spectrum obtained from sample 1A, and **Figure 3.31**, and **Figure 3.32** depict detailed IR spectra at temperatures where the Brönsted acid sites start to appear. The stretching (2850 – 3000 cm^{-1}) and bending (1350 – 1470 cm^{-1}) bands could be assigned to C-H from the organic template (DIPE), and were found to vanish completely after heating to c*a.* 420°C. Two broad bands at 3307 and 3102 cm^{-1} which could be assigned to N-H stretching due to the decomposition of the template. This band eventually vanished at 550 °C[33]. The first sign of OH peaks associated with Brönsted acid sites is introduced between the 320 – 340°C range, as a new peak in the FTIR spectra at 3561 cm^{-1}, and which is attributed to bridging hydroxyl groups (Co-OH-P)[34]. After being held at 550 °C, the area of this Brönsted acid feature starts to decrease and becomes more resolved at higher wavenumbers. Decomposition of the organic template and emptying the voids, charge compensating protons are required to charge balance. This can be attributed to the Co(II) species oxidizing to Co(III), which results in the loss of Co-OH-P species.

The peaks at 3680 and 955 cm^{-1} are present in CoAlPO- 18 (calcined and reduced) and AlPO-18 systems, and it has been observed on many aluminophosphate molecular sieves and assigned to the stretching vibration of P-OH groups in lattice defects (internal and external surface defects)[35]. According to Marchese et al.[34], the intensity of the 955-cm^{-1} peak correlates with the intensity of that at 3680 cm^{-1} and is particularly strong in CoAlPO-18. This last observation suggests that the presence of Co is associated with lattice distortions and or lattice defects. The shoulder in the Brönsted peak is due to the location of Co(II) ions in the smaller rings of the CoAlPO-18 framework. To some extent, the colour can give away information about cobalt coordination. The typical blue colour for cobalt substituted aluminophosphates indicate tetrahedral coordination of Co(II) in as-synthesized material, and substitution for Al(III). The template free sample with tetrahedral Co(III) should be bright green. However, the colour of the calcined sample was not the typical green colour of Co(III) but more yellow which discoloured very fast to blue-grey in the open air.

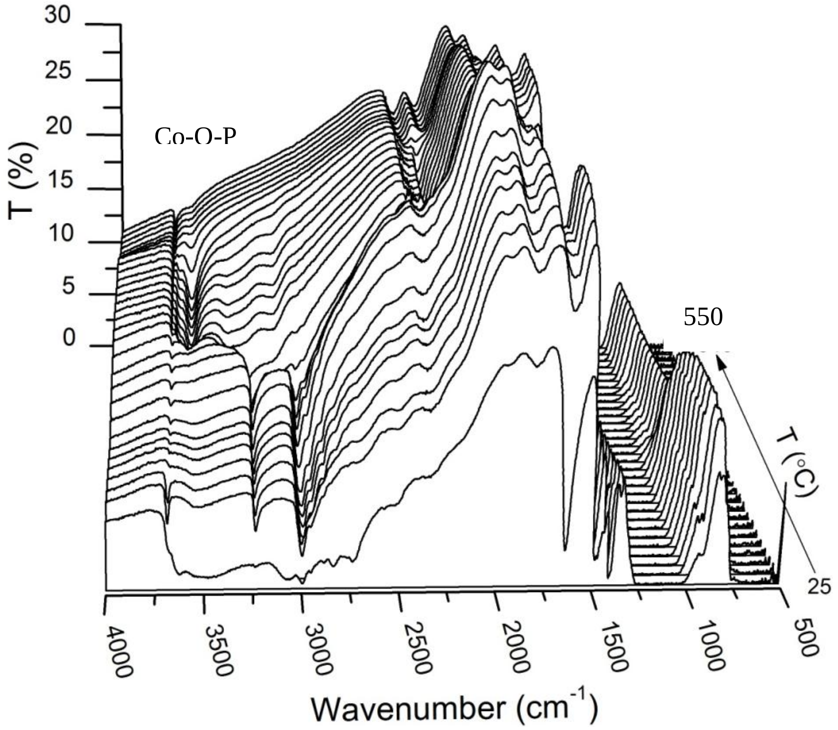

Figure 3.30. *3-D plot of full FTIR spectra during oxidation of CoAlPO18 AG6714-1A in air during calciation to 530 ^{o}C.*

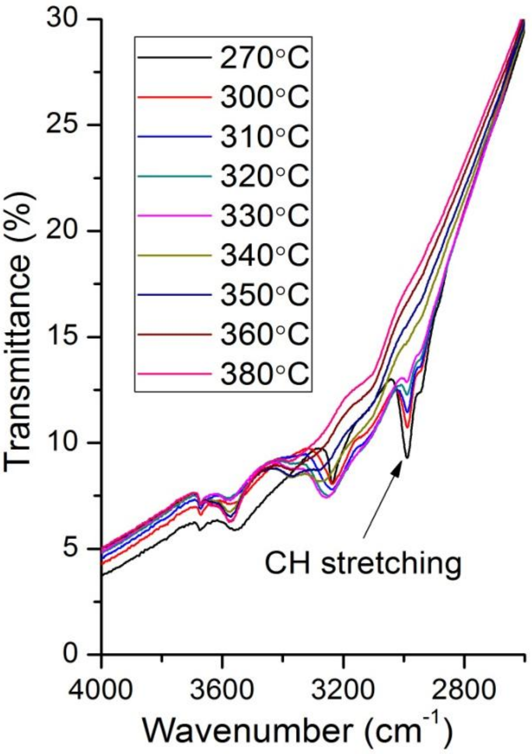

Figure 3.31. *Complete template removal and creation of Brönsted acidity of CoAlPO-18 1A.*

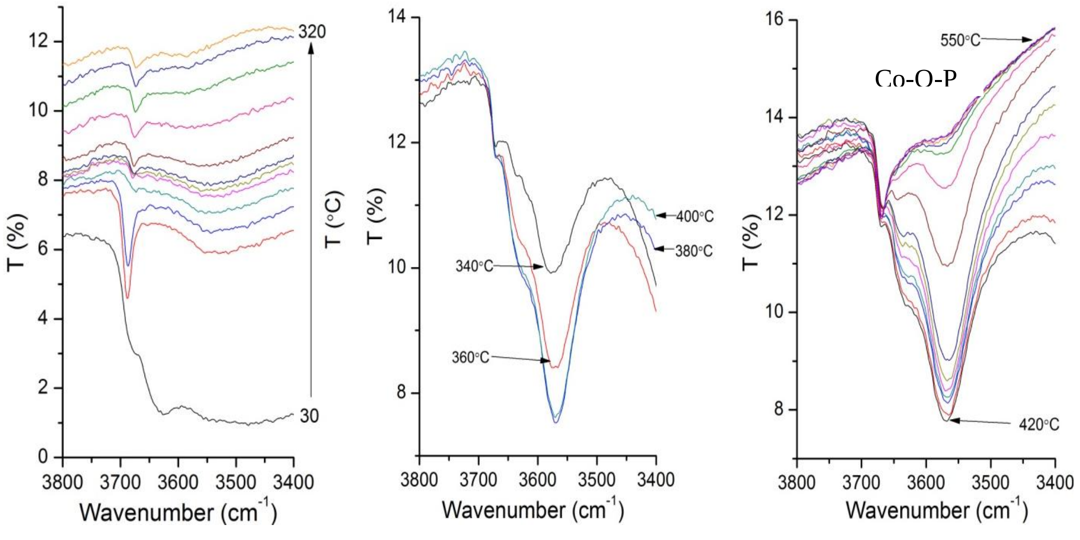

Heating in air from 30°C to 320°C.

Heating in air from 340°C to 400°C.

Heating in air from 400°C to 540°C (50min at 540°C).

Figure 3.32. *The detailed plots of creation of Brönsted acid centres during various stages of the calcination process in air.*

After the calcinations, sample 1A was heated in hydrogen, spectra are shown in **Figure 3.33**. During the reduction, oxidized Co(III) is reduced to Co(II), and the Brönsted peak reappears centred at 3650 cm^{-1}. The band is more intense in the bridging hydroxy region (*ca.* 3600 cm^{-1}) which is due to the OH stretching from the additional Brönsted acid sites when Co(III) is reduced back to Co(II).

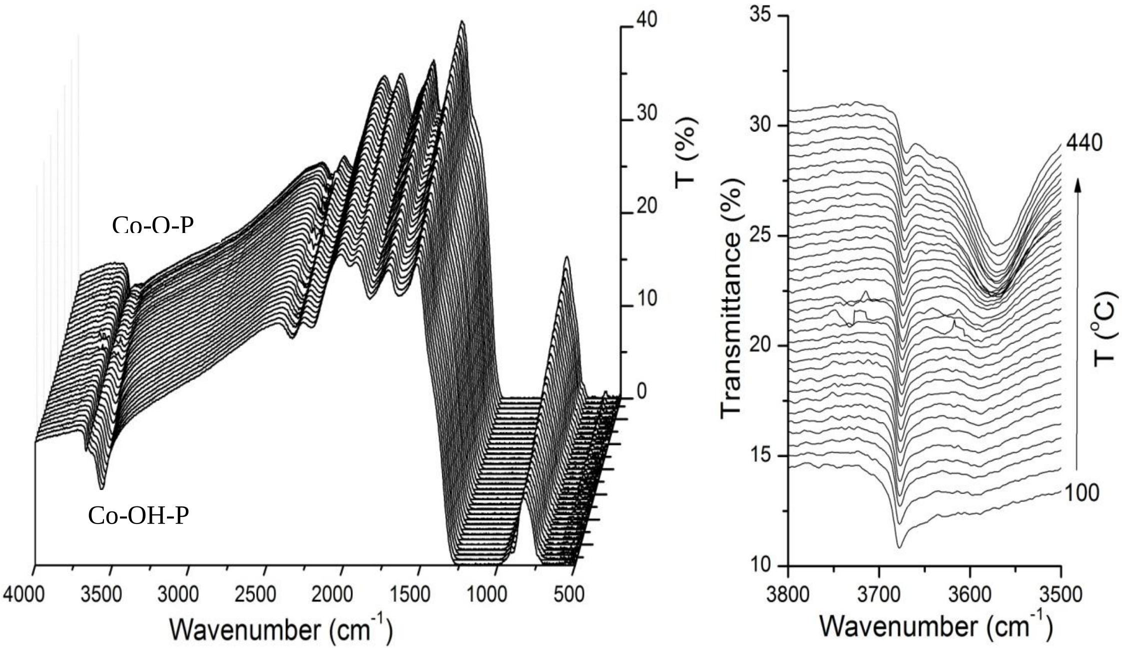

Figure 3.33. *Reduction of sample CoAlPO18 1A in hydrogen to 440 °C, (left) the full spectrum collected every 10°C and the reduction starts at the furthest point; (right) a region between 3800 – 3500 cm^{-1} where the Brönsted acid band is occurring.*

Figure 3.34 displays stacked plots of the IR spectra of the other three samples. The Brönsted acid peak can be seen in the IR spectra of all samples. The largest peak belongs to sample 2A but intensity decreases only marginally. This strongly suggests that some Co(II) ions are at inaccessible location and cannot be oxidized to Co(III). Although almost complete oxidation can be seen in samples 3A and 4A, the intensity is very low. Hence, the majority of the Co(II) ions are in extra-lattice locations, this is consistent with XAS result which also indicates cobalt sitting in the lattice.

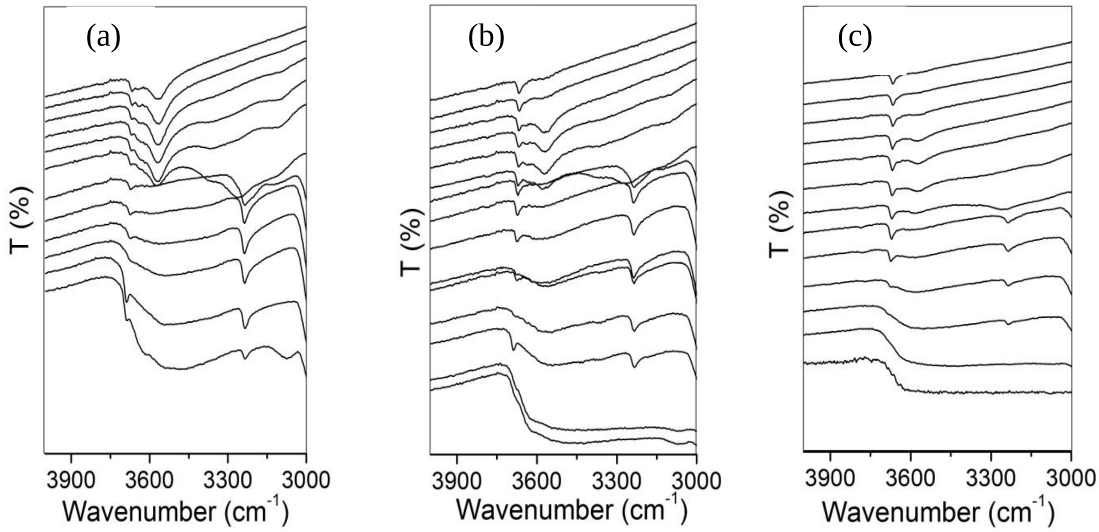

Figure 3.34. *In situ FTIR spectra during calcinations from samples: (a) - 2A, (b) - 3A, (c) - 4A.*

The findings from XAS and FTIR are in a good agreement. Although, the lattice expanded, the materials contain large amounts of cobalt in extra-framework positions. The crystallinity of the samples is, as the Al/P ratio decreases, lowered and the materials are not stable upon calcinations. To obtain phase pure materials, substitution of above 7.5 w% are required unless better method of preparation are available. The FTIR results and XAS for the samples obtained by improved method are discussed in following chapter.

3.5Summary and Conclusion

Cobalt substituted AlPO-18 catalysts prepared by different methods were synthesized by the hydrothermal method. Lattice expansion is been observed if cobalt substitutes aluminium ions in the AlPO-18 lattice. HRPD experiments showed that crystallinity of the samples is reduced with decreasing Al/P ratios. Among other things, it revealed that all cobalt substituted samples contain two phases, AlPO-18 and CoAlPO-18, which can be caused by clustering of cobalt ions in the lattice. The mixed phase has been confirmed by preparing new samples with cobalt concentrations in the synthesis gel starting from 0.5, 2.5, 7.5, and w%. Unlike others, only the 7.5 and 10 w% Co could be indexed as a single CoAlPO-18 phase which was confirmed by HRPD. The [002] reflection proved to be very sensitive for cobalt incorporation exclusively (see results in

Chapter 4) because it preferably sits in the *c*-axis direction in the lattice. *In situ* XAS revealed that the cobalt incorporation in the framework decreases with lower levels of aluminium in the synthesis gel. The imbalance in Al/P ratio creates a distortion inside the system which results in less Co(II) incorporated in the tetrahedral lattice positions and increased concentration of Co(II) in octahedral extra-lattice positions. The concentration of octahedral Co(II) increases exponentially as the Al/P decreases. The oxidation of the framework Co(II) to Co(III) was employed to calculate the approximate concentration of incorporation. The Brönsted acidity and cobalt nature was also confirmed by IR, and the results are consistent with XAS result, providing enough evidence for cobalt sitting in the lattice.

References

[1] S. T. Wilson, B. M. Lok and E. M. Flanigen, *Journal of American Chemical Society* **1988**, *196*, 207-211.

[2] a) G. Bellussi and P. Pollesel in *Industrial applications of zeolite catalysts: production and uses of light olefins*, *Vol. 158* Eds.: J. Cejka, N. Zilkova and P. Nachtigall), **2005**, pp. 1201-1212; b) J. M. Thomas, R. Raja, G. Sankar and R. G. Bell, *Accounts of Chemical Research* **2001**, *34*, 191-200.

[3] a) M. P. J. Peeters, M. Busio and P. Leijten, *Applied Catalysis A: General* **1994**, *118*, 51-62; b) D. L. Vanoppen, D. E. De Vos, M. J. Genet, P. G. Rouxhet and P. A. Jacobs, *Angewandte Chemie International Edition in English* **1995**, *34*, 560-563.

[4] J. M. Thomas, R. Raja, G. Sankar and R. G. Bell, *Nature* **1999**, *398*, 227-230.

[5] B. Modén, L. Oliviero, J. Dakka, J. G. Santiesteban and E. Iglesia, *The Journal of physical chemistry B* **2004**, *108*, 5552-5563.

[6] S. T. Wilson, B. M. Lok, C. A. Messin, T. R. Cannan and E. M. Flanigen, *Journal of the American Chemical Society* **1982**, *104*, 1146-1147.

[7] E. M. Flanigen, R. L. Patton and S. T. Wilson in *Structural, synthetic and physicochemical concepts in aluminophosphate-based molecular sieves*, *Vol. 37* Eds.: P. J. Grobet and et.al.), Elsevier Science Publishers Amsterdam, **1988**, pp. 13-27.

[8] S. T. Wilson, B. M. Lok and E. M. Flanigen in *Crystalline metallophosphate compositions*, *Vol. 4310440* (Ed. U. S. Patent), Union Carbide Corporation, USA, **1982**.

[9] J. Chen, P. A. Wright, J. M. Thomas, S. Natarajan, P. L. Gai-Boyes, R. P. Townsed and C. M. Lok, *Journal of Physical Chemistry* **1994**, *98*, 10216-10224.

[10] G. Muncaster, A. T. Davies, G. Sankar, C. R. A. Catlow, J. M. Thomas, S. L. Colston, P. Barnes, R. I. Walton and D. O'Hare, *Physical Chemistry Chemical Physics* **2000**, *2*, 3523-3527.

[11] A. Simmen, L. B. McCusker, C. Baerlocher and W. M. Meier, *Zeolites* **1991**, *11*, 654-661.

[12] in *International Zeolite Association*, *Vol.* www.iza-online.org.

[13] a) D. Bae and K. Seff, *Zeolites* **1996**, *17*, 444-446; b) D. E. De Vos, E. J. P. Feijen, R. A. Schoonbeydt and P. A. Jacobs, *Journal of the American Chemical Society* **1994**, *116*, 4746-4752.

[14] R. M. Barrer, *Hydrothermal Chemistry of Zeolites,* Academic Press, **1982**, p.

[15] A. B. P. Lever, *Inorganic Electronic Spectroscopy*, Elsevier, **1986**, p.

[16] F. A. Cotton, G. Wilkinson, C. A. Murillo and M. Bochmann, *Advanced Inorganic Chemistry*, New York, **1999**, p.

[17] K. Simmance, G. Sankar, R. G. Bell, C. Prestipino and W. van Beek, *Physical Chemistry Chemical Physics* **2010**, *12*, 559-562.

[18] L. Marchese, E. Gianotti, N. Damilano and S. Coluccia, *Catalysis Letters* **1996**, *37*, 107-111.

[19] J. M. Thomas, R. Raja, G. Sankar and R. G. Bell, *Nature* **1998**, *398*, 227-230.

[20] J. Chen, J. M. Thomas and P. A. Wright, *Catalysis Letters* **1994**, *28*, 241-248.

[21] A. Lennie, J. Parker, C. Tang, S. Thompson and F. Yuan in *Beamline I11 User Manual, Vol.* www.diamond.ac.uk, **2011**.

[22] J. Rodriguez-Carvajal and T. Roisnel, *International Journal of Crystallography, Newsletter* **1998**.

[23] P. Xu, W. Pang, Q. Huo and J. Chen, *Chemistry of Zeolites and Related Porous Materials - Synthesis and Structure*, John Wiley and sons Ltd., Singapore, **2007**, p.

[24] H. F. W. J. van Breukelen, G. J. C. Kraaijveld, L. J. M. van de Ven, J. W. de Haan and J. H. C. van Hooff, *Microporous Materials* **1997**, *12*, 313-322.

[25] J. Chen, S. Natarajan, J. M. Thomas, R. H. Jones and M. B. Hursthouse, *Angewandte Chemie International Edition in English* **1994**, *33*, 639-640.

[26] H. Furuhashi, M. Inagaki and S. Naka, *Journal of Inorganic and Nuclear Chemistry* **1973**, *35*, 3009-3014.

[27] D. Bazin, I. Kovacs, L. Guczi, P. Parent, C. Laffon, F. De Groot, O. Ducreux and J. Lynch, *Journal of Catalysis* **2000**, *189*, 456-462.

[28] a) G. Sankar and J. M. Thomas, *Topics in Catalysis* **1999**, *8*, 1-21; b) A. M. Beale, G. Sankar, C. R. A. Catlow, P. A. Anderson and T. L. Green, *Physical Chemistry Chemical Physics* **2005**, *7*, 1856-1860.

[29] G. Sankar, J. M. Thomas, F. Rey and G. N. Greaves, *Journal of the Chemical Society-Chemical Communications* **1995**, 2549-2550.

[30] P. A. Barrett, G. Sankar, C. R. A. Catlow and J. M. Thomas, *Journal of Physical Chemistry* **1996**, *100*, 8977-8985.

[31] J. A. Lercher and A. Jentys in *Infrared and Raman Spectroscopy for Characterizing Zeolites, Vol.* (Ed. H. v. B. J. Cejka, A. Corma, F. Schuth), Elsevier, Oxfoard, **2007**.

[32] I. N. Senchenya and V. Y. Borovkov, *Studies in Surface Science and Catalysis* **1991**, *65*, 635-662.

[33] J. M. Thomas, G. N. Greaves, Sankar, P. A. Wright, J. Chen, A. J. Dent and L. Marchese, *Angewandte Chemie* **1994**, *33*, 1871-1873.

[34] L. Marchese, J. S. Chen, J. M. Thomas, S. Collucia and A. Zecchina, *The Journal of physical chemistry* **1994**, *98*, 13350-13356.

[35] P. J. Gellings in *Oxidation by catalysts containing vanadium*, *Vol. 7* Eds.: G. C. Bond and G. Webb), The Royal Society of Chemistry, **1985**, pp. 105-124.

Chapter 4 Synthesis and characterization of small pore metal substituted aluminophosphates AEI – type during calcination and methanol to olefins reaction; *in situ* XAS, HRPD, and FTIR study

4.1 Chapter overview

In this chapter, attention is focused on the investigation of small pore heteroatoms substituted in AlPO-18 (AEI-type) materials prepared with a 10 w% of transition metal and by means of *in situ* structural and spectroscopic investigations. Previous experimental work[1] on silicon substituted materials has shown that this structure exhibits negative thermal expansion upon heating of template free materials. In the present study, understanding of these catalysts is further broadened by introducing other divalent metals and comparing with the silicon analogue.

A series of transition metals and silicon substituted small pore AlPO-18 aluminophosphates were prepared and examined during removal (calcination) of organic template molecules occluded in the pores, and catalytic conversion of methanol to olefins (MTO), using high resolution powder diffraction. The systems studied were AlPO-18, SAPO-18, CoAlPO-18, ZnAlPO-18 and CoSAPO-18. Understanding the structural changes during activation, catalytic reaction and the incorporation of dopant ions in the MeAlPO framework is of importance since such information provides insight into the catalytic performance and deactivation of MeAlPO*s*.

To establish successful metal incorporation, a series of spectroscopic mesurements were carried out in order to establish the metal incorporation inside the aluminophosphate lattice. In particular X-ray Absorption Spectroscopy was mainly used to probe the active centres of CoAlPO-18 and established successful cobalt incorporation. In addition, Fourier Transform Infrared Spectroscopy was used to examine the Brönsted acidity in these materials and cross correlate with our XAS data.

4.2 Introduction

Nanoporous solids are widely used in important industrial reactions which exploit their regular pore architecture and heteroatom framework substitution driven acidic and redox properties[2]. In particular, transition metal containing aluminophosphate (AlPO) molecular sieves[3] exhibit remarkable catalytic activity[4]. The redox centres of catalysts are important in the reaction mechanism of partial oxidation at high temperatures, and thus the understanding of redox properties and structural changes at these temperatures (100 – 500^{o}C) during calcination and reaction is crucial. The purpose of metal incorporation into zeolitic frameworks is to create redox centres and modify acidity. Whilst, the heteroatom substitution and concentration is limited in zeolites, a much larger range of heteroatoms and concentrations are available in aluminophosphates.

Interest in studying small pore nanoporous MeAlPO-18 aluminophosphate materials[3b] has increased since these materials were found to selectively convert a variety of organic molecules[5]. Cobalt-containing aluminophosphate zeolites (Co-AlPO*s*) have shown particularly promising activity in the partial oxidation of hydrocarbons under mild conditions[6]. Alternatively, silicoaluminophosphate (SAPO) frameworks have been shown to be highly selective catalysts for the production of light olefins[7], notably, SAPO-34 (CHA-type)[7a], with a very similar structure to SAPO-18 (AEI), has been widely studied for methanol to olefins conversion[7a, 8]. In the present work, the main focus is on small pore AlPO-18 [9] with cobalt, silicon, and zinc incorporation. The structure of AlPO-18 is similar to that of AlPO-34 (Chabazite, CHA), the main difference between these two systems being the way in which double six rings that connect the cages are oriented (see **Figure 4.1**)[10]. In general, the majority of nanoporous zeolitic solids are used as shape selective catalysts, molecular sieves and ion exchange media[11]. The shape selective catalytic properties depend on the dimension of the pores and their geometry. The majority of catalytic applications take place at temperatures between 100 and 500^{o}C, thus understanding the structural changes that occur across this temperature range is critical to evaluate the role of these structures in performing shape-selective catalysis.

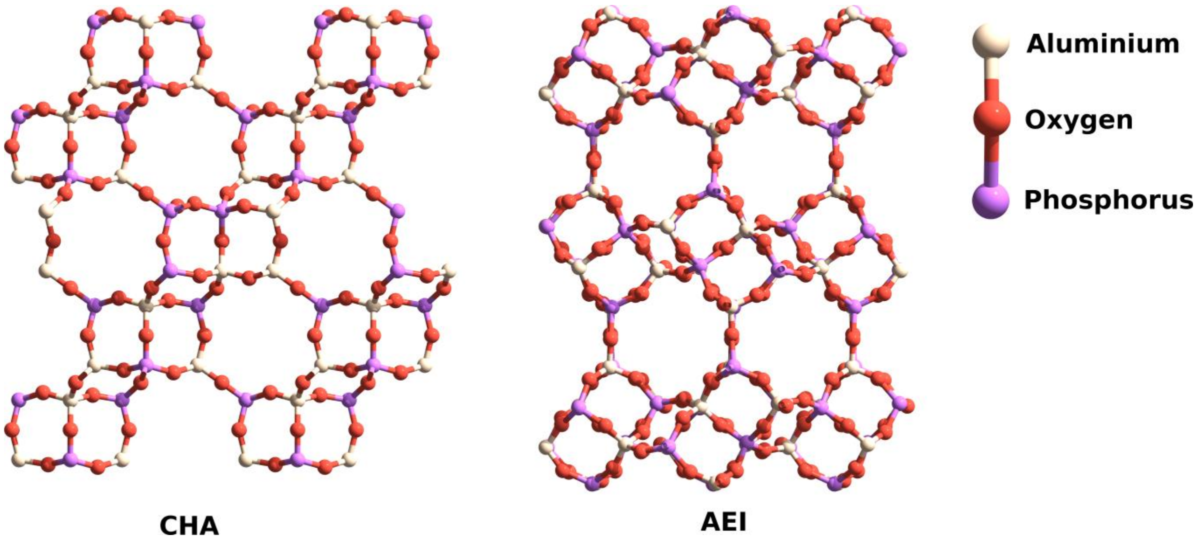

Figure 4.1. *Framework ring compositions of AlPO-34 (CHA) and AlPO-18 (AEI).*

To create solid acid catalysts, it is necessary to remove the organic template that occludes the pores in the as-synthesized material. This is conventionally carried out by heating the material in air to ca 500^{o}C. Although the majority of these systems are known to be stable after removing the organic template, some systems are found to lose their structural integrity upon calcination[12]. Thus understanding the structural changes during detemplation (activation) are of a particular interest in developing thermally stable catalysts.

Another important property of these types of small pore nanoporous materials is that they show negative thermal expansion (NTE) during heating; whilst heating of the majority of solids results in an increase of effective bond distances between atoms, and hence volume, with increasing temperature some of these materials have show a characteristic decrease in volume. Several studies have been conducted, employing X-ray powder diffraction and neutron diffraction, on materials such as MFI, AFI, DOH, MTN, DDR[13], AEI and CHA[1, 14], IFR[15], MWW, ITE, STT[16] to understand this phenomenon, since the NTE property of material can be exploited in many applications. Despite these efforts the underlying mechanism of NTE is poorly understood. The NTE properties of these materials have been explained based on inter-atomic distances which are reflected, at the macroscopic level as increase in dimension or volume. Hammonds et al.[17] proposed a mechanism for zeolites by the presence of rigid unit modes (RUMs). There the contraction is caused by rocking mode of the RUMs, which have constant bond lengths and angles of TO_4 tetrahedra. On the other hand, Tao et al.[18] concluded that the presence of RUMs is not necessary to predict the presence of NTE in oxides and zeolites. Charge compensating extra-framework cations (in some cases Na^+ or other alkali metal ions) can add additional stress in the zeolitic framework due to their size, coordination or charge and cause changes to the internal T-O-T angles of the joint bridging oxygen, due to a self-regulating mechanism which allows changes in the dimensions of the framework and depends solely on the topological, geometrical and symmetry properties of the three-dimensional nets underlying the frameworks[19]. Attfield and Sleight[20] discovered that AlPO-17 has the largest NTE in aluminophosphate materials at $\alpha_V = -35.1 \times 10^{-6}\ K^{-1}$.

The principal technique employed in these *in situ* studies has been high resolution powder diffraction (HRPD) since it provides information on the long-range order changes of structures and can also detect the locations of the template and carbon species formed inside the pores. While high-resolution powder diffraction has been used to provide evidence for the NTE property, analysis of the powder diffraction data is dominated by the symmetry of the structure. Furthermore, this technique will provide only the time-averaged structure, which may not be sufficient to explain certain structural properties[21]. High Energy X-ray diffraction (total-scattering) measurements can provide direct information on the short and medium-range order information without any dependence on crystal symmetry[22]. However analyzing the data and interpreting various distances from PDF is complicated. Nevertheless, this technique has been used widely in recent years to explain NTE properties of many solids[23].

4.2.1 Aims of the work

The aim of this work is to determine structural changes that take place during calcination and the methanol to olefin (MTO) reaction. Based on the synthesis results obtained in Chapter 3, a series of heteroatom substituted small pore aluminophosphate systems, AEI-type, were prepared and studied by high-resolution powder diffraction (HRPD) and high energy XRD (HEXRD) techniques. Using a combination of these two techniques, the effect of heteroatom substitution on the overall structure, the effect of adsorbed water molecules and evidence for the existence of NTE within these structures upon removal of the organic templates can be found. Prior to these studies, *in situ* XAS and FTIR were employed to characterize the active cobalt centers in CoAlPO-18.

4.3Experimental Section

4.3.1 Sample preparation

Samples of AlPO-18 and metal analogues were prepared using the best method obtained in the previous study (Chapter 3). The water volumes coming from the $Al(OH)_3.xH_2O$ were taken into account. The metal concentrations in the starting gels of MeAlPO-18 are shown in the **Table 4.1**.

Table 4.1. *Molar weights of the divalent (x) and tetravalent (y) metal ions used in the synthesis of AEI materials.*

Samples	*xMe(II)*	*yMe(IV)*
CoAlPO-18	0.1	0
ZnAlPO-18	0.1	0
SAPO-18	0	0.2
CoSAPO-18	0.05	0.05

In a typical synthesis, the starting gel was obtained by dissolving the divalent metal acetate salts (cobalt(II) acetate tetrahydrate ($(CH_3COO)_2Co{\cdot}4H_2O$, 98%,Sigma Aldrich), or zinc(II) acetate dihydrate ($Zn(CH_3COO)_2{\cdot}2H_2O$, 98%,Sigma Aldrich)) in a minimal amount of deionised water, with the balance of water added to phosphoric acid (85 wt % in water, Fisher). Aluminium hydroxide hydrate (99.99 wt %, Sigma Aldrich) powder was added to this phosphoric acid and water solution, and stirred until homogeneous. In the SAPO-18 synthesis, appropriate amounts of silica (SiO_2, 40 wt % in H_2O, Sigma) was added and stirred vigorously until homogeneous. The divalent metal acetate solution was added to this homogenised mixture, and again vigorously stirred. Finally, the structure directing agent N,N-diisopropylethylammonium hydroxide (40 wt % in water, Sigma Aldrich) was added to the gel which was left to stirr for 2 hours. The pH was adjusted to pH 7 through the addition of small amounts of phosphoric acid , and the gel was transferred to a Teflon-lined stainless steel autoclave (~50% fill) and heated at 160 °C for 4 days. The product of the reaction was recovered, washed with deionized water through filter paper, and finally dried at 100 °C in air overnight.

4.3.2 Laboratory XRD characterization (XRD and SEM)

XRD powder patterns were collected using a Bruker D4 diffractometer (Cu Kα radiation) which allowed phase identification and verification of sample purity by comparison to simulated patterns from published structures[9]. The stability of AlPO-18 and MeAlPO-18 catalysts upon template removal was confirmed by calcination at 550°C in a tube furnace for 4 h. Powder diffraction showed that the calcined AlPO-18 and ZnAlPO-18 materials hydrate rapidly in air with a symmetry change to lower symmetry[24] and broadening of Bragg peaks, whilst reheating above 200 °C for a couple of hours removes the adsorbed water. Similar adsorption of water has not been observed for CoAlPO-18, CoSAPO-18 and SAPO-18 catalyst, which were stable upon calcination.

The SEM images were taken with a Zeiss ultra 55 Field Emission Electron Microscope equipped with in-lens Secondary electron and backscattered detectors, based at Johnson Matthey Technology Centre in Reading. The samples were sprinkled on carbon padded SEM stubs. The two imaging modes were used:

- *A-Compositional analysis and low resolution general imaging*: Accelerating voltage: 20KV; Aperture used: 30micron; Working distance (WD): 7-8mm; Detectors: Std Secondary electron and Std backscattered electron detectors
- *B-High resolution low voltage imaging*: Accelerating voltage: 1.6KV; Aperture used: 20-30micron; Working distance (WD): 2-3mm; Detectors: In-lens Secondary electron and In-lens backscattered electron detectors

4.3.3 X-ray Absorption Spectroscopy

In situ X-ray Absorption Spectroscopy measurements were performed at the B18 X-ray absorption spectroscopy beamline[25] at the Diamond Light Source (DLS), which operates at 3 GeV energy with a current of 300 mA. The optical hutch (schematic representation shown below) was equipped with optical components (collimating mirror, monochromator, focusing mirror, harmonic rejection mirrors) and the main diagnostics elements (slits, attenuator filters, diagnostics units and removable fluorescence screen and cameras). The station was equipped with a double crystal

Si(111) monochromator, and ion chambers for measuring the incident and transmitted beam intensities (Io and It, respectively).

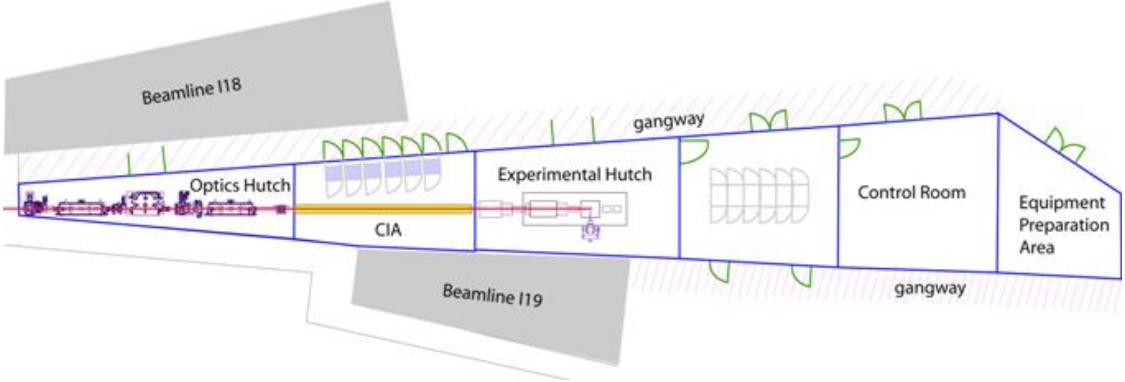

Figure 4.2. *Schematic representation of the layout for B18*[25].

In a typical experiment, the studied CoAlPO-18 material was pelletized (40 mg of sample) using a 13 mm pellet die. The sample was inserted into an *in situ* furnace and heated in a flow of dry air (Airgas,) to 550^{o}C at a rate of 5^{o}C/min. It was then calcined for about 60 min during which two XAS scans were collected in the transmission mode. $CoAl_2O_4$ and $C_4H_6CoO_4$ were used as model compounds of Co(II) in tetrahedral and octahedral coordinations respectively. The data were normalised and background subtracted using the ATHENA package[26]. Model fitting of the cobalt local environment was performed using ExCurve98[27].

4.3.4 Fourier Transform Infrared Spectroscopy

FTIR spectra were measured, in transmission mode, using a Perkin Elmer Spectrum One spectrometer and an *in situ* flow cell described in Chapter 3. Typically, 15 mg of a sample was pelletized and then a spectrum was measured at an ambient temperature (25^{o}C) in a flow of dry air (Airgas, purified by 13X molecular sieve) in the 500 and 4 000 cm^{-1} IR spectra. The samples were then heated at a rate of 5^{o}C/min to 550^{o}C and held at this temperature for 60 min to remove the template molecules trapped inside the microporous structure. FTIR spectra were collected every 10°C throughout this process to follow the formation and evolution of Brönsted acid bands. If reduction was carried out, typically the samples were cooled in N_2 (Airgas, UHP) to RT and then heated in

2% H_2/N_2 (Airgas, UHP) at the rate of 5 ^{o}C/min to 500^{o}C. Spectra were again collected every 5 ^{o}C until 500^{o}C. The sample was then cooled in nitrogen gas to RT.

4.3.5 In situ *High Resolution Powder Diffraction (HRPD)*

HRPD data were recorded at beamline I11 at the Diamond Light Source with a wavelength of 0.826061 Å using a Mythen 2 position sensitive detector, which has an intrinsic resolution of 0.004°. Powder patterns from five materials were collected. Data acquisition lasted 78 s. The pelletized materials were crushed and sieved to a size of between 0.3 µm to 0.5 µm and inserted into 2 mm quartz capillaries between plugs of silica wool. These were then placed into a custom built in situ capillary reactor. The reactor has the facility to flow gasses through the capillary, as shown schematically in Figure 4.4. The materials were heated to 530 ^{o}C employing a Cyberstar hot air blower, under a constant flow of dry air and dwelled for 1 hour to completely remove the structure directing template occluded inside the internal pores.

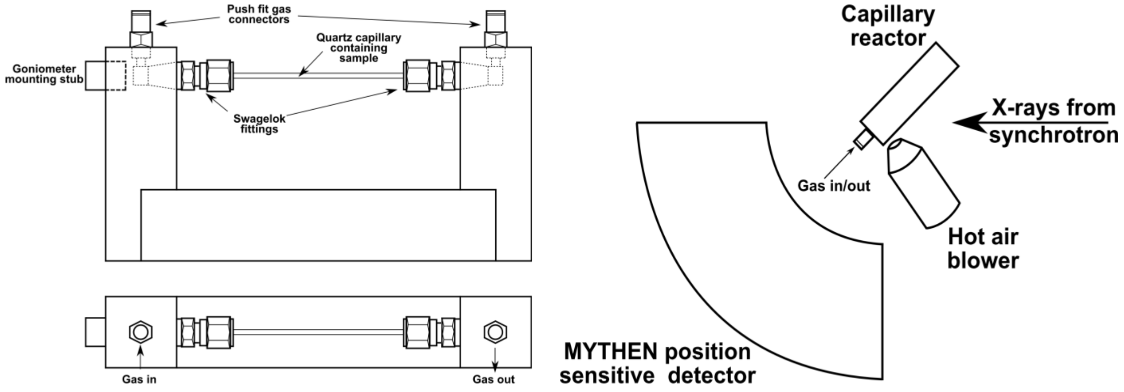

Figure 4.3. *Schematic diagram of the capillary cell (left) and an experimental setup inside the experimental hutch (right).*

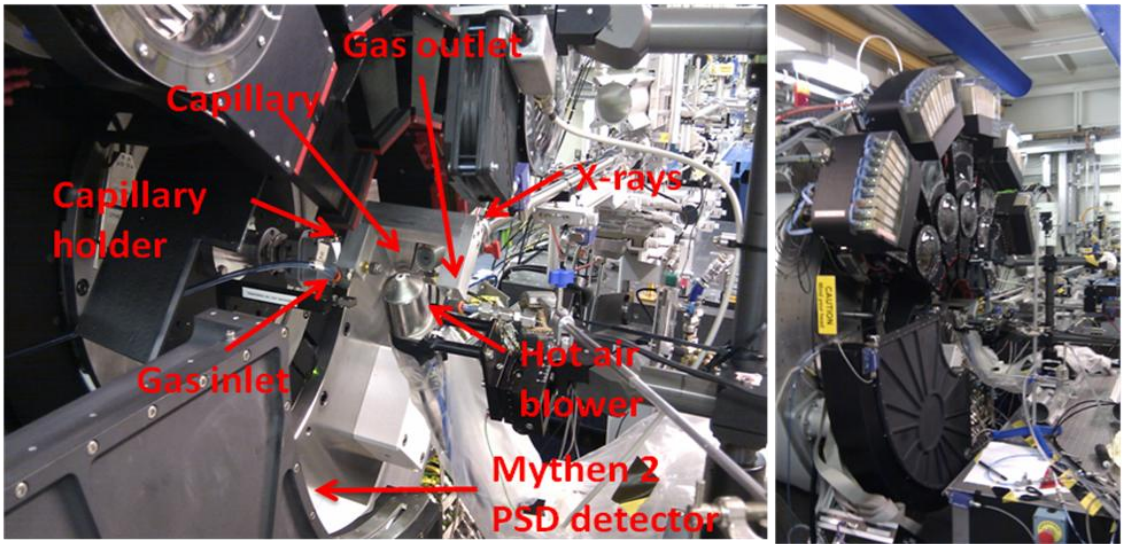

Figure 4.4. HRPD *set-up used during the in situ calcination of a small pore aluminophosphate catalyst at 530 °C under flow of dry air and MTO reaction at 400* ^{o}*C.*

Topas 4 academic[28] software was used to refine the cell parameters employing Le Bail extraction of peak intensities with the modified Thompson-Cox-Hastings pseudo-Voigt function to describe the profile. Starting model for cell parameters of the AEI phase were taken from Simmen et al.[29]. Graphic representations were performed using the data analysis and plotting software Origin Pro 8.5[30]. The EcoSys-P man portable quadrupole mass spectrometer, from European Spectrometry Systems (ESS) was used for the analysis of evolved gasses from the exhaust stream upon heating. Due to a poor resolution, the Mass Spec was only used for detection of the gas changeover and product evolution.

4.3.6 High Energy X-ray Diffraction (HEXRD)

X-ray total scattering (PDF method) measurements were performed on the high-energy X-ray diffraction beamline (HEXRD) BL04B2[23], at the third generation synchrotron radiation facility SPring-8 (Super Photon Ring) in Japan. The storage ring operated at 8 GeV energy. A two-axis diffractometer equipped with a high temperature furnace enabled *in situ* experiments to be carried out.

The studied powder samples were prepared by grinding and loading into evacuated capillary tubes (0.7 mm internal diameter) and data was collected *in situ* on a pure AlPO-18 sample at room temperature, 200°C, 400^{o}C and 530°C, and metal substituted samples at room temperature and 530°C. Each sample was measured for approximately 6 hours. For these measurements a wavelength of 0.29 Å was tuned by a Si (111) monochromator allowing for a momentum transfer, Q_{max}, of up to 25.0 $Å^{-1}$ to be achieved. Obtaining data out to a high value of momentum transfer, Q, (where $Q = 4\pi sin\theta/\lambda$) gives high real-space resolution in the pair distribution function, $G(r)$.

4.4Results and discussion

4.4.1 X-ray diffraction and SEM characterization

Figure 4.5(a) shows XRD patterns, collected on the Bruker D4 diffractometer, of as synthesised AlPO-18, a calcined and air exposed sample (AlPO-18 dh.) and a reference pattern reproduced from structural refinement (AlPO-18 ref) by Simmen *et al*[29]. The synthesised materials are phase pure, with high crystallinity, and could be indexed to the C2/c spacegroup. Upon calcination and exposure to air the material is distorted by water that is absorbed into the pores (**Figure 4.5**(a)), lowering the symmetry, however heating to 200 ^{o}C restores the C2/c symmetry. **Figure 4.5**(b) shows powder patterns of all metal substituted forms of AlPO-18 materials, all resemble the AEI-type structure. ZnAlPO-18 has the lowest number of counts.

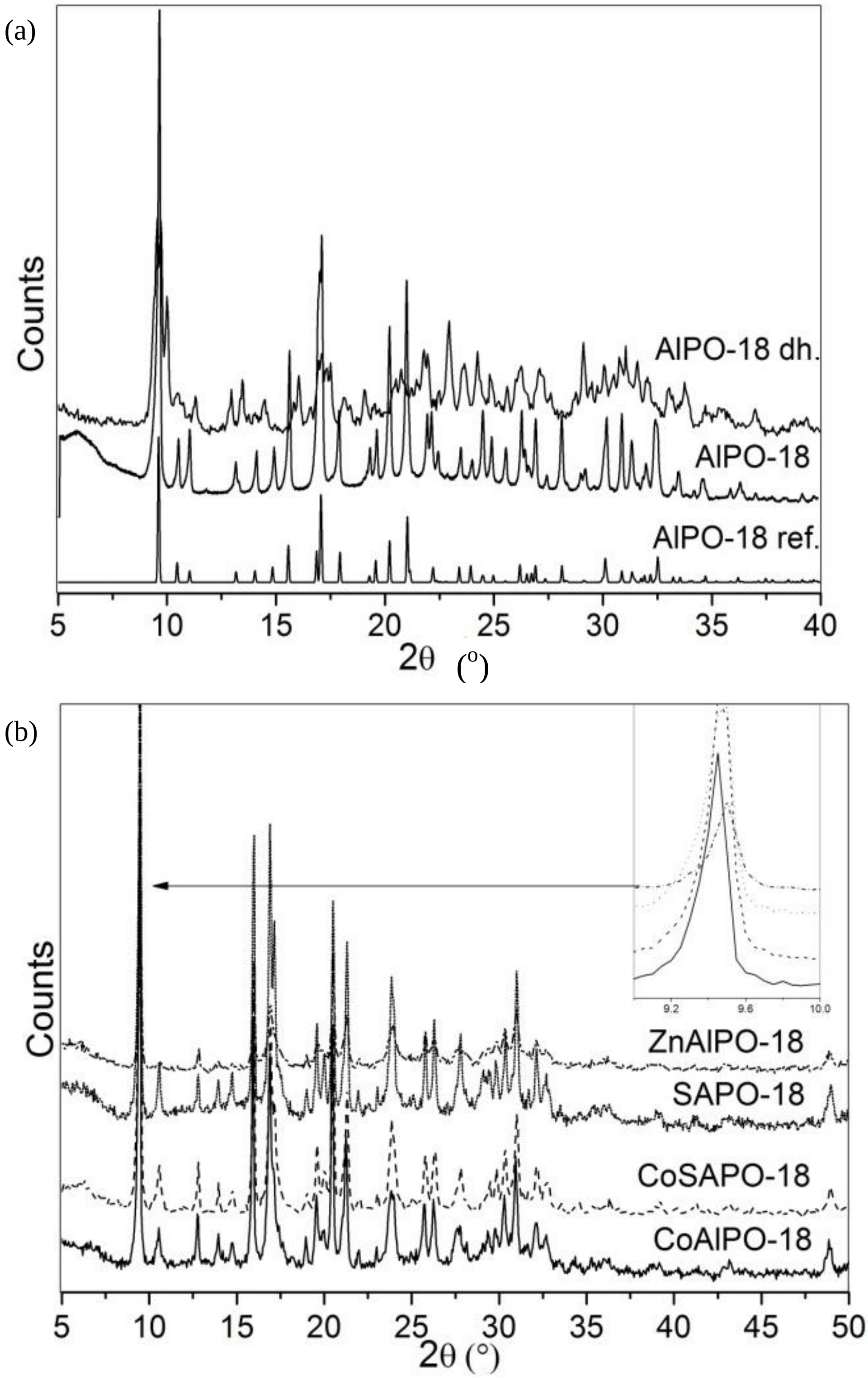

Figure 4.5. *Comparison of the XRD patterns of pure as prepared, calcined and hydrated, and structural model of AlPO-18 (a); (b) XRD patterns of metal substituted AlPO-18 materials.*

The XRD patterns of the metal substituted samples, shown in **Figure 4.5**(b), resemble that of unsubstituted AlPO-18, albeit with a significant change in the position of the first peak, which is shifted to lower 2 theta values. All samples can be indexed in the monoclinic C2/c spacegroup with no change in the overall symmetry, but with increased lattice parameters, which is due to the insertion of large metal ions into the framework.

AlPO-18, SEM shown in the **Figure 4.6** (measured at Johnson Matthey), consists of faceted material and stacks of layered material, and the shape is different to results shown in Chapter 3, and this is mainly caused by a different preparation method used. The particle sizes are not uniform, the sizes range from 1-3 µm. The EDX analysis confirmed that the sample consisted of Al, P & O (see **Figure 4.7**) and C (from template).

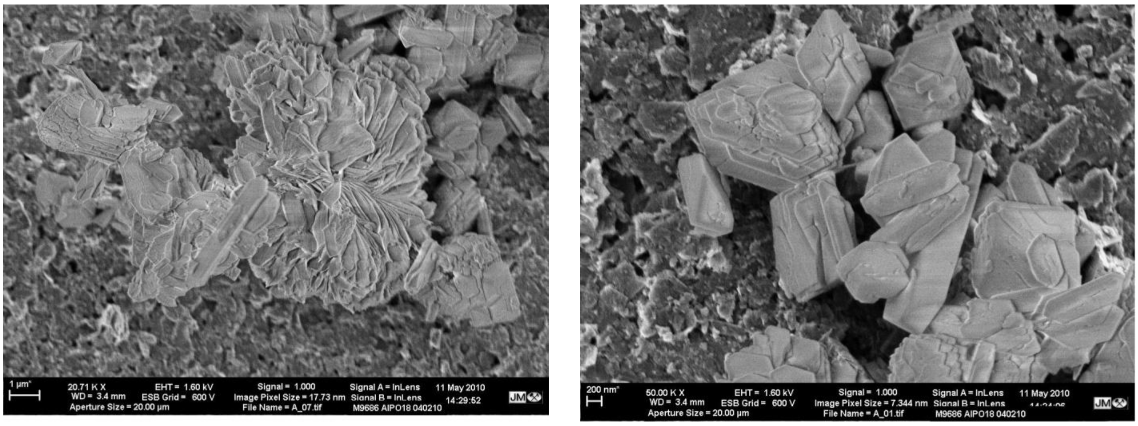

Figure 4.6. *SEM images of AlPO-18.*

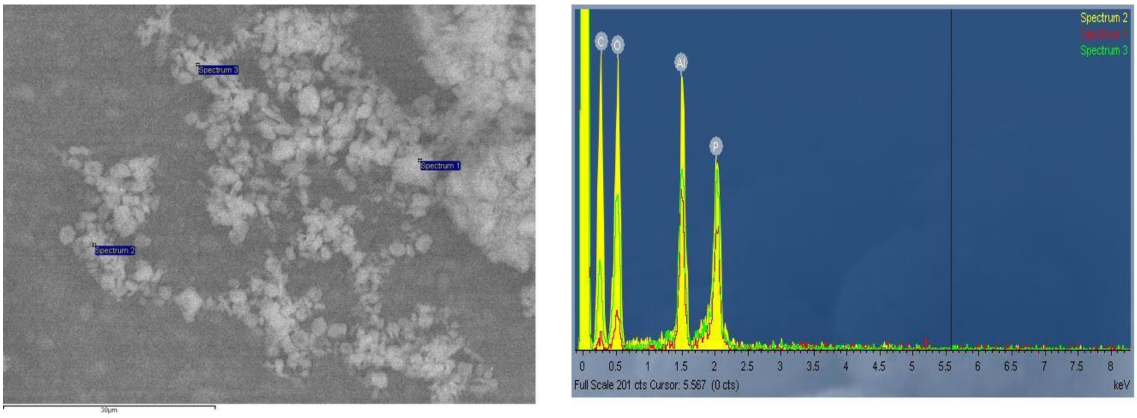

Figure 4.7. *EDX spectra of AlPO-18 from the points indicated in the image on left.*

Heteroatom substituted CoAlPO-18, ZnAlPO-18 and SAPO-18 crystals display a cubic morphology, which is consistent with the previously published work by Wendelbo et al.[31]. The SEM images of CoAlPO-18 are shown in **Figure 4.8** in two magnifications. The particles exhibit a large spread (0.5 µm to 3-4 µm) of cubic crystals mixed with small crystals concentrated in slumps (10 µm).

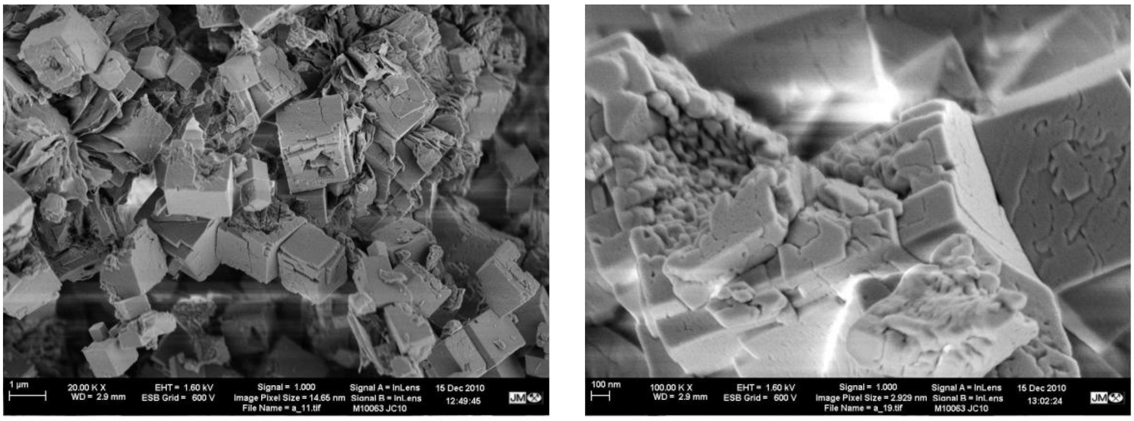

Figure 4.8. *SEM images of CoAlPO-18 in different zooming proximity.*

The SEM imaging of SAPO-18 and ZnAlPO-18 was done at UCL Department of Archeology. The SEM images and EDX analysis were performed using a JEOL 8100 electron microscope. The morphology of SAPO-18 (**Figure 4.9**) and ZnAlPO-18 (**Figure 4.10**) is similar to CoAlPO-18, with faceted cubic crystals of dimensions below 10 µm. SAPO-18 EDX confirmed that Si is on the surface of the cubic crystals. The ZnAlPO-18 crystals are more closely packed and display a more uniform crystal size and larger cluster bunches.

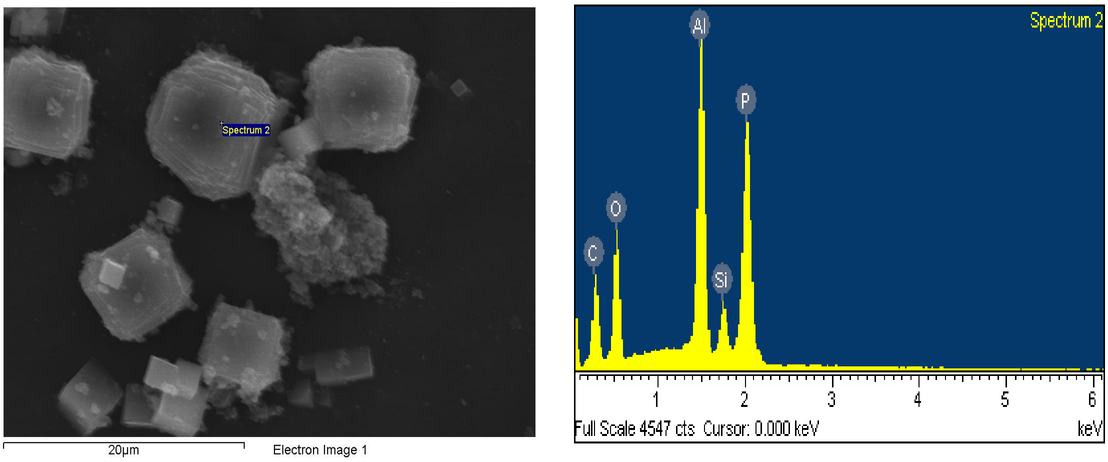

Figure 4.9. *Results obtained from EDX images of SAPO-18.*

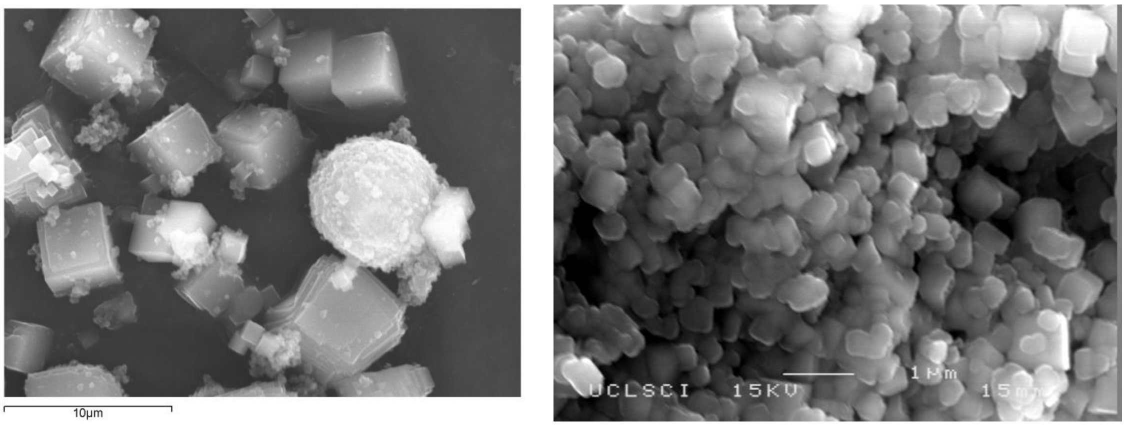

Figure 4.10. *SEM images of SAPO-18 (left) and ZnAlPO-18 (right).*

4.4.2 X-ray Absorption Spectroscopy (XAS)

Background-subtracted and normalised XANES data of CoAlPO-18 at different temperatures during calcinations, and two reference materials are, shown in **Figure 4.11**. The position and intensity of the pre-edge peak (corresponding to a spin-forbidden 1*s* → 3*d* electronic transition), is related to the geometry of the Co-O polyhedra. The pre-edge position of the as-prepared material is the same as that for $CoAl_2O_4$ and has similar intensity and is typical of cobalt in tetrahedral coordination. The existence of this feature is an indication that excitation rules have been relaxed for the formally forbidden 1*s* → 3*d* transition. This is due to *d-p* mixing of Co-O molecular orbitals, which occur in non-centrosymmetric situations, in this case, the tetrahedral coordination. The pre-edge feature intensity is reliable evidence for the fact that Co(II) ions have been successfully incorporated into the material framework. The position of this pre-edge feature shifts to higher energy as the cobalt(II) ions are oxidized to cobalt(III). $C_4H_6CoO_4$ contains octahedrally coordinated Co(II) ions and has a very small pre-edge feature as the relaxation of transition rules due to *d-p* mixing is not available, except for the very small deviations from perfect centrosymmetric octahedral coordination afforded by thermal motion of the atoms. The larger white line intensity of octahedral Co(II) in $C_4H_6CoO_4$ is due to linear O-Co-O bonds. The shift to higher energy of the white line intensity (1*s* → 4*p* transition) at 530^{o}C and room temperature after calcination are not only due to electronic factors, but also affected by the coordination geometry whereby the Co(II) are oxidizing to Co(III).

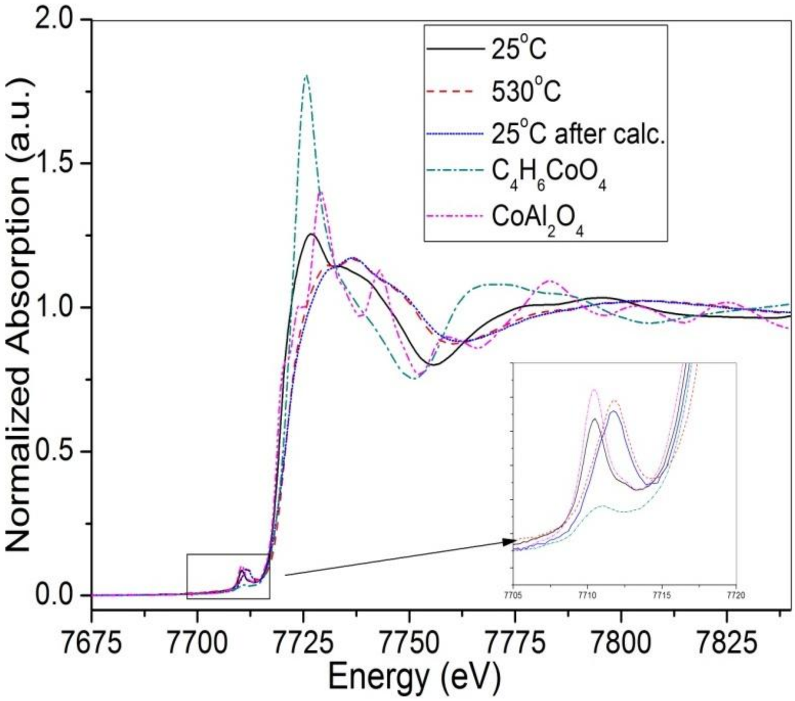

Figure 4.11. Co K-edge *XANES spectra of the CoAlPO-18 as-synthesised form at 25°C, 530°C, and at 25°C after calcination and reference material cobalt acetate and cobalt aluminate.*

The evidence for the incorporation of Co(II) in the framework can also be derived from analysing the Extended X-ray Absorption Fine Structure (EXAFS) data. Fitting results obtained for the CoAlPO-18 at different temperatures during calcinations, and two reference materials, are listed in **Table 4.2**. **Figure 4.12** shows fits to Co K-edge EXAFS spectra in *k*-space and calculated EXAFS with the corresponding Fourier transforms for CoAlPO18.

Table 4.2. *Coordination number, variation in Co-O, Co-P bond distances, Debye-Waller factor ($2\sigma^2$) were obtained from analysis of the Co K-edge EXAFS data for both CoAlPO-18 and reference materials plus edge positions with temperatures are listed.*

	Temperature (^{o}C)				
CoAlPO-18	25^{o}C	550^{o}C	25^{o}C after calc.	$CoAl_2O_4$	$C_4H_6CoO_4$
N / R_{Co-O} (Å)	4 / 1.92	4 / 1.83	4 / 1.83	4 / 1.94	6 / 2.1
$2\sigma^2$ (Å^2)	0.010	0.016	0.012	0.010	0.012
N / R_{Co-P} (Å)	4 / 3.23	4 / 3.20	4 / 3.19		
$2\sigma^2$ (Å^2)	0.030	0.050	0.040		
Edge position (eV)	7719.5	7721.9	7721.0	7718.9	7723.0

Errors in distances R_{Co-O} are ± 0.01 Å, errors in distances R_{Co-P} are ± 0.05 Å. Errors on $2\sigma^2$ are 10-20%.

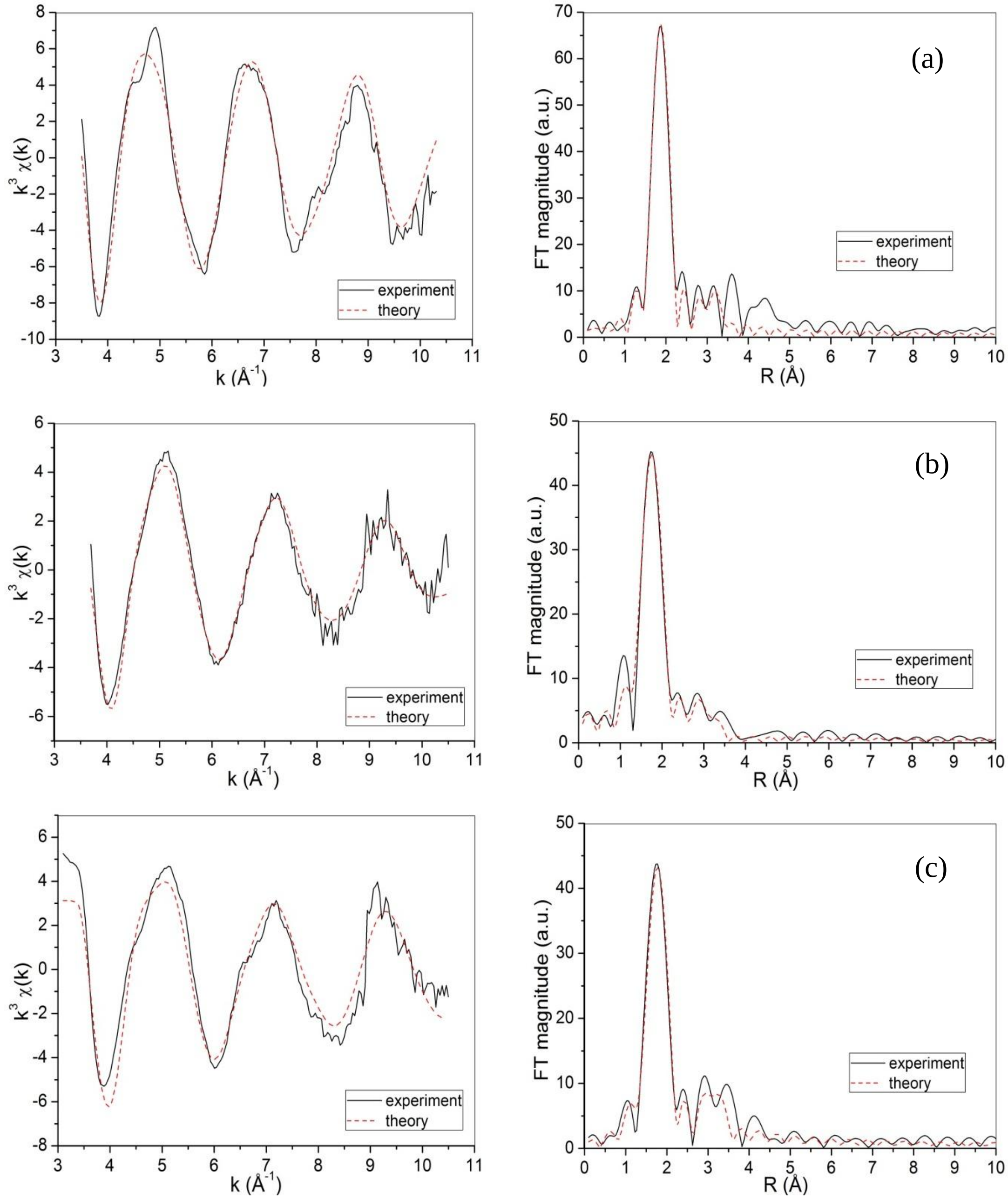

Figure 4.12. *Fits to Co K-edge EXAFS data analyzed in k-space(k*^{3}*-weighted and background subtracted) with associated Fourier transforms for the CoAlPO-18 material where, (a) is freshly prepared material at 25*^{o}*C; (b) is calcined at 530*^{o}*C; and (c) is after calcination and subsequent cooling down to room temperature,25*^{o}*C.*

Detailed analysis of the EXAFS data revealed that, in the as-prepared form, Co ions are tetrahedrally coordinated with an average Co-O bond distance of 1.92Å. The purely Co(II) tetrahedrally coordinate reference $CoAl_2O_4$ has the average bond distance Co-O of 1.94 Å.. Hence, the majority of Co ions in the CoAlPO-18sample are located in framework positions. This is in stark contrast to the 2.1 Å Co-O bond distance of Co(II) in the cobalt acetate starting material. Upon calcination, the EXAFS analysis shows a decrease in an average Co–O bond distances to 1.83Å, indicating the oxidation of Co(II) to Co(III), as it has been shown previously[32]. The amount of oxidised cobalt can be calculated using the formula $R_{EXAFS}=R_{Me(III)}x+R_{Me(II)}(1-x)$, taking Co(III)-O distance 1.82 Å and Co(II)-O 1.93 Å. For our studied material, approximately 91% of cobalt was oxidized to Co(III) during calcination. After cooling the material back to room temperature, the Co-O distance stays at 1.83 Å, if it is not exposed to atmospheric air. Exposure to air causes absorption of water into the structure, as these materials are highly hygroscopic. This causes distortion of the local cobalt ion environment. Previous study by Sankar et al.[32] showed CoAlPO-18 to be able to oxidize the largest amount of Co(II) to Co(III).

4.4.3 FTIR

In the *in situ* work, studies of catalysts during detemplation – and thus the period of Brönsted acidity - are monitored. Individual IR scans were collected every 10^{o}C, but for the presentation purposes, only scans starting with 30^{o}C, 50^{o}C and then every 50^{o}C interval have been plotted. The final scan shows the system after 60 min calcination at 550^{o}C and the penultimate scan is at the beginning of calcination at 550^{o}C.

Figure 4.13(a) shows a stacked plot of IR spectra for CoAlPO-18 during calcination while reduction is shown in **Figure 4.13**(b). Blue colouring is typical of Co(II) in tetrahedral coordination which is another strong indication that cobalt ions are substituted for Al(III) in framework positions (see **Figure 4.14**). The first time the Brönsted acid bands appear is at around 360^{o}C, after the template is completely removed, and is present also at 550^{o}C. However, after 60 min of calcination, the Brönsted acid band arising from hydroxyls bridging structural Co(II) and P(V) is lost. Simultaneously, the colour of template free CoAlPO-18 pellet changes to green as Co(II) is oxidizied to Co(III), the colour is associated with the presence of Co(III) centres. The reduction of calcined sample was performed straight after cooling down to 30^{o}C and flushing with nitrogen (**Figure 4.13**(b)). The recreation of the Brönsted acidity slowly proceeds as we heat the sample to 500^{o}C, and the band increases in intensity. After the reduction, the blue colour of the sample reappears, indicating that cobalt ions are in a bivalent state and in tetrahedral coordination. The reduction seems to increase the intensity of the Brönsted acid band. The broad peak at around 3600 cm-1 is hydroxyls hydrogen-bonded to framework or nonframework O atoms[33].

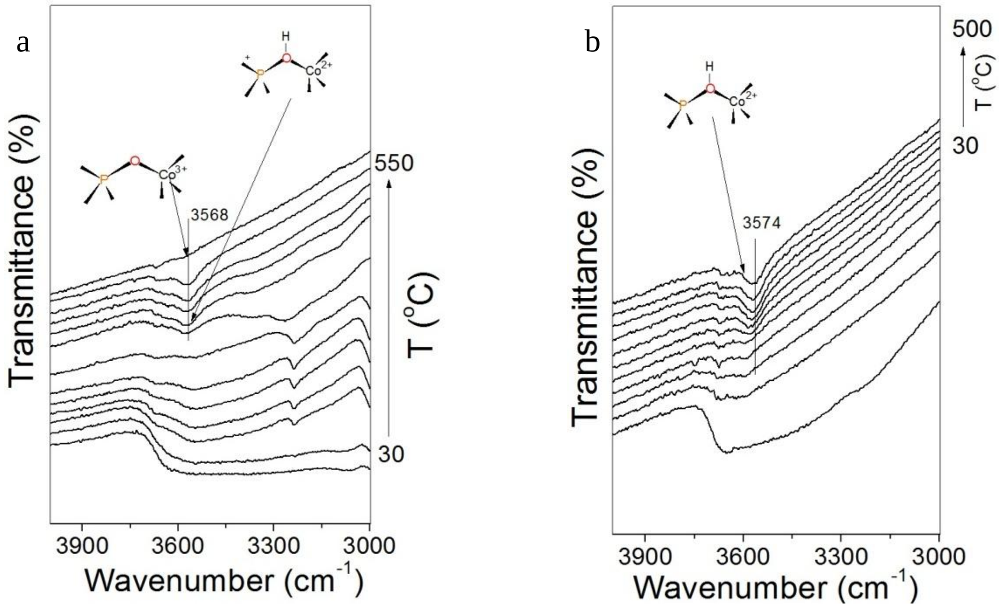

Figure 4.13. *In situ IR spectra of CoAlPO-18 during calcination (left) and reduction (right).*

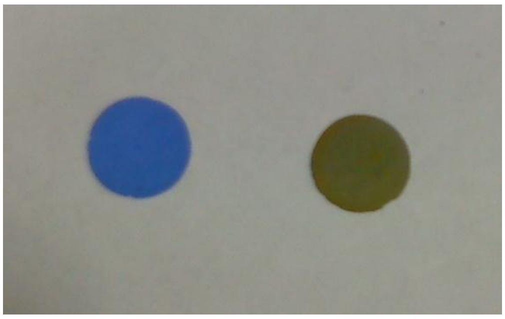

Figure 4.14. *Pellets of CoAlPO-18 before (left) and after (right) calcination in air in IR cell.*

The Brönsted peaks at 3604 and 3584 cm^{-1} in CoSAPO-18 calcination and reduction, shown in **Figure 4.15**(a) and **Figure 4.15**(b) respectively, are those attributed to bridging hydroxyls of silicon and cobalt, respectively. The peaks centred at 3604 and 3584 cm^{-1} are also observed in pure SAPO-18, shown in **Figure 4.16**(b). After 60 min of calcination, the Brönsted peaks are still present, which might not only be due to incomplete oxidation of Co(II) to Co(III) but also the bridging hydroxyl groups of silicon. Upon reduction, the peak increases on intensity, thus the Co(III) ions are reduced to Co(II).

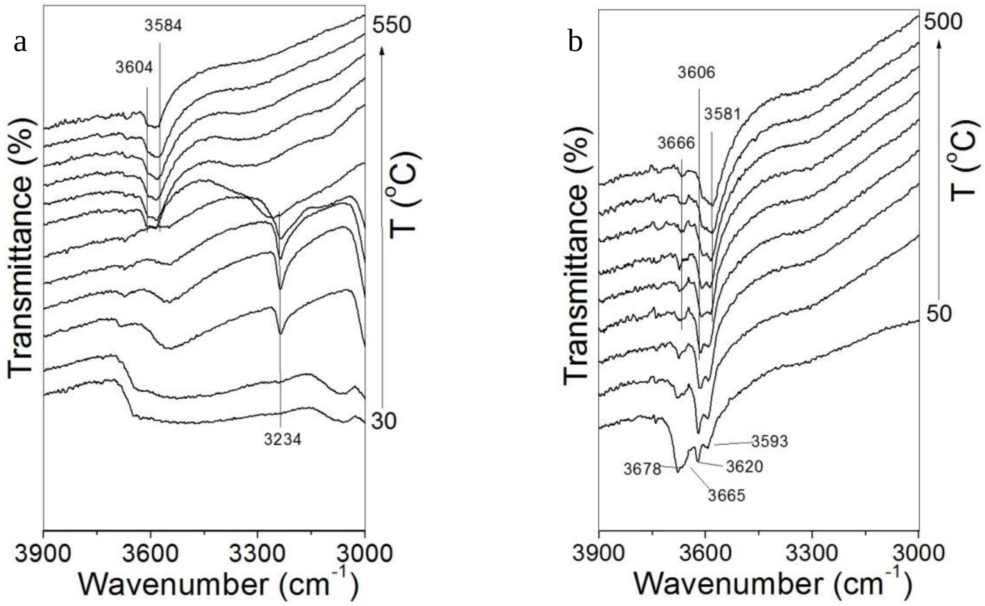

Figure 4.15. *In situ IR spectra of CoSAPO-18 during calcination (left) and reduction (right).*

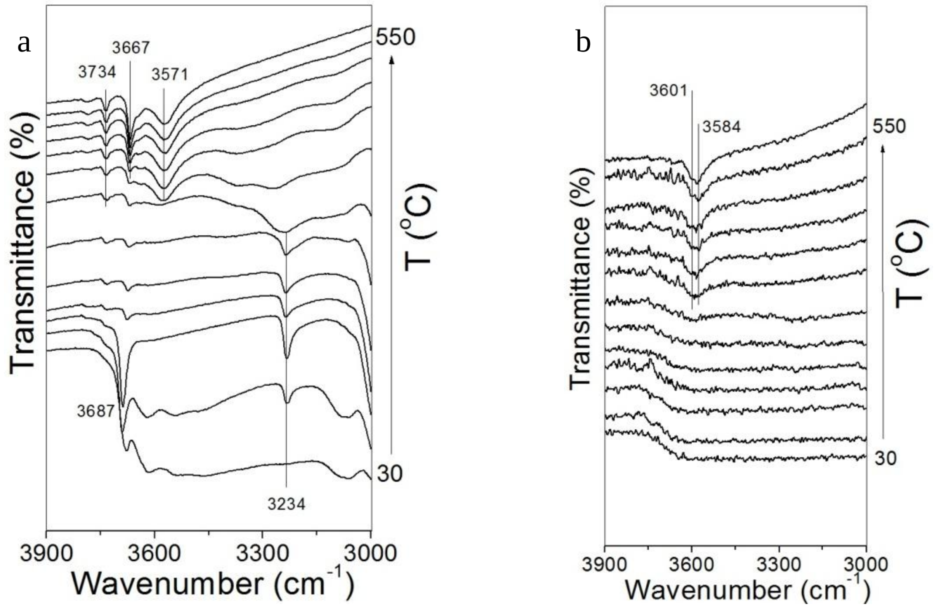

Figure 4.16. *In situ IR spectra of ZnAlPO-18 (left) and SAPO-18 (right) during calcination).*

The Brönsted acid band centred at 3571 cm^{-1} in ZnAlPO-18 (**Figure 4.16**(a)) arising from hydroxyl groups bridging structural Zn(II) and P(V) is not lost during calcination because Zn(II) cannot be oxidized to higher oxidation state. However, increased presence of P-OH, at 3619 cm^{-1} is observed with a shoulder at 3650 cm^{-1}, due to presence of isolated hydroxyl groups of P-OH in two different ring types.

Although, the quantification by IR with proper normalization procedure is difficult, it has to be noted that almost complete oxidation of Co(II) to Co(III) has been achieved for CoAlPO-18. This is consistent with XAS result which revealed 90% conversion of tetrahedral Co(II) to Co(III). The XAS measurements were not carried out for other metal substitutions, and the only evidence of the metal incorporation is based on IR results. However, the XAS and IR results in Chapter 3 are consistent, and display a high degree of accuracy in obtaining information on metal substitution.

4.4.4 High Energy X-Ray Diffraction (HEXRD)

Raw scattering data were pre-processed using Igor software with a macro developed by BL04B2 for correction of self absorption, multiple scattering and polarisation. The measured scattering intensity $I(Q)$, a function of 2θ, is reduced to the total scattering structure factor, $S(Q)$. Fourier transform of $S(Q)$ gives the total pair distribution function, $G(r)$ ($= 4\pi r(\rho(r)-\rho_o)$).

In order to determine which of the atom-pair correlations (interatomic distances) are affected during the heat treatment process, we carried out *in situ* HEXRD studies. It was not possible to carry out time-resolved measurements, and hence we measured only at two or three specific temperatures to determine the changes. In **Figure 4.17** is shown a pair distribution function (PDF) of AlPO-18 sample recorded at room temperature (RT) along with the simulated atom-correlation plots for individual pairs (taking each atom as a central atom, Al, P and O); this calculation was performed using PDFGUI software by taking crystallographic data reported by Simmen et al.[29]. The first peak in the PDF of AlPO-18 system (**Figure 4.18**) is clearly due to contributions from both P-O (typical distance of 1.51 Å for tetrahedrally coordinated P(V)) and Al-O (typical distance of 1.73 Å for tetrahedrally coordinated Al(III)) which could not be separated (due to limited *q*-range affecting the real space resolution). Although the resolution in the PDF is not sufficient to distinguish individual contributions from P-O and Al-O distances to the first peak, the room temperature data showed a distinct shoulder at higher R distances which is most likely due to the presence of octahedrally coordinated Al(III) ions; similarly octahedral coordination was observed for several Fe(III) substituted aluminophosphates with four oxygen linked to P(V) and two water molecules coordinated to the (III) cations. O-O distances appear to change from an initial 2.48 ± 0.02 Å to 2.54 ± 0.02 Å as the temperature increases. The Al-P distance (third peak) does not appear to change with the temperature and remains constant at ca 3.1 Å. More interesting changes are seen at higher *R* values (above 3.5 Å) linked to T1-T3 (or O1-O3) distances which are interact across the small 4 membered rings. It was not possible to model these changes in detail using the current data sets. All the respective distances are shown in a computer generated model of an AlPO-18 structure (only part of the structure is shown for clarity. In addition, octahedrally coordinated Al(III) have been omitted. **Figure 4.18** shows the total scattering data of pure AlPO-18 along with the respective PDF recorded at various temperatures. PDF of data recorded above 150°C showed a narrow first peak and the shoulder at high *R* distance is lost suggesting the conversion of octahedrally coordinated Al(III) ions to a tetrahedral coordination (by loosing water molecules), similar to the observation made for Fe(III) containing materials[34].

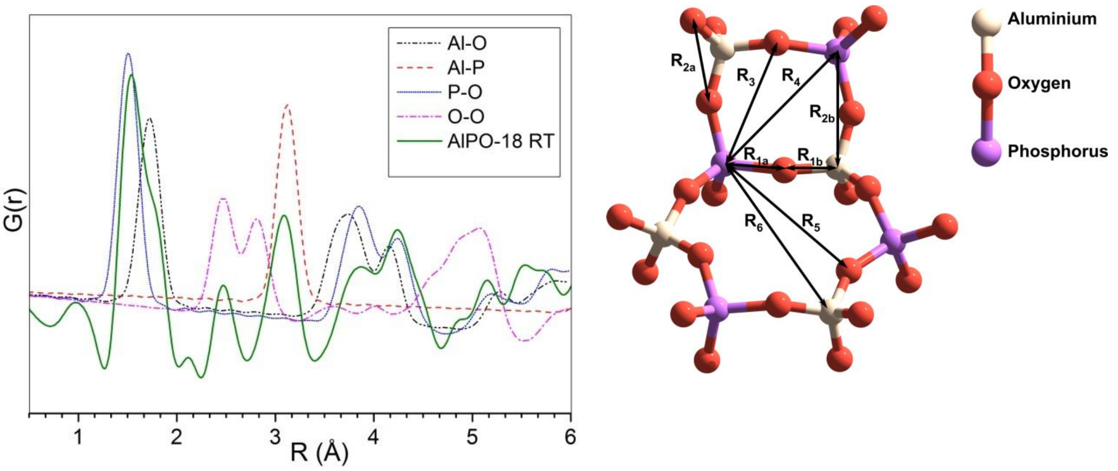

Figure 4.17. *On the left we show the G(r) of the HEXRD data modelled for AlPO-18, and a schematic diagram of 4 and 6-membered ring in AlPO-18 with distances on the right.*

From total correlation functions at RT for AlPO-18 (**Figure 4.18**), the initial P-O distance is 1.53 ± 0.01 Å and Al-O is 1.76 ± 0.01 Å (shoulder feature), these were obtained by Gaussian peak fitting. The increased temperature results in averaging of the two bond distances to 1.60 ± 0.01 Å which stays approximately constant with temperature change. The O-O bond distance changes from initially 2.48 ± 0.02 Å to 2.54 ± 0.02 Å

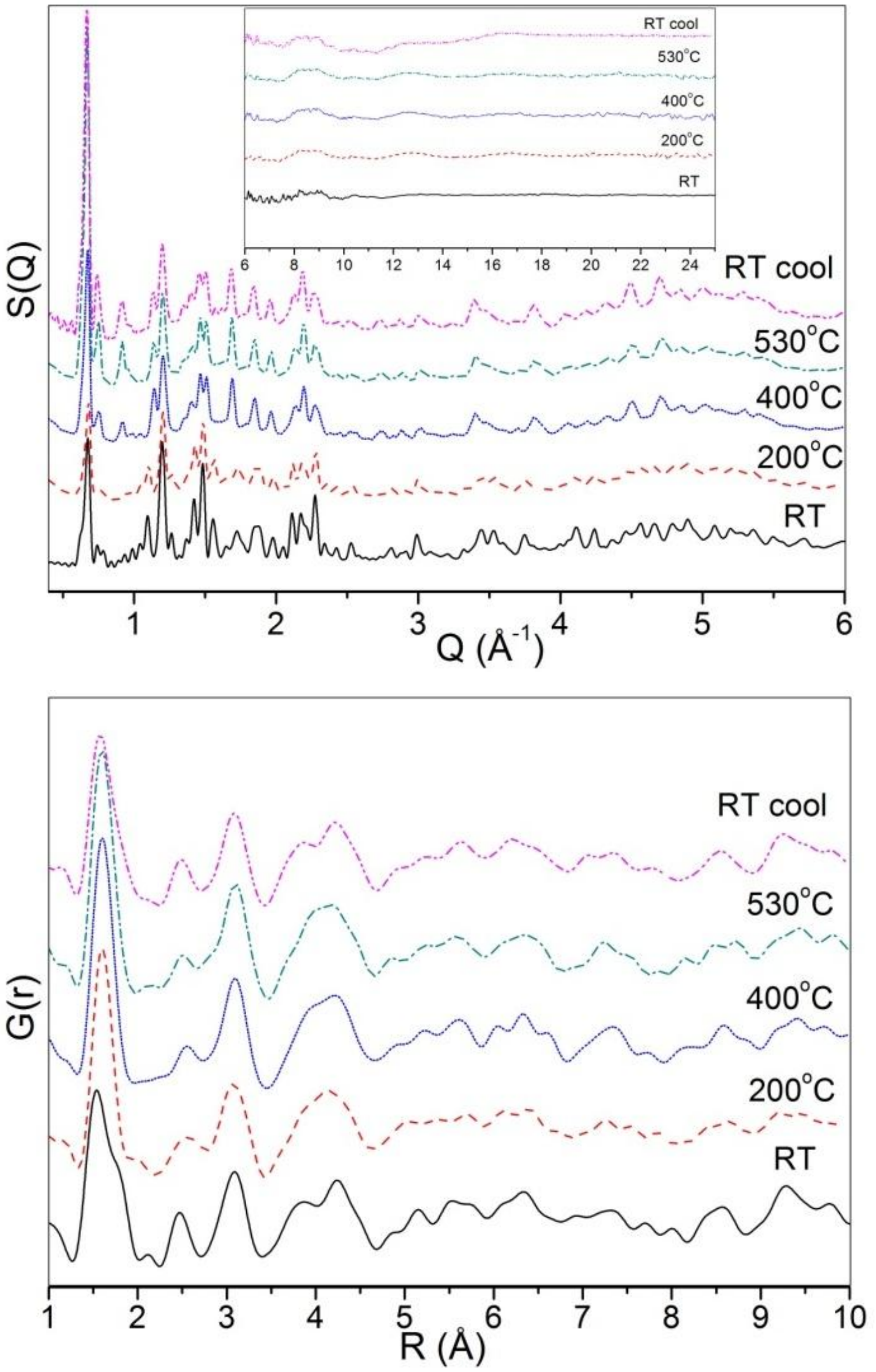

Figure 4.18. *Total structure factors S(Q) (top), and total correlation functions G(r) (bottom) of AlPO-18 at different temperatures.*

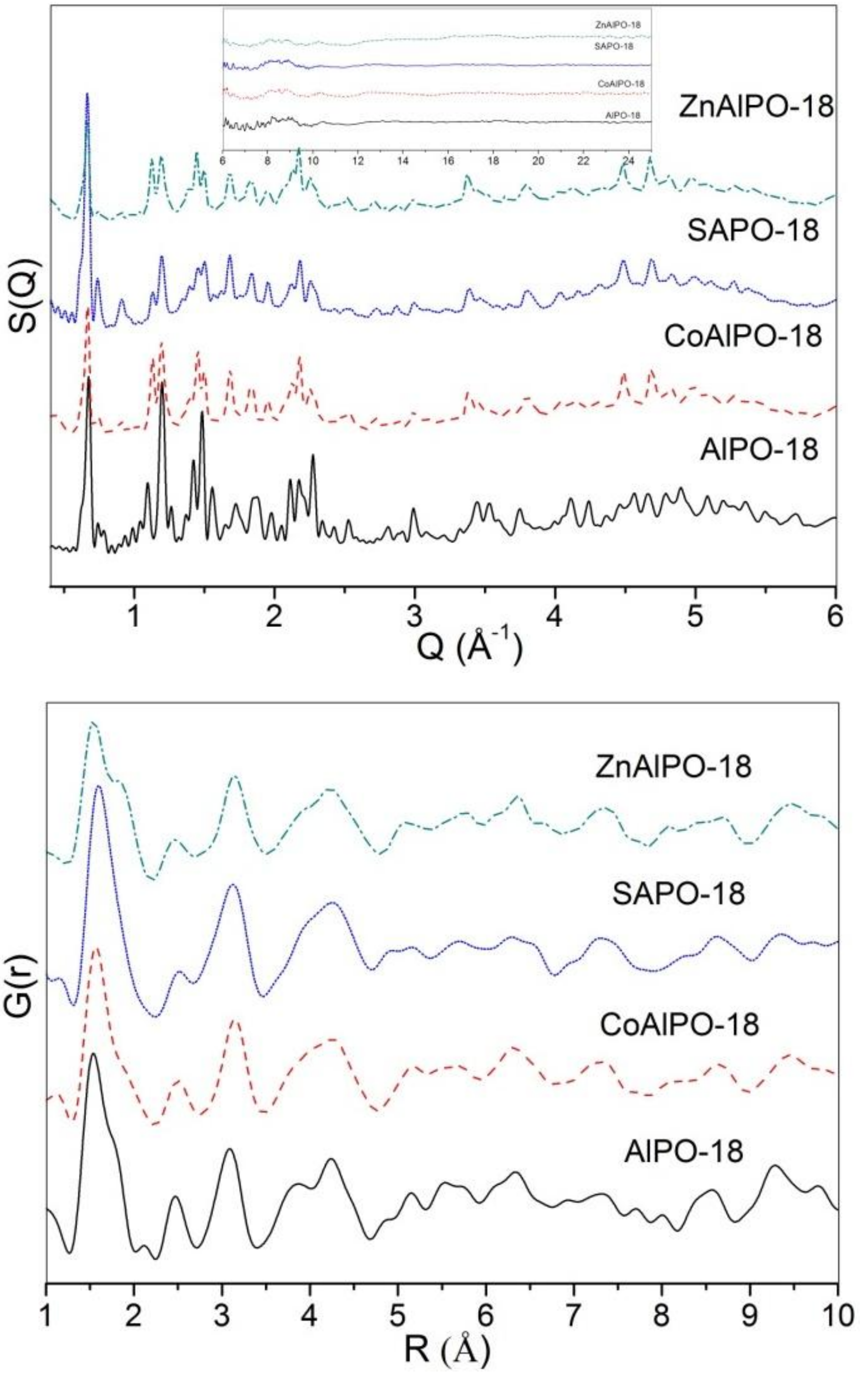

Figure 4.19. *Total structure factors S(Q) (top), and total correlation functions G(r) (bottom) of five samples at room temperature (22^{o}C).*

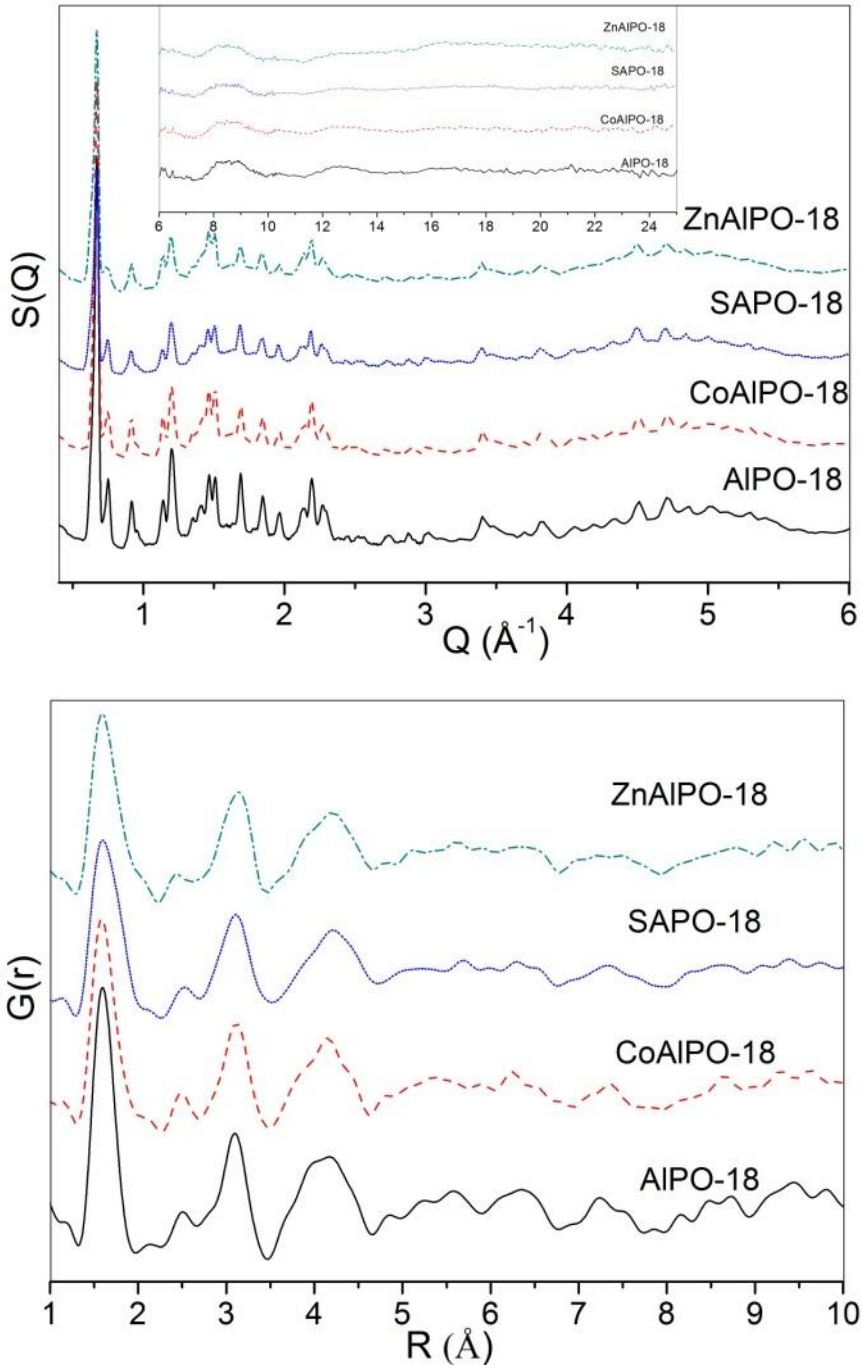

Figure 4.20. *Total structure factors S(Q) (top), and total correlation functions G(r) (bottom) of five samples at 530^{o}C.*

A closer look at the first peak in the PDF of ZnAlPO-18 (**Figure 4.19**) shows a distinct shoulder that is much more pronounced compared to AlPO-18. Once again this is most likely due to the presence of octahedral Al(III), since Zn K-edge EXAFS[35] showed the presence of only tetrahedrally coordinated Zn(II) ions. Changes in the lattice parameter and cell volume are absent for the Zn(II) substituted system, the reason for this is that the cell volume reaches maximum capacity as a result of Zn substitution and no further increase is possible (as seen in the pure AlPO-18 form). A similar observation was made by Simmance et al.[36] in a study of Zn substituted AlPO-5.

4.4.5 High Resolution Powder Diffraction (HRPD)

Room temperature HRPD data of all the samples are shown in **Figure 4.21**(a). HRPD data for samples calcined at 530°C are shown in **Figure 4.21**(b). The inset shows the first reflection in both cases, highlighting the differences between materials. All five samples are pure, highly crystalline materials which can be indexed in the C2/c space group[29].

(a)

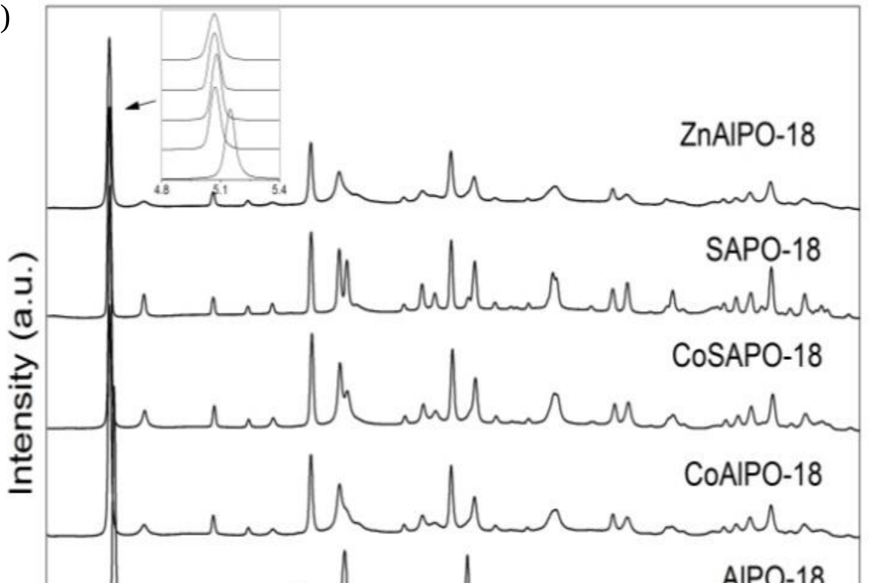

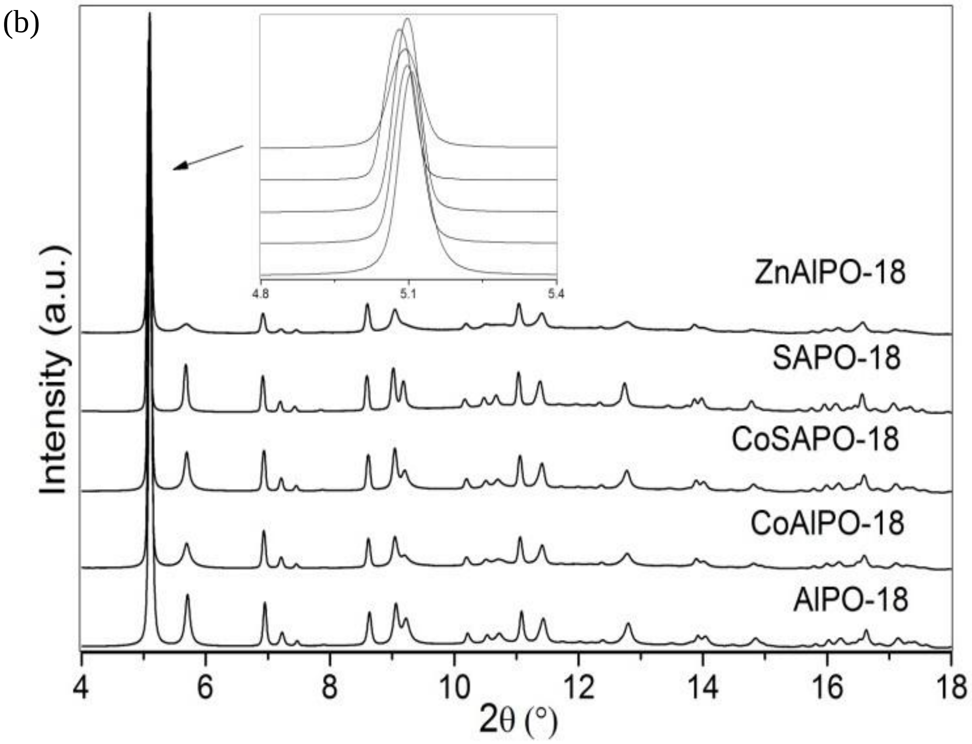

Figure 4.21. *Measured X-Ray diffraction profiles for (a) 5 freshly prepared samples and at 530 ^oC (b).*

Additionally, the plots of the HRPD data collected after calcination and at the start of the MTO reaction at 400^{o}C are shown in **Figure 4.22**. Mass spectroscopy, for mass of methanol, CO_2, propene, and ethylene, was only used to monitor the start and end of the reactions.

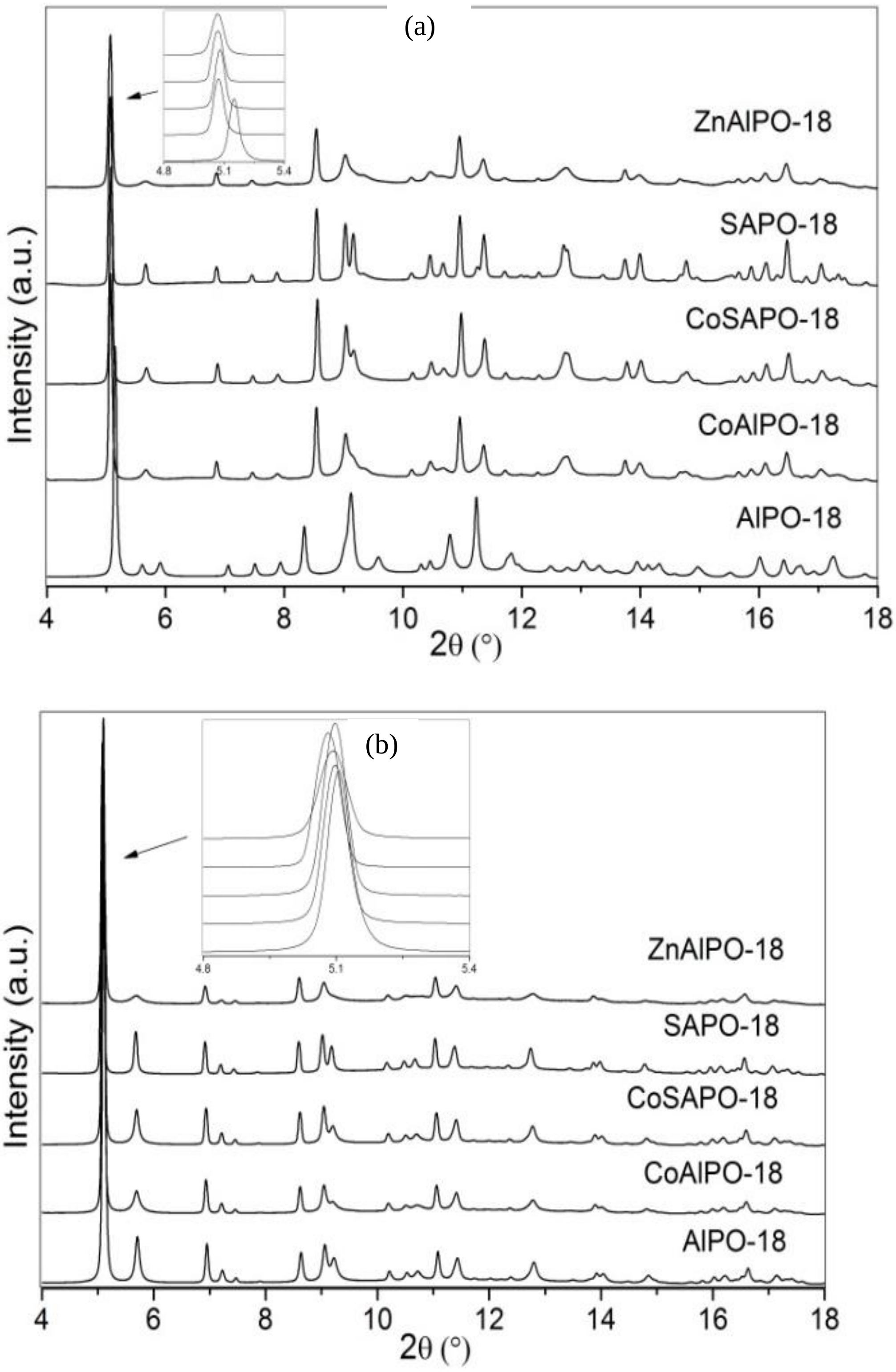

Figure 4.22. *Measured X-Ray diffraction profiles for (a) 5 freshly prepared samples and (b) calcined and cooled to 400 °C.*

The first peak is the most prominent and can be indexed as two very close reflections [110] and [002]. Upon heating to 530°C all materials were found to be stable.

Transformations or amorphisation were not observed indicating that structural integrity is maintained upon removal of the organic template. **Figure 4.23** shows a 3D stacked plot of XRD data measured during calcination/detemplation (black) and the methanol to olefin reaction(red) of AlPO-18. From **Figure 4.23**, it is clear that a number of changes take place during the heat treatment process. In particular, during the initial stages of heating the intensity of the first peak is not changed, since only physisorbed water molecules are removed from the internal pores. However, above ca 140^{o}C we see a gradual increase in intensity of the first reflection, which may be associated with breakage of the organic template that occludes the pores. Complete template removal is observed at ca 360^{o}C (consistent with TGA results[37]), after which the intensity remains constant. The change in intensity from room temperature to 530^{o}C is almost threefold. The intensity of the first reflection remains constant during the period of the methanol to olefins (MTO) reaction at 400^{o}C. This is due to electroneutrality of the aluminophosphate frameworks, which results in catalytic inactivity.

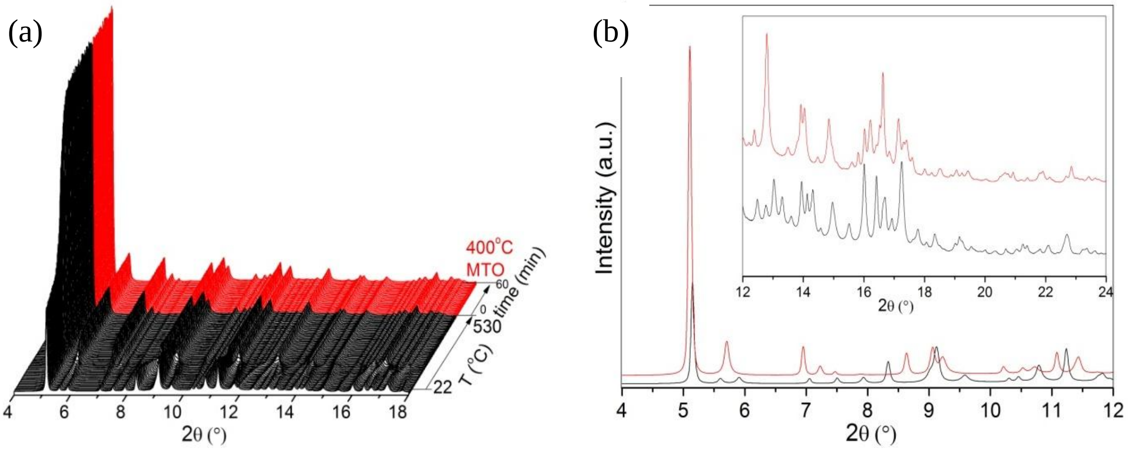

Figure 4.23. *In (a) is displayed plot of measured intensities for the AlPO-18 in the 3.5-18 ^{o} range during calcination (black coloured section) in a flow of dry air to 530 ^{o}C and MTO reaction (red coloured section) at 400^{o}C in methanol bubbling through nitrogen; and (b) is a comparison of changes XRD pattern at room temperature (black) and 400 ^{o}C before the MTO reaction (red).*

Although a similar increase in intensity of the first reflection is observed during calcination in all the hetero-atom substituted analogues (see **Figure 4.25**, calcination is displayed in black), the nature of the intensity change at the initial stages are found to differ for each material. This is possibly related to the type and amount of physisorbed water present in the pores. More interesting changes are observed during the MTO reaction where the reflection intensity decreases strongly suggesting catalyst deactivation as the result of coke build up inside the pores. These changes are observed in the catalytically inactive AlPO-18. Both [110] and [002] reflections are at the ring openings of the aluminophosphate, see **Figure 4.24**. This goes some way to explaining the decrease in intensity of the first reflection which occurs from clogging up of the ring entry.

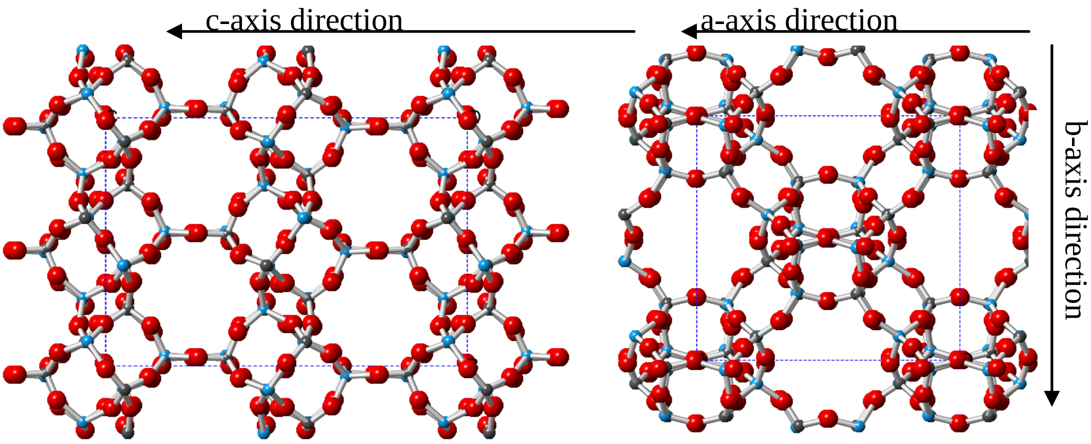

Figure 4.24. *A schematic representations of AlPO-18, two viewing directions, left is [100] and right is [002], oxygen in red, aluminium in blue and phosphorus in grey.*

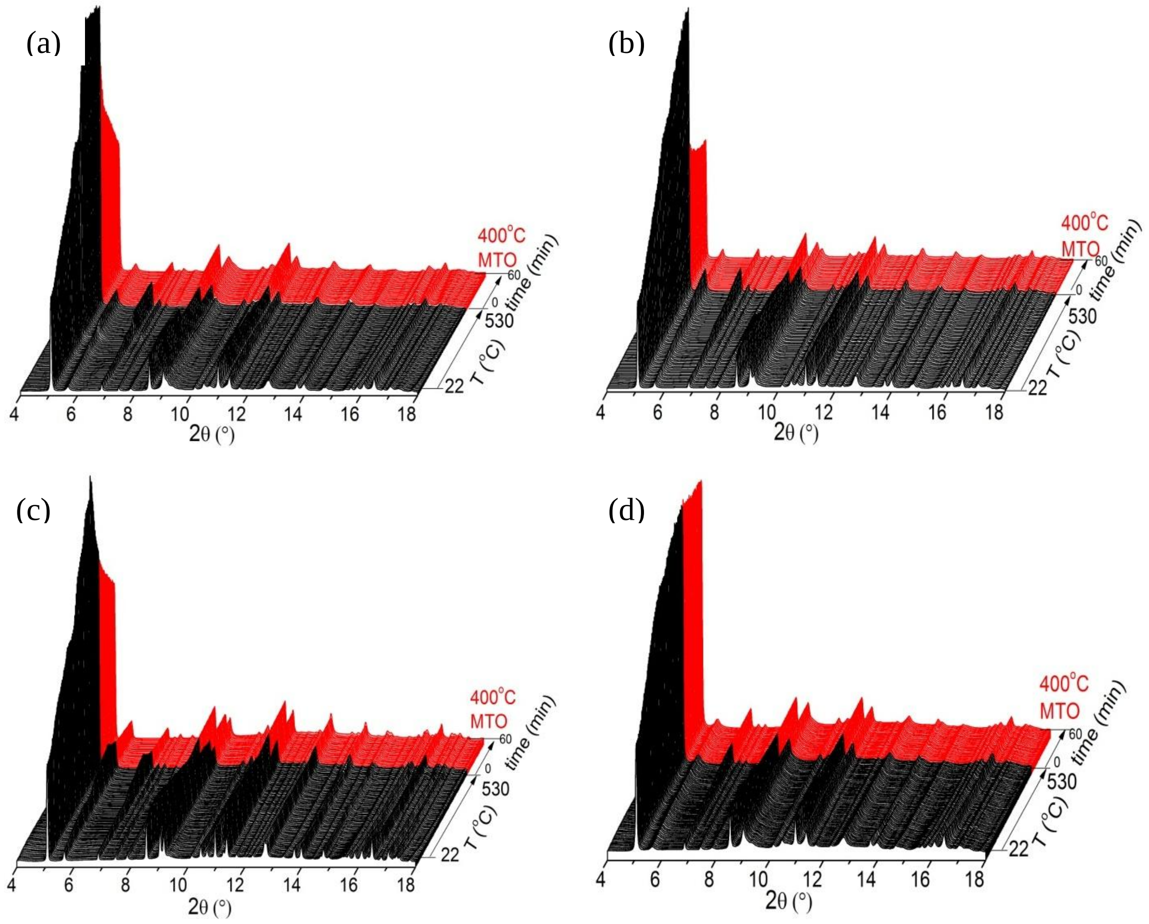

Figure 4.25. *Three D stacked plots of XRD patterns collected during calcination to 530°C (black section of the graph) and MTO reaction (red section of the graph) for: (a) CoAlPO-18, (b) CoSAPO-18, (c) SAPO-18, and (d) ZnAlPO-18.*

The fits of full width and half maximum (FWHM) and peak intensities during calcinations and MTO reaction are shown in the **Figure 4.26**.

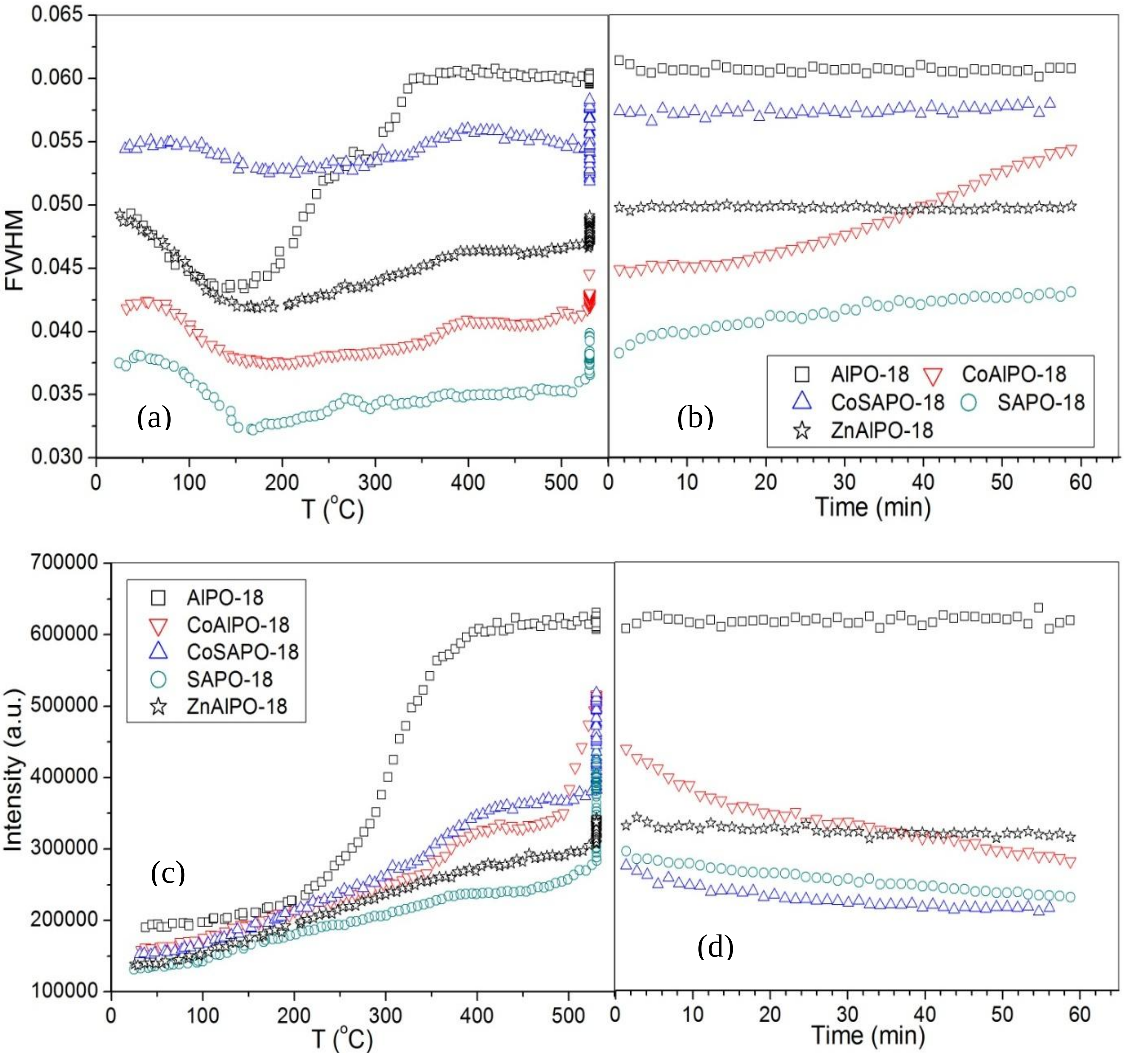

Figure 4.26. *Plots of the variation of (a) the Full Width Half Maximum (FWHM) and (c) Intensity of the first peak with temperature during calcinations, and in (b) is displayed FWHM and (d) Intensity of the first peak during MTO reaction*

Unit-cell parameters of the five AEI-type materials AlPO-18, CoAlPO-18, CoSAPO-18, SAPO-18 and ZnAlPO-18 at various stages during calcination and MTO reaction were extracted using the Le Bail method employing monoclinic C2/c space group settings. The lattice parameters obtained for AlPO-18 are compared to the one reported by Simmen et al.[29], and are in a good agreement with the templated sample of AlPO-18, the comparison is shown in **Figure 4.3**.

Table 4.3. *Comparison of lattice parameters of the five AEI-type materials obtained by Le Bail fit at the beginning 22^{o}C, after 40 min at 530^{o}C, and at the beginning of the MTO reaction (400b) and end of MTO reaction (400e), and 22* is after cooling down to room temperature.*

Material	T (^{o}C)	a (Å)	b (Å)	c (Å)	Beta (^{o})	V (Å^3)
AlPO-18[29]	22	13.5116(3)	12.6235(2)	18.4394(5)	95.55(1)	3130.3(5)
AlPO-18	22	13.494(2)	12.628(2)	18.442(1)	95.44(4)	3128.7(1)
	530	13.645(2)	12.690(1)	18.509(5)	90.14(4)	3205.0(3)
	400b	13.645(7)	12.691(7)	18.511(3)	90.13(5)	3205.6(4)
	400e	13.646(1)	12.690(6)	18.517(2)	90.10(5)	3206.6(3)
	22*	13.710(1)	12.675(6)	18.783(5)	90.62(3)	3264.0(3)
AlPO-18[29]	Calc	13.7114(1)	12.7314(1)	18.5703(1)	90.01(2)	3241.7(2)
CoAlPO-18	22	13.818(3)	12.730(2)	18.719(8)	90.3(9)	3292.9(6)
	530	13.683(1)	12.772(1)	18.647(3)	90.46(6)	3258.8(5)
	400b	13.677(2)	12.784(1)	18.654(2)	90.40(4)	3261.6(8)
	400e	13.62138	12.91878	18.707(4)	90.20(5)	3291.9(5)
	22*	13.6917	12.91839	18.795(5)	90.2(4)	3324.3(4)
CoSAPO-18	22	13.776(5)	12.716(4)	18.633(1)	90.00(3)	3264.1(2)
	530	13.680(4)	12.742(3)	18.591(3)	89.58(4)	3240.5(7)
	400b	13.666(6)	12.815(4)	18.639(3)	89.72(5)	3264.2(6)
	400e	13.674(3)	12.826(3)	18.660(4)	89.79(5)	3272.8(7)
	22*	13.701(2)	12.855(2)	18.711(2)	89.85(4)	3295.4(5)
SAPO-18	22	13.801(1)	12.702(2)	18.618(4)	89.94(2)	3263.9(3)
	530	13.685(2)	12.740(4)	18.597(1)	89.96(2)	3242.5(4)
	400b	13.667(3)	12.799(3)	18.677(5)	89.97(3)	3267.3(5)
	400e	13.650(4)	12.847(1)	18.695(4)	89.86(1)	3278.4(4)
	22*	13.678(2)	12.852(3)	18.732(1)	89.89(2)	3292.7(2)
ZnAlPO-18	22	13.807(3)	12.771(3)	18.652(5)	90.04(7)	3289.0(5)
	530	13.707(4)	12.765(3)	18.601(2)	90.35(5)	3254.5(5)
	400b	13.710(5)	12.770(4)	18.610(2)	90.34(5)	3258.3(7)
	400e	13.717(4)	12.768(3)	18.617(2)	90.39(5)	3260.7(6)
	22*	13.726(4)	12.824(5)	18.711(3)	90.2(7)	3293.7(7)

The results are also consistent with the previously published data for as-synthesised material. Refinement of the room temperature data of all hetero-atom substituted samples clearly show significant increase in the cell volume compared to the pure AlPO-18 analogue. Simmance et. al.[36] observed similar increase in cell volume for hetero-atom substituted AlPO-5 structures compared to the pure AlPO-5 material. Many hetero-atoms which can be incorporated into the aluminophosphate framework report larger ionic radius with oxygen. For example, the ionic radius of tetrahedral Co(II) and Zn(II) with oxygen are 38% and 45% larger than Al(III) respectively, and the Si(IV) ion is 36% larger than P(V) (summarized in **Table 4.4**). However, the flexibility of the nanoporous aluminophosphate framework in the initial gel allows successful incorporation. It also has to be noted that the lattice expansion cannot be used as a definite confirmation of the metal incorporation.

Table 4.4. *The ionic radii as the effective value in oxides in tetrahedral coordination, borrowed from Whittaker and Muntus[38].*

Atom	Oxidation state	Ionic radius (Å)
Al	III	0.47
Si	IV	0.34
Co	II	0.65
Zn	IV	0.68
P	V	0.25

In the **Figure 4.28**, the variations of individual cell parameters with time and temperature during calcinations are shown on the left and on the right are shown corresponding cell parameters as a function of time during the MTO reaction at 400 ^{o}C. First, the calcinations will be discussed. All three cell constants for pure AlPO-18 material were found to increase initially and yet above ca 350^{o}C they start to decrease, which may be associated with the removal of adsorbed water molecules partly coordinating with Al(III) sites[39]. At the same time, the monoclinic cell angle, β, decreases and remains constant above ca 350^{o}C. Similar behaviour is not seen for the heteroatoms substituted systems; all the cell parameters were found to gradually decrease during the heating process, while the β angle remained constant and similar to AlPO-18, above ca 350^{o}C. Another interesting observation from this study is that, while the a parameter was similar in all the hetero-atom substituted systems, b and c parameters were found to be different. In particular, for the Zn(II) substituted system the b-parameter appears to be much larger than that of cobalt and for Co(II) substituted system c (and to some degree a) was much larger compared to others. This suggests that the preference and nature of substitution of these ions are varied within the same structure. The overall cell volume appears to be similar with cobalt and zinc substituted systems showing highest cell volume and pure AlPO-18 at the lower end.

During the MTO reaction, all cell constants of AlPO-18 and ZnAlPO-18 remain constant during the time of the reaction, which confirms inactivity of both materials. In the *a*-axis direction, only CoAlPO-18 exhibit contraction whilst no changes are observed in the other materials. In the *b*-axis direction, the steepest increase is in CoAlPO-18, and smaller increase is found for CoSAPO-18 and SAPO-18. In the *c*-axis direction, the increase in CoAlPO-18 and CoSAPO-18 is very similar. A much smaller increase is observed in SAPO-18. The variation in cell parameters lengthening must be correlated to the preferred location of metals in the framework. In both CoSAPO-18 and CoAlPO-18 almost identical increases are observed in the c-axis direction and very different behaviour in the *a*-axis where the CoSAPO-18 behaves more like SAPO-18. There is very minimal or no change in β angle in all studied samples. The rate of increase in cell parameters are translated into the volume changes, where again the largest change is seen in CoAlPO-18 followed by CoSAPO-18 and SAPO-18. From the data, linear expansion coefficients were calculated for different temperature and time ranges.

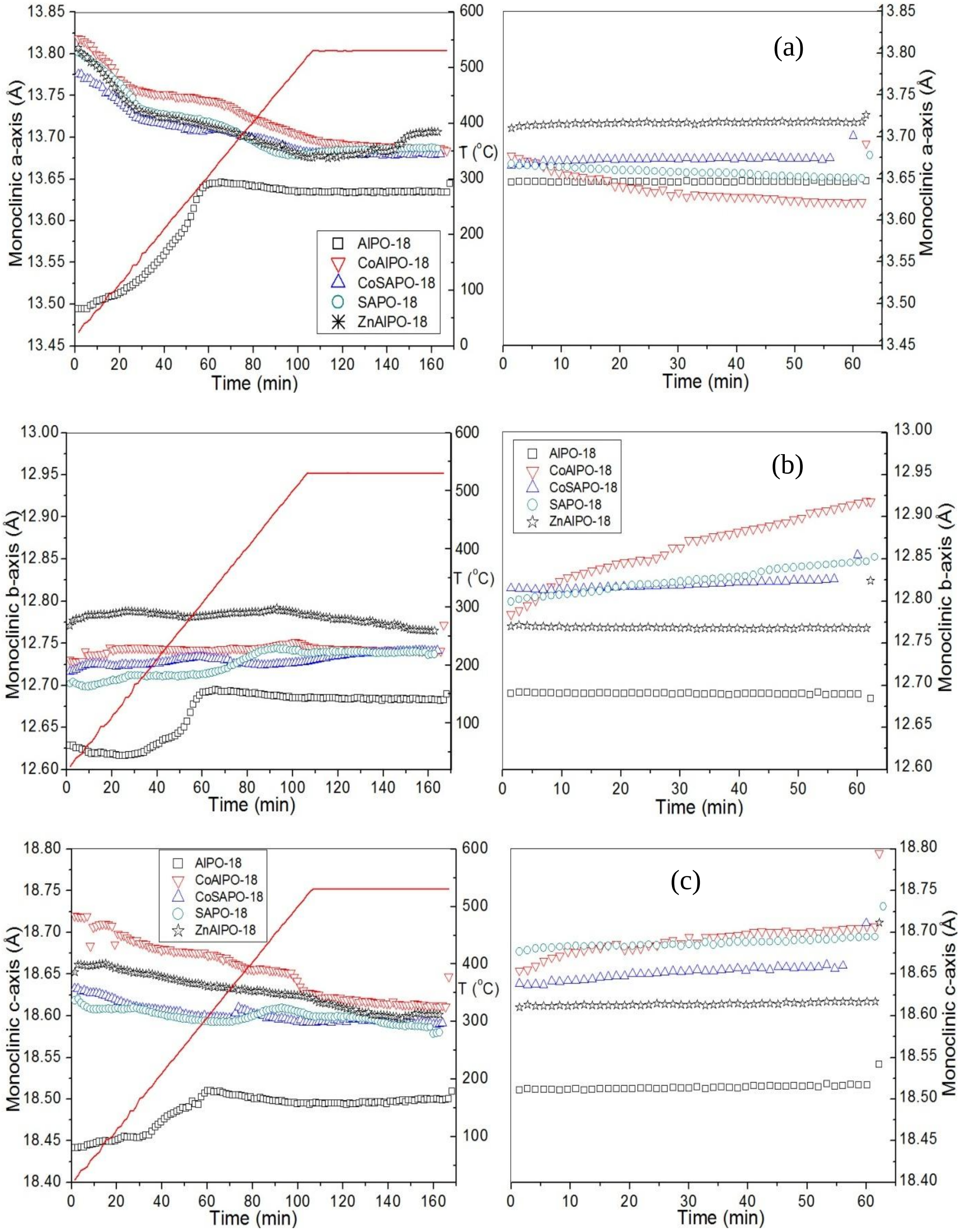

Figure 4.27. *Plots of the variation of the individual cell parameters with time during calcination (left column) and methanol to olefins reaction (right column) for metal substituted and pure AEI-type materials: (a) a-parameter, (b) b-parameter, (c) c-parameter. Please note that the error bars are considerably smaller than the points themselves. The last point in each graph is at room temperature after MTO reaction. The red line in calcination plots is a temperature graph, starting from 20^{o}C. MTO reaction was carried out at 400^{o}C in a flow of nitrogen bubbled through methanol.*

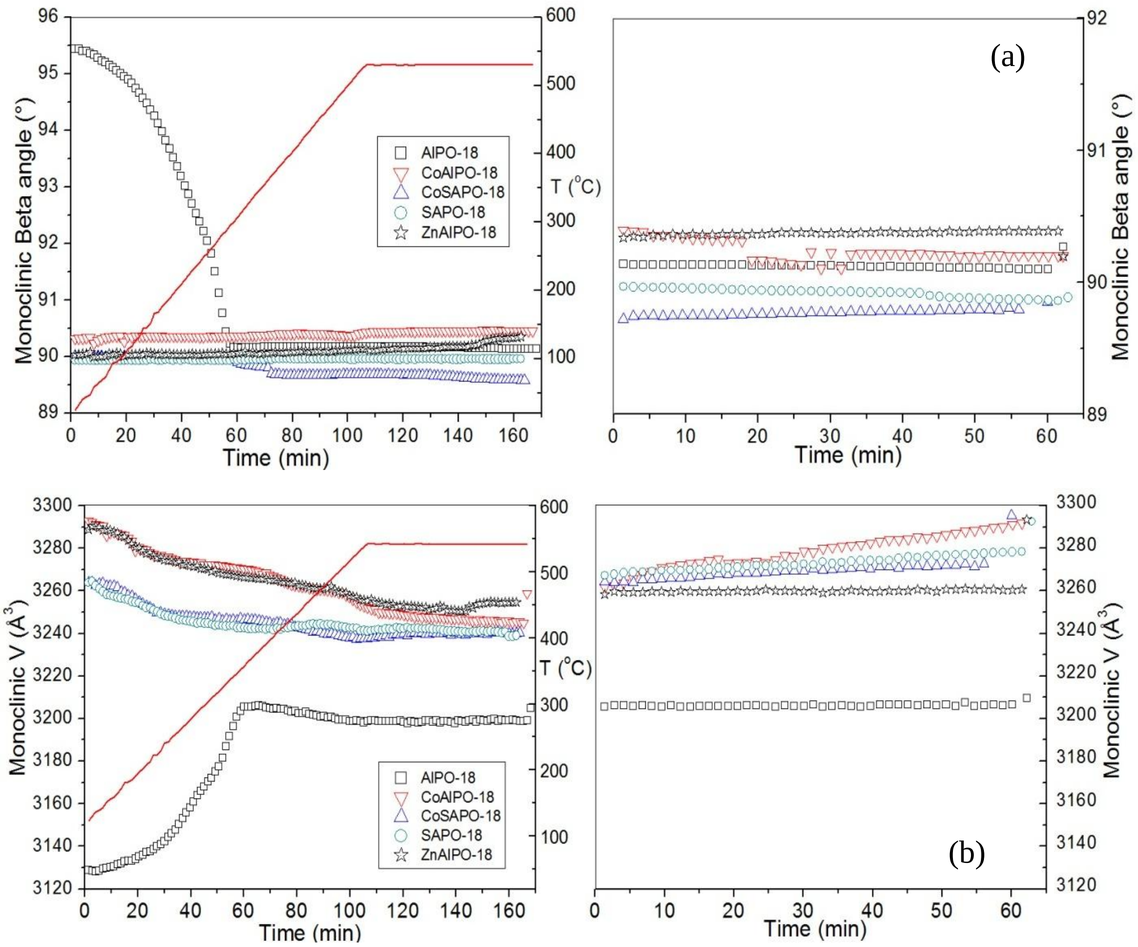

Figure 4.28. *Plots of the variation of the individual cell parameters with time during calcination (left) and methanol to olefins reaction (right) for metal substituted and pure AEI-type materials: (a) is plotted monoclinic beta angle, (b) cell volume. Please note that the error bars are considerably smaller than the points themselves. The last point in each graph is at room temperature after MTO reaction. The red line in calcination plots is a temperature graph, starting from 20°C. MTO reaction was carried out at 400°C in a flow of nitrogen bubbled through methanol.*

In the figures below are shown the best fit obtained by Le Bail refinement for SAPO-18 at different temperatures, and Rwp factors are shown in **Figure 4.32**.

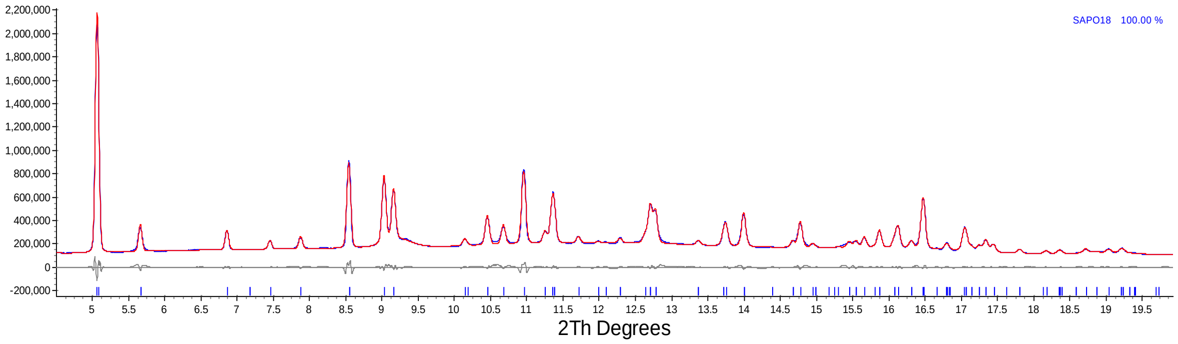

Figure 4.29. *Best fit obtained by LeBail refinement of as-prepared SAPO-18 before calcination at RT. The observed data are indicated by dots and the calculated ones by the solid red line. The short vertical lines (blue) mark the positions of Bragg reflections. The lower continuous curved line (grey) shows the difference between the observed and calculated powder diffraction patterns.*

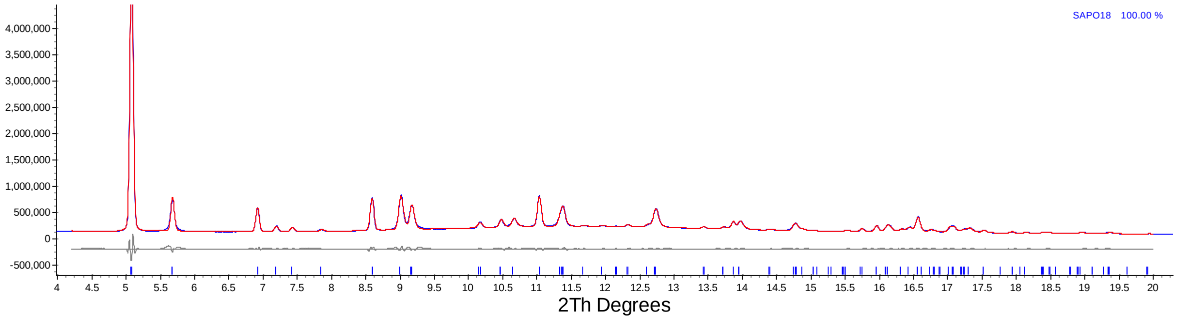

Figure 4.30. *Best fit obtained by LeBail refinement of SAPO-18 at 530^{o}C. The observed data are indicated by dots and the calculated ones by the solid red line. The short vertical lines (blue) mark the positions of Bragg reflections. The lower continuous curved line (grey) shows the difference between the observed and calculated powder diffraction patterns.*

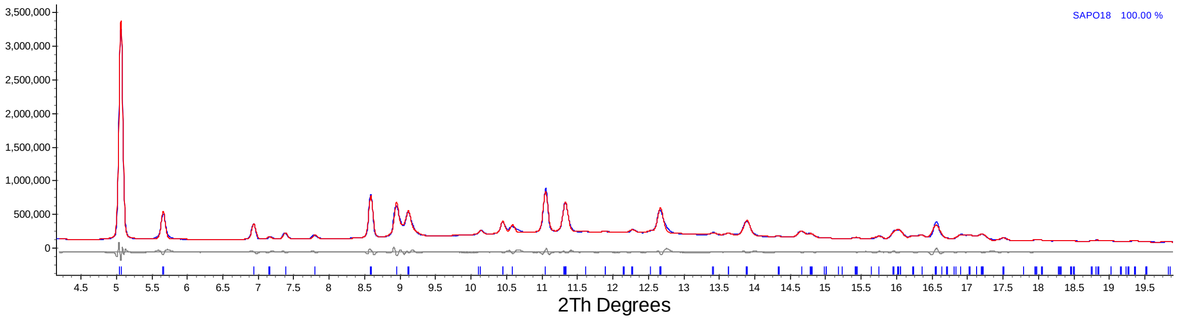

Figure 4.31. *Best fit obtained by LeBail refinement of SAPO-18 at RT after MTO reaction. The observed data are indicated by dots and the calculated ones by the solid red line. The short vertical lines (blue) mark the positions of Bragg reflections. The lower continuous curved line (grey) shows the difference between the observed and calculated powder diffraction patterns.*

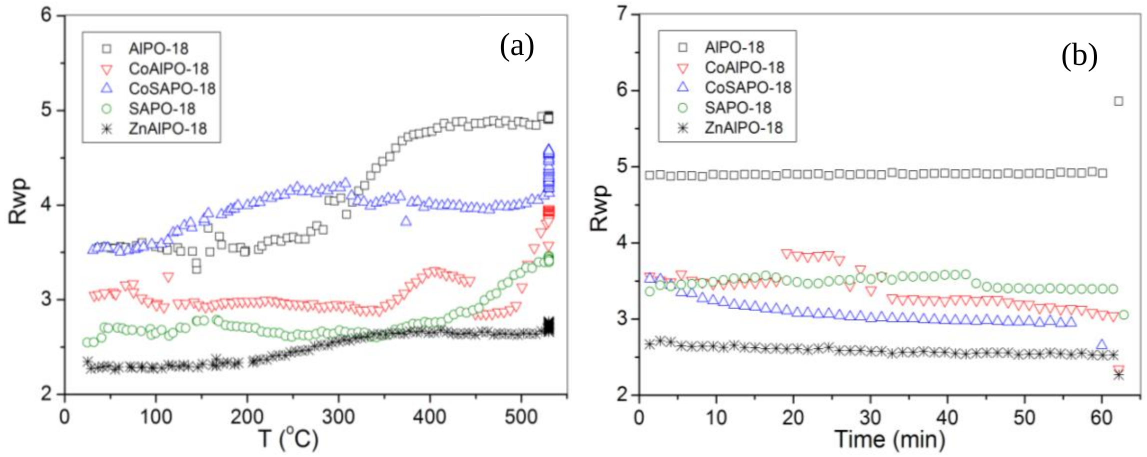

Figure 4.32. *Rwp factors, (a) as a function of temperature obtained during calcination of AEI-type materials to 530^o, and (b) as a function of time during MTO reaction at 400^{o}C.*

Table 4.5 shows the thermal expansion coefficients for our studied materials in the temperature range 350 - 530^{o}C, starting at the temperature at which the organic template is removed from internal pores. The largest volumetric NTE in this temperature range is shown by ZnAlPO-18, followed by CoAlPO-18 (Zn and Co are of similar ionic radii), and CoSAPO-18 which is about half of CoAlPO-18 (only 5 w% of cobalt in CoSAPO-18). AlPO-18 and SAPO-18 do not exhibit large changes at this temperature range. Moreover, the individual axis NTE are different for each metal, whilst ZnAlPO-18 has an equal contraction in the *b* and *c* direction, there is no change in the *a* direction. On the other hand, CoAlPO-18 framework shows significant shrinking in the *a*-axis direction, and modestly in the *c* and *b*-axis. Furthermore, the increase in the β angle is threefold in the case of ZnAlPO-18 compared to CoAlPO-18. CoSAPO-18 has the largest β angle contraction, whilst the other cell constants behave in a very similar fashion to CoAlPO-18.

Table 4.5. *Thermal Expansion Behaviour of the Materials Studied, α_a, α_b, α_c, α_β, and α_V values are those obtained by linear fitting of the variation of cells parameters with temperature and calculated using the equation $\alpha L = (L-L_{ref})/L_{ref}(T-T_{ref})$. The reference temperature T_{ref} is the lowest temperature in the specified range.*

	Expansion coefficient, (350-530 ^{o}C)				
	α_a (10^{-6} K^{-1})	α_b (10^{-6} K^{-1})	α_c (10^{-6} K^{-1})	α_β (10^{-6} K^{-1})	α_V (10^{-6} K^{-1})
AlPO-18	-0.33	-2.16	0.11	-2.05	-2.36
CoAlPO-18	-22.4	12.53	-6.83	4.2	-16.7
CoSAPO-18	-11.5	4.49	-1.92	-15.5	-9.06
SAPO-18	-10.6	9.8	1.35	0.53	0.57
ZnAlPO-18	0.39	-8.83	-9.38	0.17	-17.9

Overall, the least change is observed in the SAPO-18 and AlPO-18 frameworks. The largest NTE is observed upon cooling of the materials to room temperature. **Table 4.6** shows the thermal expansion coefficients for our studied materials in the calcinations range of temperatures 22 - 530^{o}C. Whilst in the template free materials, we saw negative thermal expansion in AlPO-18, here we observe a large positive thermal expansion. The NTE of SAPO-18 and CoSAPO-18 are very similar, such as the NTE of ZnAlPO-18 and CoAlPO-18.

Table 4.6. *Thermal Expansion Behaviour of the Materials Studied, α_a, α_b, α_c, α_{Beta}, and α_V values are those obtained by linear fitting of the variation of cells parameters with temperature and calculated using the equation $\alpha_L = (L-L_{ref})/L_{ref}(T-T_{ref})$. The reference temperature T_{ref} is the lowest temperature in the specified range.*

	Expansion coefficient (22 - 530 ^{o}C)				
	α_a (10^{-6} K^{-1})	α_b (10^{-6} K^{-1})	α_c (10^{-6} K^{-1})	α_β (10^{-6} K^{-1})	α_V (10^{-6}K^{-1})
AlPO-18	22.11	9.64	7.29	-117.76	47.6
CoAlPO-18	-19.62	6.56	-7.82	3.02	-20.9
CoSAPO-18	-14.02	3.97	-4.49	-9.35	-14.59
SAPO-18	-16.97	-1	-2.3	0.52	-13.23
ZnAlPO-18	-14.59	16.95	-5.52	6.92	-21.2

The expansion coefficients were also calculated after the MTO reaction, and areshown in **Table 4.7**.

Table 4.7. *Thermal Expansion Behaviour of the Materials Studied,* α_a*,* α_b*,* α_c*,* α_β *and* α_V *values for MTO reaction ate* 400^oC *are those obtained by linear fitting of the variation of cells parameters with temperature and calculated using the equation* $\alpha_L = (L-L_{ref})/L_{ref}*60$*. 60 is the time at which the MTO reaction was taking place.*

	Expansion coefficient, 60 min MTO reaction				
	α_a (10^{-5} K^{-1})	α_b (10^{-5} K^{-1})	α_c (10^{-5} K^{-1})	α_β (10^{-5} K^{-1})	α_V (10^{-5} K^{-1})
AlPO-18	0.05	-0.11	0.56	-0.71	0.51
CoAlPO-18	-6.76	17.52	4.75	-3.6	15.5
CoSAPO-18	1.05	1.43	1.91	1.34	4.41
SAPO-18	-2.09	6.2	1.58	-1.94	5.68
ZnAlPO-18	0.88	-0.23	0.6	0.92	1.23

The largest volumetric expansion is for CoAlPO-18 at 15.5 with most of the expansion taking place in the *b* direction. Very small values of NTE were obtained for AlPO-18 and ZnAlPO-18 which was expected as methanol is unable to react with these materials and conversion is minimal. Therefore, only small amounts of coke are accumulating inside the pores. CoSAPO-18 and SAPO-18 also have very similar values. What is more interesting, and may be associated with the cobalt position inside the lattice, is that in SAPO-18 the *a*-axis contracts while in CoSAPO-18 it expands. In CoSAPO-18, all axes expand by almost same value while the largest expansion in SAPO-18 is in *b*-axis direction, and opposite behaviour to SAPO-18 is observed for the *β* angle. AlPO-18 and ZnAlPO-18 do not exhibit any unusual changes which are in a good agreement with background knowledge: the former is electro neutral and the latter has only redox properties. In the **Table 4.8**, thermal expansion coefficients calculated for as-prepared and calcined samples after the MTO reaction are shown. The largest expansion is seen in template free AlPO-18. Very similar values are obtained for CoAlPO-18, CoSAPO-18 and SAPO-18, although different coke rates were observed during the MTO reaction. Minimal expansion is found in ZnAlPO-18, where possibly the spatial volume is exhausted and thus movement is limited.

Table 4.8. *Thermal Expansion Behaviour of the Materials Studied, α_a, α_b, α_c, α_β, and α_V values calculated for the as-prepared and calcined samples after MTO reaction, obtained by linear fitting of the variation of cells parameters with temperature and calculated using the equation $\alpha L = (L-L_{ref})/L$.*

	Expansion coefficient (400 - 22 °C)				
	α_a (10^{-5} K^{-1})	α_b (10^{-5} K^{-1})	α_c (10^{-5} K^{-1})	α_β (10^{-5} K^{-1})	α_V (10^{-5} K^{-1})
AlPO-18	4.24	0.96	4.9	-13.37	11.43
CoAlPO-18	-2.42	3.91	1.06	-0.35	2.53
CoSAPO-18	-1.43	2.88	1.11	-0.45	2.54
SAPO-18	-2.37	3.13	1.6	-1.55	2.33
ZnAlPO-18	-1.54	1.09	0.83	0.46	0.38

4.5 Summary and Conclusion

In general, it is assumed that the distribution of heteroatoms in substituted nanoporous solids are so random that diffraction will not be able to provide direct evidence of heteroatom incorporation and hence EXAFS has been used extensively[40]. Although EXAFS studies have been able to provide evidence for the presence of tetrahedrally coordinated metal ions, this technique provides average structural information which will include extra framework or non-framework species. This study has successfully shown that it is possible to accurately determine the changes in lattice parameter and correlate this with metal ion incorporation. Not only was it possible to provide direct evidence for metal incorporation into the AEI-lattice by X-Ray diffraction but also to determine the negative thermal coefficient of these materials and follow their stability during calcination. The larger Co(II) and Zn(II) ions expand the lattice of AEI by as much as 40 percent when substituted for Al(III). The substitution of Si(IV) for P(V) has also been supported by evidence obtained from HRPD, based on the expansion of the lattice constant. The HEXRD PDF method gives an insight into the direction of possible lattice contraction during calcination which may be related to shape-selective catalytic properties of these solids but further high-quality HEXRD data are necessary to precisely model the structural changes associated with the negative thermal expansion of these solids.

References

[1] M. Amri and R. I. Walton, *Chemistry of materials* **2009**, *21*, 2280-2290.

[2] a) J. Weitkamp, *Solid State Ionics* **2000**, *131*, 175-188; b) G. Bellussi and P. Pollesel in *Industrial applications of zeolite catalysts: production and uses of light olefins*, *Vol. 158* Eds.: J. Cejka, N. Zilkova and P. Nachtigall), **2005**, pp. 1201-1212; c) W. Vermeiren and J. P. Gilson, *Topics in Catalysis* **2009**, *52*, 1131-1161.

[3] a) E. M. Flanigen, B. M. Lok, R. L. Patton and S. T. Wilson, *Pure & Appl. Chem.* **1986** *58*, 1351-1358; b) S. T. Wilson, B. M. Lok, C. A. Messin, T. R. Cannan and E. M. Flanigen, *Journal of the American Chemical Society* **1982**, *104*, 1146-1147; c) S. T. Wilson, B. M. Lok and E. M. Flanigen, *Journal of American Chemical Society* **1988**, *196*, 207-211.

[4] M. Hartmann and L. Kevan, *Chemical Reviews* **1999**, *99*, 635-664.

[5] a) G. F. Froment, W. J. H. Dehertof and A. J. March, *Catalysis Letters* **1992**; b) H. O. Pastore, S. Coluccia and L. Marchese, *Annual Reviews* **2005**, *35*, 351-395.

[6] a) D. L. Vanoppen, D. E. De Vos, M. J. Genet, P. G. Rouxhet and P. A. Jacobs, *Angewandte Chemie International Edition in English* **1995**, *34*, 560-563; b) M. P. J. Peeters, M. Busio and P. Leijten, *Applied Catalysis A: General* **1994**, *118*, 51-62.

[7] a) J. Liang, H. X. Li, S. Zhao, W. Guo, R. Wang and M. Ying, *Applied Catalysis* **1990**, *64*, 31-40; b) J. M. Thomas, Y. Xu, C. R. A. Catlow and J. W. Couves, *Chemistry of materials* **1991**, *3*, 667-672; c) T. Inui, S. Phatanasri and H. Matsuda, *Journal of the Chemical Society, Chemical Communications* **1990**, 205-206; d) H.-L. Zubowa, E. Alsdorf, R. Fricke, F. Neissendorfer, J. Richter-Mendau, E. Schreier, D. Zeigan and B. Zibrowius, *Journal of the Chemical Society, Faraday Transactions* **1990**, 2307-2312.

[8] a) D. S. Wragg, D. Akporiaye and H. Fjellvåg, *Journal of Catalysis* **2011**, *279*, 397-402; b) L. Marchese, A. Frache, G. Gatti, S. Coluccia, L. Lisi, G. Ruoppolo, G. Russo and H. O. Pastore, *Journal of Catalysis* **2002**, *208*, 479-484; c) Z. Zhu, M. Hartmann and L. Kevan, *Chemistry of materials* **2000**, *12*, 2781-2787.

[9] C. Baerlocher, L. B. McCusker and D. H. Olson, *Atlas of Zeolite Framework Types, 6th edition*, Elsevier, Amsterdam, **2007**, p.

[10] J. Chen, P. A. Wright, J. M. Thomas, S. Natarajan, P. L. Gai-Boyes, R. P. Townsed and C. M. Lok, *Journal of Physical Chemistry* **1994**, *98*, 10216-10224.

[11] P. A. Wright and G. M. Pearce in *Chapter 7. Structural Chemistry of Zeolites, Vol.* Eds.: J. Prof. Dr. Čejka, A. Prof. Dr. Corma and S. Prof. Dr. Zones), Wiley, **2010**.

[12] a) P. A. Barrett, G. Sankar, C. R. A. Catlow, J. M. Thomas and Um, *Journal of Physical Chemistry* **1996**, *100*, 8977-8985; b) G. Sankar, J. K. Wyles and C. R. A. Catlow, *Topics in Catalysis* **2003**, *24*, 173-184.

[13] S. H. Park, R.-W. Große Kunstleve, H. Graetsch and H. Gies, *Studies in Surface Science and Catalysis* **1997**, *105*, 1989-1994.

[14] M. M. Martínez-Iñesta and R. F. Lobo, *The Journal of physical chemistry B* **2005**, *109*, 9389-9396.

[15] D. A. Woodcock and P. Lightfoot, *Chemistry of materials* **1999**, *11*, 2508-2514.

[16] D. A. Woodcock, P. Lightfoot, P. A. Wright, L. A. Villaescusa and M. A. Camblor, *Journal of Material Chemistry* **1999**, *9*, 349-351.

[17] K. D. Hammonds, V. Heine and M. T. Dove, *The Journal of physical chemistry B* **1998**, *102*, 1759-1767.

[18] J. Z. Tao and A. W. Sleight, *Journal of Solid State Chemistry* **2003**, *173*, 442-448.

[19] W. H. Baur, *Journal of Solid State Chemistry* **1992**, *97*, 243-247.

[20] M. P. Attfield and A. W. Sleight, *Chemistry of materials* **1998**, *10*, 2013-2019.

[21] J. S. O. Evans, T. A. Mary, T. Vogt, M. A. Subramanian and A. W. Sleight, *Chemistry of materials* **1996**, *8*, 2809-2823.

[22] a) D. A. Keen and M. T. Dove, *Journal of Physics: Condensed Matter* **1999**, *11*, 9263-9273; b) M. G. Tucker, M. P. Squires, M. T. Dove and D. A. Keen, *Journal of Physics: Condensed Matter* **2001**, *13*, 403-423; c) T. Proffen, S. J. L. Billinge, T. Egami and D. Louca, *Z. Kristallogr* **2003**, *218*, 132-143; d) T. Proffen, *Reviews in Mineralogy and Geochemistry* **2006**, *63*, 255-274.

[23] T. Wakihara, S. Kohara, G. Sankar, S. Saito, M. Sanchez-Sanchez, A. R. Overweg, W. Fan, M. Ogura and T. Okubo, *Phys. Chem. Chem. Phys.* **2006**, *8*, 224-227.

[24] J. Bauer, T. Selvam, J. Ofilia, E. Che, R. Herrmann and W. Schwieger, *Studies in Surface Science and Catalysis* **2007**, *170*, 837-844.

[25] A. J. Dent, G. Cibin, S. Ramos, A. D. Smith, S. M. Scott, L. Varandas, M. R. Pearson, N. A. Krumpa, C. P. Jones and P. E. Robbins, *Journal of Physics: Condensed Matter* **2009**, *190*.

[26] a) B. Ravel and M. Newville, *Journal of Synchrotron Radiation* **2004**; b) B. Ravel and M. Newville, *Physica Scripta* **2005**, *T115*, 1007-1010; c) B. Ravel and M. Newville, *Journal of Synchrotron Radiation* **2005**, *12*, 537-541.

[27] N. Binsted in *EXCURV98: CCLRC, Vol.* Daresbury Laboratory computer program, **1998**.

[28] A. Coelho in *Topas-Academic Version 4.1, Vol.* Brisbane, **2007**.

[29] A. Simmen, L. B. McCusker, C. Baerlocher and W. M. Meier, *Zeolites* **1991**, *11*, 654-661.

[30] in *Origin 8.5, Vol.* OriginLab, Northampton, **2011**.

[31] R. Wendelbo, D. Akporiaye, A. Andersen, I. M. Dahl and H. B. Mostad, *Applied Catalysis A: General* **1996**, *142*, 197-207.

[32] G. Sankar, R. Raja and J. M. Thomas, *Catalysis Letters* **1998**, *55*, 15-23.

[33] I. N. Senchenya and V. Y. Borovkov, *Studies in Surface Science and Catalysis* **1991**, *65*, 635-662.

[34] C. Zenonos, A. Beale, G. Sankar, D. W. Lewis, J. M. Thomas and C. R. A. Catlow, *Studies in Surface Science and Catalysis* **2007**, *135*, 358.

[35] N. Novak Tušar, A. Tuel, I. Arčon, A. Kodre and V. Kaučič in *EXAFS and NMR studies of the incorporation of Zn(II) and Co(II) cations into tetrahedral framework sites of AlPO4 molecular sieves, Vol. Volume 105* Eds.: S.-K. I. Hakze Chon and U. Young Sun), Elsevier, **1997**, pp. 501-508.

[36] K. Simmance, G. Sankar, R. G. Bell, C. Prestipino and W. van Beek, *Physical Chemistry Chemical Physics* **2010**, *12*, 559-562.

[37] C. Zenonos, G. Sankar, F. Corà, D. W. Lewis, Q. A. Pankhurst, C. R. A. Catlow and J. M. Thomas, *Physical Chemistry Chemical Physics* **2002**, *4*, 5421-5429.

[38] E. J. W. Whittaker and R. Muntus, *Geochimica et Cosmochimica Acta* **1970**, *34*, 945-956.

[39] P. Concepción, T. Blasco, J. M. López Nieto, A. Vidal-Moya and A. Martínez-Arias, *Microporous and Mesoporous Materials* **2004**, *67*, 215-227.

[40] a) G. Sankar and J. M. Thomas, *Topics in Catalysis* **1999**, *8*, 1-21; b) G. Sankar, J. M. Thomas and C. R. A. Catlow, *Topics in Catalysis* **2000**, *10*, 255-264.

Chapter 5 A study of an influence of post-synthesis treatment on vanadium substitution in ZSM-5

5.1 Chapter overview

In this chapter, vanadium ions impregnated on zeolites, in particular, ZSM-5 are investigated. Vanadium impregnated zeolites are powerful oxidation catalysts. A series of impregnated zeolites were prepared and modified by post-synthesis treatments, in particular, leaching, dealumination, and passivation. Catalytic activities of ZSM-5 samples were tested for the oxidation of decane. ZSM-5 samples showed various catalytic performances. Therefore, as-prepared and activated catalysts were characterized in order to determine the local structure of vanadium ions and relate it to their catalytic properties. More importantly, the nature and position of vanadium ions in catalysts subjected to post-synthesis treatments were ascertained and linked to decreasing catalytic activities. *In situ* X-ray absorption spectroscopy (XAS) and *ex situ* Raman spectroscopy were carried out to determine the local structure of vanadium ions.

5.2 Introduction

Vanadium containing zeolites have attracted considerable attention due to their interesting catalytic properties[1] in various redox reactions. For instance, the liquid-phase oxidation of phenol or toluene by H_2O_2[2], oxidation of butadiene[3], epoxidation of unsaturated alcohols[4], oxidation of naphthalene[5], and reduction of NO with NH_3[6]. Vanadium-containing aluminosilicate molecular sieves can be prepared by hydrothermal synthesis and also by post-synthesis treatment or impregnation[7]. The intentions are to produce catalysts with both intra-framework vanadium and intra-zeolite vanadium oxide dispersions. It has been shown that a two-step post-synthesis method can lead to substitution of vanadium into zeolite[7]. Firstly, vacant T sites must be created and then vanadium ions can be impregnated.

The activity and selectivity of vanadium oxide catalysts in oxidation reactions strongly depends on the interaction between the vanadium species and the catalyst support[8]. Therefore, vanadium-incorporated molecular sieves are expected to give a new type of catalyst support interaction. Numerous papers in literature discuss the incorporation of vanadium ions into the lattice of zeolites. For example, Centi et al.[9] reported incorporation of V(V) silicate (VS-1) by hydrothermal synthesis in small amounts, but these were related to site defects. Other authors came to a conclusion that the vanadium incorporation into the zeolite lattice occurs as V(IV) and is later transformed to V(V) during the calcination[10]. The incorporation of both V(IV) and V(V) into the zeolite lattice have been observed by Kornatowski et al.[11]. The reduction of V(V) to V(IV) has been reported by Sen et al[12] who showed that the reduction takes place due to the reactivity of the V-O-Si bonds rather than V-O[2]. Si-O-V bond formation has been observed by Das et al.[13] with isolated tetrahedral vanadium environments containing V-O during impregnation using vanadium V(V) triisopropoxide oxide. The excess charge can be compensated by the presence of the stable V-O bond, and the smaller size of V(V) ions (r = 0.46 Å) rather than the V(IV) ions (r = 0.59 Å), which are more favourable to the incorporation of the Si(IV) (r = 0.26 Å) in the zeolite lattice. More importantly, the shape selective catalysis is only possible inside the microporous structure[14], although both surfaces, external and internal, are available for reactants. Only internal pores are responsible for strict shape-selective catalysis, and therefore the easy access to external active sites needs to be minimized in order to utilize the shape selectivity. Numerous post-synthesis modifications have been developed since the pioneering work of Chen et al.[15] and Kaeding et al.[16] which include dealumination with acids[14, 17], poisoning of the surfaces by bases larger than the pores[18], and coating of surfaces with silica[19], although these have been applied to ZSM-5 in combination with passivation of external sites.

Vanadium is characteristic of "*d*-block" of elements, which can adopt different oxidation states, in particular vanadium is found in III, IV and V states resulting in its 3*d* orbital containing two, one and zero electrons respectively. In the present study, the source of V in the impregnation solution is vanadyl sulphate ($VOSO_4$) which contains vanadium not as a free cation but as part of the vanadyl ion (VO^{2+}). The multiple V=O bond of the vanadyl ion may or may not be retained upon incorporation in the framework and thus it results in changes of the physical and chemical properties of the V ion. Depending on the impregnation conditions, vanadium can adopt different coordination numbers[20].

Host structure Zeolite Socony Mobil - 5 (ZSM-5) was first patented by Argauer and Landolt[21].It is a medium pore-size zeolite with 10-membered ring openings, displayed in **Figure 5.1**.

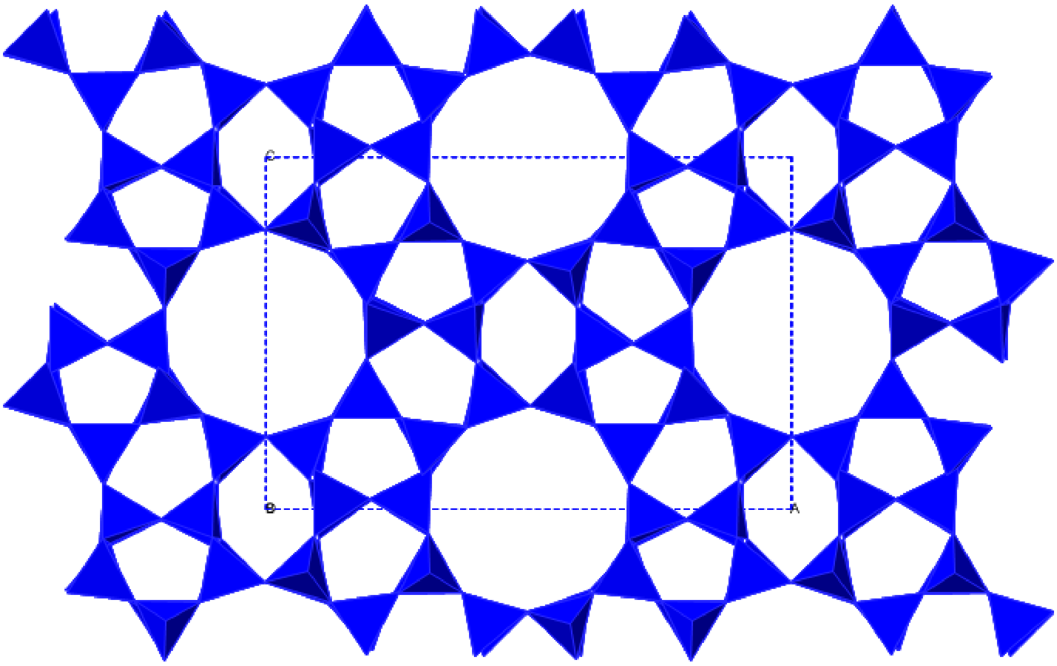

Figure 5.1. *ZSM-5 viewed along [010] axis.*

ZSM-5 is built from pentasil chains, where eight pentasil units (five-membered rings) are linked together by oxygen bridges in a *D2d* symmetry. The pentasil chains are interconnected by oxygen bridges to form corrugated sheets with 10-ring holes. If Si/Al and O are assumed to be bonded in the vertices, the interconnecting oxygen bridges for these rings form pentasil chains[22], and are classified according to IZA as a MFI-type structure[23].

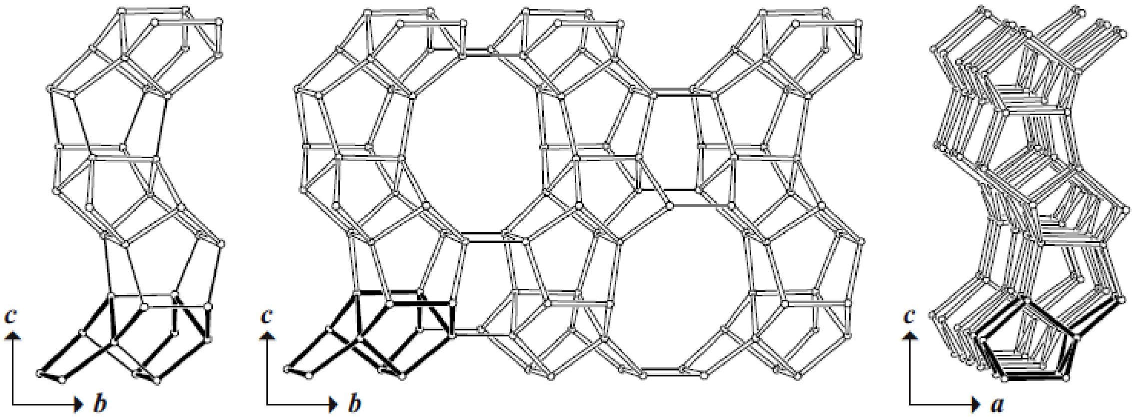

Figure 5.2. *Building scheme of MFI-type zeolite viewed along a (left), Periodic Building Unit viewed along a (middle) and along b (right)[24].*

A typical chemical composition of ZSM-5 is $Na_nAl_nSi_{96-n}O_{192}\cdot16H_2O$, $(0<n<27)$[25]. It crystallizes in orthorhombic (*Pnma*) crystal structure with lattice parameters *a* = 20.07 Å, b = 19.92 Å, c = 13.42 Å[26]. The aluminosilicate zeolite ZSM-5 can have a very high silica to alumina ratio, although the silicate version, silicate-1, can be formed as well. The presence of a positive charge (H^+, Na^+) is required in the substitution of Al(III) for Si(IV). The additional proton gives ZSM-5 a high level of acidity (HZSM-5), which causes its activity. The acidity of ZSM-5 molecular sieves depends strongly on the Al/Si ratio of the lattice. MFI type zeolitic solids are the most versatile catalysts used in the petroleum industry[25].

5.2.1 Aims of the Work

The aim is to investigate in detail using *in situ* X-ray Absorption Spectroscopy (XAS) and *ex situ* Raman spectroscopy local structure of vanadium ions in the as-synthesized and activated forms of ZSM-5, which were prepared at JM.

5.3 Experimental

5.3.1 Material preparation and chemical composition

Six samples of vanadium ZSM-5 were prepared at the Johnson Matthey Catalysis Centre, which were un-calcined prior to further studies, and chosen for the characterization. The template-free H-ZSM-5 samples were obtained in bulk from the company Zeolyst International. Samples 1 to 4 were prepared by incipient wetness using $VOSO_4$, with intended loading of 1% on H-ZSM 5 SAR 22. A series of standard post- and pre-synthesis treatments were used to modify the samples as follow:

- Sample-1: incipient wetness.
- Sample-2: incipient wetness. The sample was then heated in MeOH to remove weakly bound vanadium.
- Sample-3: prior to incipient wetness, the zeolite was partially dealuminated by refluxing in HNO_3.
- Sample-4: prior to incipient wetness the sample was passivated.
- Sample-5 same as sample 1, but using H-ZSM-5 with a SAR 80
- Sample-6 prepared by liquid impregnation (0.1M solution of $VOSO_4$, repeated 3 times) using H-ZSM-5 with SAR 23

The elemental analysis of Si, Al, and V concentration in samples were done by ICP, and the summary is displayed in the **Table 5.1**.

Table 5.1. P*reparation procedure and metal concentration obtained from chemical analysis of vanadium ZSM-5 samples. (SAR = silica alumina ratio, IW = incipient wetness).*

Sample	*SAR*	*Treatment*	*Al*	*Si*	*V*	*Si/Al (mol)*
1	23	Incipient wetness (IW), 1% V intended	3.13	38.6	0.75	11.89
2	23	As sample 1 followed by MeOH leaching	2.61	38.7	0.27	14.3
3	23	Dealumination before IW, 1% V intended	2.27	38	0.69	16.14
4	23	Passivation before IW, 1% V intended	2.40	37.7	0.56	15.15
5	80	IW, 1% V intended	0.92	41.7	0.73	43.71
6	23	Liquid impregnation	2.43	37.8	1.02	15.00

5.3.2 X-Ray Diffraction (XRD) and SEM study

All samples were first characterized by powder diffraction on a flat plate Bruker D4 X-ray diffraction instrument using Cu Kα radiation. XRD patterns were collected at a diffraction angle (2θ) range of 5 to 50° with the step size of 0.05 Å and 5 sec collection time at each step. The SEM images were collected on JEOL JSM-6301F (JEOL Ltd., Tokyo, Japan) with INCAx-sight detector (Oxford Instruments) at an accelerating voltage at the Institute of Archaeology at the UCL. Fine grounded powder samples were mounted on circular aluminium stubs with double-sided sticky tape and then coated with gold particles.

5.3.3 **In situ** *X-ray Absorption Spectroscopy (XAS)*

The vanadium K-edge XAS from five samples were measured in fluorescence mode. Data were collected at BM29 XAS beamline at the ESRF (European Synchrotron Research Facility) in Grenoble (France). The storage ring operates at 6 GeV electron energy with a maximum current of 200 mA. The beamline is equipped with a Si(111) double crystal monochromator, and 13-element fluorescence detector for fluorescence measurements.

Fluorescence spectra were measured from sample-1, -3, and -6 under heating in an oxidation atmosphere (heat treated in dry air), and the samples -4 and -5 were measured at room temperature. Approximately 100 mg of a sample was pressed into a pellet (13 mm diameter), and inserted into an *in situ* XAS cell (available at the beamline). The heating treatment of samples was started from room temperature to 300^{o}C at the rate of 2^{o}C/min. Samples were held at this temperature for 30 min. A typical scan lasted ~5min, and this was caused by the limited time availability at the beamline.

The V K-edge XAS spectra for reference materials-VO_2, V_2O_3, V_2O_5, and $VOSO_4 \cdot 3H_2O$, were recorded in the transmission mode at room temperature (RT=25^{o}C). Calculated amounts of each sample were mixed with boron nitride, and pressed into a pellet, and inserted into an in situ XAS cell (available at the beamline). Each scan was collected for 10 min.

5.3.4 Raman Spectroscopy

The Raman spectra of the zeolites were recorded with a Renishaw inVia Raman spectrograph equipped with a sensitive CCD detector coupled to a microscope for point-by-point analyses, and controlled by Wire Raman Software 2.0. Incident lasers for Raman scattering and fluorescence for the measurements ranged from the visible (514 nm) to the UV (325 nm). Samples were placed on an ordinary glass microscope slide, being both inert and weak Raman scatterers, causing little or no interference to the Raman spectrum. Data collection lasted approximately 30 min for each sample.

5.3.5 Data Analysis

XRD phase identification was achieved by indexing the reflections, and comparing with standard available XRD data sets[27]. Le Bail and Pawley profile fitting was performed employing the Thompson-Cox-Hastings pseudo-Voigt function available on TOPAS 4

Academic[28], which provided information about unit cell parameters. The XAS data were normalised and background subtracted using ATHENA[29]. Least squares fittings of EXAFS data was performed using ExCurve98[30]. All images were produced using the data analysing and graphing software Origin Pro 8[31].

5.4 Results and Discussion

5.4.1 Catalytic testing

All six samples were tested for the oxidation of decane at 120°C for 20 h at the pressure of O_2 15 bar. The tests were carried out at Johnson Matthey Catalysis Centre. The catalysts were calcined in air prior to testing at a rate of 1°C / min to 300°C for 5 hours. The conversions obtained by oxidation of decane are shown in the **Table 5.2**.

Table 5.2. *Results of catalytic testing of V-ZSM-5 samples with decane.*

	Sample 1	*Sample 2*	*Sample 3*	*Sample 4*	*Sample 5*	*Sample 6*
1 decanol	0	-	0.02	-	0.01	-
2-one+2-ol	(0.18-0.06) 0.20	(0.1-0) 0.1	(1.49-0.67) 2.16	(1.3-0.65) 1.95	(1.41-0.72) 2.13	(0.06-0.02) 0.08
3-one+3-ol	(0.15-0.05) 0.20	(0.1-0) 0.1	(1.10-0.22) 1.32	(1.05-0.26) 1.31	(1.09-0.28) 1.37	(0.05-0.01) 0.06
4-5-one+4ol	(0.27-0.03) 0.30	(0.1-0) 0.1	(2.09-0.15) 2.24	(2.0-0.19) 2.19	(2.07-0.28) 2.35	(0.08-0.01) 0.09
pentanoic acid	0.05	-	0.64	0.53	0.62	-
hexanoic acid	0.06	-	0.53	0.44	0.53	-
heptanoic acid	0.03	-	0.39	-	0.38	-
octanoic acid	0.03	-	0.33	0.28	0.27	-
nonanoic acid	0.01	-	0.11	-	0.14	-
decanoic acid	0.02	-	0.23	0.15	0.2	0.01
Total yield	**0.9**	**0.3**	**7.97**	**6.85**	**8**	**0.24**

Dealuminated sample 3 and passivated sample 4 display exceptionally high selectivity and conversion in comparison to other samples which were prepared by the incipient wetness method. However, almost identical selectivity and conversion is displayed by sample 5 which was also prepared by incipient wetness but utilizing ZSM-5 with much larger silica to alumina ratio (SAR) at 80. The larger concentration of vacancies created in sample 3 by dealumination, and larger SAR in sample 5 may increase the substitution of vanadium into the ZSM-5 lattice, and thus increase the catalytic performance. Post-synthesis passivation of external surface also improved the catalyst performance which again could create T vacancies in the lattice.

5.4.2 Diffraction and SEM study

The stacked plot of XRD powder patterns (Cu *Kα*) of pure H-ZSM-5 samples (SAR 23 and SAR 80) and reference data obtained from database[32] are shown in the **Figure 5.3**. Both materials display a high level of crystallinity and indicate only presence of MFI-type framework structures, characteristic of ZSM-5.

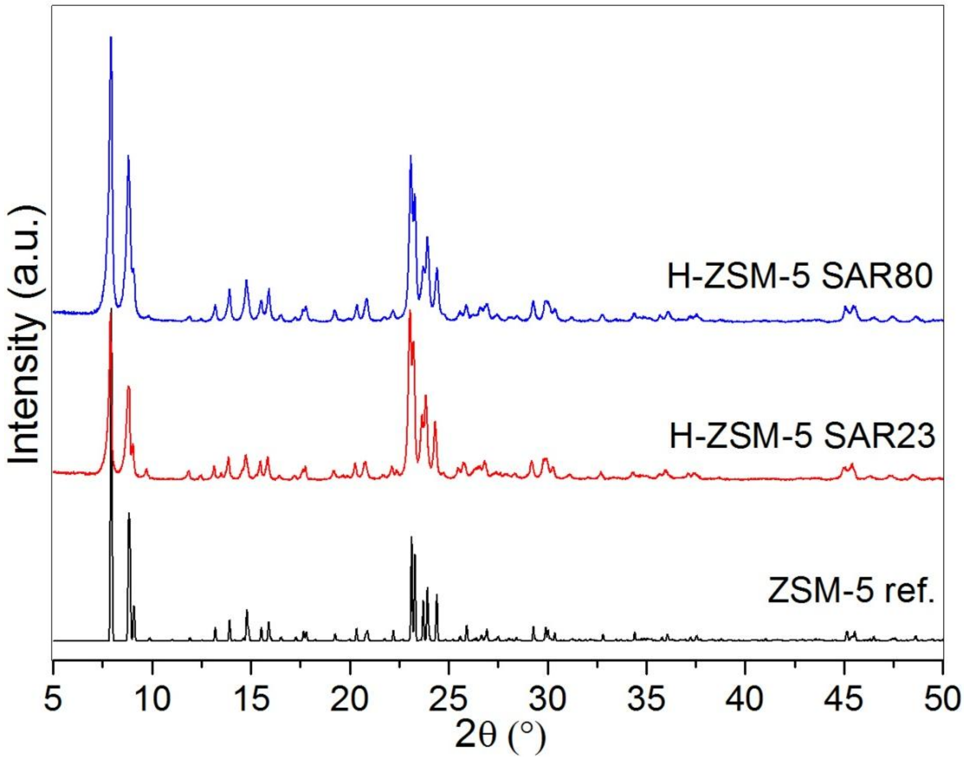

Figure 5.3. *XRD plots of H-ZSM-5 samples.*

The stacked plot of XRD patterns displayed in **Figure 5.4** is for all vanadium containing samples, and pure H-ZSM-5 with SAR 23. **Figure 5.5** displays the stacked plot of sample 5 and H-ZSM-5 with SAR 80. Indexing of the powder diffraction lines failed to expose extra reflections corresponding to the $VOSO_4$ used in the ion exchange process, though the concentrations were very low. High crystallinity was maintained after the incipient wetness treatment, and all samples were indexed in the monoclinic space group *Pnma* specific of the ZSM-5

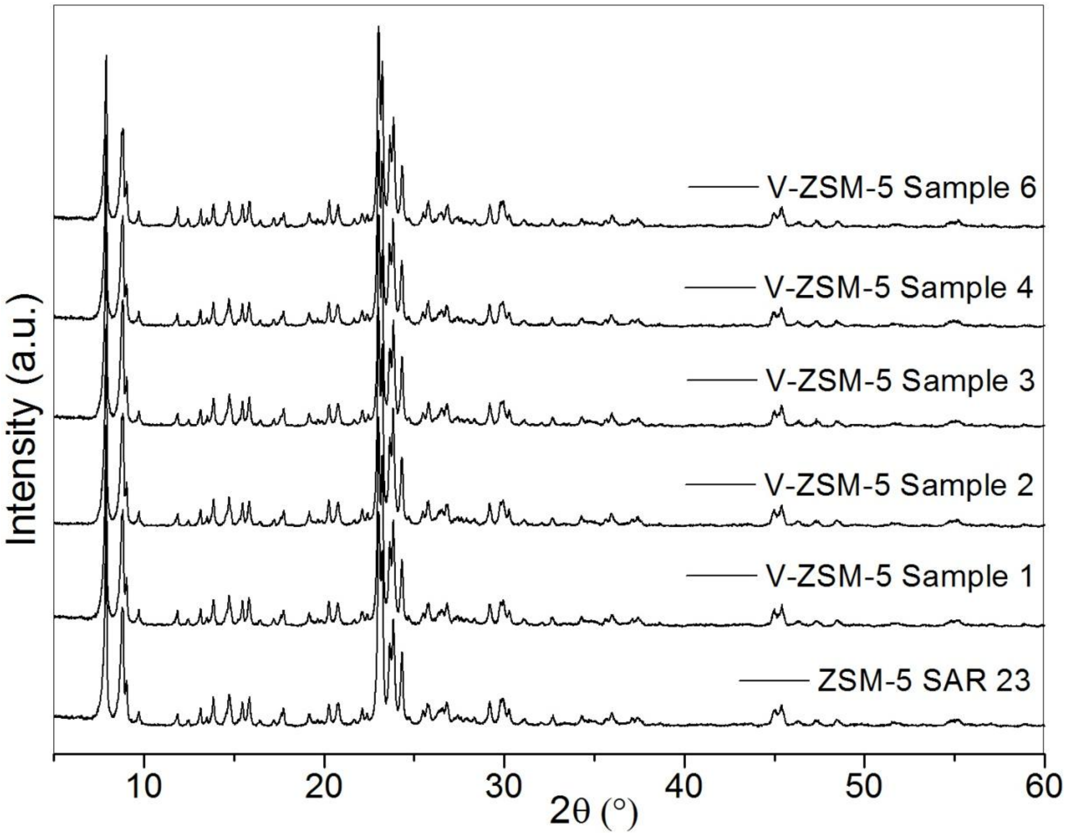

Figure 5.4. *XRD patterns of samples-1, -2,3,- 4, and -6 with their reference H-ZSM-5 SAR23.*

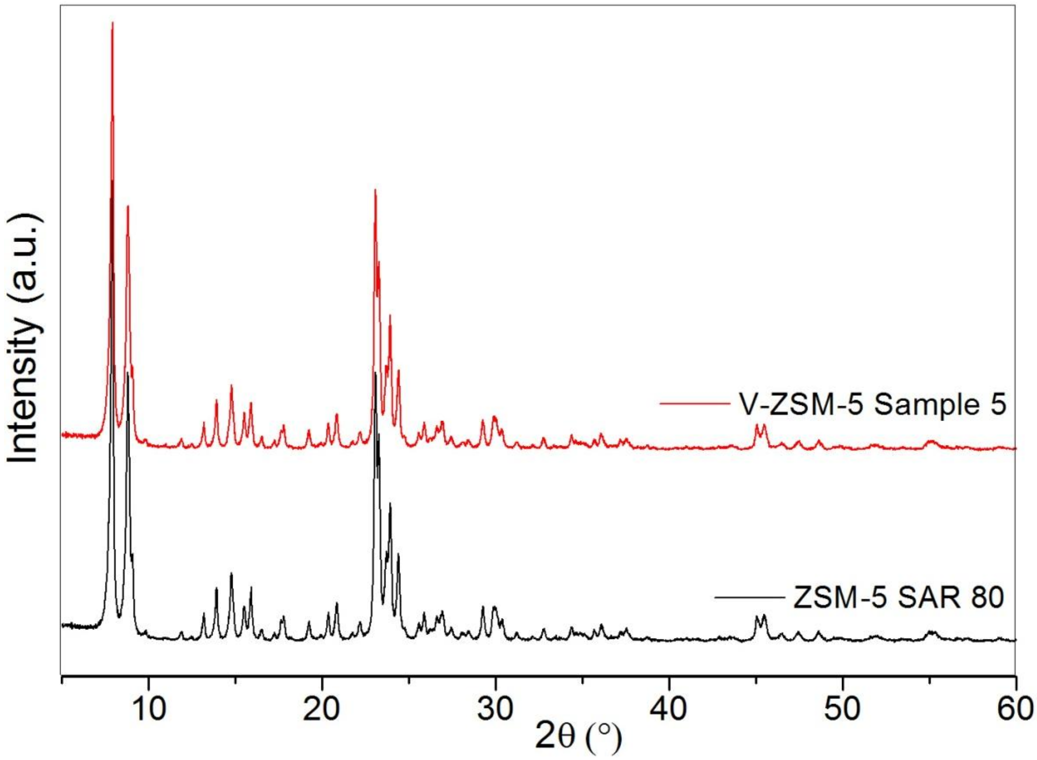

Figure 5.5. *XRD patterns of sample 5 and reference H-ZSM-5 SAR 80.*

The cell parameters obtained from the Pawley fit to the XRD data are shown in the **Table 5.3.** The lattice constants for vanadium containing ZSM-5 samples are very close to vanadium-free H-ZSM-5 samples[32-33] in samples 1 and 6 (SAR23). The lattice constants are larger in samples 2 and 4 (SAR23) and sample 5 (SAR 80), and smaller in sample 3. The lattice expansion can suggest vanadium incorporation, as it has been reported by Sen et al.[10d], however the catalysis showed that sample 2 is not very active. The lattice is smaller in samples 3 which can be related to the dealumination process.

Table 5.3. *Refined cell parameters of the ZSM-5 samples.*

Sample	*a/Å*	*b/Å*	*c/Å*	*V/Å*^{3}	*R*
ZSM-5 ref[33]	20.07	19.92	13.42	5365.2	
H-ZSM-5 SAR 80	20.100(2)	19.914(2)	13.401(1)	5364.3(1)	8.5
V-ZSM-5 Sample 5	20.106(2)	19.915(2)	13.403(2)	5366.0(1)	8.7
H-ZSM-5 SAR 23	20.125(2)	19.949(2)	13.442(2)	5397.2(1)	11.5
V-ZSM-5 Sample 1	20.135(2)	19.944(2)	13.438(1)	5396.2(8)	11.4
V-ZSM-5 Sample 2	20.143(2)	19.950(2)	13.448(2)	5404.0(9)	11.1
V-ZSM-5 Sample 3	20.125(2)	19.944(2)	13.434(2)	5392.2(9)	11.3
V-ZSM-5 Sample 4	20.147(2)	19.953(2)	13.444(2)	5404.2(9)	11.4
V-ZSM-5 Sample 6	20.144(2)	19.943(2)	13.435(2)	5397.3(9)	11.8

Crystals of H-ZSM-5 SAR 23 are formed from large agglomerates of particles which are various sizes and shapes, displayed in **Figure 5.6**(a). More uniformly shaped particles display the H-ZSM-5 SAR80, **Figure 5.6**(b), with a median size of 0.3 µm.

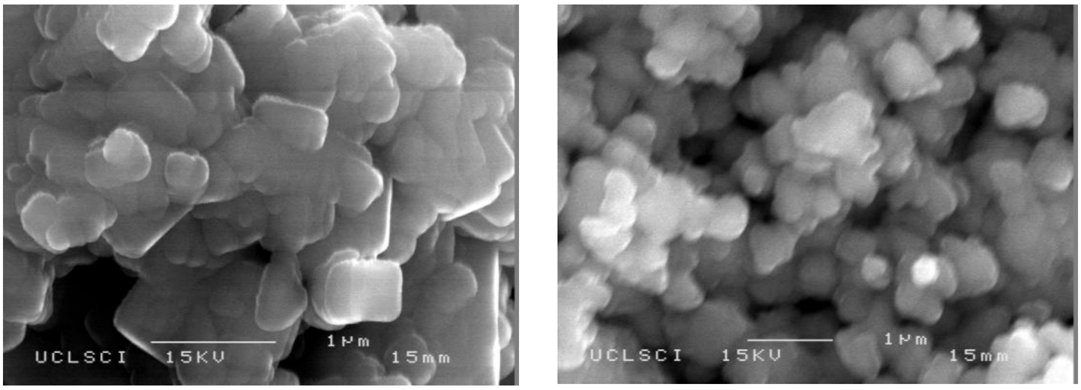

Figure 5.6. *SEM micrographs of H-ZSM-5 SAR 23 (left) and SAR 80 (right).*

Figure 5.7 displays the SEM images of the vanadium impregnated samples. There are no real changes to physical appearance of incipient wetness modified samples. They all are formed mostly form agglomerated particles concentrated into large bulks. The particles are not uniform in size.

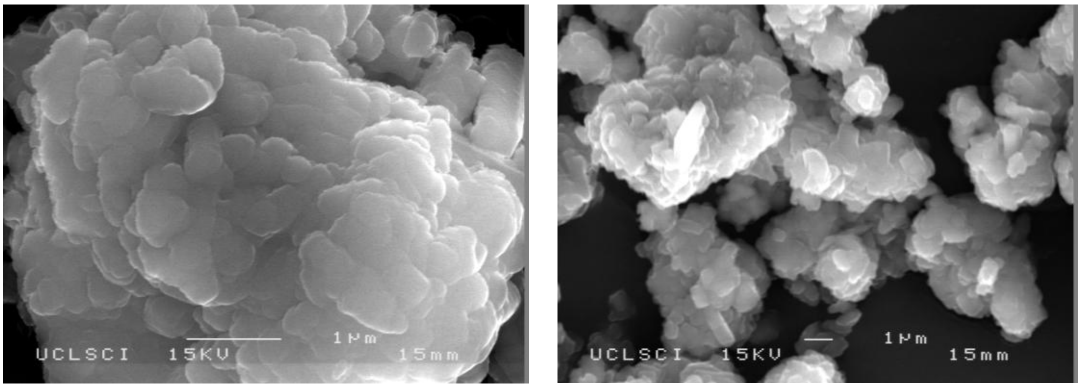

(a) V-ZSM-5 Sample 1 SAR 23

(b) V-ZSM-5 Sample 2 SAR 23

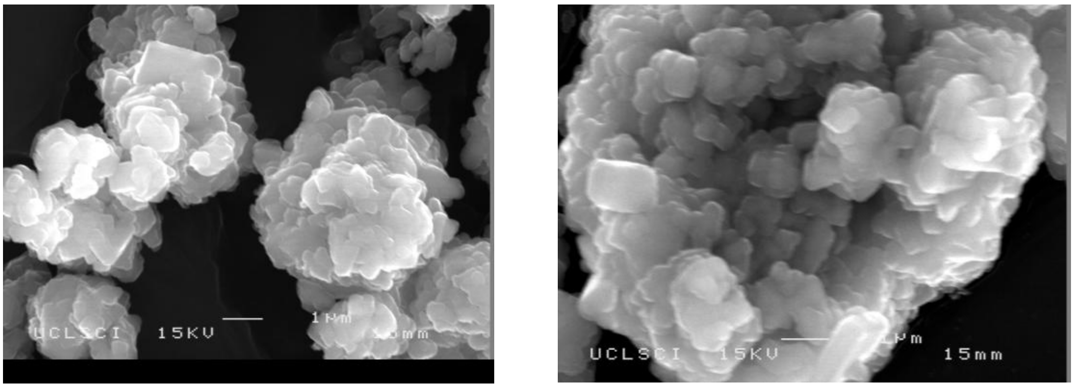

(c) V-ZSM-5 Sample 3 SAR 23

(d) V-ZSM-5 Sample 4 SAR 23

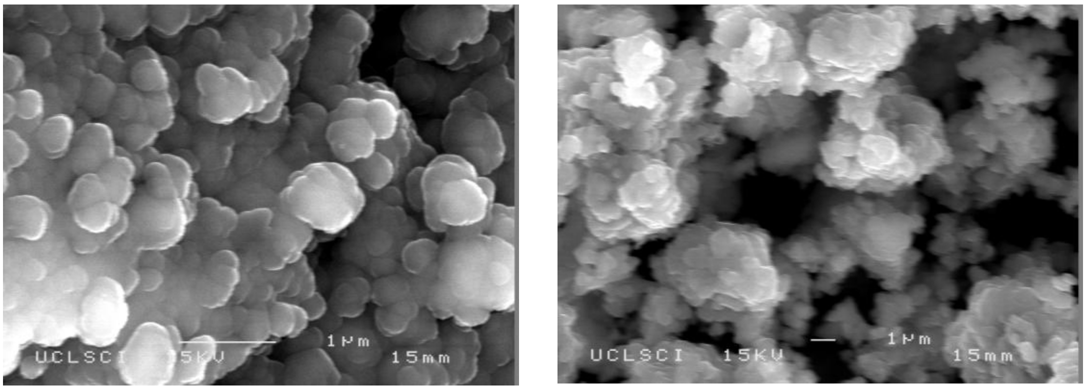

(e) V-ZSM-5 Sample 5 SAR 80

(f) V-ZSM-5 Sample 5 SAR 23

Figure 5.7. *SEM micrographs of the vanadium exchanged V-ZSM-5.*

5.4.3 In situ XAS

The stacked plot of vanadium *K*-edge XANES for standard compounds, VO_2, V_2O_3, V_2O_5, $VOSO_4$, given in **Figure 5.8**, shows that the intensity variation of the pre-edge peak is significant. The vanadium ions pre-edge feature increases in intensity from distorted octahedral coordination VO_6 groups in VO_2 and V_2O_3, to a lower coordination with a short V=O bond in a distorted square-pyramidal symmetry (V_2O_5, $VOSO_4$) which is attributed to the 1*s* - 3*d* transition. The strong pre-edge is caused by a combination of vacancies in the *d*-orbital, and mixing of 2*p* orbitals of oxygen atoms with the 3*d* character, indicating compounds where a V=O double bond is present[34]. The splitting in the 1*s* → 3*d* transition in a multiplet structure at the pre-edge peak region of V_2O_3 is caused by crystal-field splitting of the ground state[35]. In the case of V_2O_5 the XANES spectra are typified by a strong 1*s* → 3*d* pre-edge absorption[35]. The relatively small pre-edge feature in VO_2 is due to broken inversion centres as a result of the lower symmetry of the *O* ligands and the pre-edge absorption becomes dipole allowed due to a combination of stronger 3*d* - 4*p* mixing and overlap of the metal 3*d* orbitals with the 2*p* orbitals of the ligand[35]. The tetravalent vanadium center in $VOSO_4.3H_2O$ is fivefold coordinated by a short vanadyl oxygen at 1.56 Å, two oxygens from two SO_4^{2-} groups at 2.02Å, and another two oxygens from two water molecules at 2.06Å. However, there is a sixth oxygen from a third water molecule at a further distance of 2.28Å from a VO_5 unit below the vanadium which is too far to be considered in the primary coordination sphere[36].

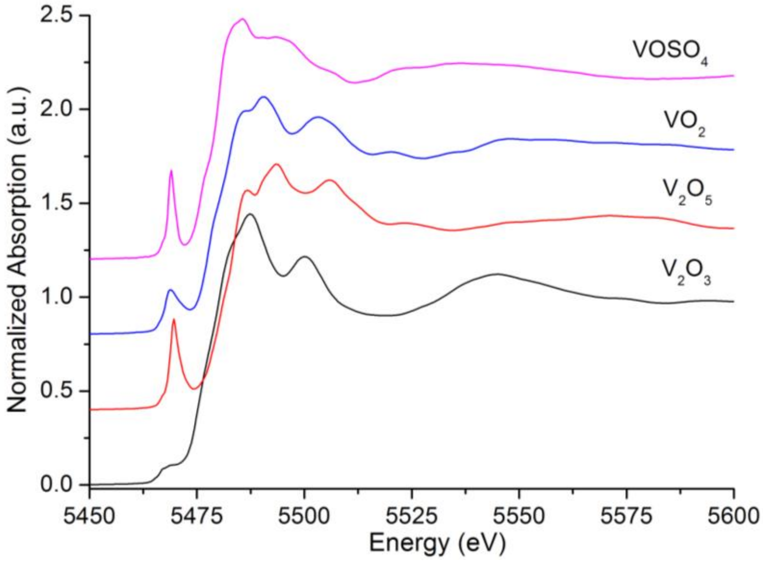

Figure 5.8. *V K-edge XANES of reference vanadium oxides collected at RT.*

The XANES spectra of standard compounds agree with those reported previously in the literature[34, 37]. The energy positions of various absorption features are correlated with the oxidation state of vanadium in the oxides. The experimental data for reference vanadium compounds are summarized in the **Table 5.4**.

Table 5.4. *Energy positions of various spectral features in the V K-edge XANES spectra of vanadium compounds (ΔE =E - 5465), errors of the pre-edge and white line positions are ± 0.1 eV, and on white line intensity ± 5%.*

Compound	*Pre-edge position (eV)*	*Δ E (eV)*	*Pre-edge intensity*	*White line position (eV)*	*Δ E (eV)*	*White line intensity*
V_2O_3	5469.4	4.4	0.11	5487.4	22.4	1.44
VO_2	5468.9	3.9	0.24	5490.5	25.5	1.26
V_2O_5	5469.6	4.6	0.48	5493.4	28.4	1.31
$VOSO_4$	5469	4	0.47	5485.6	20.6	1.28

With the increasing oxidation state, the energy of the pre-edge peak and the $1s \rightarrow 4p$ transition above the absorption edge shifts to higher energies. The chemical shifts follow Kunzl's law[38] and vary linearly with the valence of the absorbing vanadium atom. The positive shift in the threshold energy with valence increase can be understood conceptually as being due to an increase in the attractive potential of the nucleus on the 1*s* core electron and a reduction in the repulsive core Coulomb interaction with all the other electrons in the compound.

Table 5.5. *Bonding type, bond distances (R), and co-ordination numbers (N) for the reference compounds.*

Compound	Bond type	N	R (Å)	M-O coordination (M=V)	Formal valence	Structure (space group)	Reference
V_2O_5	V=O	1	1.59	Distorted square pyramidal "VO_5"	5	Orthorhombic (Pmmn)	[39]
	V-O	4	1.78, 1.88(x2), 2.02, 2.78				
	V-V	5	3.48(x2), 3.85(x7), 3.08(x2); 3.56(x3)				
VO_2	V-O	6	1.76, 1.86, 1.89, 2.01, 2.02, 2.06; average 1.94	Distorted octahedral "VO_6"	4	Monoclinic (P21/c)	[40]
	V-V	2	2.62, 3.17				
$VOSO_4.3H_2O$	V=O	1	1.56	Distorted square pyramidal "VO_5"	4	Monoclinic (P21/c)	[41]
	V-O	5	2.01, 2.03, 2.05, 2.08, 2.28				
V_2O_3	V-O	6	1.97(x3), 2.05(x3), average 2.01	Corundum structure, V(III) are six-fold-coordinated by oxygen ions	3	Tetragonal (R-3c)	[42]
	V-V	1	2.69				
		3	2.88				
V metal	V-V	8	2.625		0	Cubic (Im3m)	[43]
		6	3.097				

Curve-fitting analyses of the EXAFS data were performed for reference materials. The results for the multiple shell fitting are shown in **Error! Reference source not found.** and **Table 5.6**.

Table 5.6. *Bond distances (R), coordination numbers (N), Debye-Waller factors ($2\sigma^2$) for vanadium containing reference materials (AFAC =0.73).*

Sample	shell	N	R (Å)	$2\sigma^2$
V_2O_3	V-O	1	2.01	0.01
	V-V	1	2.68	0.012
	V-V	3	2.89	0.012
	V-O	3	3.89	0.01
	V-V	3	3.71	0.01
V_2O_5	V-O	1	1.62	0.014
	V-O	3.4	1.87	0.01
	V-O	1	2.64	0.035
	V-V	3	3.09	0.012
	V-V	2	3.6	0.018
VO_2	V-O	2	1.86	0.012
	V-O	2.4	2.02	0.013
	V-V	1	3.11	0.015
	V-V	3	3.5	0.017
$VOSO_4$	V-O	1	1.6	0.008
	V-O	4	2.01	0.007
	V-O	1	2.15	0.011
	V-O	2	3.42	0.021

Bond distances errors are ± 0.01 Å. Errors on $2\sigma^2$ are 10-20%.

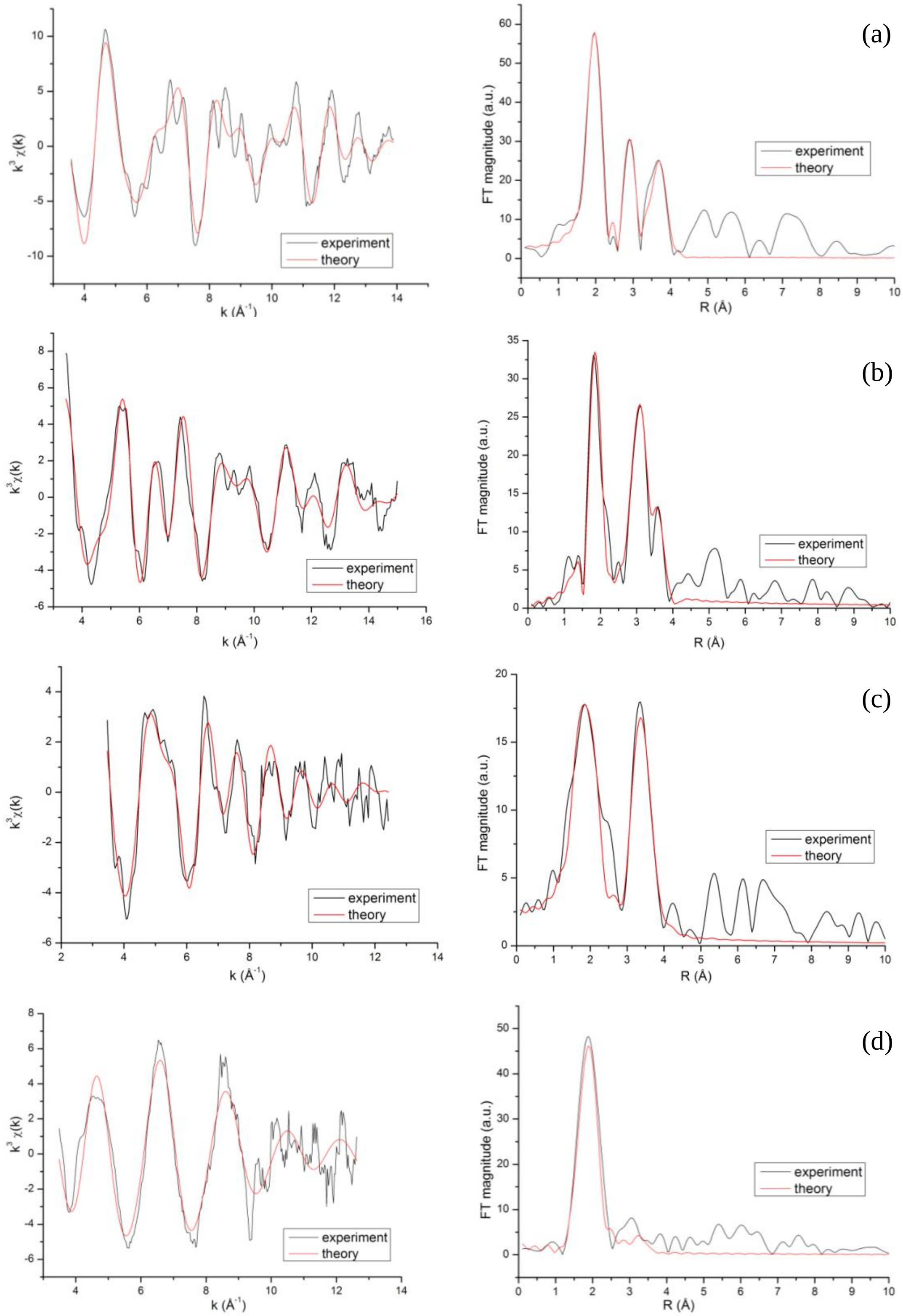

Figure 5.9. *Fits for V K-edge EXAFS data analysed in k-space (k*^{3}*-weighted and background subtracted) and associated Fourier transforms for the: (a) multiple shell fit of* V_2O_3*, (b)* V_2O_5*, (c)* VO_2*, and (d)* $VOSO_4$*.*

Figure 5.10 displays the normalized V K-edge XANES spectra for five catalysts measured at RT. The XANES spectra of all samples closely resemble $VOSO_4$. The intense pre-edge peak due to the 1*s* → 3*d* transition indicates tetrahedral coordination of the vanadium oxide species. Positions of pre-edge and absorption edge features are summarized in **Table 5.7**. The higher absorption edge intensity of sample-1 and -6 may have arisen from mixing of tetrahedral and octahedral vanadium oxide species. The Fourier transforms of a normalized k^3 weighted EXAFS spectra (without phase-shift correction), are displayed in **Figure 5.11**, in which the presence of the neighbouring oxygen atoms (V-O) at ca. 1.5 Å for sample-1 and -6, and ca.1.6 Å for sample-3, -4 and -5 can be seen. This suggests that vanadium ions are highly dispersed in the catalyst. The first peak for sample-3, -4, and -5 is much sharper than for sample-1 and -6 due to mixing of 4- and 6-coordinated ions. This observation is consistent with the XANES. Curve fitting of the EXAFS spectra were not performed due to poor data quality.

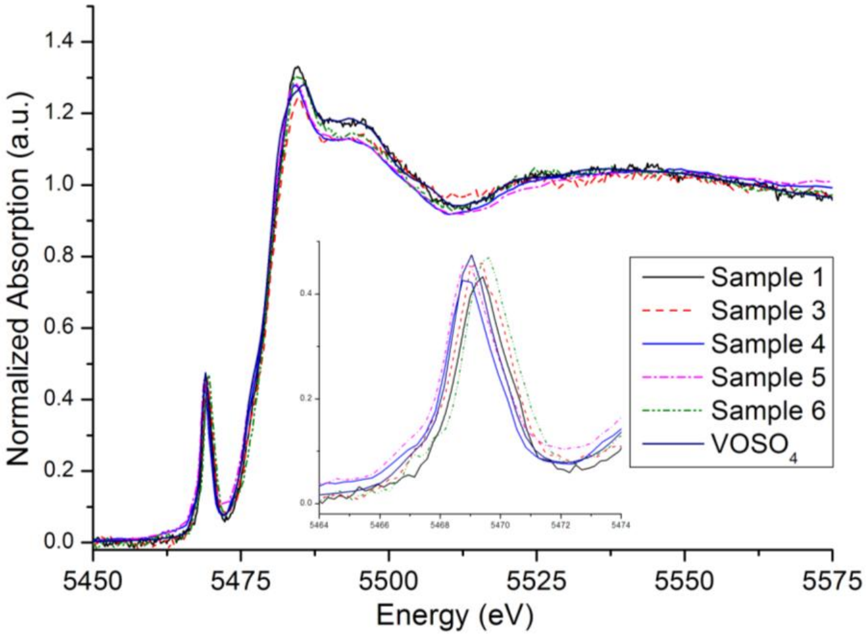

Figure 5.10. *Comparison of the V K-edge XANES of five vanadium containing ZSM-5 samples collected at RT.*

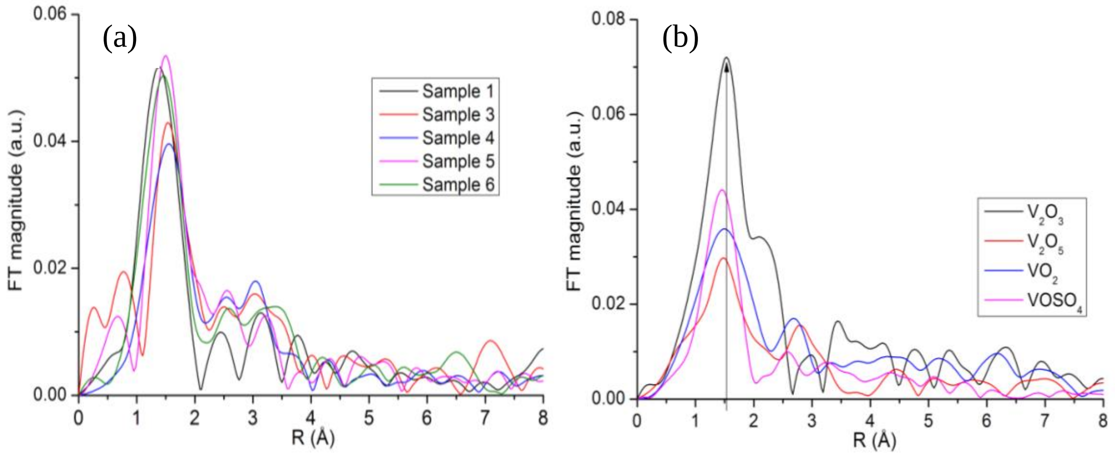

Figure 5.11. *Comparison of the V K-edge k^1 weighted Fourier transform not phase-shift corrected and measured at RT: (a) five vanadium containing ZSM-5 samples, (b) reference materials.*

Table 5.7. *Energy positions of spectral features in the V K-edge XANES spectra of vanadium containing ZSM-5 samples at RT.*

Compound	*Pre-edge position (eV)*	*Δ* E (eV)	*Pre-edge intensity*	*White line position (eV)*	*Δ* E (eV)	*White line intensity (eV)*
Sample 1	5469.3	4.3	0.43	5484.5	19.5	1.32
Sample 3	5469.2	4.2	0.46	5484.8	19.8	1.24
Sample 4	5468.9	3.9	0.42	5484.1	19.1	1.28
Sample 5	5468.9	3.9	0.47	5484.1	19.1	1.29
Sample 6	5469.5	4.5	0.47	5484.7	19.7	1.30

Errors in pre-edge and white line intensity are ± 0.1 eV. Errors in WLI are ± 5%.

Only three samples were calcined during *in situ* V K-edge XAS measurements due to time constraints. XANES spectra plotted in **Figure 5.12** depict samples calcined at 300°C for 30 min. The shift of the pre-edge peaks and the absorption edge to higher energy in sample-1, -3 and -6 (**Table 5.8**) indicates that V(IV) was oxidized to V(V) after calcination.

Similar higher absorption edge shift in sample 1 and 3 in the XANES region have been observed by Oldroyd et al.[44] and Anpo et al.[45] whose investigation revealed that the V(V) centre has an extra link V-O-Si created by vanadium with a short (1.55 Å) vanadyl bond and three longer V-O bond distances (1.77 Å) from V-O-Si linkages to the MCM-41 lattice. The larger absorption energy shift in sample-3 can be due to larger vanadium substitution in the lattice. This can also be caused by the post-synthesis dealumination in which vacancies created in the lattice were essentially filled with vanadium ions. In addition, the shift of the main edge to higher energies in XANES for sample-6 is caused by the partial oxidation of V(IV) to V(V), and the mixing of octahedrally coordinated VO_6 groups but the V(V) ions sit primarily inside the framework and are not necessary part of the lattice. The low intensity pre-edge peak for sample-1 can be caused by the dominating presence of octahedral VO_6 groups. **Figure 5.13** depicts a stacked plot of V K-edge XANES spectra during the *in situ* calcination.

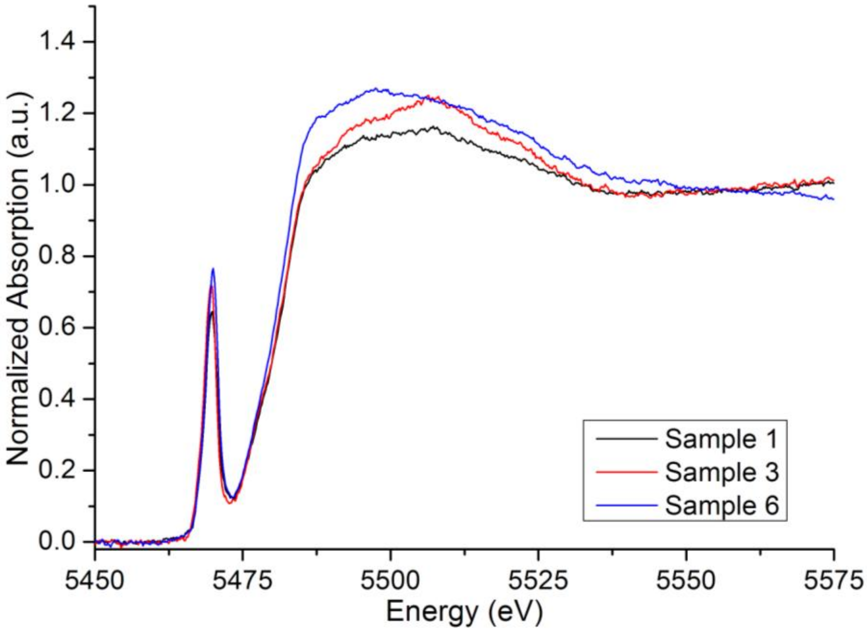

Figure 5.12. *Comparison of the V K-edge XANES of three vanadium containing ZSM-5 samples collected at 300°C.*

Table 5.8. *Energy positions of spectral features in the V K-edge XANES spectra of vanadium containing ZSM-5 samples at 300°C.*

Compound	*Pre-edge position (eV)*	*Δ* E (eV)	*Pre-edge intensity*	*White line position (eV)*	*Δ* E (eV)	*White line intensity (eV)*
Sample 1	5469.8	4.8	0.64	5506.7	41.7	1.15
Sample 3	5469.7	4.7	0.71	5507	42	1.23
Sample 6	5470	5.0	0.77	5497.7	32.7	1.27

Errors in pre-edge and white line intensity are ± 0.1 eV.

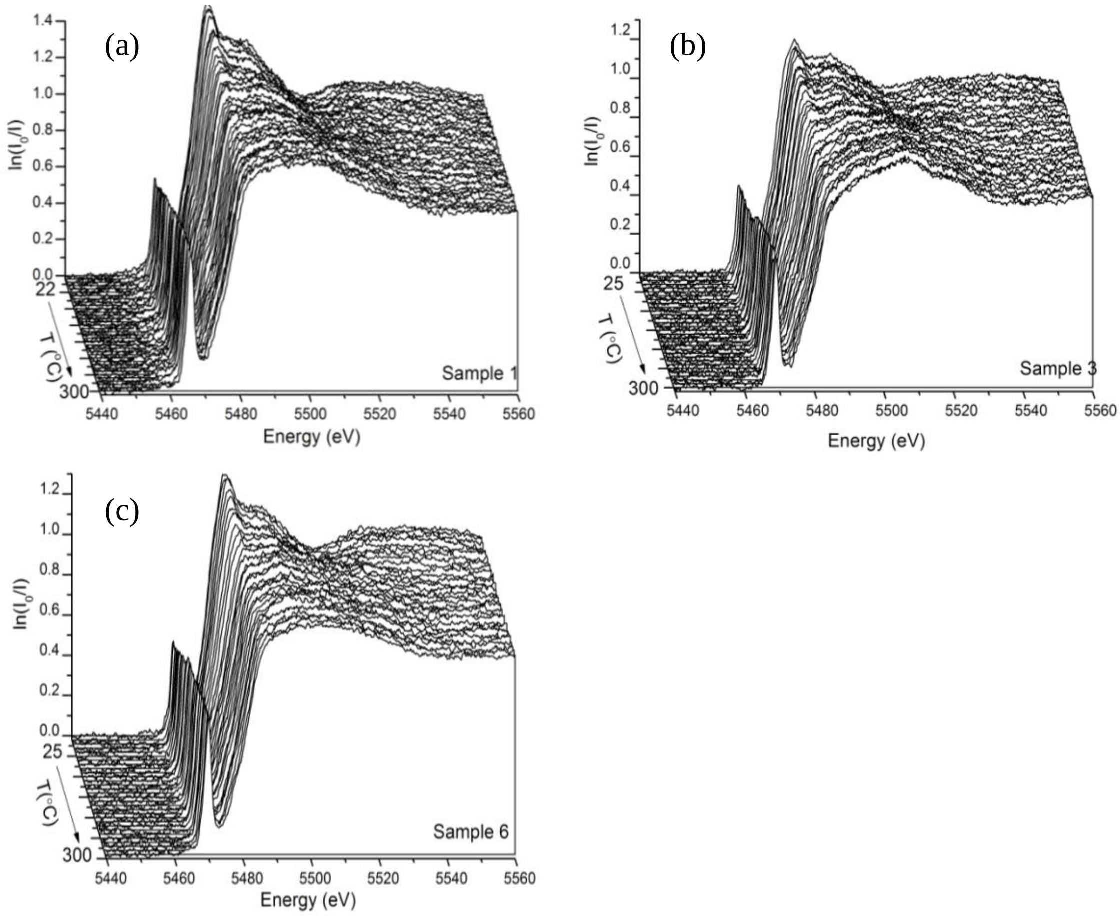

Figure 5.13. *Stacked plot of V K-edge XANES spectra , during in situ calcinations in air from RT to 300°C, (a) sample-1, (b) sample-3 and (c) sample-6.*

To estimate the amount of known species within the as-prepared samples, linear combination fits (LCF) to XANES data were performed. The LCF results are shown in **Table 5.9** and fits in **Figure 5.14**.

Table 5.9. *Linear combination fit of room temperature XANES data for sample-1 to -6, performed in the range -20 to 50 eV, errors on each component are ± 5%.*

Sample	*T (°C)*	*V_2O_3 (%)*	*V_2O_5 (%)*	*VO_2 (%)*	*$VOSO_4$ (%)*
1	25	0.05	0	0	0.95
3	25	0	0.15	0	0.85
4	25	0	0	0	1
5	25	0.07	0	0	0.93
6	25	0	0	0	1

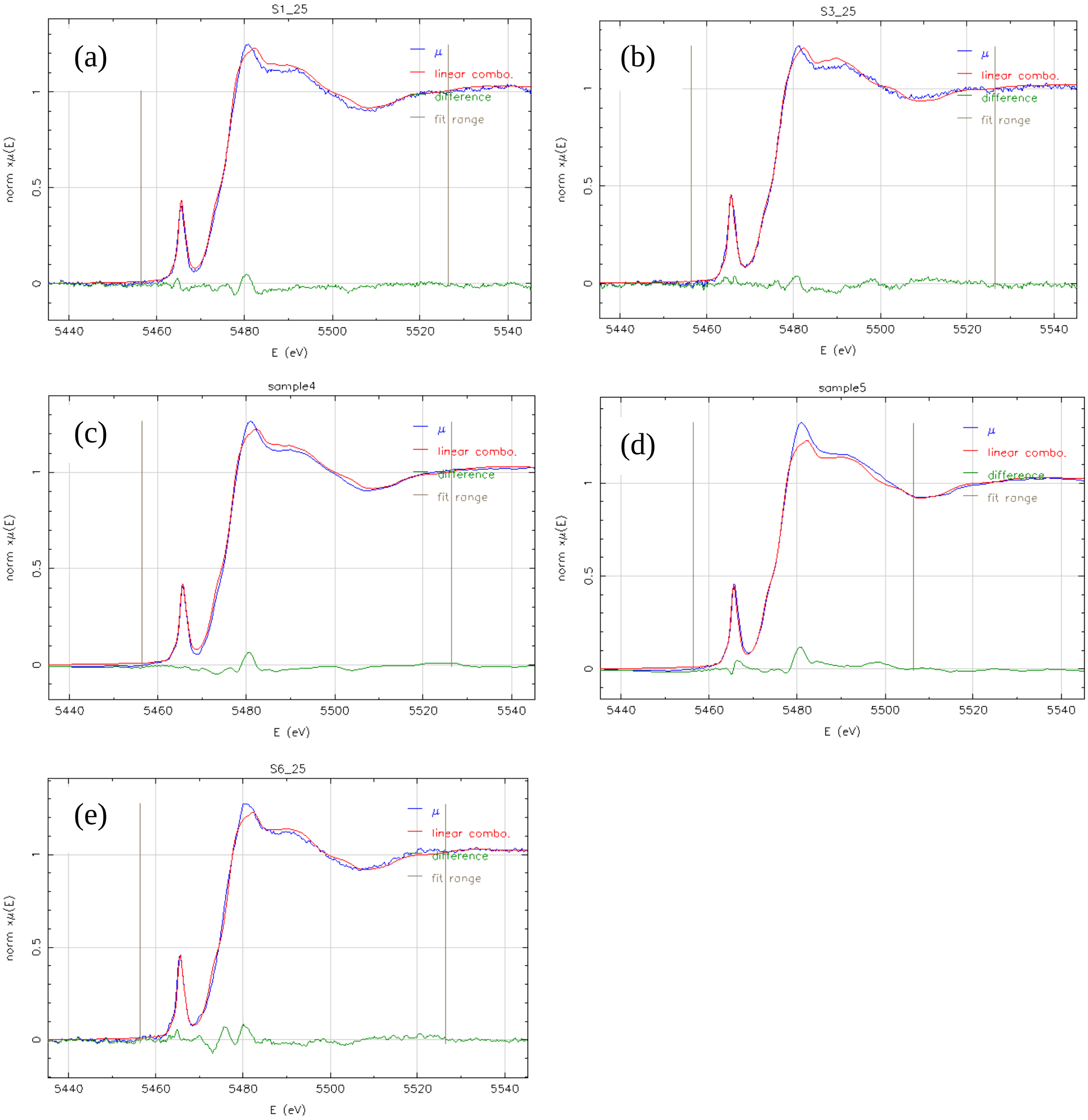

Figure 5.14. *Linear combination fits for RT scans; (a) sample-1, (b) sample-3, (c) sample-4, (d) sample-5, and (e) sample-6.*

In this case, LCF is not an ideal technique, because vanadium has a very rich chemistry, and the sensitivity of LCF is not adequate (large errors). High resolution XAS measurements are required in order to understand the real changes in the system, and ideally these experiments should be repeated.

5.4.4 *Raman spectroscopy of V-ZSM-5 samples*

The frequencies of V–O vibrations for reported Raman spectra of vanadium oxides[46] can be divided into 3 categories:

- 800cm^{-1} – the short V-O bonds are associated with terminal V=O bonds.
- 600–800 cm^{-1} – the V-O bonds of intermediate length, typical bridging V–O bonds.
- Below 600 cm^{-1} – lattice modes and the V–O bonds longer than 1.9 Å; the assignment of Raman bands in this region is associated with large inaccuracies.

Among these vibrations, critical structural information, pertaining to geometries and bond distances can be obtained from the analyses of V–O stretching features.

Raman spectrum of reference materials were collected at a wavelength of 514 nm. The V_2O_5 is well studied by Raman spectroscopy[47]. The assigned stretching frequencies are shown in the **Figure 5.15**. The structure of V_2O_5 contains chains of highly distorted VO_6 octahedra with one short apical V-O bond at 1.58Å, an opposing very long V-O bond at 2.78Å, and four bridging V-O bonds lying roughly in a plane at 1.78, 1.88(x2), and 2.02Å. The vanadium-oxygen bond lengths[48] and corresponding Raman stretching frequencies[47] for the compound V_2O_5 are listed in **Table 5.10.** Raman spectra for the remaining reference compounds are shown in **Figure 5.16** for V_2O_3, **Figure 5.17** for $VOSO_4.3H_2O$, and **Figure 5.18** for VO_2.

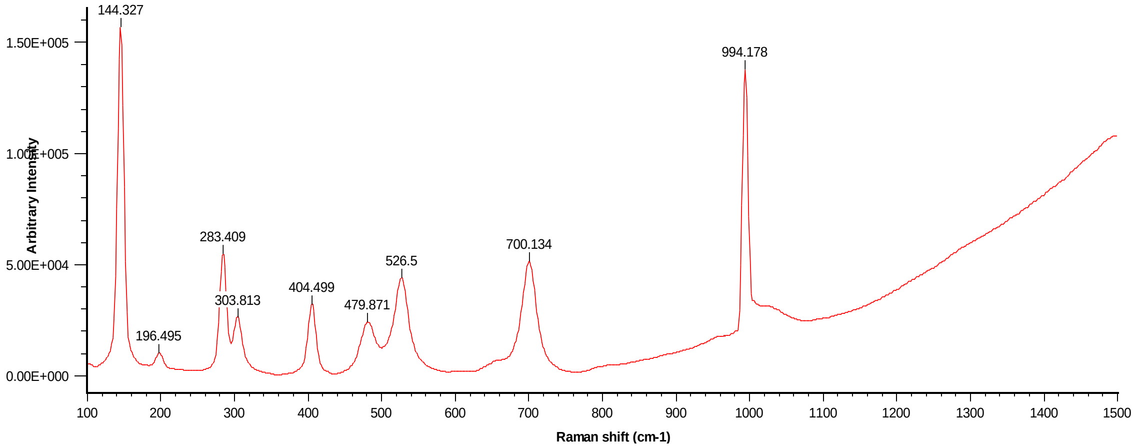

Figure 5.15. *Raman spectra of V_2O_5, collected at 514 nm.*

Table 5.10. *Bond lengths and observed stretching frequencies for V-O bonds for octahedrally coordinated V_2O_5*, wavelength *514 nm*[47].

Material	R (Å)	ν (cm^{-1})
V_2O_5	1.58	994
	1.78	701
	1.88	
	2.02	481
	2.78	104

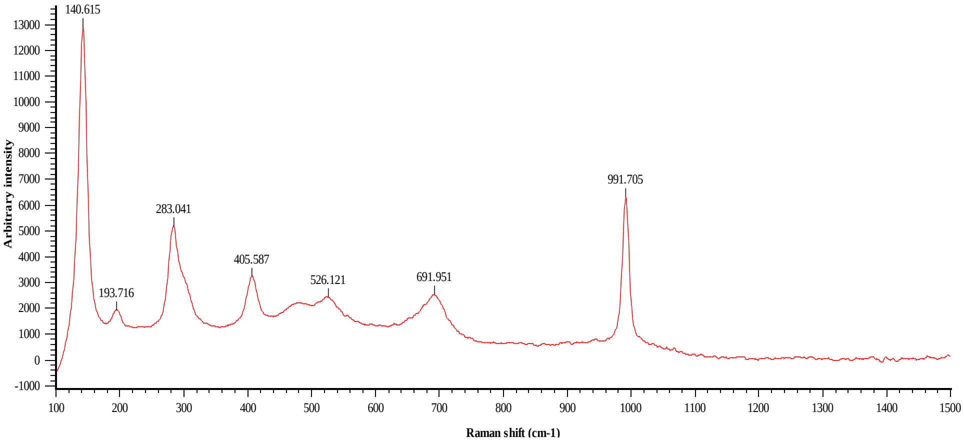

Figure 5.16. *Raman spectra of V_2O_3.*

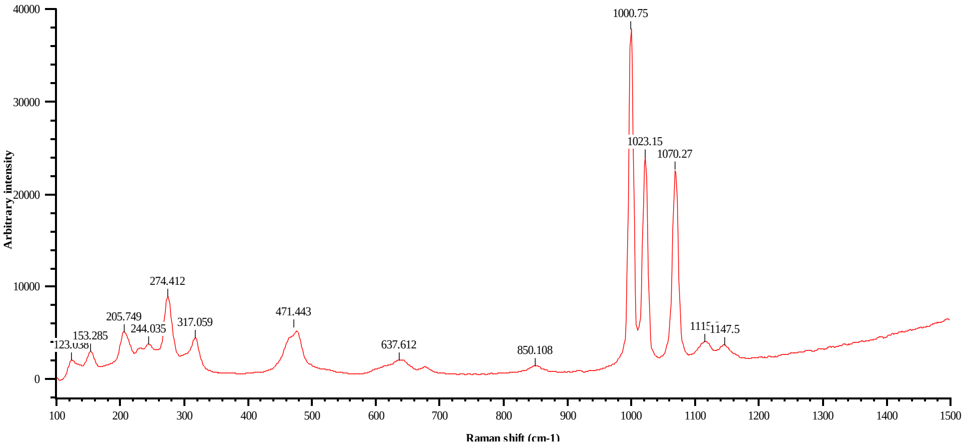

Figure 5.17. *Raman spectra of $VOSO_4.3H_2O$.*

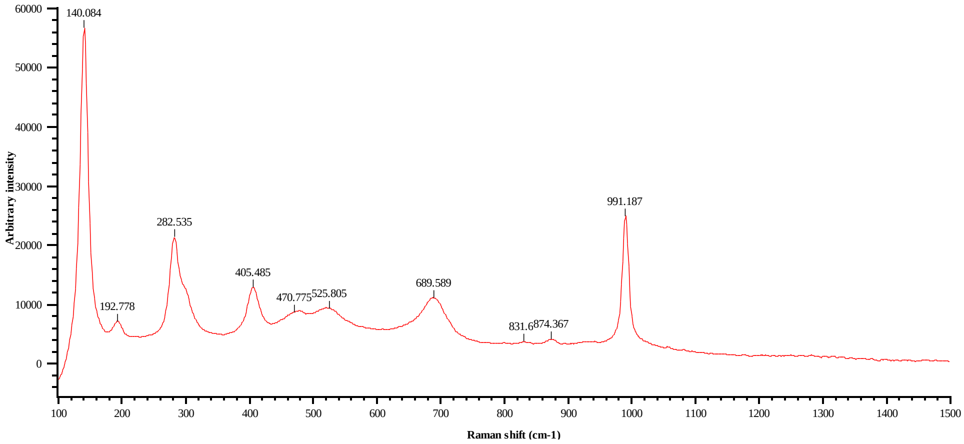

Figure 5.18. *Raman spectra of* VO_2.

Both vanadium and non-vanadium loaded samples were probed using the 514 nm, and 325 nm wavelength He-Cd laser but only 325 nm was able to provide useful information. The peaks at the 514 nm wavelength were poorly resolved, and shorter wavelength was chosen as a proffered option. A stacked plot of the Raman spectra for the vanadium-free zeolite samples is shown in **Figure 5.19**. The observed Raman stretching frequencies correlate with the literature reports for ZSM-5[49]. The frequency of the (T-0-T) bonds below 600 cm^{-1} are indicative of the ring systems present in the zeolite frameworks, and the stretching frequency of the ZSM-5 framework[50]. The large peak centred at 380 cm^{-1} is due to five-membered rings in the framework, and is highly sensitive to the degree of crystallinity.

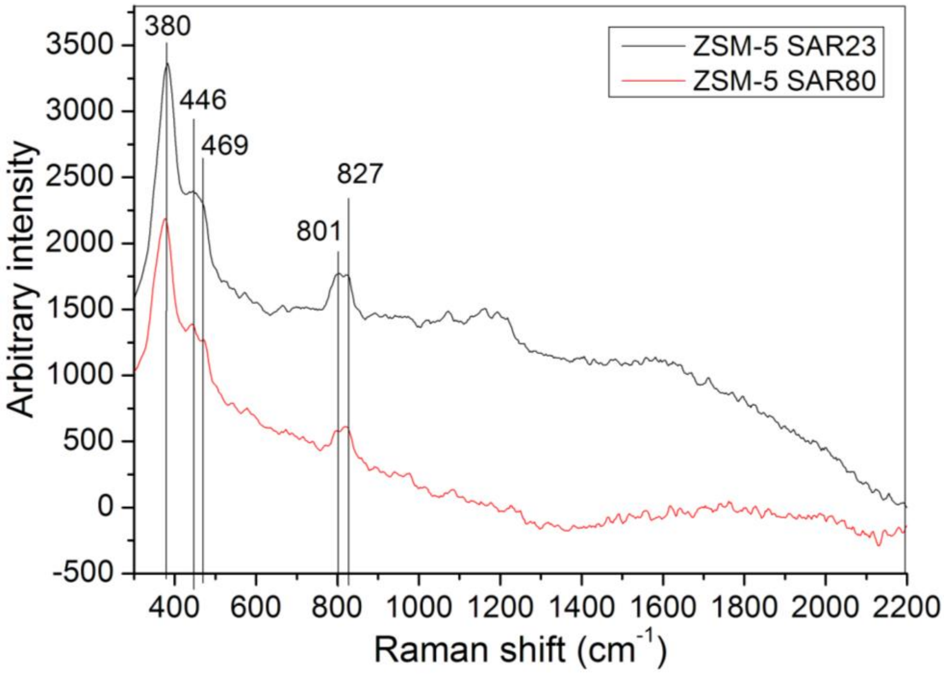

Figure 5.19. *Raman spectra of H-ZSM-5 SAR23, collected at 514 nm.*

Figure 5.20 displays stacked plot of the Raman spectra of as-prepared vanadium samples, **Figure 5.21**; of calcined vanadium zeolites, and **Figure 5.22**; of samples in as-prepared and calcined forms. The Raman bands of as-prepared vanadium zeolite samples (1, 3, 4, 5, and 6) are similar to those of $VOSO_4$. The band centred around 1044 cm^{-1} in both the calcined and as-prepared samples corresponds to the stretching frequency of a terminal V=O group bonded to silicon ions inside the framework of ZSM-5; this is similar to monomeric vanadyl species bonded to a SiO_2 support at 1042 cm^{-1}[51] and vanadium oxytrihalides[52]. The existence of supported vanadium oxide as isolated species alongside the vanadium framework gives rise to the V=O stretching mode of 961 cm^{-1}. The shift in band position can be due to the surface interaction between vanadium oxide species and the ZSM-5 framework.

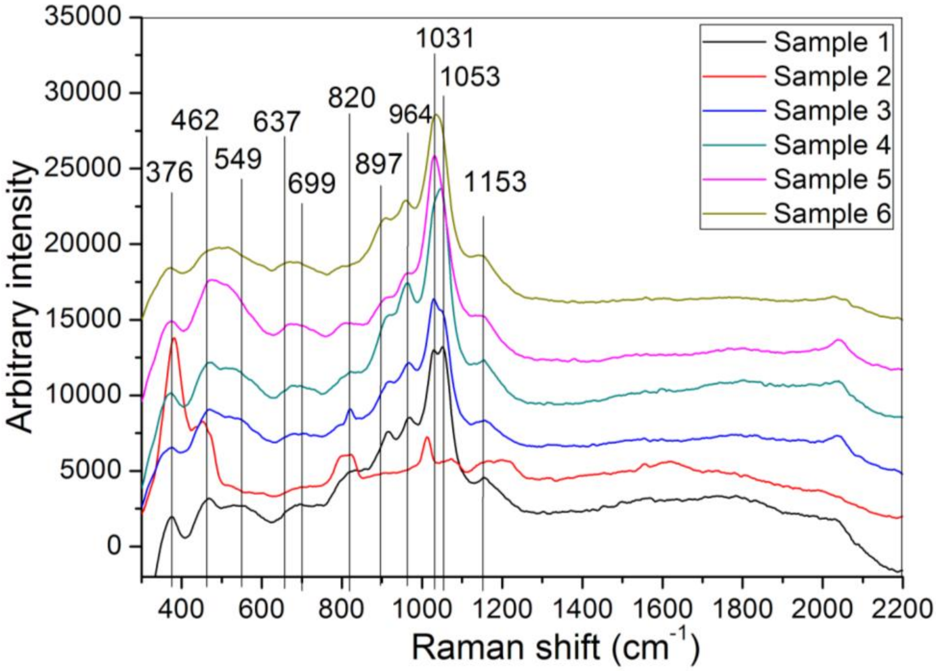

Figure 5.20. *Stacked plot of Raman spectra of as-prepared vanadium containing ZSM-5 samples.*

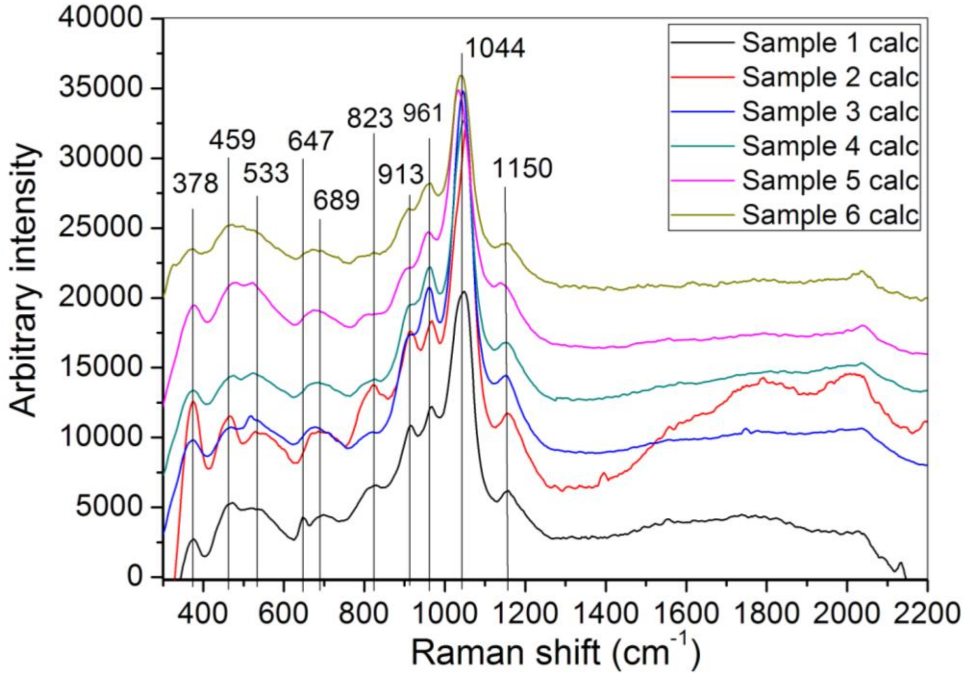

Figure 5.21. *Stacked plot of Raman spectra of calcined vanadium containing ZSM-5 samples.*

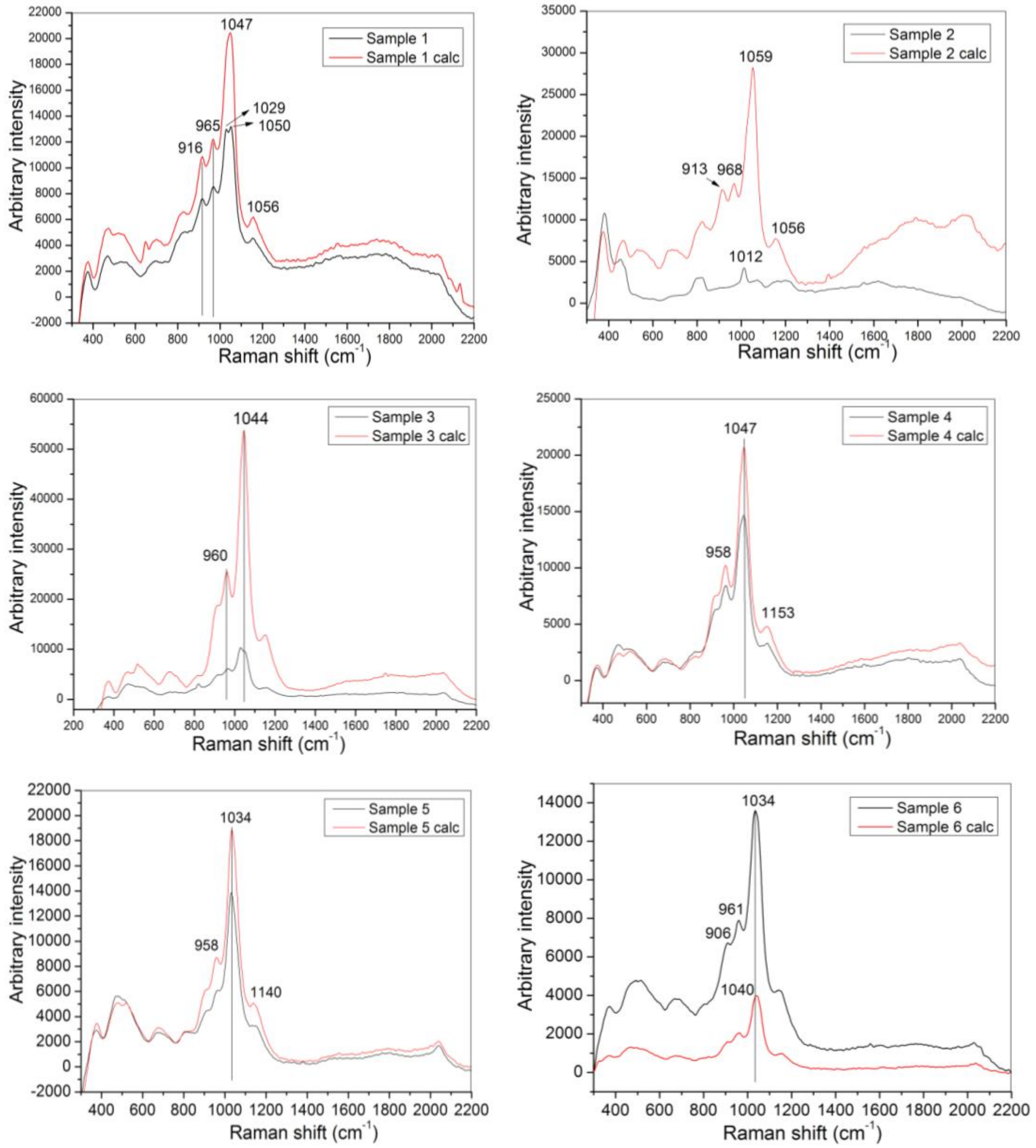

Figure 5.22. *A Raman spectrum plots of specific samples in as-prepared and calcined form.*

5.5 Summary and Conclusion

The combined use of XAS and Raman spectroscopy has allowed examining of post-synthesis treated vanadium ZSM-5. In as-prepared samples, the majority of V(IV) ions exhibit a strongly distorted square-pyramidal structure similar to $VOSO_4$. Upon calcinations, the majority of V(IV) is converted to V(V) with a non-hydroxylated pyramidal structure, whereas the remaining V(IV) adopts a distorted tetrahedral structure with hydroxylated pyramidal $(SiO)_2(HO)V{=}O$. Sample 3 has the largest number of $(SiO)_3V{=}O$ in the lattice in comparison to the other two samples studied by XAS and displays a very good catalytic activity. Further detailed *in situ* XAS studies are needed to fully understand the nature of the vanadium species.

On the other hand, the Raman spectroscopy failed to provide information about the vanadium species in activated stage, which could be caused by water interaction with vanadium ions, and by the presence of both V(IV) and V(V) species inside the zeolites. The Raman spectra of as-prepared and calcined samples are very similar, and thus cannot provide information about the active sites.

References

[1] a) W. M. H. Sachtler and Z. Zhang in *Zeolite-supported transition metal catalysts, Vol. 39* Eds.: D. D. Eley and H. Pines), Academic Press, Inc., San Diego, **1993**; b) M. E. Davis, *Acc. Chem. Res.* **1993**, *26*, 111-115.

[2] B. I. Whittington and J. R. Anderson, *Journal of Physical Chemistry* **1991**, *95*, 3306-3310.

[3] K. Habersberger, P. Jíru, Z. Tvaruzková, G. Centi and F. Trifirò, *Reaction Kinetics and Catalysis Letters* **1989**, *39*, 95-100.

[4] A. Bhaumik, R. Kumar and P. Ratnasamy in *Chemoselective oxidation of organic compounds having two or more functional groups, Vol. Volume 84* Eds.: H. G. K. H. P. J. Weitkamp and W. Hölderich), Elsevier, **1994**, pp. 1883-1888.

[5] K. R. Reddy, A. V. Ramaswamy and P. Ratnasamy, *Journal of the Chemical Society, Chemical Communications* **1992**, 1613-1615.

[6] a) M. Wark, A. Brückner, T. Liese and W. Grünert, *Journal of Catalysis* **1998**, *175*, 48-61; b) M. Inomata, A. Miyamoto and Y. Murakami, *Journal of Catalysis* **1980**, *62*, 140-148; c) R. C. Adams, L. Xu, K. Moller, T. Bein and W. N. Delgass, *Catalysis Today* **1997**, *33*, 263-278.

[7] T. L. Stemmler, T. M. Barnhart, J. E. Penner-Hahn, C. E. Tucker, P. Knochel, M. Boehme and G. Frenking, *Journal of the American Chemical Society* **1995**, *117*, 12489-12497.

[8] P. J. Gellings in *Oxidation by catalysts containing vanadium, Vol. 7* Eds.: G. C. Bond and G. Webb), The Royal Society of Chemistry, **1985**, pp. 105-124.

[9] S. P. G. Centi, F. Trifiro, A. Aboukais, C. F. Aissi, M. Guelton, *Journal of Physical Chemistry* **1992**, *96*, 2617-2629.

[10] a) M. Petras and B. Wichterlova, *Journal of Molecular Catalysis* **1992**, *96*, 1805-1809; b) A. Magneli and B. M. Oughton, *Acta Chemica Scandinavica* **1951**, 581-584; c) A. V. Kucherov and A. A. Slinkin, *Zeolites* **1987**, *7*, 28-42; d) T. Sen, V. Ramaswamy, S. Ganapathy, P. R. Rajamohanan and S. Sivasanker, *Journal of Physical Chemistry* **1996**, *100*, 3309-3817.

[11] Kornatowski, B. Wichterlová, M. Rozwadowski and W. H. Baur, *10th International Zeolite Conference* (Garmisch-Partenkirchen, Germany) **1994**.

[12] T. C. Sen, M.; Sivasanker, *Journal of the Chemical Society, Chemical Communications* **1995**, *207-208*.

[13] N. E. Das, H.; Hu, H.; Wachs, I. E.; Waizer, J. F.; Feher, F., *Journal of Physical Chemistry* **1993**, *97*, 8240-8243.

[14] H. van Bekkum, E. M. Flanigen, P. A. Jacobs and J. C. Jansen, *Introduction to zeolite science and practice*, Elsevier, **2001**, p.

[15] N. Y. Chen, W. W. Kaeding and F. G. Dwyer, *Journal of Catalysis* **1979**, *101*, 6783-6784.

[16] W. W. Kaeding, C. Chu, L. B. Young, B. Weinstein and S. A. Butter, *Journal of Catalysis* **1981**, *67*, 159-174.

[17] F. Algarra, A. Corma, H. Garcia and J. Primo, *Applied Catalysis A: General* **1995**, *128*, 119-126.

[18] a) J. C. Nunan, J. Cronin and J. Cunningham, *Journal of Catalysis* **1984**, *87*, 77-85; b) V. S. Nayak and V. R. Choudhary, *Applied Catalysis* **1982**, *4*, 333-352.

[19] a) R. W. Weber, K. P. Moller, M. Unger and C. T. O'Connor, *Microporous and Mesoporous Materials* **1998**, *23*, 179-187; b) D. V. Vu, M. Miyamoto, N. Nishiyama, Y. Egashira and K. Ueyama, *Journal of Catalysis* **2006**, *243*, 389-394.

[20] A. C. Wei and K. J. Chao, *Chinese Chemical Society* **2000**.

[21] R. J. Argauer and G. R. Landolt in *Crystalline zeolite ZSM-5 and method of preparing the same*, *Vol. 3,702,886* (Ed. U. P. Office), Mobile Oil Corporation, USA, **1972**.

[22] J. Cejka, H. van Bekkum, A. Corma and F. Schuth, *Introduction to zeolite science and practice*, Elsevier, **2007**, p.

[23] a) C. Baerlocher, L. B. McCusker and D. H. Olson, *Atlas of Zeolite Framework Types, 6th edition*, Elsevier, Amsterdam, **2007**, p; b) L. B. McCusker, F. Liebau and G. Engelhardt, *Pure and Applied Chemistry* **2001**, *73*, 381-394.

[24] R. M. Barrer, *Hydrothermal Chemistry of Zeolites*, Academic Press, **1982**, p.

[25] R. Xu, W. Pang, J. Yu, Q. Huo and J. Chen, *Chemistry of Zeolites and Related Porous Materials: Synthesis and Structure*, Wiley, **2007**, p.

[26] D. H. Olson, G. T. Kokotailo, S. L. Lawton and W. M. Meier, *Journal of Physical Chemistry* **1981**, *85*, 2238-2243.

[27] in *International Zeolite Association*, *Vol.* www.iza-online.org.

[28] A. Coelho in *Topas-Academic Version 4.1*, *Vol.* Brisbane, **2007**.

[29] a) B. Ravel and M. Newville, *Journal of Synchrotron Radiation* **2004**; b) B. Ravel and M. Newville, *Physica Scripta* **2005**, *T115*, 1007-1010; c) B. Ravel and M. Newville, *Journal of Synchrotron Radiation* **2005**, *12*, 537-541.

[30] N. Binsted in *EXCURV98: CCLRC, Vol.* Daresbury Laboratory computer program, **1998**.

[31] in *Origin 8.5, Vol.* OriginLab, Northampton, **2011**.

[32] G. T. Kokotailo, S. L. Lawton, D. H. Olson and W. M. Meier, *Nature* **1978**, *272*, 437-438.

[33] D. H. Olson, Kokotailo, G.T., Lawton, S.L. and Meier, W.M., *Journal of Physical Chemistry* **1981**, *85*, 2238-2243.

[34] T. Tanaka, H. Yamashita, R. Tsuchitani, T. Funabiki and S. Yoshida, *Journal of the Chemical Society, Faraday Transactions* **1988**, *1*, 2987-2999.

[35] J. Wong, F. W. Lytle, R. P. Messmer and D. H. Maylotte, *Physical Review B* **1984**, *30*.

[36] H. F. Bachmann, F. R. Ahmed and W. H. Barnes, *Zeitschrift fur Kristallographie* **1961**, 110-131.

[37] K. H. Hallmeier, R. Szargan, G. Werner, R. Meier and M. A. Sheromov, *Spectrochimica Acta Part A: Molecular Spectroscopy* **1986**, *42*, 841-844.

[38] C. Mande and V. B. Sapre, *Advances in X-ray Spectroscopy*, Pergamon, New York, **1983**, p.

[39] H. G. A. Bachmann, F.R.;Barnes, W.H. in *Vanadium oxid, Vol.* www.cds.dl.ac.uk, **1961**.

[40] G. Andersson in *Studies on vanadium oxides, Vol.* www.cds.dl.ac.uk, **1956**.

[41] F. R. G. Theobald, J., *Acta Cryst. B* **1973**, *29*, 2732-2736.

[42] R. E. Newnham and Y. M. de Haan in *Refinement of the Al2 O3-alpha, Ti2 O3, V2 O3 and Cr2 O3 structures., Vol.* www.cds.dl.ac.uk, **1962**.

[43] F. A. Cotton, G. Wilkinson, C. A. Murillo and M. Bochmann, *Advanced Inorganic Chemistry*, New York, **1999**, p.

[44] R. D. Oldroyd, G. Sankar, J. Meurig Thomas, M. Hunnius and W. F. Maier, *Journal of the Chemical Society, Faraday Transactions* **1998**, *94*, 3177-3182.

[45] M. Anpo, H. Yamashita, M. Matsuoka, D.-R. Park, Y.-G. Shul and S.-E. Park, *Journal of Industrial and Engineering Chemistry* **2000**, *6*, 59-71.

[46] N. Kausar, R. Howe and M. Skyllas-Kazacos, *Journal of Applied Electrochemistry* **2001**, *31*, 1327-1332.

[47] F. D. Hardcastle and I. E. Wachs, *Journal of Physical Chemistry* **1991**, *95*, 5031-5041.

[48] R. Enjalbert and J. Galy, *Acta Cryst.* **1986**, *42*, 1467-1469.

[49] S. Mintova, B. Mihailova, V. Valtchev and L. Konstantinov, *Journal of the Chemical Society, Chemical Communications* **1994**, 1791-1792.

[50] P. K. Dutta, K. M. Rao and J. Y. Park, *The Journal of physical chemistry* **1991**, *95*, 6654-6656.

[51] S. T. Oyama, G. T. Went, K. B. Lewis, A. T. Bell and G. A. Somorjai, *The Journal of physical chemistry* **1989**, *93*, 6786-6790.

[52] a) F. A. Miller and K. B. Baer, *Spectrochimica Acta* **1961**, *17*, 112-112-; b) F. A. Miller and L. R. Cousins, *Journal of Chemical Physics* **1956**, *26*, 329-332.

Chapter 6 Study of platinum impregnated zeolite catalysts by XAS and TEM.

6.1 Chapter overview

In this chapter are discussed the experiments and results of an investigation carried out by XAS, and TEM on platinum dispersed in a matrix of ferrierite and beta zeolite. The local structure of platinum was determined, and information about the size and location in the zeolite matrix was derived.

The formation of platinum clusters from an oxidized precursor were investigated in an *in situ* XAS cell under the flow of hydrogen gas, and the changes in the local environment of platinum during these treatments were monitored.

The size of the platinum clusters was determined by TEM. The information about the location in the zeolite pores was also investigated by HRPD but the result was not satisfying and therefore not discussed here.

6.2Introduction

Metal catalysts are used in a wide range of industrial applications which include some of the most important catalytic reactions in petrochemical refining[1], car exhaust converters[2], hydrogenation of carbon monoxide[3] and fats[4], fuel cells[5] and many other processes. Utilizing only pure metal is always expensive, and therefore it is more economically viable to use the metal in a highly dispersed form as particles on a surface of porous zeolitic supports. There, the metal can make up about 1 w% of the total catalytic material. The smaller the metal particles are, the larger the fractions of the metal atoms are exposed at surfaces where reactant molecules are available for catalysis. These supported metal catalysts can be prepared by impregnation of a porous support (beta zeolite) with an aqueous solution of a metal salt (H_2PtCl_6)[6], followed by heating in air (calcination) and reduction in hydrogen[7]. The resulting product consists of metal particles distributed over the surface of the support and in the pores. Supported metal particles are often non-uniform in size, and shape, and are too small to be characterized precisely which means they are still poorly understood. The support porous surfaces are also structurally non-uniform but can be characterized more precisely.

Zeolite-supported noble metal clusters are typically prepared by ion exchange followed by reduction[8]. The metals are introduced as cationic complexes, (for example by $[Pt(NH_3)_4]$ $(OH)_2$) and replace cations such as Na(I) in the zeolite. It is necessary to eliminate the complex from the metal ion (for example, NH_3 produced by thermal decomposition of NH_4^+ ions from $[Pt(NH_3)_4]$ $(OH)_2$ or amine complexes) by heating in O_2 because reduction of metal ions in the presence of evolving metal-free complexes leads to agglomeration of the metal to larger clusters which are sometimes too large to fit into the cage and can either break and/or migrate outside the cage. Due to this, it is very difficult to achieve the highest metal dispersion, and suitable treatments are often needed to minimize migration and sintering, and produce a uniform size distribution[9].

Noble metals in zeolites are easily reduced by H_2. Direct reduction of noble metal cations by H_2 at high temperatures can lead to the formation of neutral metal hydrides, which are mobile, and can cause metal agglomeration and low metal dispersion. Water interactions can also cause damage to high metal dispersion. Despite all these difficulties, proper selection of temperature and duration of calcination and reduction can lead to the formation of well dispersed metal particles in the zeolite material[10].

Zeolite supported platinum catalysts are a significant group of catalysts with a broad range of commercial applications[11]. The supported platinum clusters are structurally sensitive to reactive gases, and studies of their structure on different zeolite supports is extensively[12].

6.2.1 Zeolite support

Zeolite beta, discovered by Mobil Oil in 1967, was the first synthesized zeolite prepared by using an organic template and a very low aluminium content in comparison to natural zeolites[13]. The structure[14] is relatively open with 12-membered rings of diameters 7.5 - 8 Å and 12 - 13 Å (shown in **Figure 6.1**). The high degree of faulting and four known polymorphs[15] has long prevented full structural determination. The first structure determination was done by Treacy et. al.[15a], as an intergrowth of 2 polymorphs, polymorph A and polymorph B, in a 2:3 ratio. Polymorph C was first reported by Conradsson et al.[16] as pure germanate followed by silicogermanate reported by Corma et al.[17].

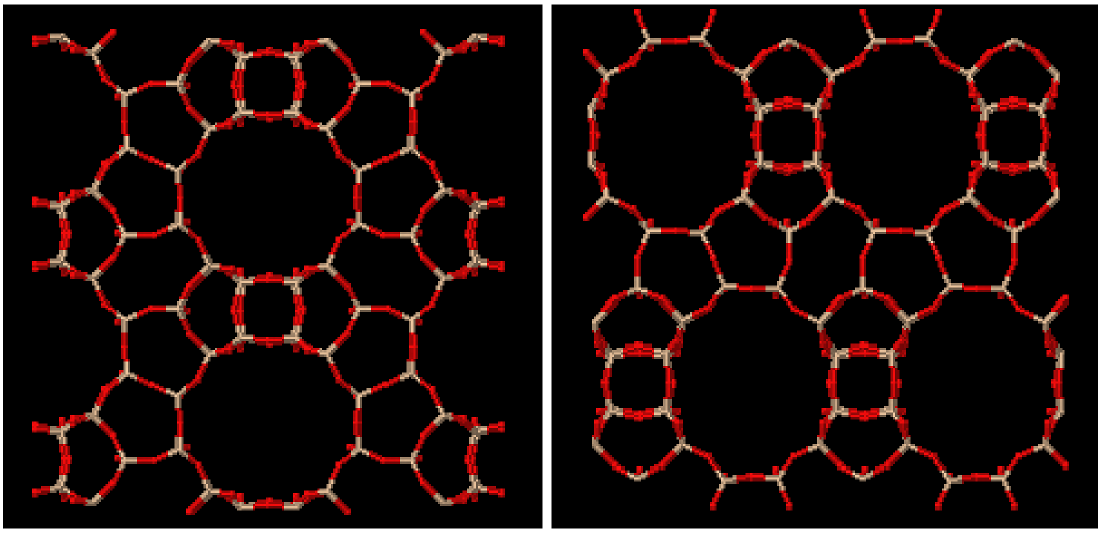

Figure 6.1. *Schematic representation of zeolite beta*[14b] *viewed along [010] (left) and [100] (right) direction.*

Beta zeolite is known for its high acidity and thermal stability compared to other synthesized zeolites which were shown to be very effective in various hydrocarbon conversion processes. Zeolite beta is used in processes such as cracking[18], hydrocracking[19], dewaxing[20] and dealkylation[21], and, as a sorbent for separations[22].

Zeolite ferrierite (FER[23]), first described and named by Graham[24], is a crystalline aluminosilicate containing 5-, 6-, 8-, and 10-membered rings[25] (displayed in **Figure 6.2**). The framework consists of two types of intersecting channels; 10-membered rings are placed along the [001] and 8-membered rings are parallel to the [010] direction. The 5-membered rings of TO_4 tetrahedra parallel to [001] are linked through complex chains. The pore sizes range from 5.4 × 4.2 Å for the 10-ring openings and for 4.8 × 3.5 Å for 8-ring openings[25b, 26]. Three types of non-framework cations occurring in natural forms of ferrierite[14b] are magnesium, potassium and sodium. The first synthetic form of ferrierite-Na,K was reported in 1977 by Cormier et al.[27].

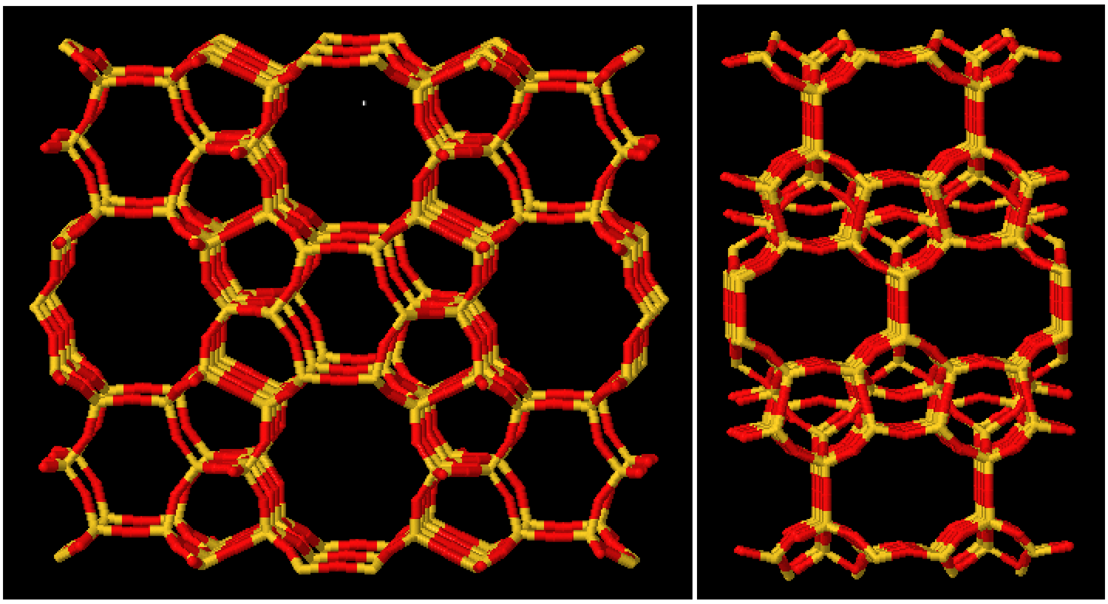

Figure 6.2. *Schematic representation of the zeolite ferrierite[14b] viewed along [001] (left) and [010] (right) direction.*

Low-silica ferrierite structures can be synthesized without the use of structure directing agents (SDA's). In contrast, the addition of an SDA is essential in synthesis of high-silica (Si/Al ratio > 5) ferrierite. High-silica ferrierites are also strongly hydrophobic and thermally stable. According to Hironaka et al.[28], using only pyridine as an SDA increases the hydrophobicity and structural stability of ferrierite. Therefore, the type of SDA used in the synthesis of ferrierite, strongly influences the hydrothermal stability and the hydrophobicity of H-FER. The versatility and high acidity of the zeolite has attracted a lot of attention from the petrochemical industry and hydrocarbon processing companies[29]. The H^+-exchanged form has been used in the isomerisation of xylenes[30], hydration of alkenes[31], cracking of n-alkanes[32], cracking of methanol[33], aromatization of alkanes[34], and other catalytic reactions.

6.2.2 Aim of the work

The aim of the work presented in this chapter was to derive information about the platinum dispersed in zeolite beta and ferrierite prepared by ion exchange. The primary objective was to determine the local structure of the platinum in as-prepared and active (reduced) form, and learn about the size and location in the zeolite lattice. To achieve this, the structures were probed by XAS, and TEM. Although, TEM was employed to provide information about morphology and size of the clusters inside the samples, XAS gave insights into structural arrangements at an atomistic level.

6.3Experimental section

6.3.1 Samples Preparation and Laboratory Characterization

The samples were prepared at Johnson Matthey Catalysts using zeolites beta, and ferrierite (SAR = 20), supplied by Zeolyst International. The impregnated samples were prepared by the incipient wetness method, and calcined in air to remove the residual components from the platinum complex. The primary aim was to achieve 1, 3, and 7 w% loading on zeolite beta, and 3 w% on ferrierite. The intended platinum concentration was confirmed by ICP. XRD measurements were collected over a 5 – 50 2θ range on a Bruker D4 diffractometer (Cu $K\alpha$) with 0.05^{o} step size and 5 sec counting time.

6.3.2 XAS Experiments

High Energy Resolution Fluorescence Detection X-Ray Absorption Near Edge Structure (HERFD-XANES) spectra of the Pt L_3 edge were collected at beamline ID-26 of the European Synchrotron Radiation Facility (ESRF, Grenoble, France) in a fluorescence setup with a Si(311) double crystal monochromator (DCM) providing an energy resolution of about 0.5 eV. The DCM was calibrated at the Pt/L_3 edge (11564 eV) by measuring an XAS spectrum for a 5 μm thick platinum foil. The incoming beam passed a Pd/Cr-coated collimating mirror, the DCM, and a Si-coated focusing mirror (to reject higher harmonics). HERFD-XAS spectra were recorded by setting the spectrometer to the maximum of the Pt $K\alpha_1$ fluorescence line. The storage ring was operated in 7/8-bunch mode at a beam current between 150 and 200 mA at 6 GeV electron energy.

In a typical XAS measurement, approximately 50-70 mg of a catalyst sample was ground and pressed into a pellet with a 13 mm diameter. The pellet was placed in a controlled environment cell (available at the ESRF) and oriented at 45° relative to the incident beam, which allowed *in-situ* EXAFS measurements at high temperatures to be taken. First, each sample was flushed in a flow of nitrogen for 10 min and then reduced at room temperature in a flow mixture of hydrogen and nitrogen (8 % H_2 in N_2). One sample (Pt/beta) was heated to 250 °C at a rate of 5 °C/min and exposed for 1 h to the flow mixture before being cooled to room temperature in flowing nitrogen.

6.3.3 Transmission Electron Microscopy (TEM)

TEM experiments were carried out to determine the size, shape and location of the dispersed particles. The samples were examined at the Johnson Matthey Technology Centre with a Tecnai F20 Transmission Electron Microscope using a 200 kV Voltage and a C_2 aperture at 30 and 50 µm. High Resolution Electron Microscopy (HREM) and High Angle Annular Dark Field (HAADF) methods were used in bright field imaging. Powder samples were embedded in resin and coated, microtomed, and placed on holey carbon coated Cu grids.

6.3.4 Data analysis

Laboratory XRD phase identification was done by comparison with standard XRD data sets [14a]. The initial model for ferrierite used in the Rietveld fit was in the orthorhombic *Immm* space group[13], with cell parameters: a = 18.868 Å, b = 14.082 Å, and c = 7.43

Å. The TOPAS-academic[35] software package was employed for Rietveld refinement using a modified Thompson-Cox-Hastings pseudo-Voigt peak shape. All graphs were prepared using the data analysis and plotting software Origin Pro 8 [36]. Background-subtraction, and normalization of XANES was performed using the XAS analysis software Athena[37].

6.4 Results and discussion

6.4.1 X-Ray Diffraction

The stacked XRD plots of the Pt/beta zeolite collected on the laboratory XRD machine are shown in **Figure 6.3**. The starting zeolite beta used for platinum impregnation is a mixture of polymorphs A and B. The intensity of the two largest peaks decreases with increased platinum loading, which suggests that the platinum is located inside the zeolite pores.

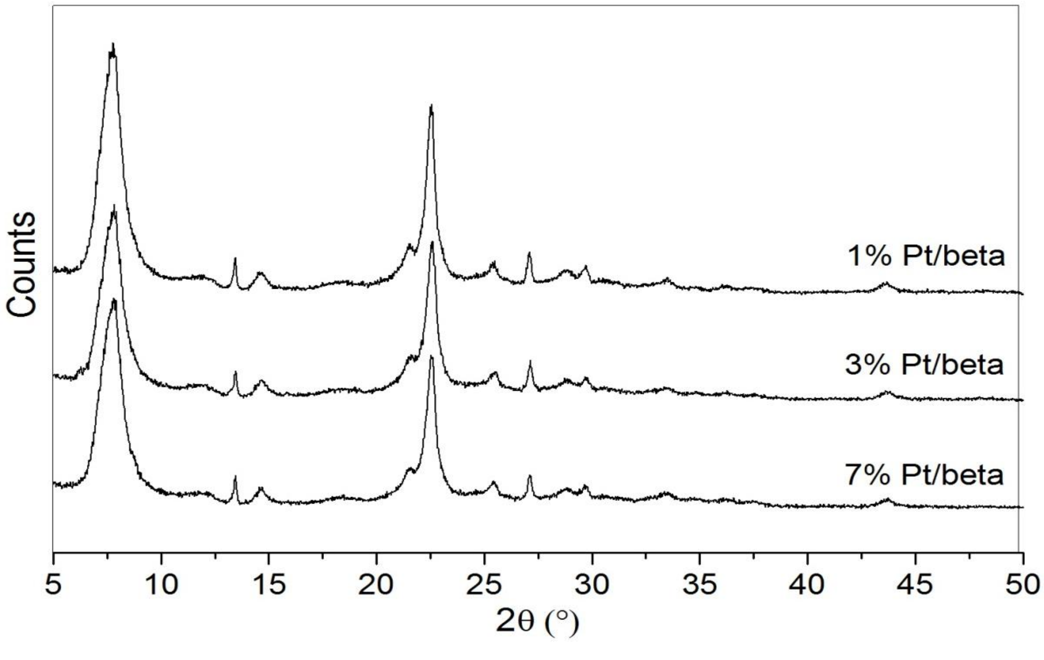

Figure 6.3. *XRD diagrams of the platinum impregnated on the zeolite beta.*

Figure 6.4 shows the XRD diagrams of parent ferrierite (SAR 20) and platinum FER samples. The intensity of the first reflection decreases upon loading of Pt, and no reflection coming from platinum oxide in as-prepared samples were detected, and ic mainly because of the very low Pt concentration.

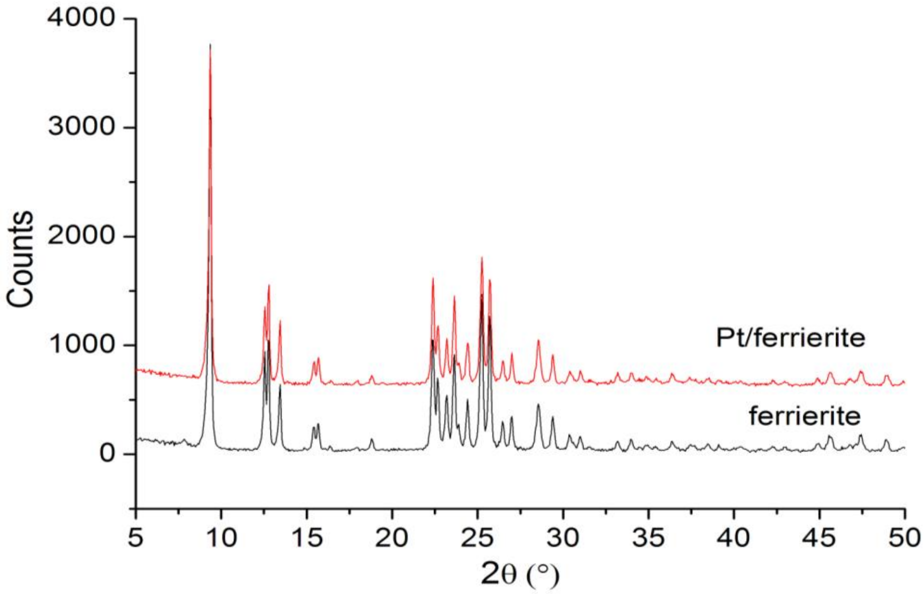

Figure 6.4. *XRD diagrams of the platinum impregnated on the zeolite ferrierite and pure ferrierite.*

6.4.2 Determination changes in the oxidation state by in situ *XAS*

Figure 6.5 shows Pt L_3-edge XANES spectra (normalized and background subtracted) of the Pt/beta and Pt/ferrierite, collected under inert nitrogen atmosphere in a specialized *in situ* cell. The spectra of as well as Pt(IV)O_2, is added as well for comparison. It revealed that the platinum in as-prepared, after the complex remains are removed through calcination, are in the form of platinum (IV) oxide.

Let’s discuss the Pt(IV)O_2 XANES first. The XANES spectra of PtO_2 are dominated by large white line intensities originating from an orthorhombic crystal structure[38] with 2 long and 4 short bonds. The white line intensity (WLI) centred at 11569 eV of the PtO_2 and Pt/ferrierite is almost identical, and less intense for Pt/beta samples, indicating that the platinum particles inside the zeolite beta are partially reduced.

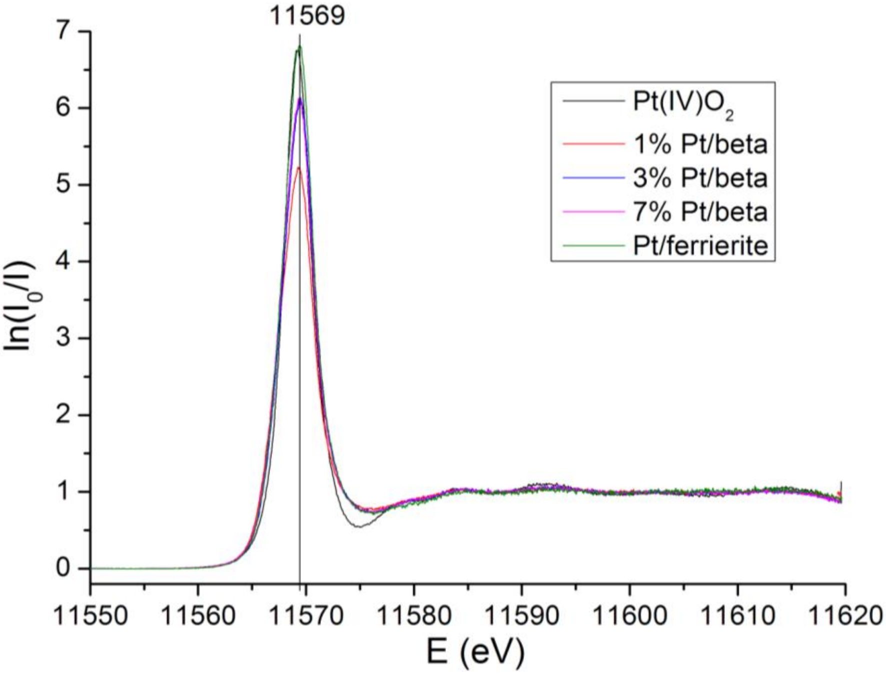

Figure 6.5. *Comparisons of the Pt L3 edge XANES of the as-prepared samples and* PtO_2.

The XANES spectra obtained after reduction with H_2 are shown in **Figure 6.6** (also plotted Pt metal), and **Figure 6.7**. The decrease of the white line intensity at the Pt L_3-edge ($2p_{3/2} \rightarrow 5d_{5/2}$) is due to the reduction of platinum ions to an oxidation state of zero. This was indicated also by a shift of the edge to lower energies, starting immediately after the introduction of the reducing atmosphere. All samples reduced in hydrogen at room temperature (1 and 7% Pt/beta, and 3% ferrierite) yielded Pt with oxidation state zero, apart from the sample 3% Pt/beta which was heated to 250°C. First, the samples reduced at RT will be discussed. The sharp change in the white line intensity in the XANES with time (**Figure 6.7**(a), (c), and (d)) was caused by the introduction of molecular hydrogen, and the subsequent reduction of the platinum clusters. After twenty minutes in a H_2 flow atmosphere, the edge of the spectrum was shifted by 1 eV and the absorption was dramatically decreased to resemble Pt metal. The edge of the spectrum was shifted by 3 eV for the heated 3% Pt/beta. The sharper Pt L_3 absorption edge of platinum clusters in the calcined sample is observed in comparison to the samples reduced at room temperature, and resemble more the edge of platinum metal. This is caused by lower interaction of the platinum clusters with chemisorbed hydrogen[39].

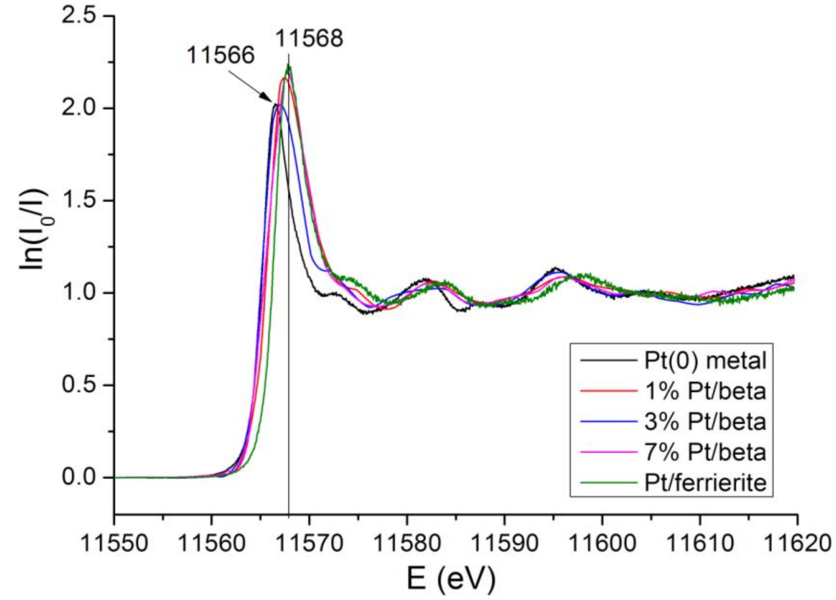

Figure 6.6. *Comparison of the Pt L_3 edge XANES of the reduced samples and platinum metals.*

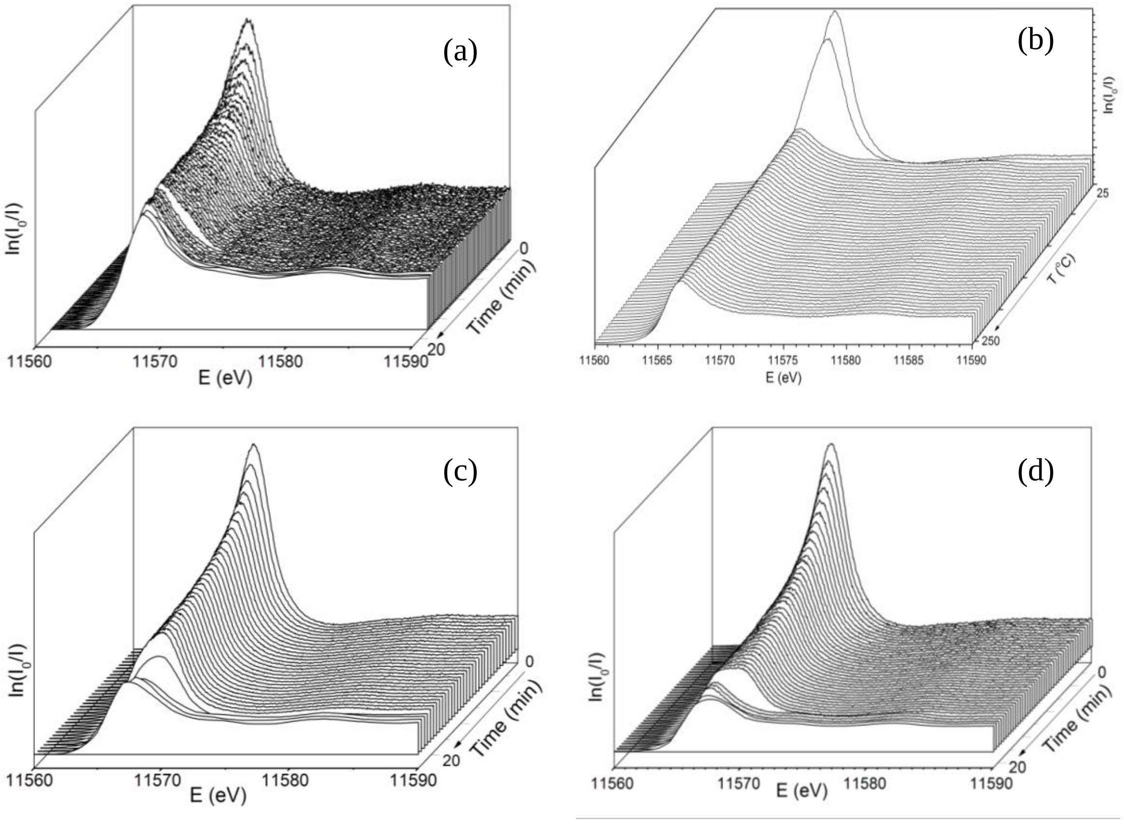

Figure 6.7. *Stacked plot of the normalized Pt L_3-edge XANES data as a function of time recorded during the reduction of: (a) 1% Pt/beta, (c) 7% Pt/beta, (d) 3% Pt/ferrierite, and (b) is displayed 3% Pt/beta as a function of temperature. Please note that that the rapid reduction in (c) and (d) was caused by increased flow of hydrogen gas into the cell.*

The reduction of the platinum clusters start by introducing hydrogen, and occur very fast (**Figure 6.7**). Complete reduction takes place below 100^{o}C in 3% Pt/beta sample.

6.4.3 TEM results

The TEM observations indicate a very high degree of metal dispersion. Images of the as-prepared and reduced samples are displayed in **Figure 6.8** for Pt/ferrierite and in **Figure 6.9** for 3% Pt/beta. In both samples, Pt particles outside the zeolite were detected. The zeolite channels are clearly seen and small Pt particles of 2-5 nm lengths are seen in as-prepared Pt/ferrierite, and which do not look crystalline. Similarities can be seen between particles in the normal and reduced form for each system, formed of 2-4 nm crystallites but no smaller particles were observed. The platinum in as-prepared 3% Pt/beta has nearly amorphous quasi-crystalline structure, and larger particles were not detected. Platinum in the reduced form is in the form of 2-4 nm crystallites within a polycrystalline structure very similar to reduced Pt/ferrierite.

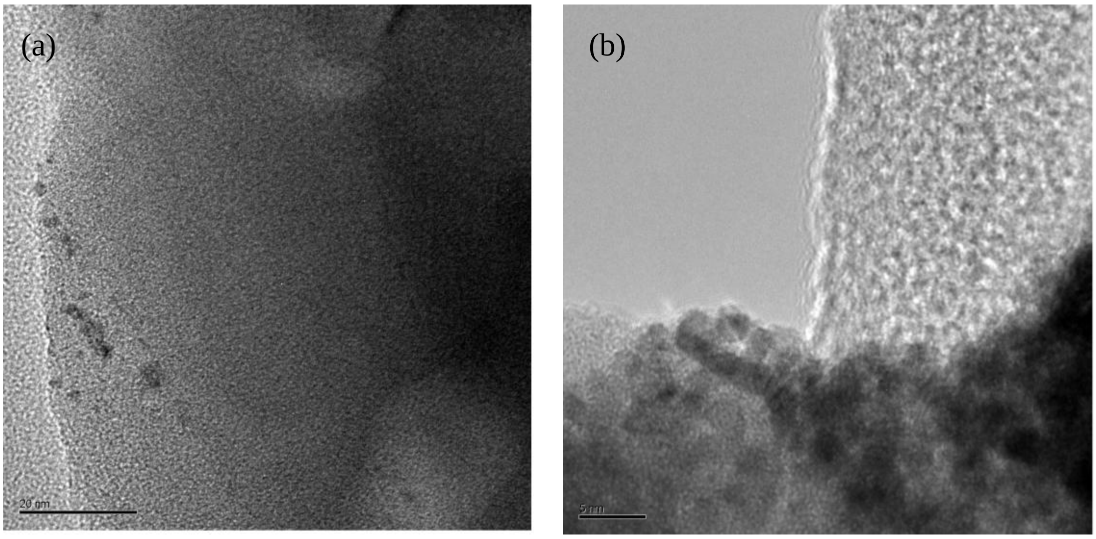

Figure 6.8. *TEM micrographs of (a) as-prepared, and (b) reduced Pt/ferrierite sample.*

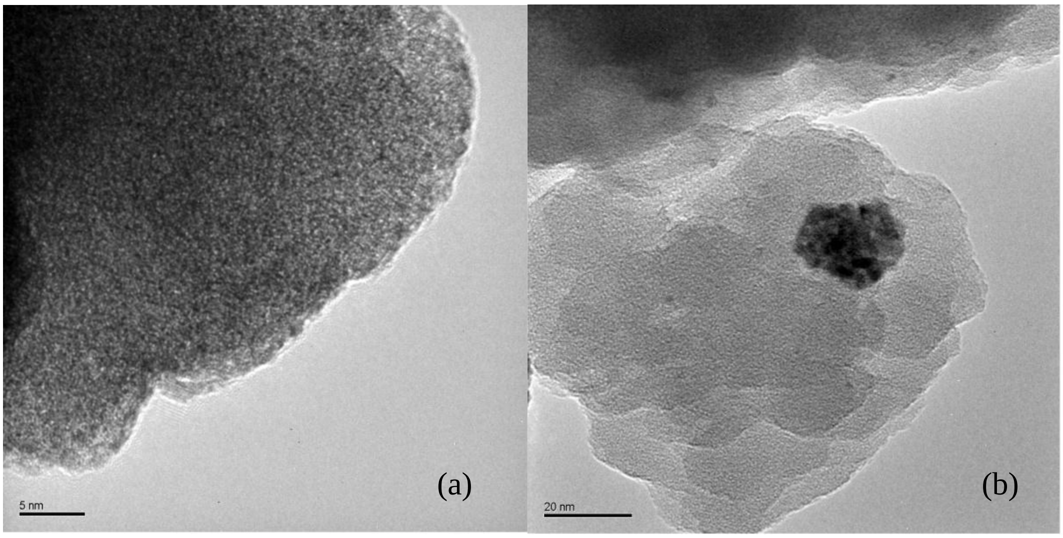

Figure 6.9. *TEM micrographs of (a) as-prepared, and (b) reduced 3% Pt/beta sample.*

6.5 Summary and Conclusion

The X-ray absorption spectroscopy of a Pt/beta and Pt/ferrierite catatalyst show that the platinum particles in as-prepared samples are in the form of Pt(IV)O_2, and can be easily reduced to metallic form even at room temperature. The Pt$_3$ XANES of metallic platinum particles reduced at 250^{o}C are much sharper than room temperature, and resemble the XANES spectra of platinum metal. This indicates that the energy distribution of the empty states in platinum clusters is affected by chemisorbed hydrogen. Higher X-ray absorption edges have been reported for Pt in zeolites if measured in presence of hydrogen. Furthermore, the platinum clusters inside the as-prepared zeolite beta are very small, and were not seen in TEM. Upon reduction, the size was estimated at 2-4 nm, which is very similar to zeolite ferrierite. The Pt clusters were detected in as-prepared Pt/ferrierite and the size estimated 2-4 nm.

References

[1] R. A. Meyers, *Handbook of petroleum refining processes*, McGraw-Hill, **2004**, p.

[2] in *International Platinum Group Metals Association, Vol.* www.ipa-news.com.

[3] F. Fischer and H. Tropsch in *Process for the production of paraffin-hydrocarbons with more than one carbon atom, Vol.* (Ed. U. S. P. Office), USA, **1930**.

[4] S. Nishimura, *Handbook of heterogeneous catalytic hydrogenation for organic synthesis*, John Willey & Sons, Inc., **2001**, p.

[5] *Oil and Gas Journal Data Book*, Pennwell Corp., **2006**, p.

[6] P. G. Smirniotis and E. Ruckenstein, *Catalysis Letters* **1993**, *17*, 341-347.

[7] E. Van Steen, L. H. Callanan and M. Claeys, *Studies in Surface Science and Catalysis* **2004**, *154*.

[8] a) H. K. Shin, H. Hirabayashi, H. Yahiro, M. Watanabe and M. Iwamoto, *Catalysis Today* **1995**, *26*, 13-21; b) D. C. Koningsberger, B. L. Mojet, G. E. van Dorssena and D. E. Ramaker, *Topics in Catalysis* **2000**, *10*, 143-155.

[9] H. G. Karge and J. Weitkamp, *Post-Synthesis Modification I*, Springer, **2002**, p.

[10] a) G. Bellussi and P. Pollesel in *Industrial applications of zeolite catalysts: production and uses of light olefins, Vol. 158* Eds.: J. Cejka, N. Zilkova and P. Nachtigall), **2005**, pp. 1201-1212; b) A. L. Ankudinov, J. J. Rehr, J. J. Low and S. R. Bare, *Journal of Synchrotron Radiation* **2001**, *8*, 578-580; c) A. L. Ankudinov, J. J. Rehr, J. J. Low and S. R. Bare, *The Journal of Physical Chemistry* **2002**, *116*, 1911-1919.

[11] a) W. M. H. Sachtler, *Catalysis Today* **1992**, *15*, 419-429; b) E. G. Derouane and D. J. Vanderveken, *Applied Catalysis* **1988**, *45*, L15-L22; c) I. E. Maxwell, *Catalysis Today* **1987**, *1*, 385-413; d) H. Igarashi, H. Uchida, M. Suzuki, Y. Sasaki and M. Watanabe, *Applied Catalysis A: General* **1997**, *159*, 159-169.

[12] a) R. Burch, J. P. Breen and F. C. Meunier, *Applied Catalysis B: Environmental* **2002**, *39*, 283-303; b) X. Liu, H. Dilger, R. A. Eichel, J. Kunstmann and E. Roduner, *The Journal of physical chemistry B* **2006**, *110*, 2013-2023; c) K. I. Pandya, S. M. Heald, J. A. Hriljac, L. Petrakis and J. Fraissard, *The Journal of physical chemistry* **1996**, *100*, 5070-5077; d) M. S. Tzou, M. Kusunoki, K. Asakura, H. Kuroda, G. Moretti and W. M. H. Sachtler, *The Journal of physical chemistry* **1991**, *95*, 5210-5215; e) C.

Besoukhanova, J. Guidot, D. Barthomeuf, M. Breysse and J. R. Bernard, *Journal of the Chemical Society, Faraday Transactions 1: Physical Chemistry in Condensed Phases* **1981**, *77*, 1595-1604; f) P. Gallezot, *Catalysis Reviews* **1979**, *20*, 121-154.

[13] R. L. Wadlinger, G. T. Kerr and E. J. Rosinski in *Catalytic composition of a crystalline zeolite, Vol.* (Ed. U. S. P. a. T. Office), Mobil Oil Corporation, United States, **1967**.

[14] a) M. M. J. Treacy and J. B. Higgins, *Collection of simulated XRD powder patterns for zeolites*, Elsevier, **2007**, p; b) H. van Bekkum, E. M. Flanigen, P. A. Jacobs and J. C. Jansen, *Introduction to zeolite science and practice*, Elsevier, **2001**, p.

[15] a) M. M. J. Treacy and J. M. Newsam, *Nature* **1988**, *332*, 249-251; b) J. B. Higgins, R. B. LaPierre, J. L. Schlenker, A. C. Rohrman, J. D. Wood, G. T. Kerr and W. J. Rohrbaugh, *Zeolites* **1988**, *8*, 446-452; c) A. W. Burton, S. Elomari, I. Chan, A. Pradhan and C. Kibby, *Journal of Physical Chemistry B* **2005**, *109*, 20266-20275.

[16] T. Conradsson, M. S. Dadachov and X. D. Zou, *Microporous and Mesoporous Materials* **2000**, *41*, 183-191.

[17] A. Corma, M. T. Navarro, F. Rey, J. Rius and S. Valencia, *Angewandte Chemie International Edition* **2001**, *40*, 2277-2280.

[18] a) R. B. LaPierre, R. D. Partridge, N. Y. Chen and N. J. S. S. Wong in *Catalytic dewaxing process*, *Vol.* (Ed. U. S. Patent), Mobil Oil Corporation, USA, **1983**; b) G. C. Edwards and A. W. Peters in *Cracking catalysts with octane enhancement, Vol. 4898846* (Ed. U. Patent), W.R. Grace & Co.-Conn., USA, **1990**.

[19] a) N. Y. Chen, A. B. Ketkar, D. M. Nace, A. Y. Kam, C. R. Kennedy and R. A. Ware in *Hydrocracking by zeolite beta*, *Vol.* (Ed. E. Patent), **1986**; b) N.-Y. Chen, H. Tracy and Jau-Hua in *Hydrocracking catalyst composition and hydrocracking process using same, Vol.* Mobil Oil Corp., **1989**.

[20] a) R. B. LaPierre, R. D. Partridge, N. Y. Chen and S. S. Wong in *Catalytic dewaxing process with zeolite beta*, *Vol. 4501926* (Ed. U. Patent), Mobil Oil Corporation, USA, **1985**; b) R. B. LaPierre, R. D. Partridge, N. Y. Chen and S. S. Wong in *Catalytic dewaxing process*, *Vol. 4419220* (Ed. U. Patent), Mobil Oil Corporation, USA, **1983**; c) S. M. Oleck and R. C. Wilson in *Process for hydrocracking and dewaxing hydrocarbon oils*, *Vol. 4486296* (Ed. U. Patent), Mobil Oil Corporation, USA, **1984**; d) P. J. Angevine, K. M. Mitchell, S. M. Oleck and S. S. Shih in *Hydrocracking*

process using zeolite beta, *Vol. 4612108* (Ed. U. Patent), Mobil Oil Corporation, USA, **1986**.

[21] L. B. Young in *Preparing phenylalkanes*, *Vol. 4301316* (Ed. U. P. Office), Mobil Oil Corporation, USA, **1981**.

[22] a) J. F. Denayer, W. Souverijns, P. A. Jacobs, J. A. Martens and G. V. Baron, *The Journal of physical chemistry B* **1998**, *102*, 4588-4597; b) A. E. Bond, C. G. V. Burgess and D. E. Martin in *Hydrocarbon separation process*, *Vol. 3793385* (Ed. U. P. Office), USA, **1974**.

[23] in *International Zeolite Association*, *Vol.* www.iza-online.org.

[24] R. P. D. Graham, *Royal Society Canada, Transactions and Proceedings* **1918**, *185*.

[25] a) I. J. Pickering, P. J. Maddox, J. M. Thomas and A. K. Cheetham, *Journal Name: Journal of Catalysis; (USA); Journal Volume: 119:1* **1989**, Medium: X; Size: Pages: 261-265; b) P. A. Vaughan, *Acta Crystallographica* **1966**, *21*, 983-990.

[26] C. Baerlocher, L. B. McCusker and D. H. Olson, *Atlas of Zeolite Framework Types, 6th edition*, Elsevier, Amsterdam, **2007**, p.

[27] W. E. Cormier and L. B. Sand in *Preparation of Synthetic Ferrierite*, *Vol.* (Ed. U. S. Patent), Zeochem Corporation, United States, **1977**.

[28] M. Hironaka, K. Itabashi and M. Nakano, *13th International Zeolite Conference* (Montpellier, France) **2001**.

[29] C. L. Kibby, A. J. Perrotta and F. E. Massoth, *Journal of Catalysis* **1974**, *35*, 256-272.

[30] a) A. A. Belhekar, R. K. Ahedi, S. Kuriyavar, S. S. Shevade, B. S. Rao, R. Anand and Z. Tvaruzkova, *Catalysis Communications* **2003**, *4*, 295-302; b) D. Seddon, *Journal of Catalysis* **1986**, *98*, 1-6.

[31] Mathys and e. al. in *Alkene oligomerization*, *Vol.* (Ed. US), Exxon Chemical Patents Inc., USA, **1997**.

[32] a) G. Onyestyák, J. Valyon, G. Pál-Borbély and L. V. C. Rees, *Applied Surface Science* **2002**, *196*, 401-407; b) T. Komatsu, H. Ishihara, Y. Fukui and T. Yashima, *Applied Catalysis A: General* **2001**, *214*, 103-109; c) R. J. Pellet, D. G. Casey, H. M. Huang, R. V. Kessler, E. J. Kuhlman, C. L. Oyoung, R. A. Sawicki and J. R. Ugolini, *Journal of Catalysis* **1995**, *157*, 423-435.

[33] a) Y. S. Jin, A. Auroux and J. C. Vedrine, *Applied Catalysis* **1988**, *37*, 1-19; b) J. F. Haw, W. Song, D. M. Marcus and J. B. Nicholas, *Accounts of Chemical Research* **2003**,

36, 317-326; c) Y. S. Jin, A. Auroux and J. C. Vedrine, *Applied Catalysis* **1988**, *37*, 21-33.

[34] a) P. Chu in *Aromatization of ethane, Vol.* (Ed. U. Patent), Mobil Oil Corporation, USA, **1978**; b) K. P. de Jong, H. H. Mooiweer, J. G. Buglass and P. K. Maarsen in *Activation and deactivation of the zeolite Ferrierite for olefin conversions, Vol. Volume 111* Eds.: C. H. Bartholomew and G. A. Fuentes), Elsevier, **1997**, pp. 127-138.

[35] A. A. Coelho in *TOPAS-Academic: General Profile and Structure Analysis Software for Powder Diffraction Data. , Vol.* **2007**.

[36] OriginLab in *OriginPro 8 SRO, Vol.* Northampton, USA, **1991-2007**.

[37] B. Ravel and M. Newville, *Journal of Synchrotron Radiation* **2005**, *12*, 537-541.

[38] S. Siegel, H. R. Hoekstra and B. S. Tani, *Journal of Inorganic and Nuclear Chemistry* **1969**, *31*, 3803-3807.

[39] M. Vaarkamp, B. L. Mojet, M. J. Kappers, J. T. Miller and D. C. Koningsberger, *The Journal of physical chemistry* **1995**, *99*, 16067-16075.

Chapter 7 Conclusion and Future Work

In this thesis, an extensive characterization study of metal doped nanoporous catalysts was presented. The main topics examined were: the effect of different methods of preparation, the structural chemistry that follows doping divalent cobalt ions in AlPO-18 frameworks, and the factors affecting the incorporation and stability of these materials. In addition to the study of materials, the thesis presents the development of a new *in situ* cell for studies of acid and redox properties of the doped frameworks using FTIR spectroscopy. A detailed investigation of structural changes of transition metal doped AlPO-18 and SAPO-18 during activation process and behaviour as a catalyst during methanol to olefins reaction were carried out using a suite of diffraction and spectroscopic techniques. The thesis also presents a detailed study to derive correlation between preparation/post-synthesis treatments on vanadium substituted ZSM-5 catalysts and their catalytic properties. Finally, a detailed investigation of the size of platinum clusters and local changes during activation of platinum containing zeolites are presented. In addition, attempts to localize the Pt clusters inside the zeolite ferrierite were made, however this was not resolved completely, and the result were not presented in this thesis.

The local environment around cobalt in CoAlPO-18 materials is increasingly distorted, if they are prepared with low aluminium-phosphorus Al/P ratio. This lack of aluminium can be caused by a variety of reasons, which is not completely clear from this study, since we focused only on the final structure of cobalt ions in the as-sythesised materials. This could be due to the nature of network of Al-O-P-O-Me formation at the initial stages, which needs a detailed study of the formation of these solids. However, the control of the synthesis can be easily achieved in laboratory condition but, when produced on industrial scale this could be a major issue. Specifically the study identified that these materials contain cobalt in the aluminophosphate lattice at very low concentrations with increased amounts of cobalt in the extraframework positions when low amounts of aluminium sources were used in the synthesis, which will directly affect the catalytic activity. The structure and concentration of framework and extraframework species have been confirmed by XAS and IR techniques. Special *in situ* IR cell was developed for this purpose to follow the formation Brönsted acid sites (when cobalt ions are present in the lattice) during activation process. The materials also show very low thermal stability when low levels of aluminium were used at the synthesis stage.

Lattice expansion has been observed if cobalt substitutes aluminium ions in the AlPO-18 lattice, and has been confirmed by high-resolution powder diffraction study. Furthermore, if the cobalt concentrations are low (below 7.5w%), mixed phase of AlPO-18 and CoAlPO-18 are observed. Many attempts were tried and the mixed phase was always present, if cobalt was incorporated, which could be caused by clustering of cobalt in the synthesis gels.

It was also possible to accurately determine the changes in the lattice parameter (CoAlPO-18, CoSAPO-18, SAPO-18, ZnAlPO-18) and correlate this with metal ion incorporation during activation of catalysts. Not only was it possible to provide direct evidence for metal incorporation into the AEI-lattice by X-Ray diffraction but also to determine the negative thermal properties of these materials and follow their stability during calcination. The larger Co(II) and Zn(II) incorporation into the framework they expand the lattice of AEI by as much as 40 percent when substituted for Al(III). The substitution of Si(IV) for P(V) has also been supported by evidence obtained from HRPD, based on the expansion of the lattice constant. The Pair-Distribution function (PDF) determined from high-energy X-ray diffraction (HEXRD) method provided an insight into the direction of possible lattice contraction during calcinations. This allowed us to rationalise some of the shape-selective catalytic properties of these solids but further high-quality HEXRD data are necessary to precisely model the structural changes associated with the negative thermal expansion of these solids.

The combined use of XAS and Raman spectroscopies only partially allowed the determination of how post-synthesis treatments are important in substitution of vanadium into zeolite lattice. In the as-prepared samples, majority of the V(IV) ions exhibit a strongly distorted square-pyramidal structure similar to $VOSO_4$. However, upon calcinations, in the good samples the majority of V(IV) is converted to V(V) with a non-hydroxylated pyramidal $(SiO)_3V{=}O$ structure, whereas in the less catalytically active ones remained in a structure that adopted a distorted tetrahedral structure with hydroxylated pyramidal $(SiO)_2(HO)V{=}O$ structure. However, further XAS studies are needed.

The X-ray absorption spectroscopy of a Pt/beta and Pt/ferrierite catatalyst showed that the platinum particles in as-prepared samples are in the form of Pt(IV)O_2, and can be easily reduced to metallic form even at room temperature. The Pt L_3 XANES of metallic platinum particles reduced at 250^{o}C are much sharper than room temperature, and resemble the XANES spectra of platinum metal. This indicates that the energy distribution of the empty states in platinum clusters is affected by chemisorbed hydrogen. Higher main absorption intensities have been reported for Pt in zeolites if measured in presence of hydrogen. Furthermore, the platinum clusters inside the as-prepared zeolite beta are very small, and could not be seen in TEM. Upon reduction, the size of the clusters were estimated to be 2-4 nm, which is very similar to the pores of zeolite ferrierite. The PtO_2 clusters were detected in as-prepared Pt/ferrierite and the size estimated 2-4 nm. Attempts were made to locate the platinum cluster inside the ferrierite structure, and one probable location was identified in this work (but not presented). However, this needs to be verified by further studies. Similar structural determination of Pt clusters in zeolite beta was not possible, since zeolite beta has more than one polymorph and they co-exist which makes the diffraction analysis very difficult.

Although the investigation carried out in the thesis allowed us to complete the aims of the project outlined at the start of the project, it is necessary to expand the successful implementation of various techniques to gain further knowledge on these systems. For example, it is necessary to carry out further studies on why only limited amount of cobalt ions are incorporated into the framework when low Al/P ratio is used in the initial stages of the synthesis. Similarly, modelling of the high-energy diffraction data needs to be developed further to clearly to determine the accurate structural changes that take place when the nanoporous materials are heated to high-temperature.